Coronary Artery Segmentation and Motion Modelling

Dong Ping Zhang

A dissertation submitted in partial fulfilment
of the requirements for the degree of
Doctor of Philosophy
of
Imperial College London

June 2010
Department of Computing
Imperial College London

谨以此书献给我的父亲母亲：

张朝英先生和刘琤芝女士

Declaration of originality

This document consists of research work conducted in the Department of Computing at Imperial College London between 2006 and 2010. I declare that the work presented is my own, except where specifically acknowledged in the text.

Abstract

Conventional coronary artery bypass surgery requires invasive sternotomy and the use of a cardiopulmonary bypass, which leads to long recovery period and has high infectious potential. Totally endoscopic coronary artery bypass (TECAB) surgery based on image guided robotic surgical approaches have been developed to allow the clinicians to conduct the bypass surgery off-pump with only three pin holes incisions in the chest cavity, through which two robotic arms and one stereo endoscopic camera are inserted. However, the restricted field of view of the stereo endoscopic images leads to possible vessel misidentification and coronary artery mis-localization. This results in 20-30% conversion rates from TECAB surgery to the conventional approach.

We have constructed patient-specific 3D + time coronary artery and left ventricle motion models from preoperative 4D Computed Tomography Angiography (CTA) scans. Through temporally and spatially aligning this model with the intraoperative endoscopic views of the patient's beating heart, this work assists the surgeon to identify and locate the correct coronaries during the TECAB precedures. Thus this work has the prospect of reducing the conversion rate from TECAB to conventional coronary bypass procedures.

This thesis mainly focus on designing segmentation and motion tracking methods of the coronary arteries in order to build pre-operative patient-specific motion models. Various vessel centreline extraction and lumen segmentation algorithms are presented, including intensity based approaches, geometric model matching method and morphology-based method. A probabilistic atlas of the coronary arteries is formed from a group of subjects to facilitate the vascular segmentation and registration procedures. Non-rigid registration framework based on a free-form deformation model and multi-level multi-channel large deformation diffeomorphic metric mapping are proposed to track the coronary motion. The methods are applied to 4D CTA images acquired from various groups of patients and quantitatively evaluated.

Acknowledgements

I am immensely grateful to Prof. Daniel Rückert for his support, feedback and advice throughout my MSc and PhD years. This thesis would not have been possible without his encouragement and guidance. I also would like to show my gratitude to Prof. Duncan Gillies and Dr. Kawal Rhode for examining this thesis and providing valuable comments.

I thank and offer my regards to all of the colleagues who supported me in any respect during the completion of this thesis: Dr. Laurent Risser, Dr. Philip Edwards, Ose Pedro, Claire Donoghue, Dr. Fani Deligianni, Dr. Emma Robinson, Dr. Paul Aljabar, Dr. Kanwal Bhatia, Dr. Raghavendra Chandrashekara, Maria, Tom, Duncan White, Prof. David Hawkes, Xiahai, Amani, Dr. Uri Zafarty, Dr. Michael Figl, Prof. Kensaku Mori, Dr. Ola Friman, Coert Metz, Prof. Wiro Niessen *et al.* Special thanks to Claire for those long nights and weekends working together in the office. I owe my deep gratitude to Paul and Kanwal who have provided many invaluable suggestions towards my confusions in both work and life abroad.

I am heartily thankful to many friends who have enriched my life and lightened my days in many ways, particularly, Lee Howes, Meital Covo, Ronglin Zhao, Carlos Tavares, Kulwant Bhatia, Xiaohan Pan, Ruifen Hu, Adiya, Ann Julia, Yolanda and many others. I would have never felt London is another home if not for the wonderful friendship shared with you.

Lastly, my brother Xinqin Zhang has brought me tremendous comfort and love. It is a huge pleasure to grow together with him.

Contents

List of Figures

List of Tables

Nomenclature

I	Image
Ω	Image domain
$\mathbf{x}$	Location in image domain $\mathbf{x} = (x, y, z)$
$\mathbf{T}$	Transformation
$\mathbf{T}^{-1}$	Inverse of transformation
$\mathbf{T}(\mathbf{x})$	Transformed position of location $\mathbf{x}$
$\mathbf{u}(\mathbf{x})$	Deformation of location $\mathbf{x}$
$I(\mathbf{x})$	Intensity of location $\mathbf{x}$ in image I
$I(\mathbf{T}(\mathbf{x}))$	Intensity of transformed location of $\mathbf{x}$ in image I
$\phi_{i,j,k}$	Location of control point (i, j, k)
Φ	Control point domain
$\mathbf{v}$	Velocity field
$p(i)$	Probability of a voxel with an intensity of i
$\mathcal{S}$	Similarity metric
$H(I)$	Entropy of image I
$\mathcal{H}$	Hessian matrix
λ_1, λ_2, λ_3	Eigenvalues of Hessian matrix
$\vec{v}_1$, $\vec{v}_2$, $\vec{v}_3$	Eigenvectors of Hessian matrix
$\mathcal{V}(\mathbf{x})$	Maximal vessel response at voxel $\mathbf{x}$ in a multi-scale framework
$v(\mathbf{x}, \sigma)$	Vesselness response at location $\mathbf{x}$ with pre-specified scale σ
∇	Vector differential operator del acting on the space coordinates
Δ or ∇^2	Laplacian operator
$\mathbf{J}$	Jacobian of deformation field
μ	Mean
$\mathcal{A}$	3D probabilistic atlas of the coronaries
$\mathcal{M}_{\mathrm{ED}}$	Patient-specific probabilistic atlas of the coronaries at end diastole
$\mathcal{C}$	Coronary centreline of a CTA image

Chapter 1

Introduction

"The heart . . . is the beginning of life; the sun of the microcosm . . . for it is the heart by whose virtue and pulse the blood is moved, perfected, made apt to nourish, and is preserved from corruption and coagulation; it is the household divinity which, discharging its function, nourishes, cherishes, quickens the whole body, and is indeed the foundation of life, the source of all action."

—— by William Harvey, 1628 [88].

1.1 Motivation

Conventional cardiac surgery is one of the most invasive and traumatic forms of open-chest surgery, because it requires exposure of the heart and its vessels through median sternotomy. In contrast to this, minimally invasive heart surgery for coronary artery diseases includes several approaches for bypassing critically blocked arteries. These approaches allow access to the heart through small incisions without stopping the heart, or separating the breastbone and ribcage, or putting the patient on a heart-lung machine during the surgery. Three different chest wall incisions for cardiac surgery are illustrated in Figure 1.1. Figure 1.2 shows a small left anterior thoracotomy for anastomosis without using a cardiopulmonary bypass.

Patients who have minimally invasive procedures instead of conventional open heart surgery have a lower risk of complications associated with heart-lung machines such as stroke, lung problems, kidney problems, and problems with mental clarity and memory. In addition to reduced complications, by eliminating the need for a painful sternotomy, the greatest benefit for the patient is to recover and resume normal activities more quickly than those patients who endure the conventional cardiac surgery [56, 186].

For the year ending March 2005, 35,986 heart surgeries were performed in UK.

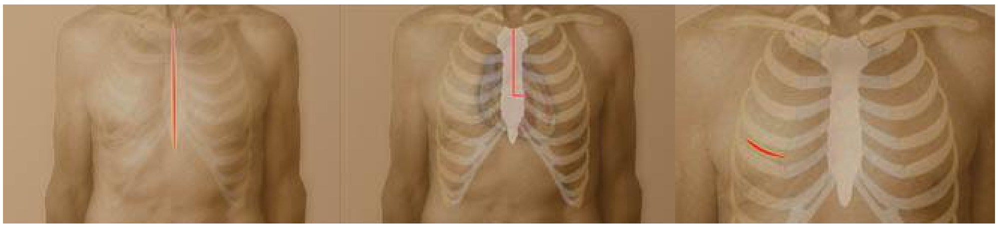

Figure 1.1: Chest wall incisions for a heart surgery [100]. Left: median sternotomy incision. Middle: minimally invasive approach with partial upper sternotomy. Right: minimally invasive approach with small right thoracotomy incision.

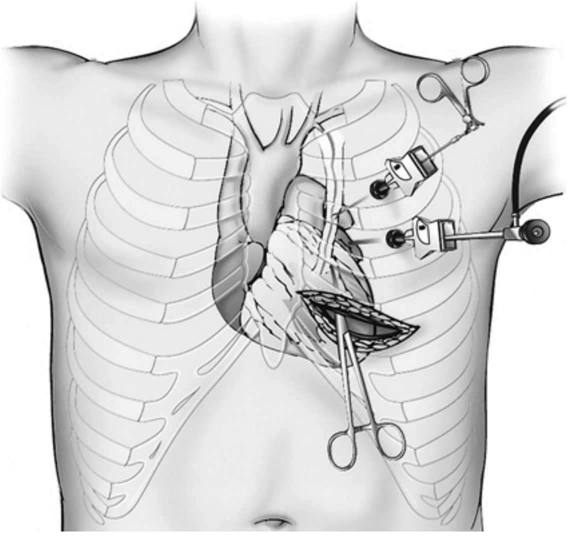

Figure 1.2: A small left anterior thoracotomy used to construct limited anastomosis without the use of cardiopulmonary bypass (CPB) [78].

These surgeries include coronary bypass, repair or replacement of heart valves and many other types of operations, such as repairing holes in the heart, dealing with scars on the heart and diseases of the aorta (the main artery from the heart). On average, over half of the operations are coronary bypass graft surgery, a third are aortic valve replacement operations and the rest are a mixture of combined operations (e.g., a coronary bypass combined with a valve operation) and other operations [7]. Currently, there are three main types of minimally invasive coronary artery bypass procedures: minimally invasive direct coronary bypass (MIDCAB), off-pump coronary artery bypass (OPCAB) and robotic assisted coronary artery bypass (RACAB).

Robotic assisted heart surgery [157], also referred to as closed-chest heart surgery, is a type of minimally invasive heart surgery performed by a cardiac surgeon with the support of robotic surgery system (for example, the da Vinci robotic surgical system shown in Figure 1.3). The surgeon uses a specially designed computer console to control surgical instruments on thin robotic arms. First, three small incisions or ports are made in the spaces between the ribs. The surgical instruments and one stereo camera attached to the robotic arms are then inserted through these ports. After the surgeon's fingers grasp the master controls below the display, the system then seamlessly translates the surgeon's hand, wrist and finger movements into precise, real-time movements of surgical instruments inside the patient during the operation.

Figure 1.3: Da Vinci surgical system [101].

The surgeon sits at a computer console and looks through two displays (one for each eye) that show images from the two tiny cameras placed inside the patient. Foot pedals provide precise camera control, so the surgeon can instantly zoom in and out to change the surgical view. The surgeon's hands control the movement and placement of the endoscopic instruments. The robotic arm and wrist movements mimic those of the surgeon, yet are possibly more precise than the surgeon's natural hand and wrist movements, because of the motion scaling and tremor reduction by the instruments.

Robotically-assisted surgical techniques can be used in many heart operations, including mitral valve repair and replacement, tricuspid valve repair and replacement, coronary artery bypass graft, removal of cardiac tumors and so on. But performing surgery on a beating heart through "pinholes" is technically more difficult than working on a heart that has been stopped with the help of the heart-lung machine due to the movement of heart and the lack of visibility of clinically relevant anatomical structures. In addition, the stress on the heart during the procedure may lead to more heart muscle damage, lower blood pressure, irregular heart beat and, potentially, brain injury if blood flow to the brain is reduced for too long during surgery. In some cases, it is necessary to convert to conventional heart surgery methods on an emergency basis.

1.1.1 Coronary Heart Disease (CHD)

It is widely acknowledged that coronary heart disease is the leading cause of death and disability worldwide. CHD is responsible for approximately 7.2 millions of deaths worldwide in 2004. It accounts for 12.2% of all deaths worldwide. Nearly 82 percent of these deaths occur in low and middle-income countries [39].

As the most common cause for CHD, coronary artery disease (CAD) occurs due to the failure of the blood circulation to supply adequate oxygen and nutrition to cardiac tissues. CAD is typically caused by the excessive accumulation of atheromatous plaques and fatty deposits within certain regions of the arteries that restrict the blood flow. Lifestyle changes, medicines, and medical procedures (for example, percutaneous transluminal coronary angioplasty and bypass surgery) can effectively prevent or treat CAD in most people. When treating this disease by performing coronary bypass surgery, arteries or veins grafted from the patient's body are used to bypass the blockages and restore the supply to the heart muscle. Figure 1.4 illustrates the anatomy of coronary arteries together with the ventricles. Figure 1.5 shows a segment of normal artery with normal blood flow and also one narrowing of the artery with the corresponding cross-sectional view.

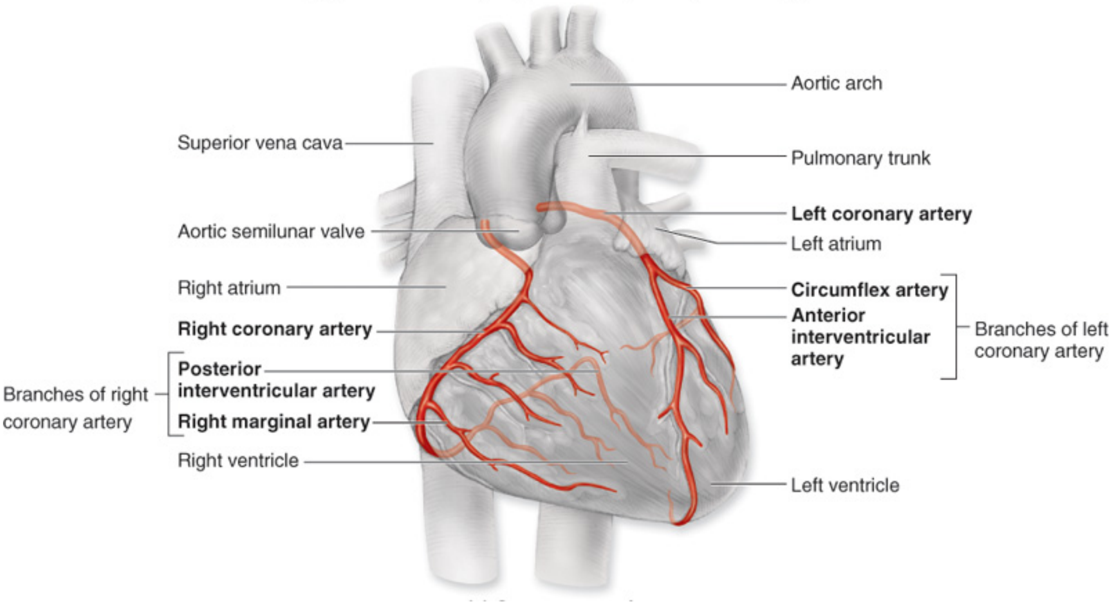

Figure 1.4: Coronary arteries [91]

Using image-guided robotic surgical systems, totally endoscopic coronary artery bypass (TECAB) surgery techniques have been developed to allow clinicians to perform bypass surgery off-pump with three pin-hole incisions in the chest cavity, through which two robotic arms and one stereo endoscopic camera are inserted. However, 20-30% conversion rates from TECAB surgery to the conventional invasive surgical approach [60, 158] have been reported due to the vessel misidentification and mislocalization caused by the restricted field of view of the stereo endoscopic images.

The goal of our work is to construct a patient-specific 4D coronary artery motion model from preoperative cardiac Computed Tomography Angiography (CTA) sequences. By temporally and spatially aligning this model with intraoperative endoscopic views of the patient's beating heart captured by the endoscopic cameras in the da Vinci surgical system, this work potentially can be used to assist the surgeon to identify and locate the correct coronaries during the TECAB procedures [67, 68].

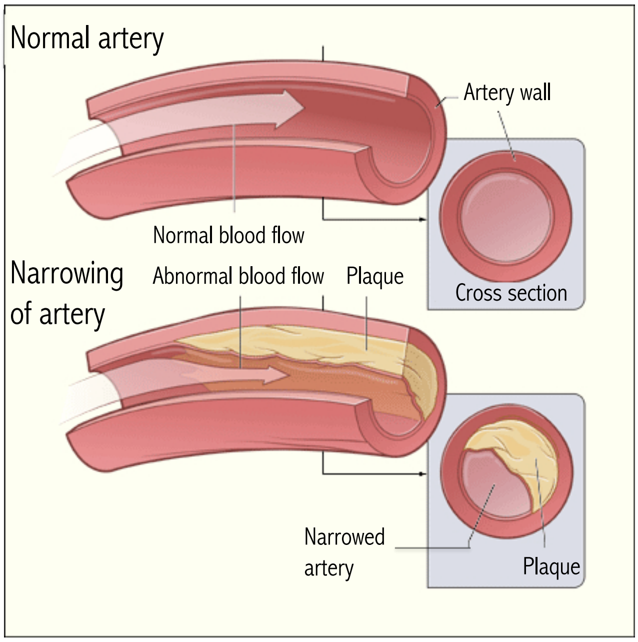

Figure 1.5: A normal artery with normal blood flow (top) and an artery with plaque buildup (bottom) [143].

1.1.2 Image Guidance for Cardiac Surgery

Under the increasing pressure to lower healthcare costs and improve outcomes, minimally invasive methods are replacing traditional surgical procedures as quickly as the technology allows. Many treatments that would previously have required open surgery can already be carried out using endoscopes, catheters and other instruments. Such minimally invasive approaches reduce trauma, thus minimizing damage to healthy tissue and requiring less pain medication. This shortens recovery times and is better for the patient. Many minimally invasive procedures can even be carried out in an outpatient setting. Generally, they are also less costly for the hospital, which is always important in delivering the best possible healthcare on ever tightening budgets. There are, however, challenges: During open surgery, surgeons can see where the organs are and what they are doing. For minimally invasive interventions, interventional specialists need other information sources to be able to view their actions. To provide image guidance for cardiac surgery, pre-operative medical images and intra-operative images are acquired.

1.1.2.1 Pre-operative Imaging

To analyse the pre-operative images and build motion models prior to the operation would help the surgeon to better visualise the structure of interest, understand the intra-operative images and plan the procedure. The most popular pre-operative scans for cardiac interventions are echocardiography [159], magnetic resonance imaging (MRI) [213] and computed tomography (CT).

Echocardiography, also known as cardiac ultrasound, traditionally uses standard ultrasound techniques to image two-dimensional slices of the heart. The latest ultrasound systems now employ 3D real-time imaging. Echocardiography is one of the most widely diagnostic tests for cardiovascular diseases. It can provide rich information to allow the assessment of cardiac valve areas and function, any abnormal communications between the left and right side of the heart, any leaking of blood through the valves, and calculation of cardiac output as well as ejection fraction. By assessing the motion of the heart wall, echocardiography can help detect the presence and assess the severity of coronary artery disease, as well as help determine whether any chest pain is related to heart disease. Echocardiography can also help detect hypertrophic cardiomyopathy. The biggest advantage to echocardiography is that it is non-invasive, easy to acquire and has no known risks or side effects.

MRI uses powerful magnetic fields that cause hydrogen nuclei within the body's water molecules to resonate, emitting radio-frequency energy. The spin of the atomic nuclei can be considered as a magnetic vector, causing the protons to behave like a magnet. Even tiny differences in tissue change the rates at which this energy is emitted. The image acquisition involves an initial sequence of exciting pulses and the recording of the emitted signal. The amplitude of the signal is used to generate maps showing the anatomy of the body. MRI provides remarkably clear and detailed pictures of internal organs and soft tissues with high contrast. The procedure is valuable in diagnosing a broad range of conditions in all parts of the body, including heart disease, cancer and joint and musculoskeletal disorders. Compared with X-ray, CT and other imaging techniques, MRI does not require exposure to radiation or the introduction of radioisotopes to the body, and it is suitable for routine screening. Even without the use of contrast material, MRI often shows sufficient detail of the heart to be valuable in diagnosis and treatment planning. When contrast is used, MRI contrast material is less likely to produce an allergic reaction than the iodine-based materials used for conventional X-rays and CT scanning. Nevertheless MRI should be avoided for patients with metal implants, because the strong magnetic field can affect the implants.

Recent advances in MRI allow a wide range of cardiovascular applications. Cardiovascular MRI is becoming very important in the initial diagnosis and subsequent treatment of heart disease. It can help clinicians to look closely at the structures and function of the heart and major vessels quickly and thoroughly, without the risks associated with traditional, more invasive procedures. Using MRI, clinicians can examine the size and thickness of the chambers of the heart, and determine the extent of damage caused by a heart attack or progressive heart disease. After a heart attack, for example, a MRI examination can help the cardiologist understand how well the heart is contracting and expanding, whether the flow of blood is blocked in any chamber or major vessel, whether the heart muscles are damaged or whether the lining of the heart is swelling. Cardiovascular MRI can also help to detect the buildup of plaque and blockages in the blood vessels, making it an invaluable tool for detecting and evaluating coronary artery disease.

CT is a medical imaging method that is based on the tomographic reconstruction procedure. A 3D image of an object can be reconstructed from a series of 2D X-ray images taken around a single axis of rotation. For more details on CT image reconstruction, we refer to [108] by Kak *et al.*.

Since the introduction of the first clinical system by Hounsfield in 1972, five generations of scanners have been produced, with different tube-detector configuration and scanning motion. Table 1.1 summarises the five generations of CT scanner technology. Fishman *et al.* provide more details of CT scanner technology in [64].

Table 1.1: Different generations of CT scanner technology [64]

Generation	Configuration	Number of detectors	Beam	Minimum scan time
1st	translate-rotate	$1 \sim 2$	pencil thin	2.5 min
2nd	translate-rotate	$3 \sim 52$	narrow fan	10 sec
3rd	rotate-rotate	$256 \sim 1000$	wide fan	0.5 sec
4th	rotate-fixed	$600 \sim 4800$	wide fan	1 sec
5th	electron beam	1284	wide fan electron beam	33ms

The new development of CT scanners means a promising future for CT imaging used in cardiovascular disease diagnosis. The speed advantages of 64-slice CT have rapidly established it as the minimum standard for newly installed CT scanners intended for cardiac scanning. Dual Source CT scanners with dual X-ray tube and dual array of 64-slice detectors were introduced by Siemens in 2005. Dual source CT allow higher temporal resolution by acquiring a full CT slice in only a quarter of a rotation, thus reducing motion blurring at high heart rates and potentially allowing for shorter breath-hold time. This is particularly useful for ill patients who have difficulty holding their breath or who are unable to take heart-rate lowering medication.

With the advent of subsecond rotation speeds combined with multi-slice CT (up to 320-slice by 2009 [225]), high resolution and high speed CT scanning can be obtained at the same time, allowing excellent imaging of the cardiovascular system. CT also allows for the study of multiple components of cardiac parameters within one exam. Images with an even higher temporal resolution can be formed using retrospective ECG gating. In this technique, the patient heart is imaged multiple times during one heart-beat while an ECG trace is recorded. The ECG signal is then used to correlate the CT data with their corresponding phases of cardiac contraction. A sequence of 3D CT images can then be reconstructed according to this information. By doing so, individual frames in a cardiac CT sequence have a better temporal resolution than the shortest tube rotation time.

Despite its advantages, CT scanning is not a substitute for other imaging techniques in all cardiovascular conditions. Relatively poor tissue contrast in CT images when compared to MRI can be a problem, despite the use of contrast agents. Unlike an echocardiogram machine, the CT scanners cannot be brought to the bedside of an acutely ill patient. Although CT scans account for only 4% of X-ray examinations, they contribute to more than 20% of the radiation dose to the population by medical X-rays. Typically, the dose for CT chest examination is around 400 times of that of a single X-ray examination [230].

The remarkable advantage of MRI and CT modalities is the high-resolution volumetric imaging of the cardiac anatomy in tomographic planes of any desired position. Both MRI and CT imaging allow not only the acquisition of high-resolution 3D cardiac images that describe the cardiac anatomy but also the acquisition of 4D image sequences that describe both the cardiac anatomy and function. The high tissue contrast of MRI images enables the assessment and measurement of different cardiac structures, facilitating a comprehensive evaluation of cardiac health. However, cardiac CT is more frequently used in acquiring 4D cardiac images due to its fast scanning speed that leads to the minimal disturbance from respiratory motion.

In summary, echocardiography, CT and MRI techniques all are very useful for imaging structures such as cardiac ventricles and aorta. Due to the relatively longer acquisition time that is required for MRI, CT and echocardiography are more frequently used to monitor the motion of those structures. Unlike CT, both standard MRI and echocardiography could not image small structures like coronaries up to the level of visibility required for the diagnosis or treatment procedures. In section 1.2, we will present the enhanced imaging techniques specially focusing on coronary artery.

1.1.2.2 Intra-operative Imaging

During the operation, stereo endoscopic videos can be captured by the inserted cameras to provide intra-operative views while using the da Vinci System for the TECAB surgery. Figure 1.6 shows a pair of static stereo images from the endoscopic videos acquired at 50 frames per second during the TECAB operation.

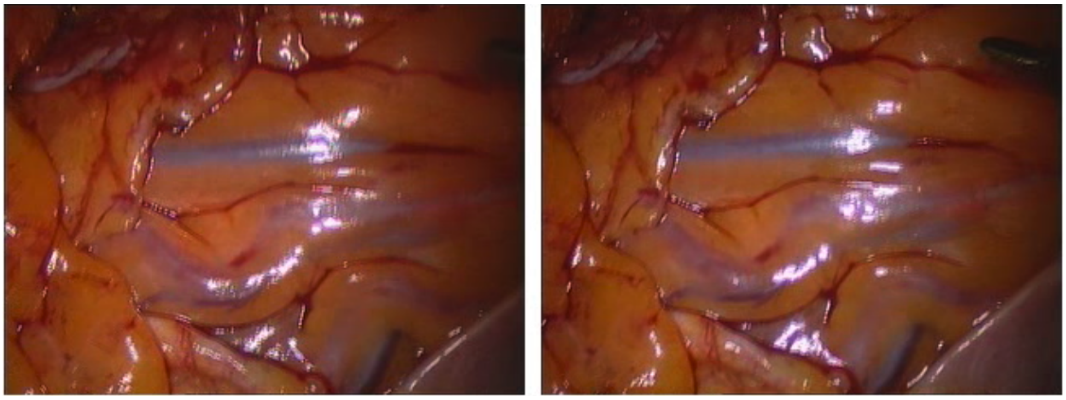

Figure 1.6: Endoscopic stereo views (left and right) of the coronary arteries.

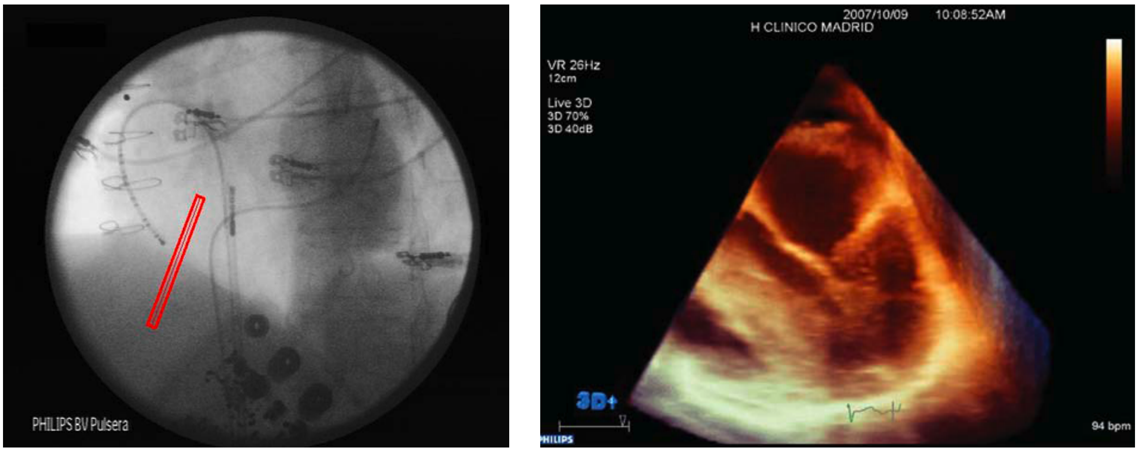

(a) (b)

Figure 1.7: (a): A manually delimited region of interest for tracking diaphragm motion in live fluoroscopic X-ray images [113]; (b): 3D echocardiography evaluation of the mitral valve [229].

Fluoroscopy and echocardiography have also been long used in the medical community to provide intra-operative image guidance for the cardiac surgery. As a type of medical imaging, fluoroscopy shows a continuous X-ray image on a monitor, like an X-ray movie. It is used for the diagnosis of disease or treatment for patients by displaying the movement of objects of interest (e.g. organs, instrument or contrast agent). During a fluoroscopy procedure, an X-ray beam is passed through the body. The image is transmitted to a monitor so that the structure of interest and its motion can be seen in detail. Fluoroscopic images can be taken intra-operatively to assist cardiac surgery or interventions, e.g., [177, 65, 113]. In many surgical procedures, echocardiography is also employed during the operation to provide guidance [229, 16, 95, 114]. Figure 1.7 shows examples of fluoroscopic X-ray and echocardiography images.

1.2 Coronary Artery Imaging

Following the discussion of image guidance for cardiac surgery from the pre-operative and intra-operative perspectives, in this section we introduce the medical imaging techniques that can be used to image the coronary arteries, as listed in Table 1.2. We focus on the image modalities closely related to our work, e.g, MRA, CTA and others.

Table 1.2: Advances in medical imaging techniques related to coronaries

1895	Chest X-ray
1896	Fluoroscopy
1931, 1937	Angiography
1958	Selective coronary arteriography
1972	Computed tomography
1979, 1990	Ultrafast computed tomography
1984	Magnetic resonance imaging of cardiovascular system [92]
1990	Electron beam tomography for coronary calcium
1990s	Single-photon emission computed tomography
1991	Optical Coherence Tomography [97]
1994	Intracoronary ultrasound [165]
2004	64-slice CT scanning (Siemens Somatom Sensation 64-slice CT system)

1.2.1 Biplane X-ray Angiography

A biplane X-ray system employs two X-ray tubes and two X-ray detectors for obtaining images from the subject in two different planes respectively. Subsequently, biplane coronary angiograms allow visualisation of the coronary morphology from two different directions. Figure 1.8 illustrates Philips Allura Xper FD10/10 as an example of biplane X-ray systems.

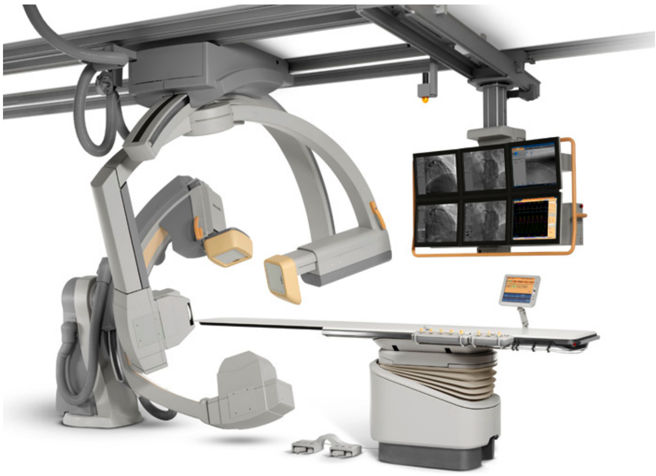

Figure 1.8: Biplanar cardiovascular X-ray system: Philips Allura Xper FD10/10 (www.healthcare.philips.com).

Biplane X-ray angiograms deliver twice the information with a single contrast injection, compared with monoplane X-ray angiograms. Figure 1.9 shows a pair of biplane X-ray angiograms of the coronary arteries from one subject. The state-of-art biplane X-ray systems are flexible enough to operate both pre-operatively and intra-operatively. However, the major drawback of biplane angiography is being invasive and also lacking of 3D information. A 3D reconstruction of the vascular structures becomes essential after acquiring the two 2D X-ray angiograms.

Figure 1.9: Biplane X-ray angiograms of coronaries (left: view 1; right: view 2)

1.2.2 Magnetic Resonance Angiography

Magnetic resonance angiography is a variant of MRI specially for imaging vasculature structures. MRA is often used for the arteries in the brain, neck, abdomen and legs where less motion is at present. When it is used for imaging coronary arteries, navigator echo-based respiratory gating technique is used to eliminate the respiratory motion [213]. Also, to ensure complete freezing of cardiac motion, data acquisition is generally limited to the coronary artery rest period (mainly found during mid-diastole).

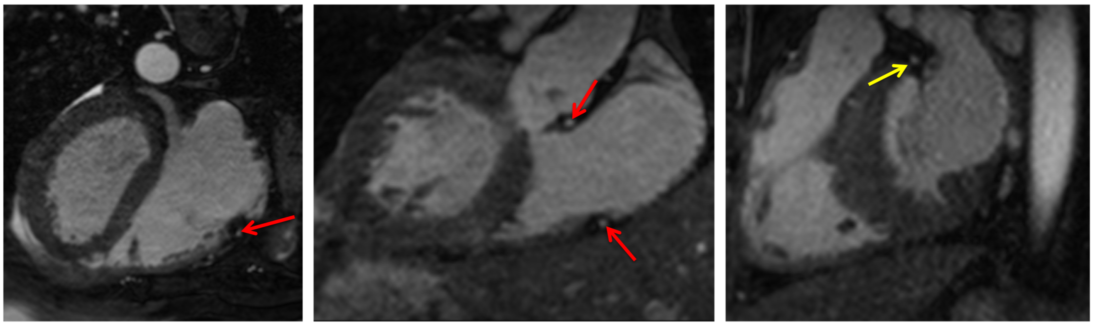

Figure 1.10: MRA images (transversal, coronal and sagittal views). Red arrows point to the right coronary artery; Yellow arrow shows the left coronary artery.

Figure 1.10 shows contrast enhanced MRA images from one subject in three different views. To acquire this type of MRA scan, a MRI contrast agent is injected into a vein. Images are then acquired when the contrast medium is passing through the arteries.

1.2.3 Computed Tomography Angiography

Developments in multi-detector CT and reconstruction techniques allow for fast acquisition of high-resolution images, with large impact on cardiac imaging. Images acquired with contrast injection (CTA) contain many details of the complex heart and surrounding vessel structures, with promising perspectives for assessment of coronary artery disease in a less invasive manner than conventional angiography.

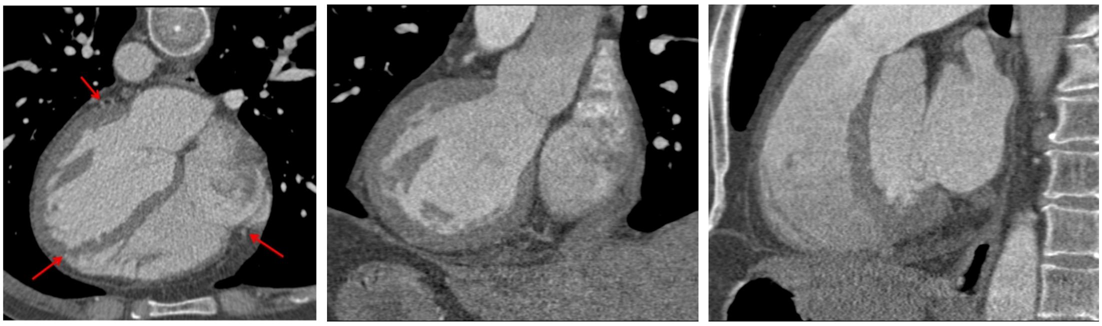

Figure 1.11: Cardiac CTA images (transversal, coronal and sagittal views). Red arrows point to the coronary arteries.

Similar to MRA, CTA is an imaging technique specialised in visualising arterial and venous vessels. It can be used to generate images of the coronaries in order to evaluate them for stenosis, occlusion or aneurysms. Based on standard CT techniques, a CTA scan is performed simultaneously with a high-speed contrast medium injection into a small peripheral vein. Figure 1.11 displays three views of the CTA scan from one patient.

Compared with MRA, acquiring a 4D CTA sequence is much faster and less affected by respiratory motion or body motion of the patient. CTA images also provide higher in-plane and out-of-plane resolution that is essential for visualising tiny distal parts of the vessels. For further comparison between CTA and MRA imaging, see [204, 29]. In this thesis, 4D CTA sequences are used to study the motion of the left ventricle and coronary arteries.

1.2.4 Other Modalities

Apart from the aforementioned conventional coronary imaging techniques, there are other imaging modalities which can be used to acquire images of the coronaries, such as coronary artery microscopy [218], intraoperative fluorescence imaging [94] and vascular elastography [150]. Two more recently developed intra-vascular imaging modalities are intravascular ultrasound and optical coherence tomography. Since both modalities are promising techniques we will briefly describe them.

1.2.4.1 Intravascular Ultrasound (IVUS)

The current “gold standard” of invasive angiography shows only the lumen, as the X-ray produces a “shadow image” created by the injection of contrast dye (as seen in Figure 1.9). Although angiography can show the “narrowing” of vessels and a dynamic picture of the blood flow, it does not differentiate plaque and the other layers within the vessel wall. Angiographic imaging is also considered unreliable when visualising regions with multiple overlapping arterial segments. In contrast, intravascular ultrasound (IVUS) can provide physicians with a better understanding of blocked vessels, which allows for proper selection for bypass surgery or placement of stents and other devices to restore blood flow at the site of the blockage.

IVUS is a medical imaging technology using a specially designed catheter with a miniaturized ultrasound probe placed on the tip of it. The proximal end of the catheter is attached to computerized ultrasound equipment. This tiny catheter is inserted into a vessel where high-frequency sound waves reflect off tissue or vessel walls. The reflected sound waves create a cross-sectional image from within the vessel throughout the surrounding blood to aid in visualising inner wall of vessel structure in vivo. Figure 1.12 shows an IVUS image of the coronary artery. It shows distinct circular layers inside a cross-sectional view of the artery. As the figure shows, IVUS allows clinicians to see the composition of the vessel wall in real-time. It yields information that goes beyond what is possible with routine imaging methods, such as coronary angiography or even non-invasive multislice CT scans. The information from IVUS can aid in stenosis grading, stent sizing, and in confirmation that the stent has been placed optimally.

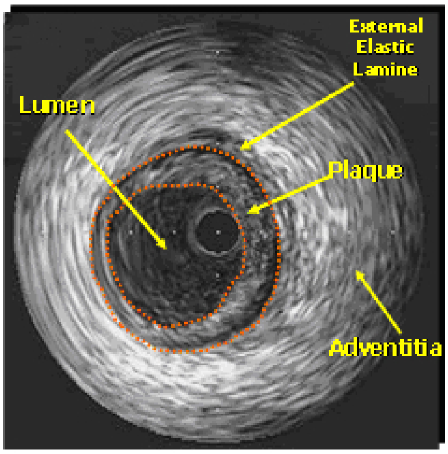

Figure 1.12: Example of IVUS imaging segmentation and its major components (www.incor.usp.br/spdweb/projetos_eng/ivus.htm).

Coronary arteries are the most frequent imaging target for IVUS. IVUS can be used in coronary artery imaging to determine the amount of atheromatous plaque built up at any particular point inside the artery. The progressive accumulation of plaque within the artery wall over decades may lead to stenosis of the artery and heart attack. IVUS can be used not only to determine both plaque volume and the degree of stenosis, but also to assess the effects of treatments of stenosis such as with hydraulic angioplasty expansion of the artery with or without stents, and the results of other medical therapies over time. Figure 1.13 shows an example of combination of non-invasive imaging with multislice computed tomography (MSCT) angiography and invasive imaging with coronary angiography and intravascular ultrasound [225].

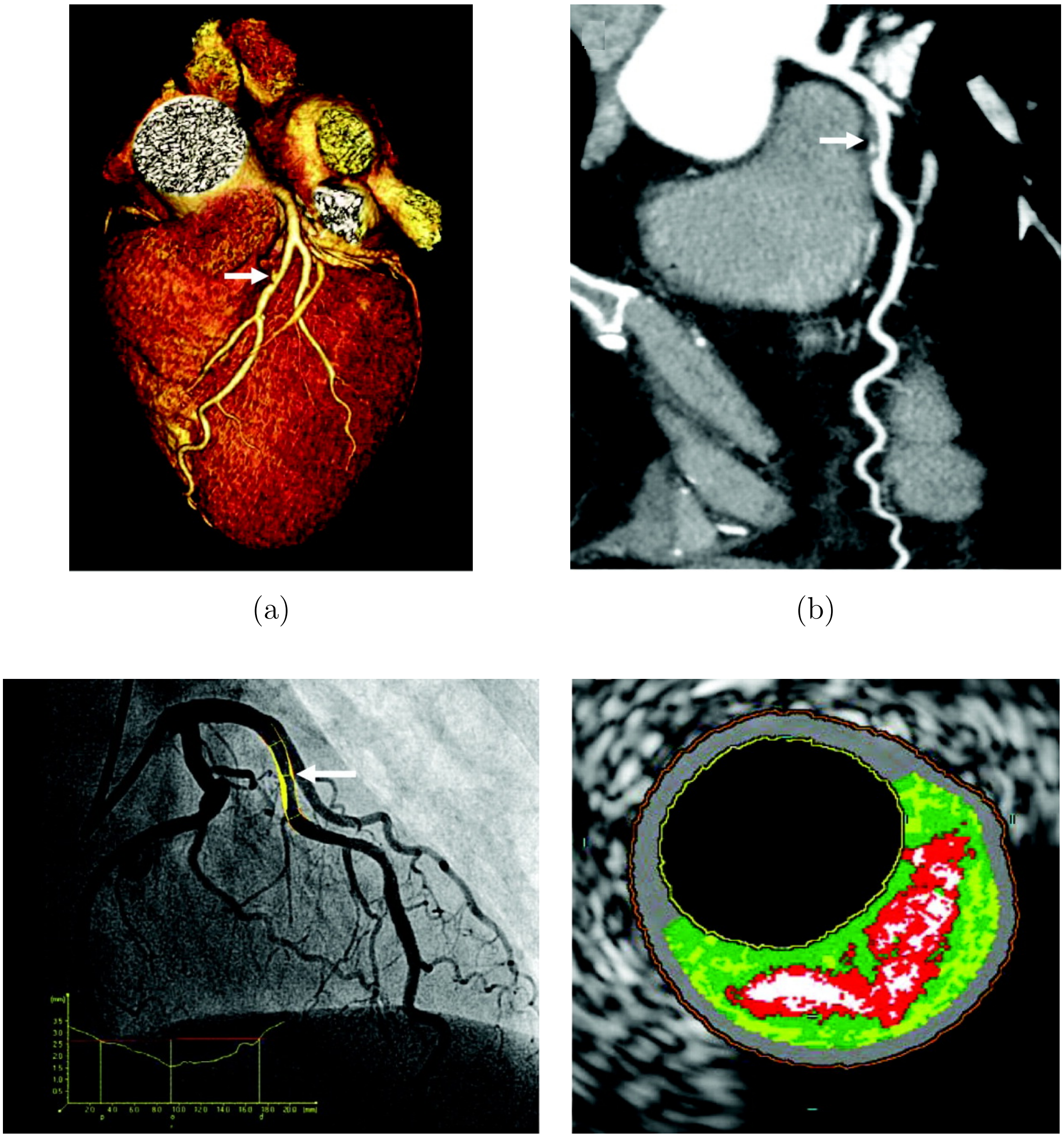

(a) (b)

(c) (d)

Figure 1.13: Combination of MSCT angiography, coronary angiography and IVUS. (a): Volume rendering of CT reconstruction, with arrow pointing to a lesion with intermediate luminal narrowing in the mid-section of the left anterior descending (LAD); (b): Curved multiplanar reconstruction of the LAD and its corresponding lesion; (c): Conventional coronary angiography, with the narrowing found on MSCT image confirmed; (d): A substantial amount of necrotic core (labelled in red) is shown in the corresponding IVUS image of the coronary segment [225].

1.2.4.2 Optical Coherence Tomography (OCT)

As a new type of optical imaging, optical coherence tomography (OCT) is an intravascular diagnostic modality capable of imaging the arterial wall with a resolution of around 10 μm. OCT performs high resolution, cross-sectional tomographic imaging of the internal microstructure in biological systems. It is analogous to intravascular ultrasound, except that it measures the magnitude and echo time delay of light rather than sound. The advantage of OCT lies in its ability to perform 'optical biopsy', yielding cross-sectional images of pathology in situ and in real time.

The axial resolution in OCT is determined by the bandwidth of the light source used for imaging. Current OCT imaging technologies have axial resolutions ranging from 1 μm to 15 μm, approximately $10 - 100$ times finer resolution than standard ultrasound imaging. The inherently high resolution provided by OCT imaging enables the visualization of tissue architectural morphology. OCT is ideally suited for ophthalmology, because of the ease of access to the eye and the lack of other methods for obtaining microstructural information. The principal disadvantage of OCT imaging is that light is highly scattered by most biological tissues. In tissues other than the eye, optical scattering limits image penetration depths to ~2 mm. However, because OCT is an optical technology, it can be integrated into a wide range of instruments such as endoscopes, catheters, laparoscopes, or needles, which enable the imaging of internal organ systems.

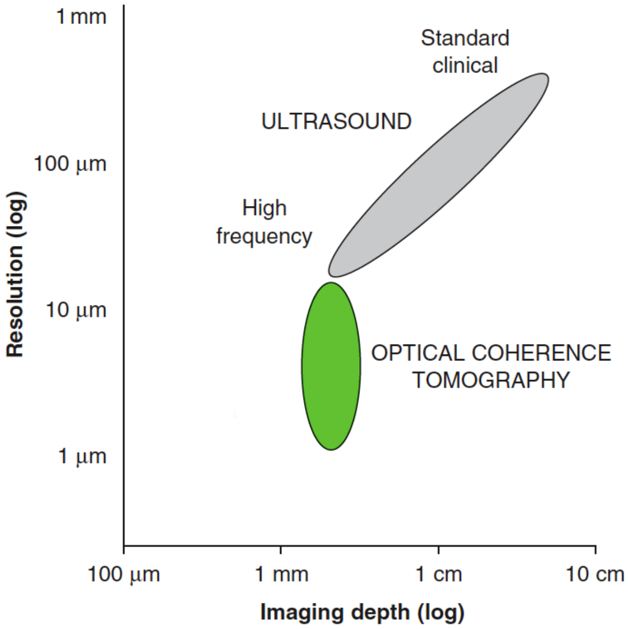

Figure 1.14: Resolution and imaging depth of ultrasound and OCT ([185]).

Figure 1.14 displays the resolutions and imaging depths of ultrasound and OCT. Standard clinical ultrasound imaging can image deep structures but has very limited resolution. Higher frequencies yield finer resolution, but ultrasonic attenuation is also increased, which limits image penetration. The axial image resolution in OCT ranges from 1 μm to 15 μm and is determined by the coherence length of the light source.

In most biological tissues, image depth is limited to 2 − 3 mm by attenuation from optical scattering.

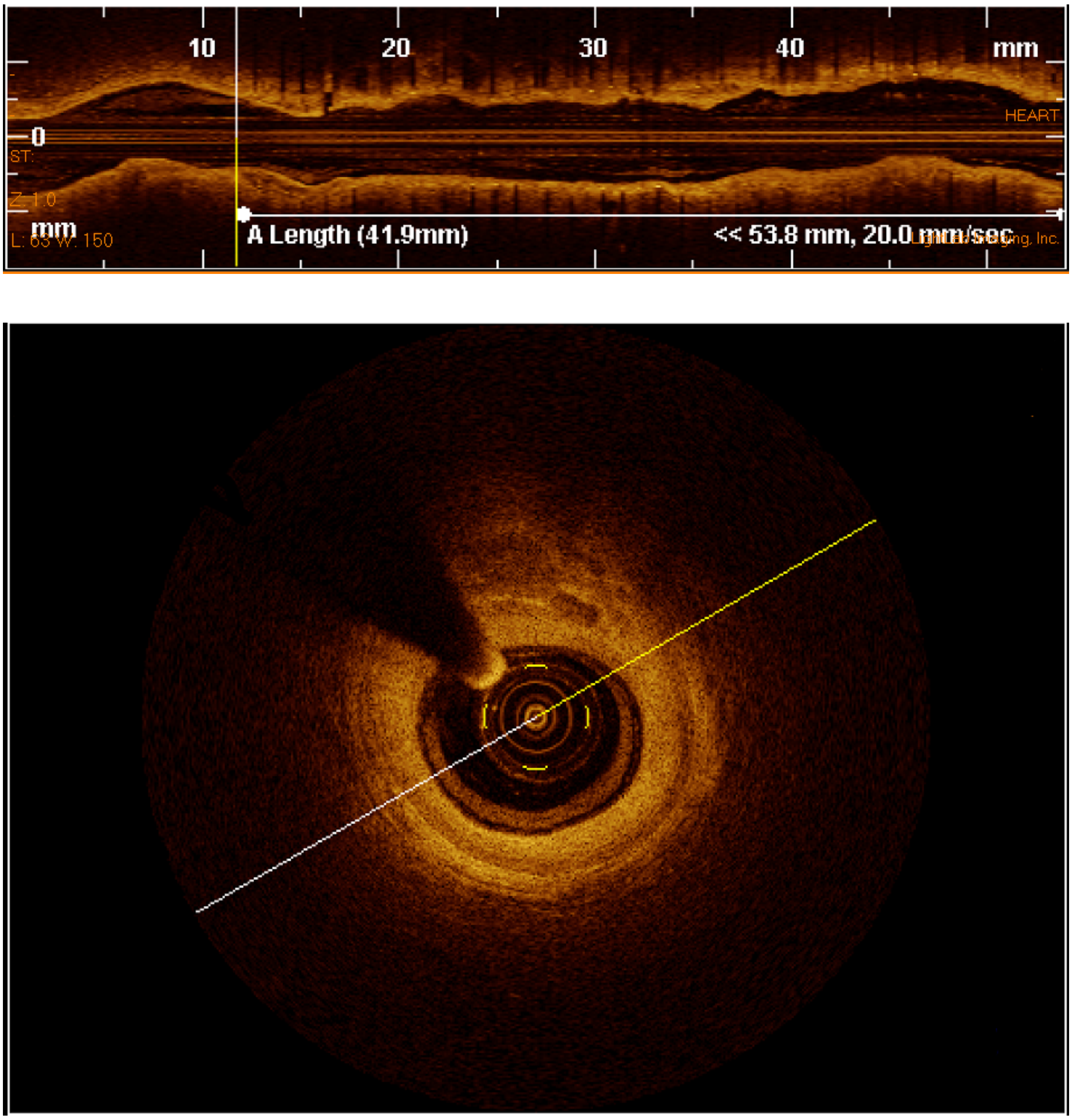

Figure 1.15: OCT image (top: pull-back view of a coronary segment with length 53.8 mm; bottom: cross-sectional view of the coronary at length 41.9 mm.)

In Figure 1.15, a cross-sectional view of a coronary segment is shown in the bottom, with the pull-back view at the top. The yellow vertical line in the pull-back view indicates the position of the cross-sectional view. The corresponding X-ray angiogram image of the coronary segment is shown in Figure 1.16.

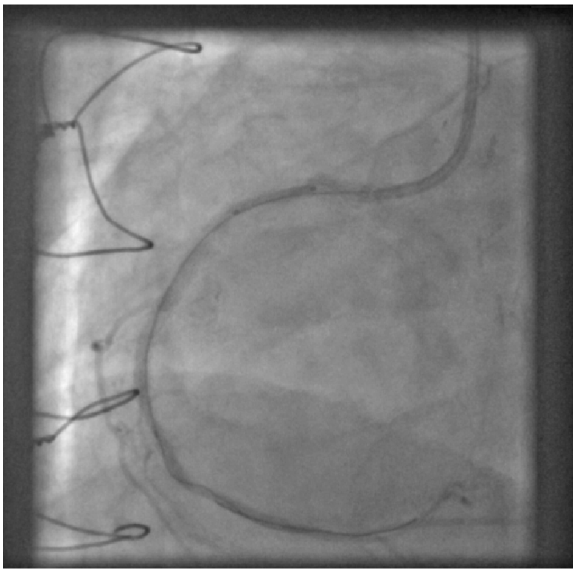

Figure 1.16: X-ray angiogram of the same coronaries as in Figure 1.15.

1.3 Contribution

In this thesis, we aim to construct patient-specific 3D + time coronary artery and left ventricle motion models from preoperative Computed Tomography Angiography (CTA) scans.

To achieve this goal, the thesis makes several contributions that focus on developing methods addressing the following three aspects of the problem:

1. Segmentation of coronary arteries from 4D CTA images. Segmenting coronary arteries from 4D CTA sequences is challenging because of the low image quality and frequent presence of artefacts. This thesis proposes several methods to extract the coronary centrelines in pre-operative 4D CTA images.

2. Coronary artery motion tracking from 4D CTA sequences. This task is the main focus of our work. The thesis proposes several approaches to construct the coronary motion models in order to tackle the challenges imposed by the variations of the 4D CTA image qualities acquired from the patients suspected of CAD. The methodology and evaluation of each approach are presented in Chapter 4 to Chapter 7. A short summary of each chapter is provided in next section.

3. Simultaneous motion tracking of the coronary arteries and left ventricle from 4D CTA. As part of the future work arising in this thesis, we propose to use a 3D cardiac atlas to facilitate the segmentation of cardiac components in CTA

image, and simultaneously track the motion of coronaries and LV using a non-rigid registration approach incorporating local phase information.

Registration of pre- and intra-interventional data is one of the key technologies for image-guided radiation therapy, radiosurgery, minimally invasive surgery, endoscopy and interventional radiology. Despite its importance and close relation to our work, it is not included in this thesis. Nevertheless, it is a potential extension for this thesis. To give some idea of how the work in this thesis could be extended we refer to these recently published work [68, 148].

1.4 Thesis Outline

This thesis is organized as follows: In Chapter 2, a review of state-of-the-art literature on vascular segmentation techniques is presented. We survey vessel enhancement techniques that are routinely used to improve the visibility of vasculature structures prior to the vessel segmentation. We review segmentation methods with regards to their search strategy, how they detect the vessel wall and branching, and degree of user interaction. We also review different strategies for evaluation and comparison of vessel segmentation techniques. Chapter 3 reviews motion modelling techniques of coronary arteries. In particularly, we survey motion modelling techniques for different imaging modalities: X-ray angiography, MRA, CTA and others.

Following this, Chapters 4 to 7 present the original contributions of this thesis, dedicated to the segmentation and motion modelling of coronary arteries from the 4D cardiac CTA data. An overview of each chapter is given below:

- In Chapter 4, we assume the coronary motion can be recovered through cardiac motion tracking in the 4D CTA sequence. The cardiac motion is then estimated throughout the cardiac cycle by using a non-rigid image registration technique based on a free-form B-spline deformation model. The coronary centrelines are extracted at end-diastole using a ridge traversal algorithm. The centrelines are then deformed to all other time points by applying the estimated deformation field.

- In Chapter 5, coronary motion models are constructed by extracting coronaries in all time frames via a graph search algorithm using prior information. A pair of start and end nodes are supplied for each vessel branch by the user. The centrelines are segmented as minimal cost paths in all phases of the 4D CTA and used to construct the coronary motion model.

- In Chapter 6, we presented two template-based approaches. In both approaches, non-rigid registration is used to derive the cardiac motion from each phase to end-diastolic phase. In the first approach (Section 6.5), we only transform the start and end nodes of each coronary branch at end-diastole to the other phases. Afterwards, we use template fitting to refine these two nodes' positions until they are located approximately on the ridge of the coronary vessel. Finally, we extract the centrelines from the start to end node using a graph search algorithm. In the second approach (Section 6.6), we transform the extracted centrelines at end-diastole to all other phases via applying the estimated cardiac motion. Template fitting and matching is then used to refine the equidistant samples of the estimated coronary centreline voxels at each phase. The refined voxel locations are chained together using the B-spline interpolation to generate the centrelines of the coronaries at each phase.

- In Chapter 7, we propose an approach incorporating multi-channel information into the registration framework. It combines a probabilistic atlas of the coronaries, intensity information from CTA images to be registered as well as vesselness information to fully automate the coronary motion tracking procedure and improve its accuracy. We performed pair-wise 3D registration of time frames of the 4D CTA by using a multi-channel and multi-level implementation of the large deformation diffeomorphic metric mapping (LDDMM) framework. The segmented coronary centrelines at end-systolic phase are transformed to end-diastolic phase using this registration framework.

For the validation of each proposed motion tracking method, experiments conducted on clinical 4D CTA data are presented at the end of each chapter.

Finally, a summary of the work presented in this thesis, their limitations and potential future work is given in Chapter 8. In particular we explore one possible extension of the work in this thesis: simultaneous motion tracking of coronary arteries and left ventricle. A list of publications, the links to the e-thesis and videos are also presented for reference.

Chapter 2

Review of Coronary Artery Segmentation

Visualisation and quantitative analysis of coronary arteries is an important step in the diagnosis of cardiovascular diseases, stenosis grading, surgical planning, blood flow simulation and post-surgery monitoring. Vessel centreline extraction can be used to generate specific visualisations, such as endovascular views or multiplanar reformats. Vessel segmentation can be used for quantification, e.g., stenosis grading or determining the dimension of stents to be used in interventions. The aim of this chapter is to survey the important coronary segmentation methods proposed in last two decades, classify them into groups and provide analysis both of the methodology and the application aspects.

In this review, we mainly focus on the work on CTA and MRA coronary imaging, since these modalities contain 3D information of the arteries and can be directly used to build pre-interventional models. In our survey, both centreline extraction and lumen segmentation of the coronary arteries are included. Segmentation of coronary arteries from 2D DSA or X-ray images are also briefly reviewed. Although techniques developed for other applications might also be appropriate to coronary artery segmentation, such as the segmentation of other tubular like structures, finger prints, cerebral vessels, pulmonary veins and others, most of the publications on those topics are not included in this chapter with the exception of those directly relevant to this thesis.

Given the different nature of the coronary segmentation approaches (e.g. automatic, semi-automatic, manual), the variation of the user skills for manual or semi-automatic methods and the lack of an accepted gold standard for evaluation, we do not attempt to compare the approaches in terms of performance. However, recently, attempts at evaluating and comparing the performance of various algorithms for coronary artery centreline extraction from the same CTA data set have been proposed in the Rotterdam Coronary Artery Algorithm Evaluation Framework [153, 200].

2.1 Previous Reviews

To the best of our knowledge, several reviews have been published on the topic of vessel segmentation [66, 215, 216, 33, 115, 128]: Felkel *et al.* [66] summarized several methods on vessel segmentation from the literature and discussed their applicability to 3D peripheral vessel segmentation in CTA datasets of the human leg.

The review by Suri *et al.* [215, 216] has two parts: Part I focuses on the physics of MRA generation and prefiltering techniques applied to MRA data sets. It also discusses the prefiltering algorithms that are necessary for removing the background and nonvascular structures in MRA data sets. Part II of the review presents the overview in vessel segmentation algorithms. The vessel segmentation techniques are divided into two groups, eight methods classified as nonskeleton and three others classified as skeleton. Skeleton-based techniques compute the skeleton of the vessels first and then reconstruct the vessel lumen by computing the vessel cross-sections. Nonskeleton-based techniques compute the vessels directly.

In [33], Buhler *et al.* surveyed several geometric methods to solve basic visualisation and quantification problems for vessel analysis, such as centreline computation, boundary detection, projection techniques, and geometric model generation. In [115], vessel extraction algorithms are divided into six main categories: pattern recognition, model-based, tracking-based, artificial intelligence-based, neural network-based and tube-like object detection approaches.

In the most recent review on vascular segmentation, Lesage *et al.* [128] presented their analysis along three axes: models, features and extraction schemes. Model-based assumptions about the vessel appearance and geometry together with extracted image features used for evaluating these models are combined in the extraction schemes to perform the segmentation tasks. Each component is viewed as an independent module. Through the combination of the three components, various segmentation methods are organised into one framework. This facilitates the discussions and comparisons of theoretical and practical properties of the reviewed segmentation methods.

2.2 Vessel Enhancement

Vessel enhancement, either as a pre-processing step for vessel segmentation or as a technique to improve visualisation of volumetric data, is widely used in computer-aided diagnosis. It facilitates vessel centreline extraction and lumen segmentation. In this section, we will examine vessel enhancement techniques from the literature. Since these methods can either be applied directly to coronary arteries or with minor adjustment, we include not only the ones proposed for enhancing coronary arteries in CTA images, but also those proposed for other vessel or line structures (e.g., finger prints, cerebral vessels, *etc.*) and other modalities.

2.2.1 Subtraction Filtering

Subtraction is the simplest technique to remove undesired structures in an image. It is routinely used in many image processing methods. There are two types of subtraction. One is to subtract one mask image from the image to be processed; the other is to subtract certain structures in the image to be processed based on the information derived from this image itself.

The first method is used in producing digital subtraction angiograms by subtracting a pre-contrast image from the post-contrast image. This effectively enhances the visibility of blood vessels by removing the unwanted bone and soft tissue structures from the angiograms. However, the noise level in the resulting subtraction image is higher than in either of the two original images because of the random distribution of the noise within each image.

Often the second method is used to reduce the size of the image to be analysed, e.g., subtracting a heart chamber mask from a 3D CTA scan helps to speed up and improve the accuracy of vessel analysis. Moreover, it can be used to enhance the visibility of vessels. For example, Sen *et al.* [205] proposed a nonlinear adaptive filtering to remove the background structures and consequently enhance the foreground vascular structures in the unsubtracted angiograms without generating artefacts. A filter mask with a size approximately twice that of the largest vessel is used for this purpose [205]. The filtering process has two rounds: Firstly, the local average of the pixel values within the mask region centred on a pixel location $\mathbf{x}$ is calculated as $m_1(\mathbf{x})$. All the pixels in this region with values below the local mask average $m_1(\mathbf{x})$ are used for the calculation of a second average, $m_2(\mathbf{x})$. As for contrast-enhanced angiograms, the vessels appear to be brighter than background. Therefore, pixels with values below $m_2(\mathbf{x})$ most likely belong to background. By subtracting $m_2(\mathbf{x})$ from the original pixel intensity $I(\mathbf{x})$ at location $\mathbf{x}$, the filtered result is obtained as:

$$\hat{I}(\mathbf{x}) = \begin{cases} I(\mathbf{x}) - m_2(\mathbf{x}), & I(\mathbf{x}) > m_2(\mathbf{x}); \\ 0, & I(\mathbf{x}) \leq m_2(\mathbf{x}). \end{cases} \tag{2.1}$$

By repeating this procedure for all the pixels in image I, the background is effectively subtracted from image I and the visibility of vascular structures is enhanced.

2.2.2 Hessian-based Filtering

Many methods for vessel enhancement and segmentation are based on the knowledge that vessels are tubular structures defined by their central axes and width. We group them into three categories: Hessian-based, diffusion and model-based filtering to be discussed in Section 2.2.2, 2.2.3, and 2.2.4 respectively.

Hessian-based filtering is the most popular vessel enhancement technique in the literature, because of its geometric properties and versatility. The vessel enhancement based on the analysis of the eigenvectors and eigenvalues of the Hessian matrix can be formulated flexibly according to any application requirements. It also can be incorporated into the diffusion filtering as presented in Section 2.2.3.

Hessian-based filters calculate 2nd-order derivatives of the image I, build the Hessian matrix $\mathcal{H}$ at each voxel $\mathbf{x}$, decompose it into eigenvalues (λ_1, λ_2, λ_3) and eigenvectors $(\vec{v}_1, \vec{v}_2, \vec{v}_3)$ and analyse them to determine the likelihood of the voxel $\mathbf{x}$ belonging to a vessel. This analysis is based on the following hypothesis: In the case of bright vessels on a dark background and with the following ordering of eigenvalues $|\lambda_1| \leq |\lambda_2| \leq |\lambda_3|$, the direction along the central vessel axis is approximated by $\vec{v}_1$ when satisfying the following three criteria:

$$\begin{aligned} (1):& \qquad \lambda_1 \approx 0; \\ (2):& \qquad \lambda_2 \approx \lambda_3 < 0; \\ (3):& \qquad |\lambda_1| \ll |\lambda_2|. \end{aligned}$$

Table 2.1 lists different geometric patterns in 2D and 3D, with reference to the magnitudes and signs of the eigenvalues of the Hessian matrix. For second-order 3D variation, Figure 2.1 shows the shape space, highlighting the bright string that typically represents the vessel structures in CTA images.

Table 2.1: List of geometric patterns in 2D and 3D, depending on the eigenvalues $\lambda_1, \lambda_2, \lambda_3$ (adapted from [71]). H: high value; L: low value; +/-: the sign of the eigenvalue.

2D		3D			geometric patten
λ_1	λ_2	λ_1	λ_2	λ_3	
L	L	L	L	L	noise, no preferred direction
		L	L	H-	bright plate-like structure
		L	L	H+	dark plate-like structure
L	H-	L	H-	H-	bright tubular structure
L	H+	L	H+	H+	dark tubular structure
H-	H-	H-	H-	H-	bright blob-like structure
H+	H+	H+	H+	H+	dark blob-like structure

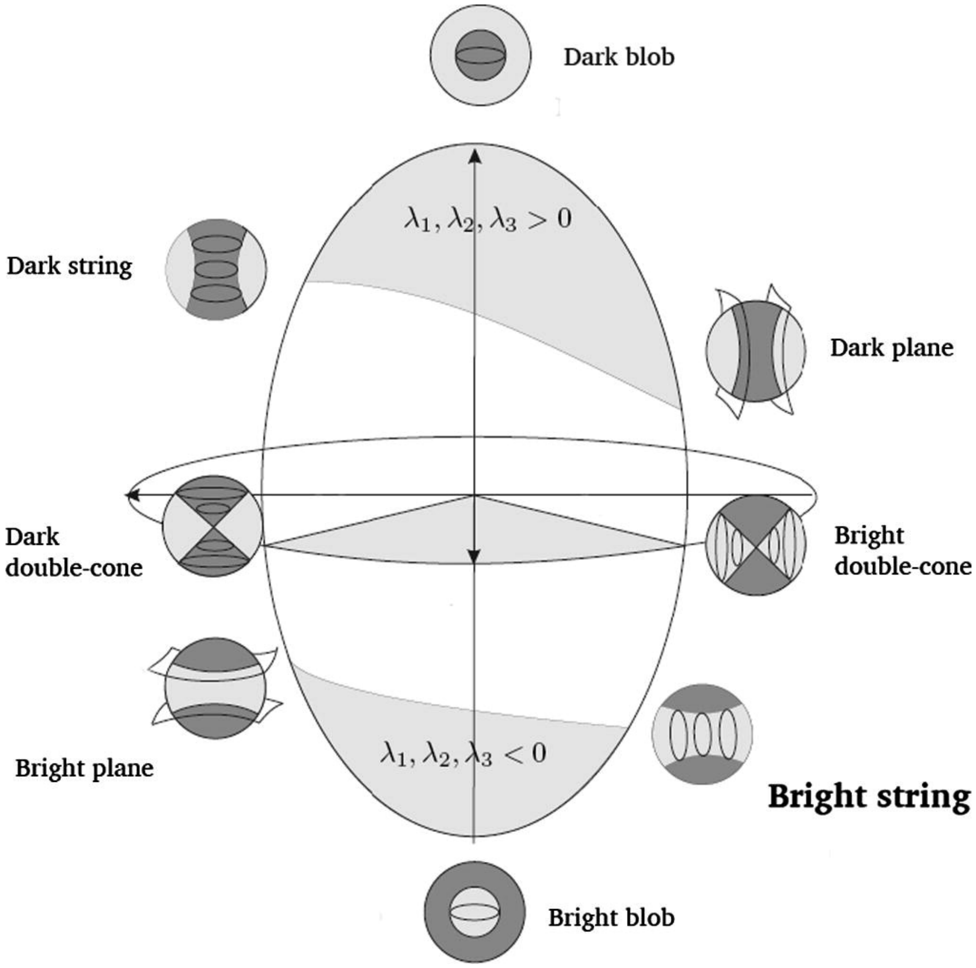

Figure 2.1: Shape space for Hessian matrix in 3D [133]

To extend Hessian-based filtering to a multi-scale framework, a multiscale Hessian-based vessel enhancement filter is then defined in [73] as:

$$\mathcal{V}(\mathbf{x}) = \max_{\sigma} v(\mathbf{x}, \sigma), \tag{2.2}$$

where $\mathbf{x}$ is a voxel in the image I, v represents the filter response at one specific scale, and σ is the scale for calculating Gaussian derivatives in order to derive the Hessian matrix at each voxel.

The vesselness response $v(\mathbf{x})$ is calculated at a range of scales ($\sigma_{\min} \leq \sigma \leq \sigma_{\max}$) by computing the Hessian matrix at each scale. At every voxel, the largest vesselness response $\max_\sigma v$ and its corresponding scale is selected. By calculating $\mathcal{V}(\mathbf{x})$ for all voxels in image I, a vessel enhanced image is obtained. The corresponding σ value for voxel $\mathbf{x}$ can be used to approximate the radius of the vessel.

There have been several filters proposed in the literature following this framework, to be listed in chronological order. The proposed filters analyze the main modes of

2nd-order variation in image intensity to determine the type of local structure present in the image. They differ in how they define vessel-likelihood $v(\mathbf{x}, \sigma)$. In all cases, $v(\mathbf{x}, \sigma) = 0$, if $\lambda_2 > 0$ or $\lambda_3 > 0$, as also shown in Table 2.1 and Figure 2.1.

In [138], Lorenz *et al.* presented a multi-scale segmentation technique for tubular-like structures in 2D and 3D medical images. It is based on normalized first and second derivatives and on the eigenanalysis of the Hessian matrix $\mathcal{H}$. The filter defined by Lorenz *et al.* [138] is:

$$v_{\text{Lorenz}}(\mathbf{x}) = \sigma^{\eta} \left| \frac{\lambda_2 + \lambda_3}{2.0} \right|, \tag{2.3}$$

where η normalises responses across scales.

Sato *et al.* also presented a method for the enhancement of curvilinear structures such as vessels and bronchi in 3D medical images [197]. The filter proposed by Sato *et al.* is formulated as:

$$v_{\text{Sato}}(\mathbf{x}) = \begin{cases} \sigma^2 |\lambda_3| \left(\frac{\lambda_2}{\lambda_3} \right)^{\xi} \left(1 + \frac{\lambda_1}{|\lambda_2|} \right)^{\tau}, & \lambda_3 < \lambda_2 < \lambda_1 < 0; \\ \\ \sigma^2 |\lambda_3| \left(\frac{\lambda_2}{\lambda_3} \right)^{\xi} \left(1 - \rho \frac{\lambda_1}{|\lambda_2|} \right)^{\tau}, & \lambda_3 < \lambda_2 < 0 < \lambda_1 < \frac{|\lambda_2|}{\rho} \end{cases} \tag{2.4}$$

where $\xi \geq 0$ controls cross-section asymmetry, $\tau \geq 0$ controls the sensitivity to blob-like structures, $0 < \rho \leq 1$ controls sensitivity to the vessel curvature and σ^2 normalises responses across scales.

In order to develop a vessel enhancement filter, Frangi *et al.* examined the multi-scale second-order local structure of an image and proposed a vesselness measure on the basis of all eigenvalues of the Hessian $\mathcal{H}$ [73]. The filter suggested by Frangi *et al.* [73] is:

$$v_{\text{Frangi}}(\mathbf{x}) = \begin{cases} 0, & \lambda_2 > 0 \quad \text{or} \quad \lambda_3 > 0; \\ \\ \left(1 - e^{-\frac{A^2}{2\alpha^2}} \right) e^{-\frac{B^2}{2\beta^2}} \left(1 - e^{-\frac{S^2}{2\gamma^2}} \right), & \text{otherwise} \end{cases} \tag{2.5}$$

where

$$A = \frac{|\lambda_2|}{|\lambda_3|}, \quad B = \frac{|\lambda_1|}{\sqrt{|\lambda_2 \lambda_3|}}, \quad S = \sqrt{\lambda_1^2 + \lambda_2^2 + \lambda_3^2}.$$

Controlled by α, parameter A discriminates plate- from line-like structures; B (dominated by β) accounts for deviation from blob-like structures and S (controlled by γ) differentiates between high-contrast region (e.g., one with bright vessel structure in dark background) and low-contrast background region. Scale normalisation is achieved by multiplying $\mathcal{H}$ by σ^2 before eigenvalue decomposition. The weighting factors α, β

and γ are to be specified in order to determine the influence of A, B and S.

For the early detection of lung cancer from the radiographs and CT images, it is vital for the pre-processing filtering to not only enhance nodules, but also suppress the other anatomical structures such as ribs, blood vessels and airway walls. To address this issue, Li *et al.* developed three selective enhancement filters for point (blob), line, and plane-like structures which can simultaneously enhance objects of a specific shape (for example, blob-like nodules) and suppress objects of other shapes (for example, line-like vessels) [132]. Therefore, as pre-processing steps, these filters are useful for improving the sensitivity of nodule detection and for reducing the number of false positives. The point, line and plane filters are formulated as the following three equations respectively:

$$\mathcal{LI}_{\text{point}}(\mathbf{x}) = \begin{cases} \dfrac{|\lambda_1|^2}{|\lambda_3|}, & \lambda_1 < 0, \lambda_2 < 0, \lambda_3 < 0; \\ 0, & \text{otherwise} \end{cases} \tag{2.6}$$

$$\mathcal{LI}_{\text{line}}(\mathbf{x}) = \begin{cases} \dfrac{|\lambda_2|(|\lambda_2| - |\lambda_1|)}{|\lambda_3|}, & \lambda_2 < 0, \lambda_3 < 0; \\ 0, & \text{otherwise} \end{cases} \tag{2.7}$$

$$\mathcal{LI}_{\text{plane}}(\mathbf{x}) = \begin{cases} |\lambda_3| - |\lambda_2|, & \lambda_3 < 0; \\ 0, & \text{otherwise} \end{cases} \tag{2.8}$$

In [170], Olabarriaga *et al.* evaluated the aforementioned three Hessian-based filters [138, 197, 73] for enhancement of the central axis of coronary arteries in multi-detector CTA images acquired with contrast injection. The average filter response obtained with different parameter configurations was measured at fixed distances from a reference central axis determined manually. Results were compared according to two objective measures, namely the response decay rate at the centre and the overall response within 5 mm (approximately the largest radius for coronary arteries). It was noted that the Frangi filter [73] provided better central vessel axis enhancement in general [170].

One of the drawbacks of Hessian-based filtering methods for the enhancement of tubular structures is that they have high computational cost, particularly when a multi-scale framework is used. For each scale, for each voxel, the Hessian $\mathcal{H}$ must be computed and decomposed before measuring the vesselness. In [172], Orlowski *et al.* presented guidelines for a computationally efficient implementation of multiscale image filters based on eigenanalysis of the Hessian matrix for the application to 3D medical images of blood vessels. The method uses the Hessian trace, Hessian determinant and sign to discard voxels unlikely to belong to vessels, prior to the calculation of the Hessian eigenvalues.

In summary, despite their drawbacks, Hessian-based vessel enhancement filters have been shown to be applicable to various imaging modalities (e.g., DSA [138, 73], CTA [197, 170], MRA [197, 73, 245]) and several types of vessels (cerebral [138, 197], peripheral [73], hepatic [197], pulmonary [197], and cardiac [245, 170]).

2.2.3 Diffusion Filtering

Multiscale approaches for vessel enhancement [138, 197, 73] show good noise and background suppression results. However, these methods do not consider the local coherence of vessel appearance. If a given voxel is considered to be part of a vessel, there should be neighbouring voxels in the direction of the vessel axis that also are part of the vessel. Filters that aim at increasing the coherence of the features in the images by anisotropic diffusion can be found in [235, 236].

The different diffusion filtering techniques are briefly described and compared in the following of this section. In scale space theory, an image evolves according to a diffusion equation

$$\Phi_t = \nabla \cdot (\mathbf{D}\nabla\Phi). \tag{2.9}$$

with the original image as the initial condition Φ_0. A family of images can be generated where the features of interest are enhanced or blurred gradually. The diffusion tensor $\mathbf{D} : \mathbb{R}^{m\times m} \to \mathbb{R}^{m\times m}$, with m denoting the dimension, is used to control the diffusion flow. Diffusion-based vessel enhancement techniques essentially differ only in the formulation of this diffusion tensor. In its simplest form, $\mathbf{D}$ is the identity matrix and the diffusion equation is essentially equivalent to the heat equation:

$$\Phi_t = \nabla \cdot (I\nabla\Phi) = \Delta\Phi \ . \tag{2.10}$$

In Krissian *et al.* [118], the anisotropic diffusion is based on a multidimensional diffusion flux. The diffusion flux is decomposed in a 3D orthogonal basis that depicts the directions of principal curvature, effectively enabling enhancement of contours as well as diffusion along the contours. The diffusion function associated with each vector of this basis depends on the first-order derivative of the intensity along this direction, instead of the traditional norm of the smoothed gradient. The minimal principal curvature direction of the isosurface is then used to steer the diffusion, which requires the calculation of the gradient vector field. This may pose a problem along the central axis as the gradient vanishes at these locations, possibly leading to unstable behavior.

Canero *et al.* [38] presented an anisotropic diffusion filtering method to enhance the local coherence of tubular structures in 2D X-ray coronary angiograms. The diffusion strength is determined by the vesselness measure proposed in [73]. This vesselness measure is used to steer the diffusion process and also determine the scale of the diffusion tensor to be applied at each voxel.

Manniesing *et al.* [146] proposed a method to enhance vascular structures within the framework of scale space theory. They combine a smooth vessel filter which is based on a geometrical analysis of the Hessian $\mathcal{H}$, with a non-linear anisotropic diffusion scheme. The amount and orientation of diffusion depend on the local vesselness. Vessel enhancing diffusion (VED) is applied to patient and phantom data and compared to linear, edge and coherence enhancing diffusion. The method performs better than most of the existing techniques in visualising vessels with varying radii and in enhancing vessel appearance. A diameter study on phantom data shows that VED least affects the accuracy of diameter measurements. It is shown that using VED as a pre-processing step improves level set based segmentation of the cerebral vasculature, in particular segmentation of the smaller vessels of the vasculature. VED is also compared with the vesselness filter proposed by Frangi *et al.* [73] on patient data. It can be observed that the shrinkage effect of the vesselness filter is not present in VED. In other schemes, the shrinkage effect is due to the increasing deviation from an ideal tubular structure when approaching the boundaries of the vessel. Furthermore, VED has better performance with respect to reducing the noise in the background area compared to standard vesselness filtering.

Compared with Canero *et al.* [38], the tensor function used by Manniesing *et al.* in [146] satisfies a smoothness constraint that is imposed by the diffusion process to ensure that it is well-posed. Another difference is related to the steering of the diffusion: Instead of having small diffusion for non-vessel structures, the VED approach [146] exhibits strong isotropic diffusion to reduce background noise. Between the extremes of isotropic and anisotropic diffusion, the parameter s is used to control the sensitivity of the vesselness response $\mathcal{V}$. Furthermore, in contrast to Canero *et al.* [38], the method is extended to 3D.

The discontinuities in 3D vasculature images pose a problem for vessel extraction and visualisation. Gaps may cause early termination of the vessel centreline extraction processes or lead to leakage into non-vascular bright structures. In order to recover the vessel network correctly, the gaps between the closest discontinuous vessels need to be filled first. In [187], the authors presented a gap filling method which merges discontinuities in images of micro-vascualar networks with undesirable gaps along the vessels. The algorithm is based on the skeletonisation of the segmented network followed by a tensor voting method. It merges the most common types of discontinuities found in microvascular networks.

2.2.4 Model-based Filtering

The second order derivatives of the image are sensitive to local intensity variations. This is undesirable for vessel enhancement in images with noise or artefacts. Consequently, Hessian-based vessel enhancement techniques have two main drawbacks:

1. Noise in the background region can lead to false positive responses which interfere with the segmentation process.

2. The noise inside a vessel can cause the vesselness responses of the vessel to be discontinuous, due to the false negative responses. Also, crossings (where two relatively straight vessels meet) or vessel branching can produce false negative responses. These effects degrade visualisation results and can cause serious problems for the subsequent vessel segmentation.

To address these issues, several researchers proposed model-based filtering techniques.

2.2.4.1 Flux-based Vessel Enhancement

Flux and MFlux are oriented, local flux-based medialness measurements designed for coronary artery enhancement [127]. Gradient flux-based segmentation methods exploit the orientation and magnitude of gradient vectors around the boundaries of the structure of interest. A cross-sectional geometric model is adopted for this purpose. It assumes a cross-sectional vessel contour $C(\mathbf{p}, r, \mathbf{d})$ with centre $\mathbf{p}$, orientation $\mathbf{d}$ and radius r as shown in Figure 2.2 (a). $\mathbf{x}_i$ is a point on the contour after it is equi-angularly discretized into N points $\mathbf{x}_i$ with $i = 1, ..., N$, satisfying $\|\mathbf{x}_i - \mathbf{p}\| = r$.

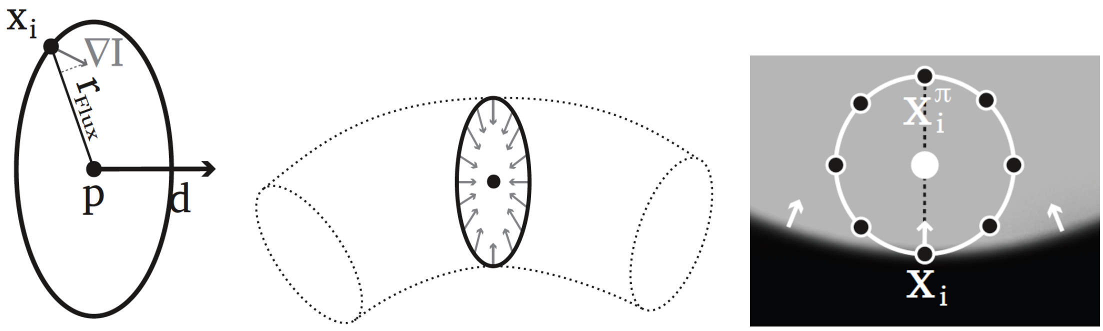

(a) (b) (c)

Figure 2.2: Flux-based vessel enhancement. (a): Geometric model for computing flux response; (b): maximal flux response is achieved when the model (a) is aligned with tubular structure in the image; (c): asymmetric gradient flux contribution over the test contour [124].

The gradient flux F through the cross-sectional contour C is formulated as:

$$F(\mathbf{p}, r, \mathbf{d}) = \frac{1}{N} \sum_{i=1}^{N} \nabla I(\mathbf{x}_i) \cdot \frac{\mathbf{p} - \mathbf{x}_i}{\|\mathbf{p} - \mathbf{x}_i\|} \tag{2.11}$$

It effectively computes the normalised sum of the scalar product of the gradient vector and the unit inward surface normal from all points $\mathbf{x}_i$ on the contour C.

To penalise the asymmetric response from the underlying image, MFlux only takes the smaller contribution from a set of two diametrically opposed voxels $(\mathbf{x}_i, \mathbf{x}_i^{\pi})$ along the contour as illustrated in Figure 2.2 (c).

$$MF(\mathbf{p}, r, \mathbf{d}) = \frac{2}{N} \sum_{i=1}^{\frac{2}{N}} \min \left(\left(\nabla I(\mathbf{x}_i) \cdot \frac{\mathbf{p} - \mathbf{x}_i}{\|\mathbf{p} - \mathbf{x}_i\|} \right), \left(\nabla I(\mathbf{x}_i^{\pi}) \cdot \frac{\mathbf{p} - \mathbf{x}_i^{\pi}}{\|\mathbf{p} - \mathbf{x}_i^{\pi}\|} \right) \right) \tag{2.12}$$

where $\mathbf{x}_i^{\pi} = \mathbf{x}_{\frac{N}{2}+i}$ for an even number N of points on the contour C. By choosing the minimal contribution from points $\mathbf{x}_i$ and $\mathbf{x}_i^{\pi}$, MFlux performs better with increased discriminative power when the vessels run close to large non-vascular structure, e.g., the heart chamber.

2.2.4.2 Probabilistic Model Based Vessel Enhancement

The design of Hessian-based filtering relies on the observation that the ratio between the minimum principal curvature and the maximum principal curvature should be low on tubular objects and high on spherical objects. The principal curvatures are obtained as the eigenvalues of the Hessian matrix of the intensity function. The principal directions of curvature are the corresponding eigenvectors. The calculation of the Hessian of the image intensity involves second order partial derivatives and is highly sensitive to noise. Consequently, smoothing of the image at multiple scales is essential. Due to noise and smoothing, junctions in real image data are characterized by high ratio of the minimum principal curvature and the maximum principal curvature; thus they tend to be suppressed by vessel enhancement filters which in turn leads to the apparent discontinuity of blood vessels.

Ideally, vessel enhancement filters should enhance vessels and vessel junctions while suppressing nodules and other nonvessel elements. In [6], Agam *et al.* proposed using probabilistic vessel models from which vessel enhancement filters capable of enhancing junctions while suppressing nodules are derived. The proposed filters are based on eigenvalue analysis of the structure tensor that is a first order differential quantity and thus less sensitive to noise. The authors derived parametric models for nodules, vessels, T or X junctions, and Y junctions separately. By choosing a suitable model selection technique, this method showed better performance when compared to Hessian-based techniques [6].

Beyond the aforementioned vessel enhancement techniques, there are many others proposed in literature, e.g., structure tensor [5, 57], multiscale model-based approaches [119], directional filter bank [221], local line model [252] and multidimensional adaptive filtering [238].

2.3 Segmentation Methods

All vascular segmentation methods essentially can be classified either as lumen segmentation or centreline extraction. After vessel lumen segmentation, various skeletonisation methods can be employed to obtain the vessel centreline in a post-processing step. The vessel skeleton tree can then be created by connecting these centrelines. As for methods starting from extracting the centrelines, the cross-sectional vessel lumen region can be found via fitting geometric models, finding the boundaries of largest gradient variation or others. In the following, we will discuss several search strategies for vessel centreline extraction.

2.3.1 Search Strategy

2.3.1.1 Region Growing

Region growing techniques start from a seed point or a selected small region, and then incrementally recruit pixels to a larger region based on pre-defined criteria [32]. Two important segmentation criteria are intensity similarity and spatial proximity. It is assumed that pixels that are close to each other and have similar intensity values are likely to belong to the same object. The main disadvantages of region growing approaches are that they require user-input and often lead to holes or leakage due to noise and variations in image intensities. Consequently, user-interaction is essential to guide the region growing. Post-processing is often required to refine the segmentation results.

2.3.1.2 Thresholding

There are two basic types of thresholding: The first method only uses one supplied threshold value to perform the thresholding, whilst the second one, hysteresis, uses a pair of threshold values, a lower and an upper threshold. Compared with the first one, hysteresis thresholding produces better connected segmentation as demonstrated in Poli *et al.* [181].

More advanced thresholding technique use expectation maximisation [243], adaptive region growing [44], or other statistically-based schemes to select which voxels are part of the object of interest and which are background.

Thresholding techniques do not normally compute connectivity information between voxels and as a result produce no structural information. Both region growing and thresholding techniques are susceptible to noise and varying intensity within the structure of interest. They also tend to produce holes or leakage and are difficult to control.

2.3.1.3 Morphology

Morphology is routinely applied in image processing, thanks to its simple mathematical formulation. Mathematical morphology for image processing can be divided into two categories, namely binary morphology and grey-level morphology:

- The former uses a simple, pre-defined shape (named as structuring element) to test an image and draw conclusions on how this shape fits or misses the regions in the image. The basic operations include erosion, dilation, opening, closing and the binary hit-or-miss transform.

- The latter category use a greyscale structure function to probe the image instead of a binary structuring element. In this category, there are the grey-level hit-or-miss transform [175, 162, 163], the top-hat transform and others.

For a more detailed discussion of morphological operations for image analysis, we refer to [211].

Mathematical morphology can be either used as pre-filtering process as in [86, 161, 217] or as a vessel extraction strategy in [142, 32]. In [149], mathematical morphology, region-growing schemes and shape features are combined together for 3D vascular segmentation and bifurcation structure extraction. Haris *et al.* [86] used a top-hat transform to filter pre-segmented images before employing an artery element model to track the coronaries. Wilkinson *et al.* [242] used morphological connected set filters for the extraction of tubular structures from medical images. The advantages of these filters are that they are shape preserving and do not amplify noise.

Luengo-Oroz *et al.* [142] present an algorithm based on a morphological greyscale reconstruction of 2D slices for the extraction of the 3D coronary artery tree. In order to segment the coronaries from 3D CT images, a priori information of the radius of the coronary and the z-axis sampling is used to define the size of the object that is being searched and the area of search in the next slice respectively. A seed point on the coronary artery is selected by a human expert in the first slice. A 2D morphological reconstruction by dilation is performed from the seed point to segment the coronaries in this slice. Afterwards, a set of potential seed points is generated for the morphological segmentation of the coronaries in next slice. This procedure is repeated until no more potential seed points for the tubular structure can be generated.

Another automatic algorithm utilising grey-level mathematical morphology is presented for coronary artery segmentation from 3D CT sequences of a cardiac cycle consisting of 10 phases in [32]. The algorithm relies on the blur grey-level hit-or-miss transform [31] that is an extension of the blur binary hit-or-miss transform [28]. The segmentation algorithm consists of three steps:

1. Detection of heart zone is accomplished by using a grey-level hit-or-miss transform considering the lungs as background and the heart as the structure of interest. The heart zone is consequently detected with two structuring elements, a sphere for the heart zone and ellipsoids for the background (shown in Figure 2.3 (b)).

2. Detection of the aorta is achieved by locating a circular shape using the blur grey-level hit-or-miss transform, followed by a region-growing as depicted in Figure 2.4 (a). The final result is shown by the red region in Figure 2.3 (c).

3. Detection of coronary arteries is performed by using a blur grey-level hit-or-miss transform based region growing initialised from seeds obtained in the second step, using structuring elements as in Figure 2.4 (b).

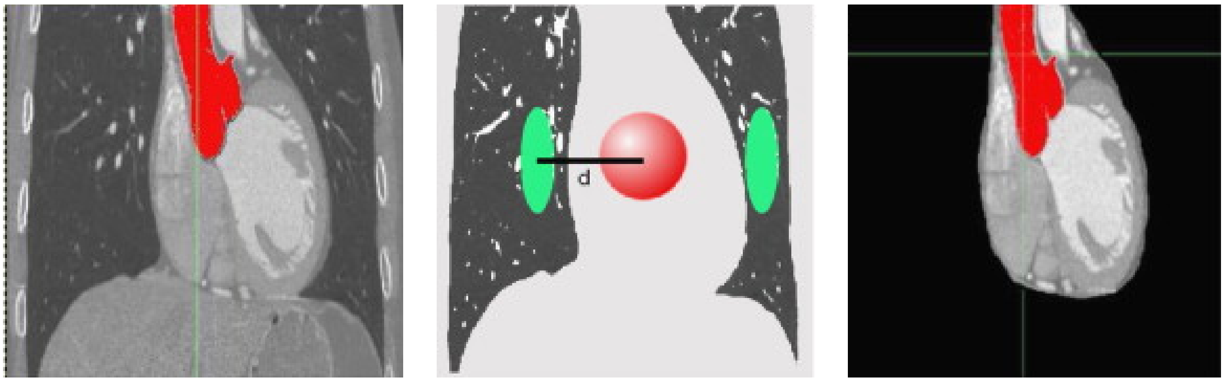

(a) (b) (c)

Figure 2.3: Heart zone and aorta detection [32]. (a): original image with segmented aorta in red; (b): structuring elements used for the heart zone detection; (c): detected heart zone.

It is reported that the application of the proposed method on three selected phases from 20 patients 4D CTA scans led to correct segmentation in 90% of the cases. The 10% remaining incorrect cases corresponded to images where the signal-to-noise ratio was very low [32].

The small variation of the radius along the coronary vessels promotes the usage of mathematical morphology for their segmentation, but this segmentation procedure can also easily be compromised by the presence of other surrounding structures in the images. Moreover, mathematical morphology does not perform well for noisy images as reported in [32].

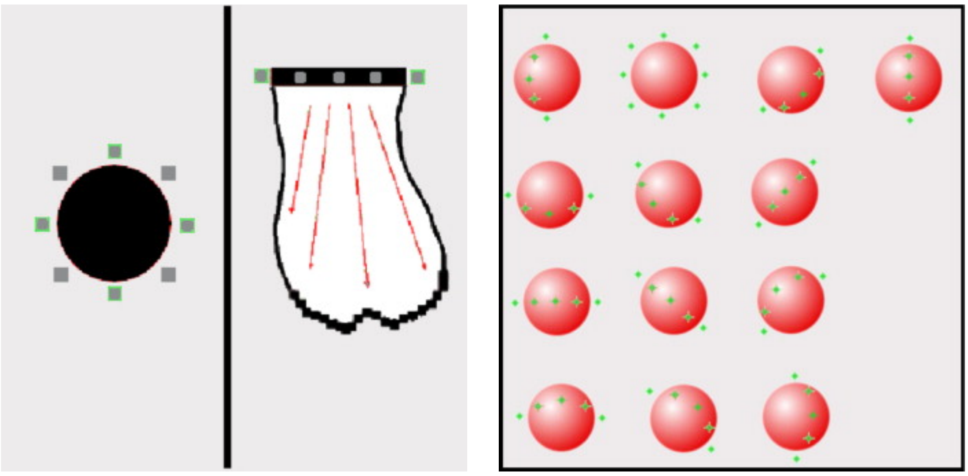
(a) (b)

Figure 2.4: Structuring elements for aorta and coronary segmentation [32]. (a): Aorta segmentation: structuring elements for the circular axial section detection (left) and region growing (right); (b): Structuring elements for coronary detection.

2.3.1.4 Level Set Methods

Level set evolution methods are based on an implicit surface that evolves according to geometric and image-based forces in an attempt to adapt to structures in the image. This type of technique has been applied successfully in vascular segmentation [140, 141, 9, 107, 147, 256]. However, using level set methods for vessel segmentation may encounter difficulties when segmenting small vessels with high curvatures and irregularities or when the local image contrast is low [76].

For instance, the curve evolution algorithm (CURVES) proposed in [140, 141] produces an accurate vascular segmentation by combining the modified curvature diffusion equation (MCDE) with a level-set based technique. In [9], a 3D level set approach is used to extract the blood vessels from angiography. The CURVES level set method is evaluated together with a ridge traversal approach in [107]. It is reported that the CURVES approach tends to leak outside the vessel structure making the skeleton less reliable.

2.3.1.5 Deformable Models

Deformable model fitting methods for vascular segmentation generally aim to find the approximate medial axes of the tubular structures and then locate the boundaries of the tubular structures by fitting models based on the medial axes to the image data.

In [96], Hoyos *et al.* developed a method for stenosis quantification in MRA images. The algorithm starts from a user-selected point within the vessel and tracks the vessel axis spatially to obtain its centreline. An extended active contour method is then used to detect the vessel boundaries in the planes locally orthogonal to the centreline. Finally, area measurements based on the resulting contours allow the calculation of stenosis parameters. The algorithm is reported to perform well even for severe stenosis and high vessel curvatures [96].

Due to vascular branching and thinning as well as the decrease of image contrast from the root of the vessel to distal parts, it is very challenging to segment blood vessels accurately. Leakage poses a severe threat when only image intensity is used to guide the deformable models at areas where the image information is ambiguous. To alleviate this problem, Nain *et al.* [164] combine the image statistics and a soft shape prior to derive a region-based active contour that segments tubular structures and penalises leakage. The results for a CT data set are shown in Figure 2.5 [164].

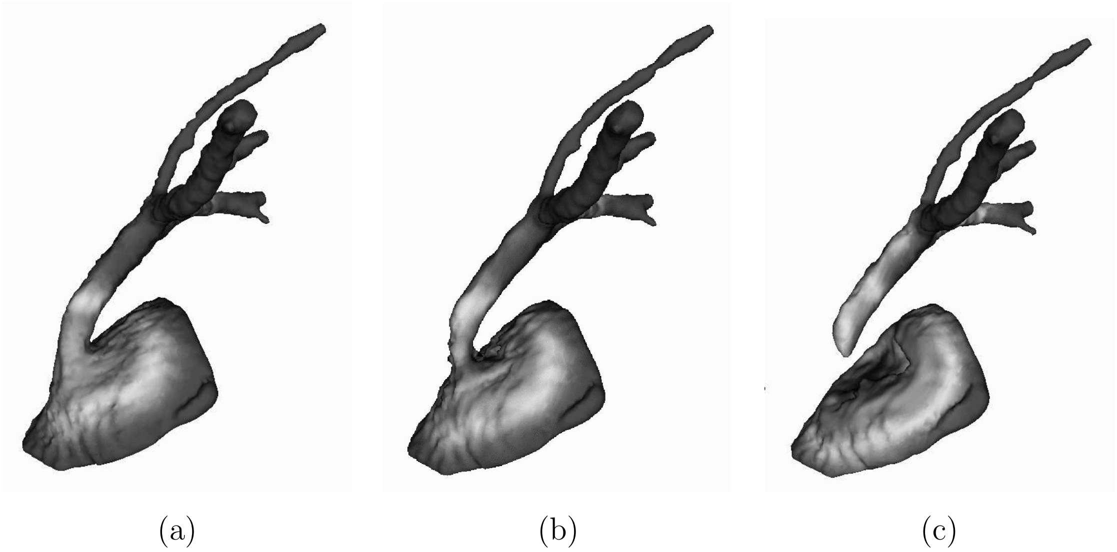
(a) (b) (c)

Figure 2.5: Segmentation of coronaries from CT data [164]. (a): Deformable model based on image statistics without a shape prior; The artery "leaks" into the aorta. (b): Deformable model based on image statistics and a shape prior after 400 iterations; (c): Deformable model based on image statistics and a shape prior after 800 iterations. The leak "pinches" off from the aorta.

In [155], Mille *et al.* used a deformable tube to model the varying cross-sections orthogonal to the vessel's local direction for vascular segmentation and reconstruction in 3D images. The method starts from a unique user-supplied root point to search for minimal paths in order to build an initial vessel tree. An explicit representation of a deformable tree is then introduced to model the vessel cross-sections and topological relationships between segments. The final model is produced by evolving the central curve of each segment and its associated variable radius function to minimise an energy function representing a region homogeneity criteria.

The following sections survey the vessel tracking techniques in the spatial domain, namely ridge traversal, probabilistic tracking, tracking based on model matching and others. These techniques are different from those in Chapter 3 which focus on coronary motion tracking in the temporal domain.

Tracking methods in spatial domain only consider the pixels in close proximity to the vessel centreline, therefore they tend to be relatively fast. Such methods are iterative in nature. At each step, a filter is applied to compute a point on the centreline and a direction in which to search for next point. These methods often need to restart after being trapped in an erroneous region, or fail to extract the correct vessel in the presence of image artefacts.

2.3.1.6 Ridge Traversal

Ridge-based methods treat n-dimensional greyscale images as $n+1$ dimensional elevation maps by plotting the voxel intensity information as the $(n+1)_{th}$ dimension. Figure 2.6 shows an example of an intensity ridge marked by the dark line within the vessel lumen of a 2D image and the corresponding 3D elevation map of this 2D image. In this newly created elevation map, intensity ridges approximate the skeleton of the tubular objects. The ridge points are effectively the local peaks in the direction of maximal surface gradient. For each local region, a ridge point can be obtained by tracing the elevation map from an arbitrary point along the steepest ascent direction. Since ridge-based approaches detect the skeleton from tubular structures, it can be regarded as a specialised skeleton-based approach.

As a method for extracting vessel centrelines, ridge traversal has been originally presented in [14] and further developed in [12]. The method starts from a user-supplied seed point near the vessel centre and a scale factor σ. The scale factor defines the width of the Gaussian kernel used to blur the image to suppress noise. Thus, it is crucial for effective vessel extraction. The Gaussian blurring here acts as a matching filter and creates the maximal responses at the vessel centreline. The user supplied seed is moved towards the centreline iteratively by minimising a ridgeness function $\mathcal{J}$ through a quasi-Newton minimisation method.

Aylward *et al.* evaluate the effects of initialization, noise and singularities on intensity ridge traversal and present multiscale heuristics and optimal-scale measures that minimise these effects [12]. It is also shown that dynamic-scale ridge traversal is insensitive to its initial parameter settings, operates with little additional computational overhead, tracks centrelines with subvoxel accuracy and passes branch points [12]. The major drawback of this method is that once the computed vessel centre point deviates from the true vessel point, it is difficult for the algorithm to recover from the error.

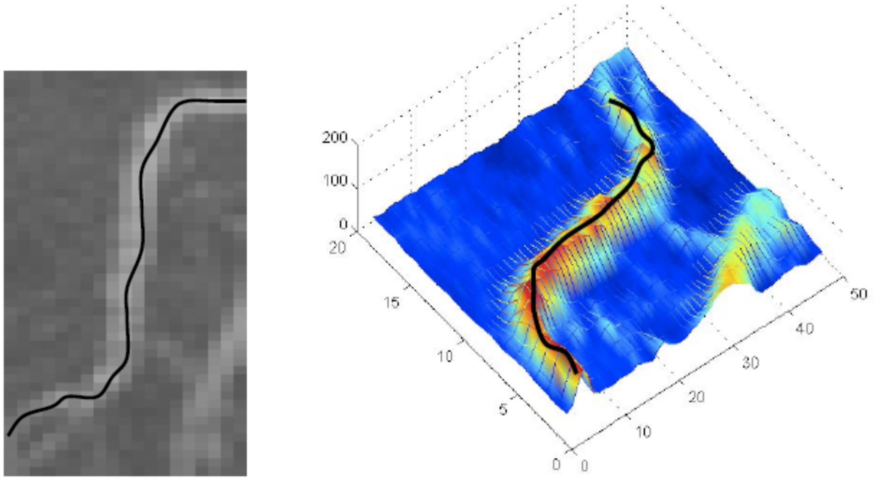

(a) (b)

Figure 2.6: Vascular intensity ridge in 2D slice and its elevation map in 3D [248]. (a): An example of an intensity ridge of the vascular structure in a 2D slice. (b): The corresponding 3D elevation map of the 2D slice where the intensity value of each pixel is plotted as the height.

2.3.1.7 Minimal Cost Path

Minimal cost path techniques reformulate the centreline extraction problem as an optimisation problem. The cost function is usually based on the likelihood of a voxel belonging to a vessel centreline. Various ways can be used to measure this likelihood, *e.g.*, vesselness, medialness, distance map towards the two vessel boundaries, a geometric energy functional [25], or region statistics [154].

Wink *et al.* [244] investigated two types of minimal path search algorithms: Dijkstra's algorithm and the A* algorithm. A* is a variant of Dijkstra's algorithm, with heuristic function $h(\mathbf{x})$ to steer the search process. A common heuristic term is the Euclidean distance between the current node and the end node. Without this heuristic term, A* is essentially equivalent to Dijkstra's algorithm. It starts from the root node, searches through all the neighboring voxels, selects the one with lowest cost and continues this process until reaching the end node. When the heuristic term is introduced, the search space is bounded to a smaller region and the end node is reached faster. Both search algorithms can be performed either uni-directionally (beginning from the start node only) or bi-directionally (beginning the search simultaneously from start and end nodes). Combining them together offers four different search methods. The application of these four different search methods are evaluated in 2D and 3D images in [244]. It is shown that the number of nodes visited in the search process strongly depends on the discriminative power of the feature used. Furthermore it is also shown that for a specific application, using a simple heuristic function leads to a considerable reduction in the number of nodes evaluated as compared with the search approach without heuristic term.

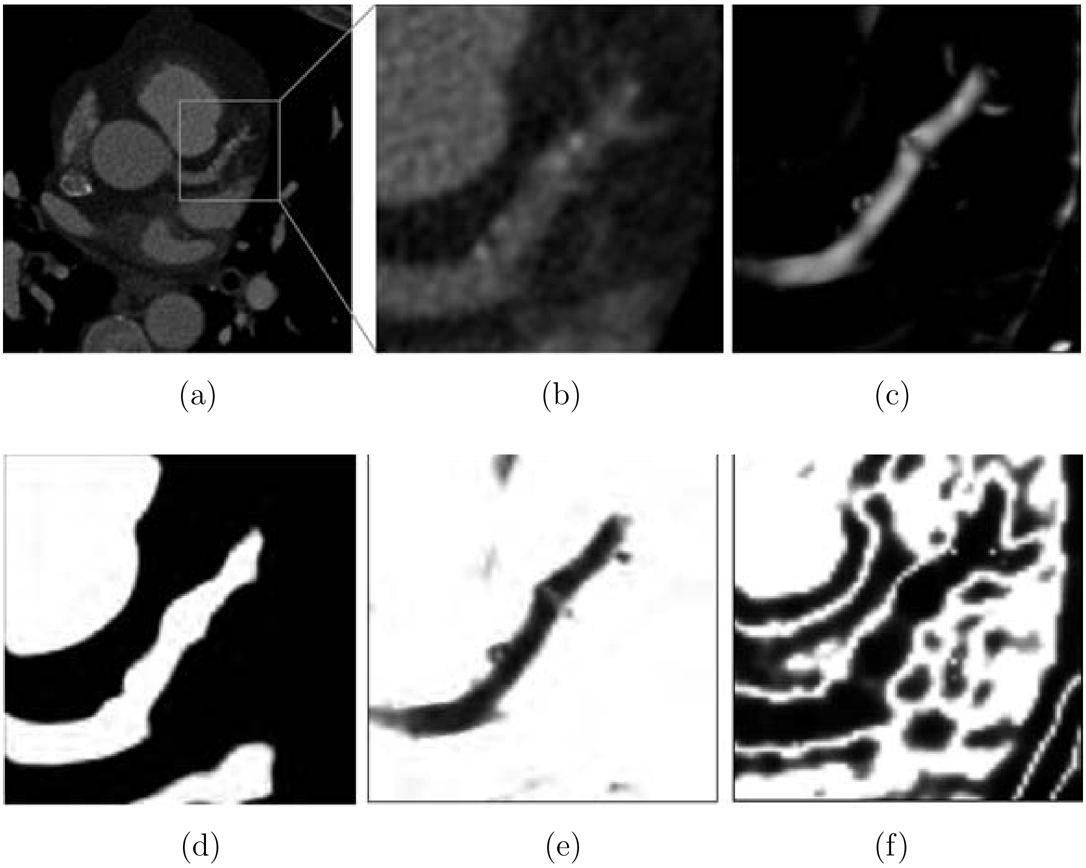
(a) (b) (c)

(d) (e) (f)

Figure 2.7: Examples of CTA image and its corresponding cost images [154]. (a): CTA image; (b): Region of interest; (c): Vesselness; (d): Post-processed intensity image; (e): Cost image combining vesselness and intensity measures; (f): Region statistics cost image.

In [245, 171, 152, 151, 154], the minimal cost paths representing coronary centrelines are obtained using the measurement constructed from vesselness information. The multiscale filter based on the eigenvalue analysis of the Hessian matrix is used to highlight tubular structures in the image prior to the vessel extraction. As comparison, in [161], a mathematical morphology technique is employed to filter the structures of interest before the minimal cost path is used to extract the centrelines. Region statistics are also used for constructing the cost image in [154]. Figure 2.7 shows an exemplar region of coronary CTA image and its two types of cost images derived from it.

The minimal cost path method not only can be used for extracting vessel centrelines, but also for delineating vessel surfaces. In [246], the centreline is first found by using a probabilistic vessel axis tracing method. The vessel contour in 3D space is then determined as the minimal cost path on a weighted directed acyclic graph from each cross-section derived from the extracted axis.

Similarly, Li *et al.* represent vessels as 4D curves by adding radius to the 3D location. They use the minimal path technique to extract tubular surfaces [129, 131]. Moreover, Benmansour *et al.* developed a method for segmenting closed contours and surfaces using a front propagation approach and a variant of minimal cost path search strategy [25]. As for open curve segmentation, the stopping criteria is required to be user-defined. In [23, 24, 22], the extraction of centrelines and boundaries of the vessels is demonstrated by finding the globally optimal trajectories between two or more user-supplied points via the fast marching algorithm. However, the minimal path technique may fail if the image lacks contrast or the object of interest is long and curvy. In these cases, the obtained minimal cost paths tend to be a straight line between the starting and ending points. Benmansour *et al.* proposed to detect recursively new vessel points along the curve of interest between the two given points [25]. These detected vessel points guide the front to propagate further in the direction of the curve without propagating in all directions. Thus, it not only reduces considerably the search space in the image, but also prevents the early termination or short cut of the minimal path.

2.3.1.8 Model-matching

In this section, we classify the vascular segmentation methods based on model matching into five categories, according to the underlying geometric models.

Core model

Blood vessels can be described as trees of branching tubes. Fridman *et al.* [75, 74] extracted the vessel tubes and branching geometry in 3D via skeletons computed as cores. Cores are height ridges of a graded measure of medial strength called medialness, which measure how much a given location resembles the middle of an object as indicated by image intensities. The authors use a core-following technique that optimizes a medialness measure over position, radius, and orientation. It combines methods for branch-finding, branch-reseeding, and core-termination with core-following to produce a tool that can extract complex branching objects from 3D images without the need for user interaction. The core-based method is evaluated on synthetic images of branching tubular objects as well as blood vessels in clinical data. The results reported in [75, 74] show impressive resistance to noise and the capability to detect branches spanning a variety of widths and branching angles.

2D disk (3D sphere) model

Haris *et al.* proposed to use a circular template model for coronary segmentation in 2D angiograms [86], as shown in Figure 2.8. Where there is no bifurcation, crossing or termination, the tracking problem is essentially to find a subsequent artery element $\mathcal{C}_{i+1}(\mathbf{p}_{i+1}, \mathbf{d}_{i+1}, w_{i+1})$ from the current artery element $\mathcal{C}_i(\mathbf{p}_i, \mathbf{d}_i, w_i)$. Parameter $\mathbf{p}_i$ is the centre of artery element $\mathcal{C}_i$, $\mathbf{d}_i$ is the displacement vector pointing from current centre $\mathbf{p}_i$ to next centre $\mathbf{p}_{i+1}$ and w_i is the diameter of the vessel at $\mathbf{p}_i$. After a sample of centre points $\mathbf{p}_i$ and corresponding radii $r_i = \gamma(w_i/2)$ are created shown as $c_0, c_1, c_2, \ldots$ in Figure 2.8 (a), they are then analysed to detect the vessel wall, based on the magnitude of 1st-order derivative using Gaussian filtering. Once the vessel points $\mathbf{b}_i^1$ and $\mathbf{b}_i^2$ are detected, the position of next vessel element $\mathbf{p}_{i+1}$ is derived as $\mathbf{p}_{i+1} = \frac{1}{2}(\mathbf{b}_i^1 + \mathbf{b}_i^2)$, the displacement vector $\mathbf{d}_{i+1} = \mathbf{p}_{i+1} - \mathbf{p}_i$ and width $w_{i+1} = \|\mathbf{b}_i^1 - \mathbf{b}_i^2\|$ shown in Figure 2.8 (b). Using circular templates with radius r larger than vessel radius $w/2$ ($r_i = \gamma(w_i/2)$, $1.1 \leq \gamma \leq 1.4$) facilitates the vessel branch detection [86]. Bifurcation occurs when there are more than two artery points detected as shown in Figure 2.8 (c).

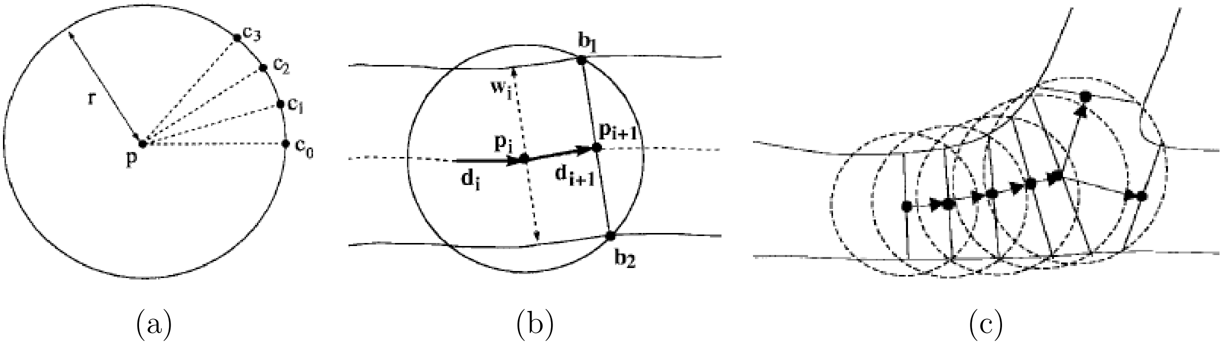

(a) (b) (c)

Figure 2.8: (a): Circular template model with centre $\mathbf{p}$, radius r, and a sequence of $\lfloor 2\pi r \rfloor$ samples taken over the circumference of circle, noted as $c_i, i = 0, 1, ..., \lfloor 2\pi r \rfloor - 1$ (b): Circular artery element model $\mathcal{C}_i(\mathbf{p}_i, \mathbf{d}_i, w_i)$ and subsequent artery model $\mathcal{C}_{i+1}(\mathbf{p}_{i+1}, \mathbf{d}_{i+1}, w_{i+1})$ obtained in the tracking process. (c): Tracking mode near a bifurcation point [86].

Nain *et al.* proposed a ball measurement by introducing the local neighbourhood $B(\mathbf{p}, r)$ in the shape of a ball centred at voxel $\mathbf{p}$ with radius r [164]. For a 2D image, this model is effectively a disk as shown on the left in Figure 2.9. The measure ϵ_1 for voxel **p** is then defined as the percentage of voxels that fall both within the ball centred at **p** and the region R inside the contour of the object. In 2D, for a radius r similar to the vessel width, most pixels on the contour have the same ϵ_1 measure since locally the same percentage of neighbors fall within the filter radius. This is illustrated in the middle of Figure 2.9. To differentiate the contour points near a leak region from those falling on the tube surface, Nain *et al.* further proposed measurement ϵ_2: For each voxel **p**, it looks at the ϵ_1 measure of voxel **p**'s neighbors inside the contour since their measure is high for points inside widening regions. $\epsilon_2(\mathbf{p})$ is defined as $\epsilon_1(\mathbf{p})$ plus the sum of the ϵ_1 measure of **p**'s neighbouring voxels that are inside the contour. Filter ϵ_2 guarantees that contour points close to the widening of the vessel have a higher measure than contour points on the normal part of the vessel, as shown in the right of Figure 2.9.

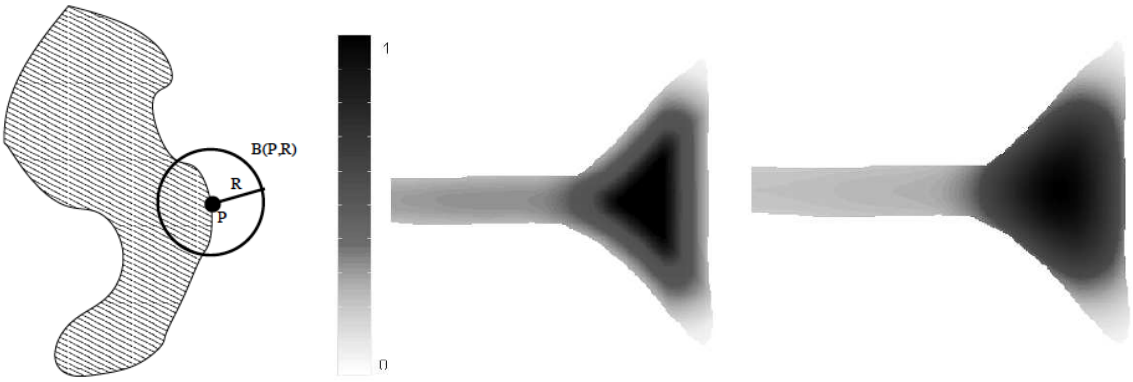

(a) (b) (c)

Figure 2.9: Illustration of ball measurement [164]. (a): Example of a 2D disk overlapping with 2D image region in grey; (b): The local ball filter response ϵ_1 for a synthetic shape that represents a potential leak, given a radius that is the width of the tube; (c): The local ball filter response ϵ_2 for the same synthetic shape.

Similar 2D disk and 3D sphere models are also used by Whited *et al.* in [241, 240] who referred to them as "pearls". The segmentation process thus becomes "pearling". Figure 2.10 shows the pearling and user-refined results on a rotational angiography scan of a head with an aneurysm. Following these early works, Slabaugh *et al.* proposed to use partial differential equations for generating smooth tubular surfaces from an ordered set of 3D balls [210]. Sphere models are also used by Lesage *et al.* in [125, 126].

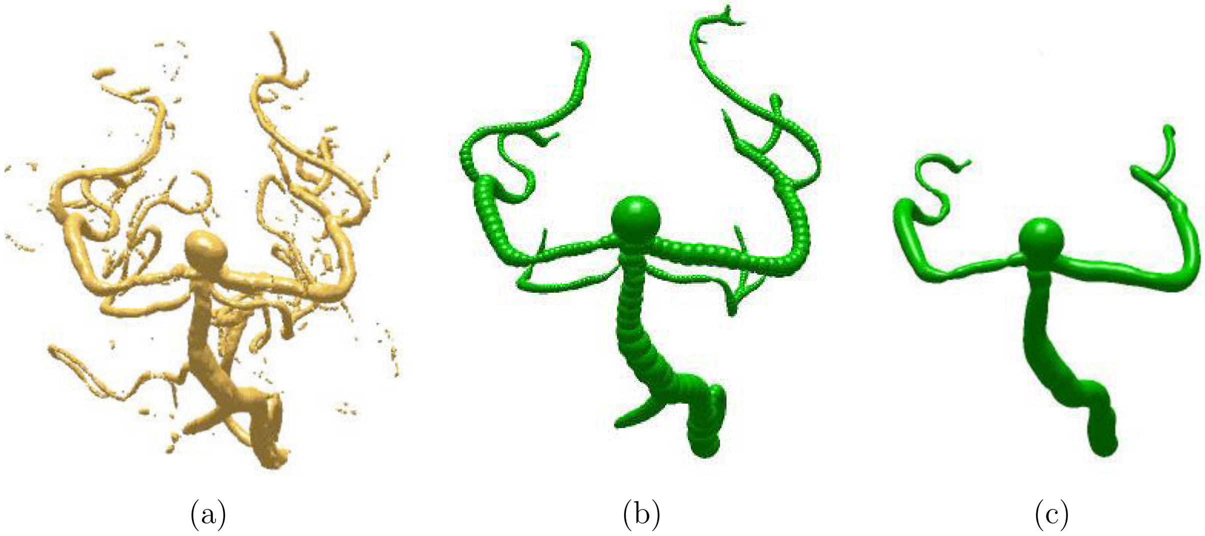

Figure 2.10: Example of pearling. (a): Thresholded volume rendering of the brain angiography dataset; (b): Initial result of the pearling algorithm; (c): User-refined pearling result [241].

Tubular/Cylinder Model

A multiple hypothesis tracking approach using a tubular template to segment 3D vessel structures was proposed by Friman *et al.* in [77] and further extended in [76]. Here, the vessel segmentation is essentially formulated as finding the maximum model matching path. At each potential location, the best fit of the template structure with the image region is found, thus constructing this path. The authors propose to simultaneously track multiple hypothetical vessel trajectories that potentially could traverse low contrast regions and lead to an improved spatial tracking performance in areas of low contrast. The vessel template model proposed in [77] has a flatter vessel profile than the Gaussian profile used in [45, 119] and allows for flexible central position, radius and orientation adjustment. 2D tube models are also used by Pechaud *et al.* in [176] for extracting tubular structures from 2D images.

In [247], Worz *et al.* also pointed out that the 2D cross-section of medium and large sized vessels is plateau-like as shown in Figure 2.11 which cannot be accurately represented by a 2D Gaussian profile. The authors consequently proposed to model vessels of varying sizes using a Gaussian smoothed 3D cylinder as shown in the bottom row in Figure 2.11.

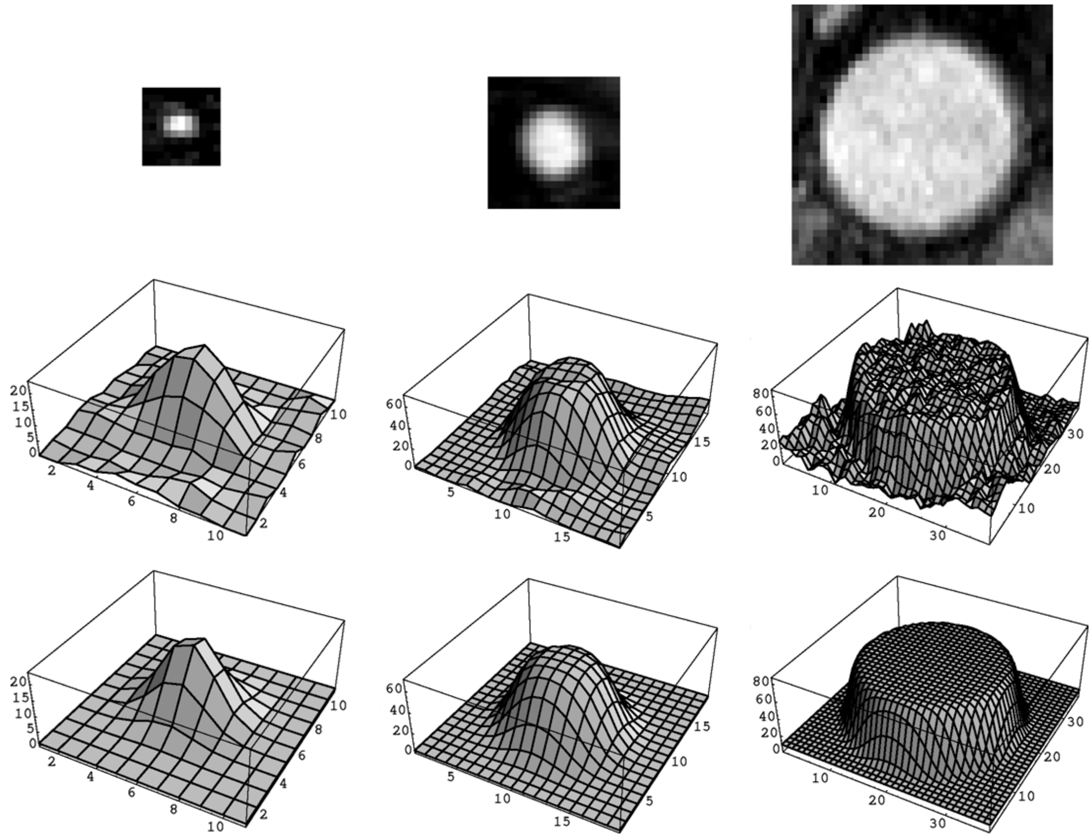

(a) (b) (c)

Figure 2.11: Intensity plots of orthogonal 2D slices through (a) a thin vessel in the pelvis, (b) the artery iliaca communis, (c) the aorta; Top row: 2D slice from 3D MR images; Middle row: Intensity profile of the 2D slice; Bottom row: 2D cross-section of generated 3D cylindrical intensity model [247].

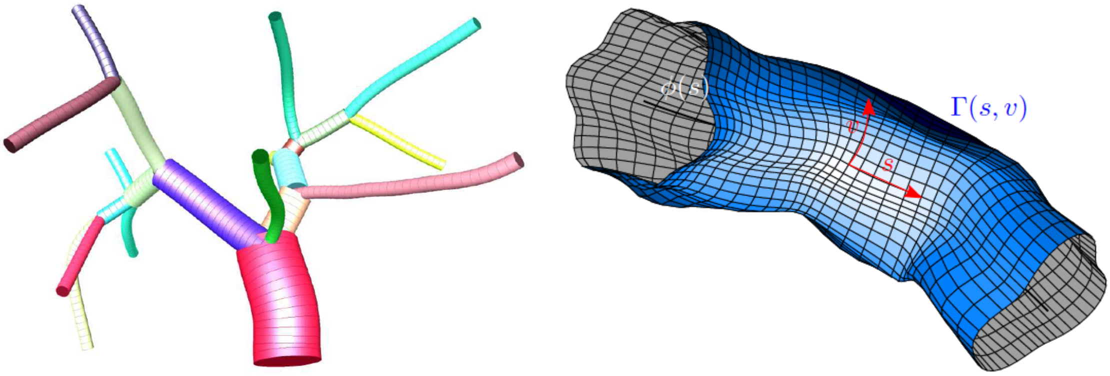

(a) (b)

Figure 2.12: Cylinder models for vasculature [156]. (a): 3D tree structure with generalised cylinders representing branch segments; (b): Deformable generalised cylinder with radius varying both along and around the axis.

Extending from previous work on generalised cylinder models in [169, 251, 21], Mille *et al.* proposed to use generalised cylinders to represent a deformable tree explicitly in order to segment and reconstruct the 3D vascular tree [156]. The topological relationships between segments are modelled explicitly as in the example shown in Figure 2.12 (a). Compared to other methods, this allows easy quantitative analysis, such as measuring diameters or lengths of vessels. The method first builds an initial tree with a technique relying on minimal paths, given a unique user-supplied root point. Within this constructed tree, the central curve of each branch segment and an associated variable radius function evolve in order to satisfy a region homogeneity criterion. As an example, a deformable generalised cylinder is shown in Figure 2.12 (b).

Elliptical cross-sectional models

Circular models have been widely used to represent vessel cross-sectional shapes. Although requiring fewer parameters, the circular model lacks the flexibility to represent non-circular sections, compared with the elliptical model. Krissian *et al.* compared the circular and elliptic cross-sectional models in [120]. The authors showed that the elliptic model not only is more versatile in representing vessel bifurcation and malformation, but also provides higher accuracy when representing the segmented vessel surfaces. Elliptical cross-sectional models have also been used for coronary artery segmentation [70] and for cerebral arterial segmentation [209].

Superellipsoid model

In yet another approach, Tyrrell *et al.* proposed to use cylindroidal superellipsoid models to represent 3D vessel segment for the segmentation of complex vasculature in 3D images [224]. Figure 2.13 illustrates the superellipsoids with varying shapes. Figure 2.14 shows how the superellipsoid model is incorporated together with vessel traversal scheme to segment the vascular structures.

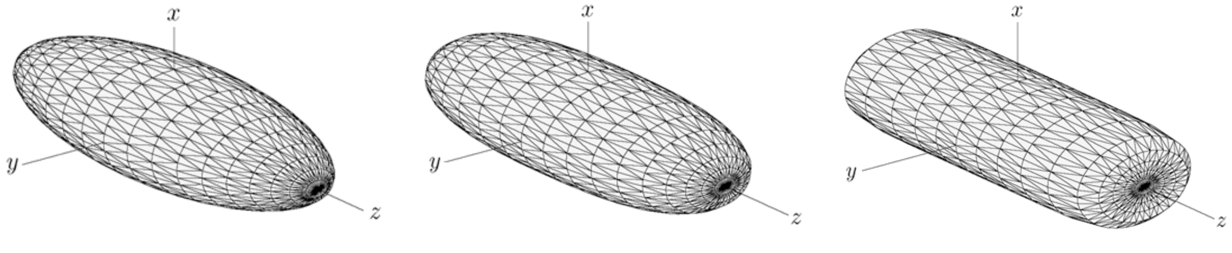

(a) (b) (c)

Figure 2.13: Superellipsoid models with fixed shape parameter $\epsilon_2 = 1$ and varying parameter ϵ_1 [224]. (a): $\epsilon_1 = 1$; (b): $\epsilon_1 = 0.75$; (c): $\epsilon_1 = 0.25$.

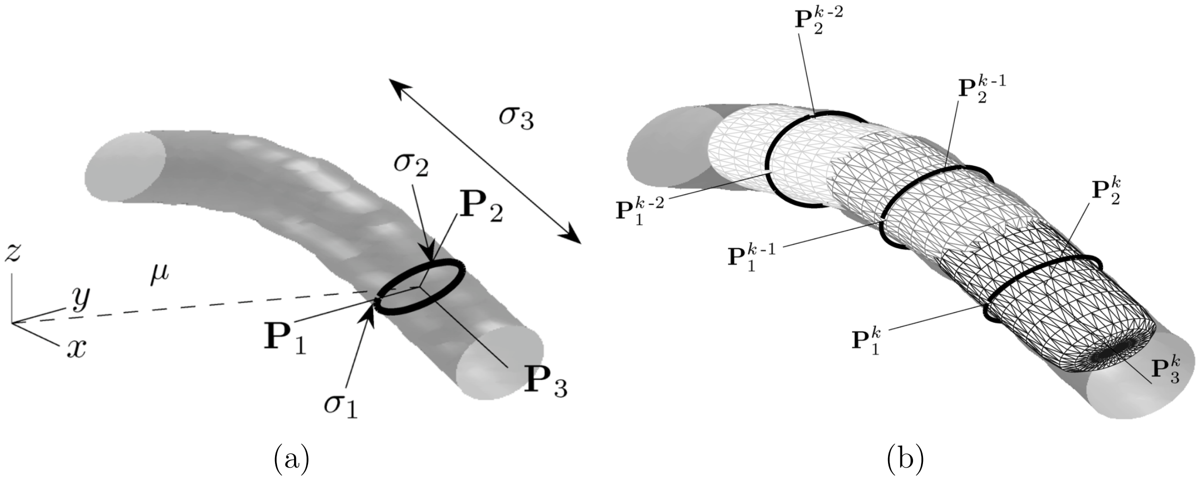

Figure 2.14: Superellipsoid model parameters and vessel traversal. (a): Dashed line μ is the offset from the origin to the centre of a vessel segment. $[\mathbf{P}_1, \mathbf{P}_2, \mathbf{P}_3]$ are the principal axes of the localised vessel segment. Dark ellipse oriented relative to the principal axes denotes the local vessel boundary with cross-sectional scales σ_1 and σ_2. Line σ_3 is the approximate length over which the vessel segment is locally cylindriodal. (b): A sequence of fitted superellipsoids denoted $k-2$, $k-1$ and k superimposed on a vessel. At step $k+1$, the local pose $\mathbf{P}_3^k$ determines the next shift in the traversal [224].

2.3.1.9 Probabilistic Tracking

Florin *et al.* proposed using a particle filter approach for the segmentation of coronary arteries in [70]. The coronary segmentation problem is reformulated as recovering the successive elliptical cross-sectional planes of the vessel in a probabilistic fashion with numerous possible states. Such states consist of the orientation, position, shape and appearance of the vessel. They are recovered in an incremental fashion, using a sequential Bayesian filter (particle filter). Given a starting position, the vessel tracking essentially aims to find a state vector that upon its successful propagation provides a complete segmentation of the coronaries. A Monte Carlo sampling rule that propagates in parallel multiple hypotheses is used to account for bifurcations and branchings in [70]. This work has been extended further to segment the cerebral arteries from CTA in [209].

Schaap *et al.* proposed a Bayesian tube tracking algorithm that allows for incorporating a prior shape knowledge of the structure of interest [202, 199]. The vessel is considered as a series of tube segments as shown in Figure 2.15. Each tube segment at iteration t is characterised by a state vector $\mathbf{x}_t = (\mathbf{p}_t, \mathbf{v}_t, r_t, \hat{I}_t)^{\mathrm{T}}$ with location $\mathbf{p}_t$, orientation $\mathbf{v}_t$, radius r_t and average intensity value $\hat{I}_t$. The method was applied to track coronary arteries [202] and carotid arteries [199] from CTA data. It is shown that the non-deterministic character of Bayesian tracking increases the robustness of the tracking method [199].

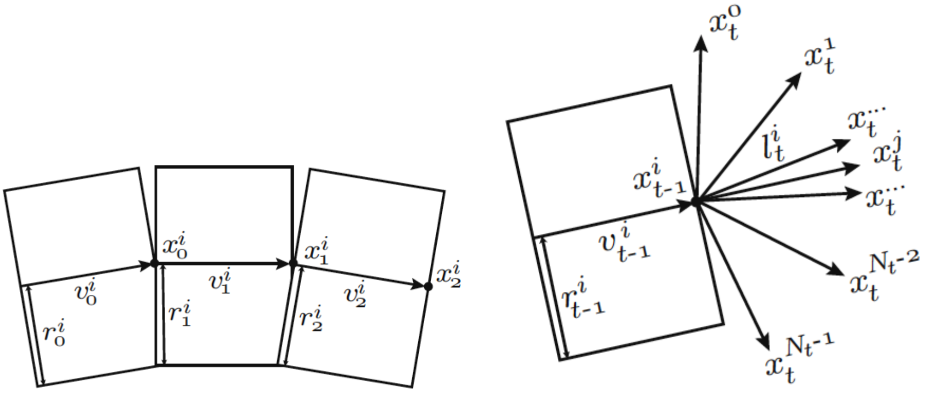

(a) (b)

Figure 2.15: Tube model and prediction of a new tubular segment. (a): A part of the tube configuration $\mathbf{x}_{0:t}$; (b): The prediction of new tube segments from iteration $t-1$ to t [202].

Furthermore, Schaap *et al.* used the extracted coronary centreline to segment the coronary lumen using graph cuts and robust kernel regression [201]. The authors propose a two-stage approach for segmenting the coronary lumen given a centreline:

1. Find an optimal labelling of lumen and background by searching for the image region with intensities similar to the centreline intensity and also surrounded by strong edges. This is based on the observation that the gradients of image intensity are large on the boundary of the coronary lumen, while the image intensities within the lumen vary smoothly in CTA images.

2. Remove falsely segmented regions that do not belong to the vessel of interest using the fact that the segmented lumen should not contain any holes, that the surface should be smooth and that side-branches should not be segmented. This is done by using robust kernel regression and a cylindrical parameterisation of the lumen boundary.

Figure 2.16 illustrates this process with a cross-sectional image.

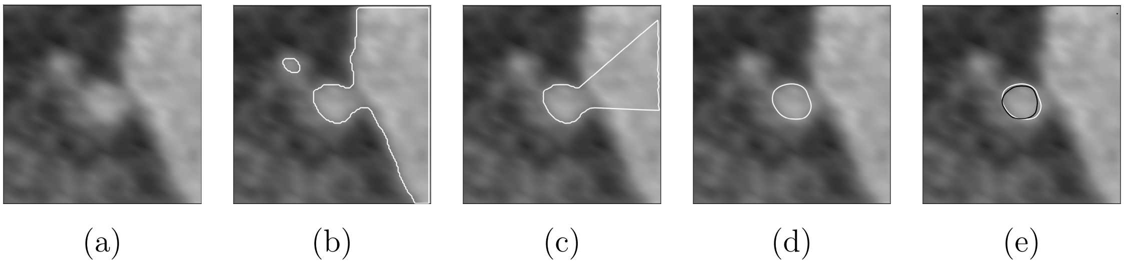

Figure 2.16: An example of coronary lumen segmentation. (a): Cross-section of the input image; (b): Segmentation result after first step; (c): Initialisation for step 2; (d): Final segmentation; (e): Automatic segmentation (white) shown together with the reference standard (black) [201].

Inspired by the previous works of using particle filters for vessel segmentation, Lesage *et al.* proposed another stochastic Bayesian tracking algorithm for coronary segmentation in CT images [125]. The main contributions of this work are the proposal of a constrained, medial-based geometric model and a new sampling scheme that takes into account a distribution of hypotheses broader than classical particle filters for the selection. For the details of this sampling scheme, we refer to Section 3 [125]. Before the tracking process, prior knowledge was learned from a manually segmented database of images. The experiments show that this method performs very well even for clinical data with pathologies and local anomalies as shown in [125].

2.3.1.10 Gradient Vector Flow

Conventional vascular filters try to identify tubular objects at different scales and combine all vesselness response into one multi-scale vesselness response. The first- or second-order gradient vectors used for vesselness response calculation are typically derived in a Gaussian scale space. However, this process is essentially an isotropic diffusion that does not preserve any edge information and may even lead to nearby features to diffuse into each other as shown in the 3rd column in Figure 2.17. To address this problem, Bauer *et al.* proposed in [19] to replace the multi-scale computation of the gradient vectors by the gradient vector flow (GVF) because the latter allows for an edge-preserving diffusion of the gradient information. The resulting vector field (shown in the 4th column of Figure 2.17) is then used for detection of tubular objects by applying Frangi's vesselness measure. This not only prevents the merging of the nearby structures, but also supersedes the computation at multiple scales.

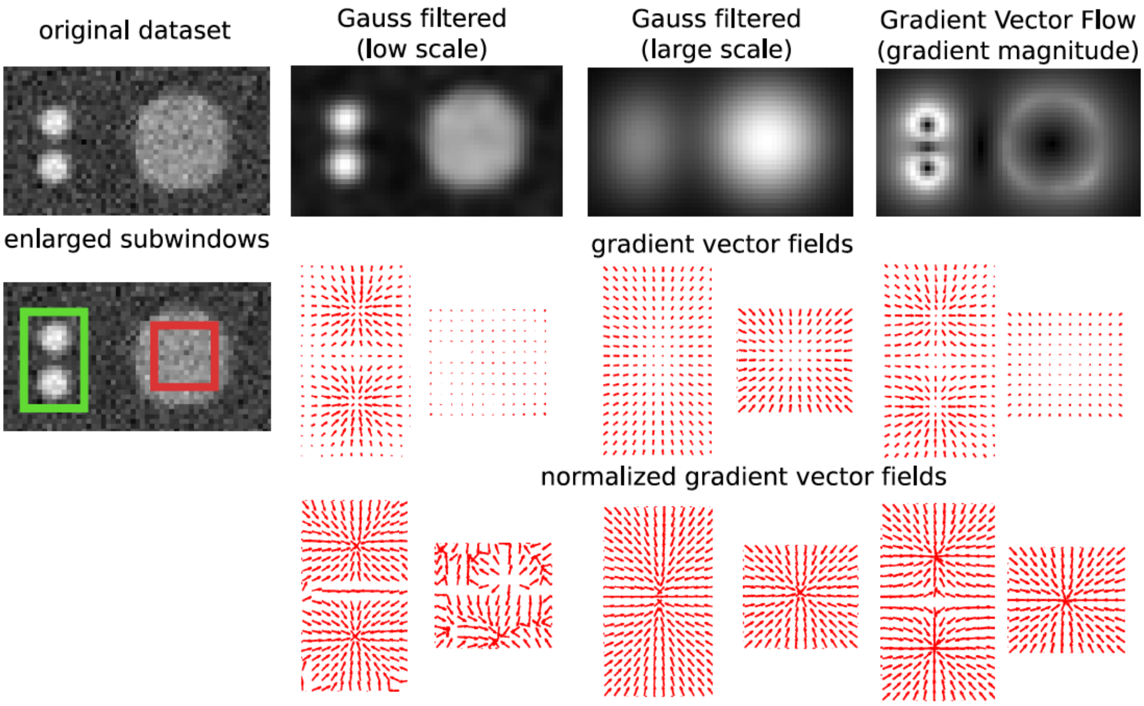

Figure 2.17: Orthogonal cross sections of 3D tubes and intermediate processing results of multi-scale gradient vector computation compared with the GVF [19].

In [18], Bauer *et al.* extended their previous work [19] further to detect the medial curves of structures of interest in 3D images. The gradient vectors computed by the GVF are used to derive the vesselness measure $\mathcal{V}(\mathbf{x})$ [73]. Based on this vesselness term, a medialness measure $\mathcal{M}(\mathbf{x}) = 1 - \mathcal{V}(\mathbf{x})$ is proposed to highlight the medial curves. Since the magnitude of the GVF vanishes at medial curves for both tubular objects and non-tubular objects, the complete medial curves of both types of structures can be extracted independently of the size and contrast of these objects. This not only allows the detection of centrelines of vascular structures, but also the extraction of the medial curves in cases where the structures are not tubular such as junctions or stenoses.

The strategies discussed above are often integrated with each other vertically or horizontally to achieve best segmentation results, e.g., [149, 161].

2.3.2 Branch Detection

Several vessel extraction algorithms deal with branching implicitly, for example mathematical morphology [142], particle filters [70], model-based tracking [86, 76] *etc.* Another group of algorithms explicitly represent bifurcations [9, 10] or perform vascular tree connection after obtaining the vessel branches [106]. The third group of algorithms first segment vessel-like structures and then perform tree pruning to remove the unwanted branches [254, 241]. The tree pruning approach can be either based on information about the absolute and relative lengths of branches, intensity profile information, or information about the structure of the identified tree.

Carrillo *et al.* proposed to recursively track the branches and detect the bifurcations by analysing the binary connected components on the surface of a sphere that moves along the vessels [37]. In [155], Mille *et al.* build the vessel tree by back-propagation starting from endpoints, which ensures that the junctions are detected. In [131], Li *et al.* proposed to use a 4D interactive key point searching scheme. After identifying the key points, the entire multi-branch structure extraction is reduced to finding structures between all adjacent key points pairs as shown in Figure 2.18.

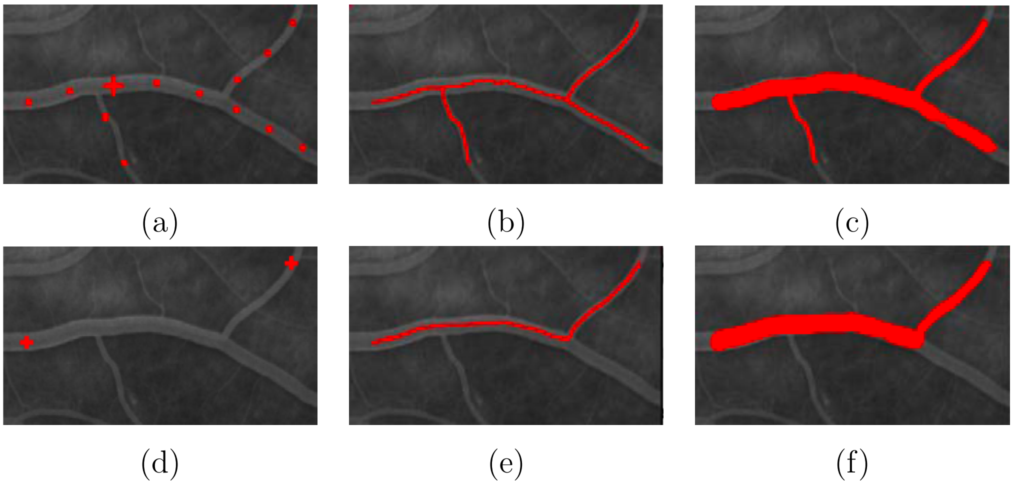

Figure 2.18: Vessel segmentation from an 2D angiogram based on 4D iterative key points scheme (top row) versus 4D minimal path method (bottom row) [131]. Seeding point is shown as red cross in (a) and (d). (a): Initial points and detected key points shown in red; (b) and (e): Detected multi-branch centrelines; (c) and (f): Detected vessel surfaces.

2.3.3 Radius Estimation

Vascular centreline extraction is not sufficient for the diagnosis and treatment planning of coronary artery disease. Accurate quantification of coronary lumen and plaque parameters is essential for stenosis grading, stenting and surgical planning. There have been a few publications addressing vessel lumen segmentation implicitly or explicitly [86, 76, 140, 144, 96, 131, 202, 125, 240, 247, 70, 224, 201, 250, 237].

All geometric-model based segmentation algorithms and Hessian-based methods estimate the local vessel radius during the vessel centreline extraction. For Hessian-based approaches, the vessel size is estimated to be roughly same as the size of the kernel which produces the maximal vesselness response. For model-matching based segmentation methods, the optimal fitting of the geometrical model with the local region produces the best estimation for the centre position and the size information of the model which can be used to derive the radius of the vessel segment.

2.3.4 User Interaction

While researchers make every effort to develop fully automatic vessel segmentation algorithms, most methods require some user interaction at least for the final verification of the results. According to the required user-interaction, methods can be classified to three categories: automatic, semi-automatic or interactive.

Fully automatic vessel segmentation algorithms only require the input of the image to be processed, e.g., [224, 32]. Contrary to automatic methods, interactive ones are performed by the user interactively using software tools which provide visual feedback of the segmentation and also take input from the user during the process, e.g. [255, 12]. Thus, interactive segmentation can be time-consuming. It also relies on the skill and experience of the users. Often the level of user interaction is between these two extremes, e.g., semi-automatic. For the semi-automatic methods, it is essential that the user provides initialisations for the algorithm or corrections during the segmentation procedure, such as specifying the start and end points for a coronary branch, or restarting the segmentation after the algorithm fails to pass through the stenosis segment, or steering the algorithm by accepting or rejecting the current segmentation. Most vessel segmentation methods are semi-automatic and require various levels of user-interaction to initialize the segmentation process, to visually inspect the results, to correct the error if it happens and to post-process the segmentations if necessary [164, 25, 244, 154].

2.4 Evaluation and Comparison of Segmentation Methods

The comparison of segmentations is the topic of several papers [232, 107, 233, 123, 51]. These works mainly aim at evaluating the segmentation of anatomical structures, with the potential of being extended for evaluating the coronary vessel segmentation. The recent Rotterdam coronary segmentation challenge [153] has initiated an active investigation and comparison of various coronary segmentation methods. It has also prompted subsequent work on comparing the segmentation results from various extraction algorithms [200] and combining multiple annotations [226].

To evaluate an automatic or semi-automatic segmentation result, one can compare it with a manual segmentation from an experienced clinician. However, different clinicians may annotate slightly differently which leads to *inter-observer* variability. Even if the annotations for the same image are marked by same clinician at different time, the results may also vary. This difference is referred to as *intra-observer* variability. The performance of manual annotation, automated and semi-automated methods also depend on the initialisation for each method and the length of the vessel being tracked.

2.4.1 Non-vascular Structures

Zijdenbos *et al.* [259] proposed an average similarity index (SI) to evaluate whether or not an automatic segmentation technique could match or reduce the inter- and intrarater variability of the manual method. The similarity index (SI) is defined as twice the ratio between the volume of the intersection (overlap) and the mean volume of a pair of labels in the same coordinate system. This definition ensures that SI is sensitive to both the differences in size and location.

Assume L_1 and L_2 are the set of voxels classified with same label in two different segmentations of the same image, respectively, $n(L_1)$ and $n(L_2)$ are the numbers of elements in each set. The similarity index is then formulated as:

$$SI = \frac{2n(L_1 \cap L_2)}{n(L_1) + n(L_2)}. \tag{2.13}$$

The higher the SI value is, the better two segmentations agree with each other.

A slight change of SI formulation gives us a similar measure referred to as overlap ratio (OR) as in Heckemann *et al.* [90]. OR is defined as:

$$OR = \frac{n(L_1 \cap L_2)}{n(L_1 \cup L_2)}, \tag{2.14}$$

In [232], Warfield *et al.* used the expectation-maximization (EM) algorithm for simultaneous truth and performance level estimation (STAPLE). Given a collection of segmentations, the algorithm computes a probabilistic estimate of the true segmentation and a measure of the performance level represented by each individual segmentation. The source of each segmentation in the collection can either be a human observer or an automatic segmentation algorithm. This work is further developed in [233] by estimating observer bias and variance. Furthermore, STAPLE is straightforward to apply to both non-vasculature and vasculature segmentation.

Besides the comparison of different segmentation results, how to utilise multiple segmentations also poses an interesting question. Rohlfing *et al.* proposed a shape-based averaging method to combine multiple segmentations in [189]. Individual segmentations are combined based on the signed Euclidean distance maps of the labels in each input segmentation. Compared to label voting [116, 184], this combination method produces smoother, more regular output segmentations and avoids fragmentation of contiguous structures as shown in [189].

2.4.2 Vascular Structures

In [245], the difference between the automated or semi-automated method and the individual manual annotations is quantified and compared to the differences between the manual annotations to determine whether the automated method can replace manual annotations. The robustness of its proposed minimum cost path approach is tested by varying the user-initialized seed points. Intra-observer variability is assessed by performing multiple manual annotations for each observer. To ensure the fairness, the evaluations are also carried out with multiple coronary segments of different lengths.

The Simultaneous Truth and Performance Level Estimation (STAPLE) algorithm as proposed in [232] generates ground truth volumes from a set of binary expert segmentations as well as a simultaneous accuracy assessment of each expert. In [107], Jomier *et al.* combined morphological operators and the STAPLE algorithm together to obtain ground truth of centreline extractions as well as a measure of accuracy of the methods to be compared for the validation of vascular segmentations.

In [123], Lange *et al.* utilised quantitative evaluation metrics for clinical 3D images containing vessel trees of the brain and liver. The authors first presented a method to identify corresponding points on different vessel trees interactively. They then proposed four different metrics based on these correspondences. Although these metrics were initially suggested for validating the results of registration, they can also be applied in evaluating the vessel segmentation, assuming the ground-truth segmentation as target image, the segmentation to be evaluated as the transformed source image.

Assume E is the reference segmentation (ground truth) and $\hat{E}$ is the segmentation to be evaluated. Let $(\mathbf{p}_i, \hat{\mathbf{p}}_i), i = 1, ..., n$ be all pairs of corresponding points on all the vessel segments, while $\forall \mathbf{p}_i \in E$ and $\forall \hat{\mathbf{p}}_i \in \hat{E}$. The average distance of corresponding points on extracted centre lines is formulated as:

$$D_{\text{average}}(E, \hat{E}) = \frac{1}{n} \sum_{i=1}^{n} \|\mathbf{p}_i - \hat{\mathbf{p}}_i\| \tag{2.15}$$

The weighted distance is defined as:

$$D_{\text{weighted}}(E, \hat{E}) = \frac{1}{n} \sum_{i=1}^{n} (\mathbf{p}_i - \hat{\mathbf{p}}_i)^T \mathbf{W}_i (\mathbf{p}_i - \hat{\mathbf{p}}_i) \tag{2.16}$$

where $\mathbf{W}_i$ is a 3×3 covariance matrix, representing the anisotropic location uncertainty for the point pair $(\mathbf{p}_i, \hat{\mathbf{p}}_i)$ [190]. The distance between the two points are different in different directions. Thus a weight matrix $\mathbf{W}_i$ is used instead of a scalar weight for each pair.

From the vessel centrelines and a given corresponding point pair $(\mathbf{p}_i, \hat{\mathbf{p}}_i)$ (except in the branching points) a normalised tangential vector pair $(\mathbf{d}_i, \hat{\mathbf{d}}_i)$ can be computed.

The cross product of these two vectors is used to evaluate the deviation of $\hat{\mathbf{d}}_i$ from the ground truth $\mathbf{d}_i$, referred to as directional deviation [123]. It is formulated as:

$$D_{\text{dir}}(E, \hat{E}) = \frac{1}{n} \sum_{i=1}^{n} \|\mathbf{d}_i \times \hat{\mathbf{d}}_i\| \tag{2.17}$$

Lange *et al.* [123] also proposed a metric that is less dependent on the centreline extraction. The metric calculates the relative volume overlap of corresponding vessel segments. Similar to the overlap ratio as formulated in Equation 2.14, here the volume overlap metric is defined as:

$$D_{\text{vol}}(E, \hat{E}) = \frac{1}{n} \sum_{i=1}^{n} \frac{V_i \cap \hat{V}_i}{V_i \cup \hat{V}_i} \tag{2.18}$$

where V_i and $\hat{V}_i$ are the volumes of the corresponding vessel segments in the segmentation E and $\hat{E}$ respectively.

These four evaluations metrics [123] can be used to evaluate both the accuracy of vascular image registration and the accuracy of vessel centreline/lumen segmentation. Even though most of the evaluation metrics have not been proposed for coronary artery segmentation, they are in general applicable to any kind of vascular segmentations. Similar as the volume overlap measure as in Equation 2.18, the Dice similarity metric is used in [130, 201] to evaluate the vascular segmentation results.

As part of the 2008 MICCAI workshop "3D Segmentation in the Clinic: A Grand Challenge II", a coronary artery tracking competition has been started. For the detailed information of this competition, see [153]. Without the ground-truth segmentation, it is essential to generate a reference standard from multiple manually annotated datasets. One of the contributions of this work is the design of a consensus reference standard for vessel tracking data with multiple observers using the weighted averaging of 3D open curves. van Walsum *et al.* proposed to use the mean shift algorithm to derived a weighted average of multiple paths [226]. This is shown to handle bifurcations of vessel structures or disagreements among observers better than arithmetic averaging.

Figure 2.19 shows the averaging via the mean shift algorithm for determining the reference standard from the various observations, as proposed in [226]. The mean shift algorithm used here is extended from [50], where it originally was designed to iteratively shift a data point along the gradient of a density that is determined by a set of data points and kernel functions until the gradient vanishes, and the point has arrived at the maximum of the density.

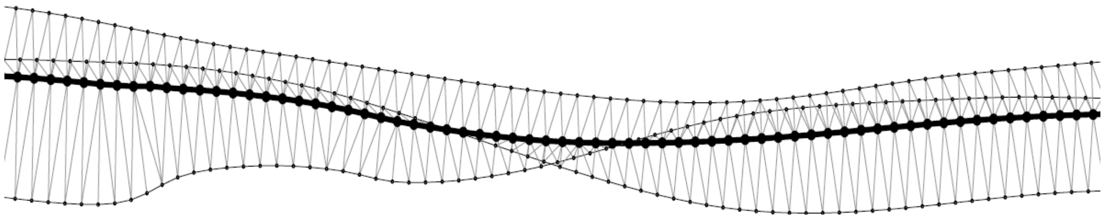

Figure 2.19: Illustration of averaging via the mean shift algorithm [200]. Thin black lines: The annotations of three observers; Thick black line: The resulting average. The correspondence used during the last mean shift iteration is shown in light-gray.

To summarise the work involved in this coronary segmentation challenge, in [200], Schaap *et al.* proposed a standardized evaluation methodology for the quantitative evaluation of coronary artery centreline extraction algorithms on the same reference database as in [153]. The major contributions of this work are defining measures for the evaluation of coronary artery centreline extraction algorithms as illustrated in Figure 2.20 and providing thirty-two CTA datasets with corresponding reference standard. Thirteen coronary centreline extraction algorithms were quantitatively evaluated and compared according to the proposed four measurements in [200].

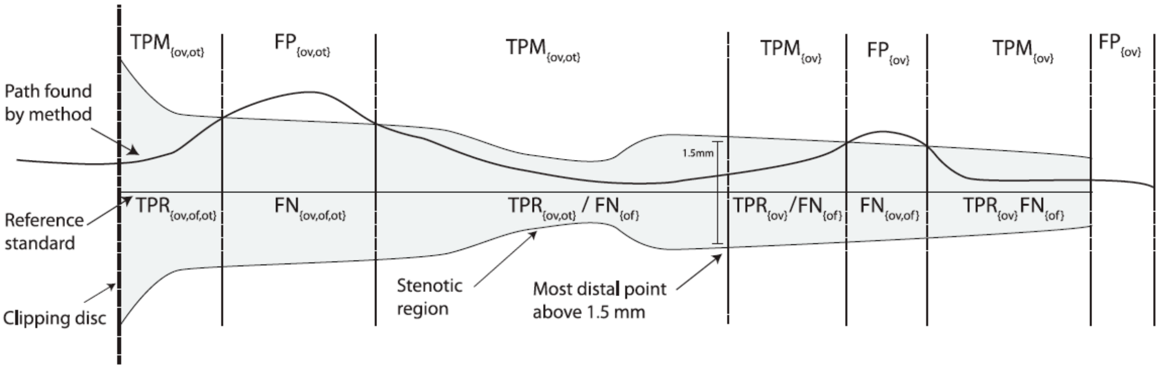

Figure 2.20: Illustration of different quantities for the assessment of vessel segmentation [200]. The reference standard is shown as the horizontal line in the middle with annotated radius depicted as the grey region. The metrics used to evaluate the segmented coronary path are labelled above and below the reference standard. For further details on the metrics, see [200].

Yuan *et al.* proposed to use a vessel model as prior knowledge by modelling a vessel segment as a local line model and exploiting the second order information along the line to capture potentially existing line structures in images. To test their method, the authors proposed the following angular discrepancy measure in [252]: Let Ω be the image domain and $\Omega_v \subseteq \Omega$ be the vessel region, given the ground truth of an image $I^*(\mathbf{x}) = \begin{cases} 1 & \text{if} \quad \mathbf{x} \in \Omega, \\ 0 & \text{otherwise,} \end{cases}$ and $\mathbf{d}^* : \Omega_v \to \mathbb{R}^2$, the true vessel direction, an angular discrepancy measure can be defined as:

$$D_{\text{angle}} = \frac{1}{N_v} \sum_{\mathbf{x} \in \Omega_v} \left| \mathbf{d}(\mathbf{x}) \cdot \left(\begin{bmatrix} 0 & -1 \\ 1 & 0 \end{bmatrix} \mathbf{d}^*(\mathbf{x}) \right) \right|, \tag{2.19}$$

where $N_v = |\Omega_v|$, $\mathbf{d}(\mathbf{x})$ is the estimated vessel direction at point $\mathbf{x}$. The more consistent the estimated directions of vessels and the true directions are, the less angular discrepancy there will be.

2.5 Visualisation of Vessel Structures

The visualisation of tubular structures such as blood vessels is an important topic, particularly for vascular disease diagnosis and treatment. CTA and MRA provide 3D high-resolution volumetric data sets of the human body, containing the vessels of interest. However, they also contain many other objects of less or no interest. Also, the vessels of interest often lie across multiple slices. This makes direct visualisation (e.g., volume rendering, maximum intensity projection and shaded surface display) without pre-processing unable to visualise all the vascular structures of interest or to achieve satisfactory accuracy. Two ways of pre-processing are often used to assist the visualisation:

- One is to remove the irrelevant structures before using the aforementioned visualisation techniques.
- The other is to obtain the central axis segmentation for the tubular structures of interest. The central axis as an input for the visualisation algorithms is then used as a camera path to reorganise the image and display the whole length of tubular structure within a single image using curved planar reformation (CPR).

2.5.1 Visualisation without Reformation

Previously, there have been a few papers discussing this type of volume visualisation technique [63, 145]. Here we briefly summarise all major algorithms proposed for visualising 3D volume, with a focus on tubular objects.

Maximum intensity projection (MIP) is a visualisation method for 3D data. This algorithm casts a ray through the 3D data for each pixel in the resulting image. Only the highest-attenuation voxels found on a ray are preserved. It provides a 2D projection in the visualisation plane of the voxels with maximum intensity that fall in the way of parallel rays traced from the viewpoint. It picks up the maximum intensity voxel encountered in the projected ray. The disadvantage of MIP is that it loses the 3D depth information and over-estimates stenoses [89]. It also does not allow depiction of overlapping structures. The main advantage of MIP lies in its computational efficiency.

Due to the general infusion of contrast medium, not only the coronary arteries are filled with contrast medium, but also the cavities of the heart and other vascular structures. When full-volume MIP is applied, these cavities and other vascular structures are likely to overlap and obscure parts of coronary arteries.

To avoid obscuring of the vessels by other high density structures (e.g., bone and calcification), a Sliding-Thin-Slab MIP (STS-MIP) was proposed [166]. To obtain STS-MIP, a thin-slab (3-10mm) is selected from which an MIP image is reconstructed. This slab is moved through the volume, with the distance of slab movement smaller than the slab thickness, and at each step an MIP is created. This method provides vascular visibility within a sequence of overlapping thin-slaps. Another way of addressing the overlapping problem is to segment all contrast-enhanced structures except the coronary arteries before computing the MIP projections. This requires the segmentation of all cavities and other non-coronary vascular structures in the pre-processing step. After that, a good projection of coronary arteries can be obtained.

Local maximum intensity projection (LMIP) developed by Sato *et al.* [198] is an extended and improved version of maximum intensity projection (MIP). As MIP, the basic principle is to create an image by tracing an optical ray traversing 3D data from the view point in the viewing direction. However, LMIP differs from MIP in that the latter method selects the maximum value along an optical ray, whereas LMIP selects the first local maximum value encountered that is larger than a preselected threshold value. This characteristic allows LMIP to depict geometric information.

Volume rendering uses a similar ray-casting technique and calculates the sum of the weighted contributions of all voxels along the casted ray. In contrast to MIP and its extended methods, volume rendering uses nearly all of the data, allows demonstration of overlapping structures, and produces few artefacts. Other advantages of volume-rendering over MIP and shaded surface display (SSD) are illustrated by the examples in [104]. The disadvantage is that it requires substantially more computing power. For small structures like vessels, it only provides restricted views without segmenting the image prior to the volume rendering. For all the visualisation methods discussed so far, the user cannot directly manipulate the individual anatomical objects.

In [34], Bullitt *et al.* present a method of combining ray casting with segmented tubular objects, such as blood vessels. The method first projects segmented tubes using a modified z-buffer that records additional information about the objects projected. A subsequent step selectively performs volume rendering only through the object volumes recorded by the z-buffer. This method is extended for arbitrary shape objects in [35]. Basically, the proposed method combines object-ordered and image-ordered rendering techniques. The former is used to project the selected points onto the viewplane. The latter is used to cast selected rays through a defined volume of space. This approach also allows smoothly and interactively dilating segmentation boundaries along all axes, and selectively not displaying the unwanted structures.

A surface rendering gives better information of the relative position of the vessels, allowing rendering effects like lighting and depth cueing. It requires a binary segmentation of the image for selecting the viewed surface. In the case of an isosurface view, this segmentation is simply done by choosing a threshold on the image intensity, and a smoothed surface can be obtained using marching cubes algorithm [136].

The shaded surface display (SSD) algorithm fits surface primitives such as polygons or patches to constant-value contour surfaces in volume data. For a detailed description about the algorithm, we refer to Magnusson *et al.* [145].

2.5.2 Curved Planar Reformation and Its Extensions

The traditional volume visualisation techniques described in previous section may provide incomplete clinical information due to the occlusions caused by irrelevant structures. It is also difficult to measure the degree of calcification or stenoses quantitatively using those visualisation techniques.

To address the these problems, Kanistsar *et al.* [111, 110] proposed the curved planar reformation (CPR) method and presented an automated vessel-tracking tool for computing CPRs. CPR is a process of displaying tubular structures for diagnostic purposes by generating longitudinal cross-sections to show vessel lumen, wall, and surrounding tissue in one plane. Given a vessel centreline, CPR provides the visualisation of the vessel in its entire length within one single image. Three different CPR methods were proposed in [111], as illustrated in Figure 2.21. Furthermore, Kanistsar *et al.* presented enhancements to these three CPR methods: thick-CPR, rotating-CPR and multi-path-CPR.

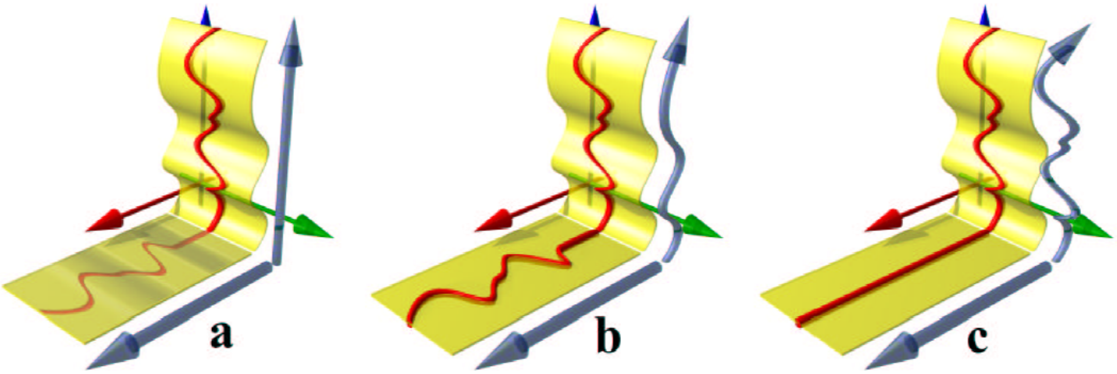

Figure 2.21: Curved planar reformation. (a): Projected CPR; (b): Stretched CPR; (c): Straightened CPR [110].

Despite the capability of visualising vessel lumen together with surrounding structures along the vessel centrelines clearly, CPR techniques are highly sensitive to the input vessel centreline. Wrong centreline localisation can distort the vessel lumen and lead to the misidentification of stenosis. As an exception, thick-CPR projects a slab of a certain thickness, and therefore it is less sensitive to the precise centreline localisation.

The six CPR methods discussed above still have diagnostically relevant limitations. The vascular abnormalities may not be shown in the visualisation plane. Rotating the re-sampled plane around the input centreline axis addresses this problem, but results in a large set of images to be interpreted by the radiologists. Therefore, in [112], Kanitsar *et al.* proposed helical CPR to display the entire vascular lumen in one representative image. Helical CPR resamples a spiral around the vessel central axis to make sure that no features of the vessel may be hidden by other structures as long as the vessel area is sampled densely enough. To address the issue that parts of vessels might be superimposed by other vessels, untangled CPR is proposed in [112]. Different from the multi-path-CPR, untangled CPR produces an unobscured display of a vascular tree, independent of the viewing direction.

2.6 Vasculature Registration

In this section, we survey the existing algorithms developed for the registration problems involving vascular structures. It is included in this review chapter because vasculature registration can assist segmentation, e.g., by forming vascular atlases or deforming the segmented vascular structures at one time point to predict their position and shape at next time point. Moreover, vessel-based registration allows pre-operative and intra-operative images to be aligned for diagnosis and treatment purposes. It can also potentially improve the accuracy of vessel atlas constructing from single-modality data sets acquired from a selected population. Furthermore, by registering vessel images of the same subject from different modalities, the benefits of different imaging and visualisation techniques can be fully explored and utilised by the clinicians. As for the application, vasculature registration is essential for diagnosing vascular diseases, providing guidance for surgery, assisting the evaluation of the effects from medical treatment.

Vasculature to image registration proposed in [13, 15] allows propagation of the segmented vessels in one image (I_0) to a set of other images ($I_{i,1 \leq i \leq n}$) in order to obtain the vascular structures in these images. This approach only requires segmenting the vessels in one of a set of vasculature images. The proposed method [13] consists of the following steps:

1. Prior to the registration, an accurate segmentation of the vessel structures I_0^v is obtained [14] for image I_0.

2. For each image I_i, its vessel structures I_i^v can be obtained without any segmentation by registering I_i with the vessel model I_0^v. A point-based similarity metric with a rigid-body transformation model [15] is used for aligning the images I_i and I_0^v. The centreline points from I_0^v are resampled and transformed to best fit the intensity ridges in the target image I_i. The rigid-body transformation parameter space of the proposed similarity metric and its derivatives are quantitatively analysed and searched for the best alignment.

The second step is repeated until the vessel structures $I_{i,1\leq i\leq n}^v$ are obtained for all the images $I_{i,1\leq i\leq n}$. In [47], the aforementioned vasculature to image registration method is further developed from rigid registration with six degrees of freedom to an affine registration with 12 degrees of freedom.

Jomier *et al.* [105] further extended the vasculature to image registration [13] to a hierarchical approach combining both rigid and deformable transformation models. Following the global rigid vasculature to image registration as in [13], two more steps are introduced in the new registration algorithm in [105]:

- A local piece-wise rigid transformation is applied to each vessel from the root to branches in a hierarchical manner. This step utilises the detected branching points and the typical tree structure of blood vessels. The root of the vessel tree is first aligned. Then its children are registered to the image, one branch at a time, from root to leaves in order.

- A non-rigid registration is then performed to align the vessels with the image, under the elasticity and rigidity constraints. The elasticity constraint limits the movement of vessel points along a tubular structure in the image. The rigidity is defined as the maximum angle between the initial tangent vector and the actual tangent vector. It is used to constrain the bending of the vessel.

The proposed method was validated in both simulated and patient data sets. Sub-voxel accuracy, robustness to noise and efficiency are reported by the authors [105].

2.7 Summary

A review of the work on coronary artery segmentation has been presented in this chapter. Our primary goal is to guide the designing of coronary artery segmentation algorithms for our applications by analysing the existing techniques. Various methods surveyed in this chapter form the basis of our work in Chapter 4 to Chapter 7.

The work presented in this chapter mainly focuses on the segmentation of coronary arteries from high-quality static 3D CTA or MRA images and some approaches for 2D X-ray angiograms. To the best of our knowledge, little work has been dedicated to coronary segmentation from 4D CTA sequences. This is possibly because the difficulties imposed by the low image qualities of 4D CTA sequences. However, segmenting coronaries from pre-operative 4D CTA images would facilitate the identification and localisation of the artery to be operated on during the TECAB surgery. In the following chapter, we review the methods proposed in literature for modelling coronary artery motion.

Chapter 3

Review of Coronary Artery Motion Modelling

Quantitative and accurate characterisation of abnormal wall and vascular patterns (location, shape, and motion) of the heart is of major importance for diagnosis and treatment. For a long time, monoplane and biplane X-ray techniques were the only techniques available to dynamically visualise coronary and ventricular structures. Early attempts focused on static reconstruction and were based on computer vision approaches relying on epipolar geometry and feature matching. A first dynamic reconstruction algorithm was proposed in [192]. It led to a fast and efficient scheme to recover the centrelines from two sequences of projection images. However, all X-ray image based methods suffer from one major drawback: the motion based on one 2D image only reflects the movement of the coronary in the projection plane. Even if X-ray sequences acquired from different viewpoints are used for motion modelling, the 3D reconstruction of the vessels is required prior to or after the motion tracking. Table 3.1 summarises the important publications on coronary motion tracking from X-ray angiograms.

Technical advances in 3D echography, cine-MRI, tagged-MRI, and multi-slice computed tomography (MSCT) have opened new perspectives during last decade. It is now possible to describe the dynamic behaviour of the heart over the entire cardiac cycle without 3D reconstruction from 2D image sequences. MSCT offers, in particular, full 3D imaging of all cardiac structures, including right and left coronary trees, and significantly improves pre-operative planning capabilities [208, 48]. However, a contrast agent is routinely used prior to the image acquisition in order to visualise the blood pool or coronaries better. Because of the variations of contrast medium distribution spatially and temporally, the brightness of coronaries and blood pool is not perfectly constant which may hinder the motion tracking.

Although promising, few works have been devoted to motion analysis in MSCT.

Of those published, most have focused on the left ventricle [212, 81, 80]. Much less attention has been paid to the estimation of coronary motion. Some studies have been performed on biplane angiography [192, 206], electron beam CT (EBCT) [4, 109] and MRA [93, 195, 54]. Only a few papers have attempted to deal with coronary motion from MSCT [98, 249].

Table 3.1: Coronary motion tracking from X-ray angiograms. Column 2: Only the landmarks are tracked temporally. Column 3: The coronary tree is constructed before or after the tracking. Column 4: The coronaries are only tracked in 2D projections. Column 5: Coronary motion is tracked temporally prior to its 3D reconstruction. Column 6: A 3D reconstruction of the coronary tree is obtained before tracking its motion.

Image modality	Landmarks	Vessel tree	Tracking (2D only)	Tracking before reconstruction	Tracking after reconstruction
DSA		[191], [196] [183]	[191], [196]		[183]
Biplane Angio	[117] [103]	[192], [62] [205], [99] [46], [160] [206], [139] [137], [167]	[62]	[160], [167], [103]	[192], [206] [139], [137]
Rotational Angio	[178] [203]	[26], [30] [222]	[203]		[26], [30], [178] [222]

3.1 Coronary Motion Modelling from Digital Subtracted Angiography (DSA)

Coronary motion estimation from a sequence of Digital Subtracted Angiography (DSA) has been first proposed by Rong *et al.* in [191]: Coronary vessel centrelines are extracted in the first image $I_{t=1}$. A differential motion estimation method is then used to estimate the coronary motion along its centrelines, based on images I_t and I_{t+1}. After obtaining the motion between these two phases, the centrelines are extracted from image I_{t+1} guided by the motion model from previous step. In the context of a sequence, the extracted centrelines from previous phase are used to guide the extraction for current phase until the end of the sequence. The motion estimation and centreline extraction are combined to act iteratively. There are two main drawbacks of this method:

- The motion based on the 2D DSA only reflects the movement of the coronaries in the projection plane.

- The method is based on the brightness of coronaries which is not perfectly constant because of variations of contrast medium distribution spatially and temporally.

Puentes *et al.* [183] overcame the restrictions of 2D DSA images by acquiring nearly orthogonal, simultaneous biplane angiographic image sequences corresponding to standard examination views (left anterior oblique - LAO 60° and 20°, and right anterior oblique - RAO 30°). Two sequences acquired from distinct views enable the 3D reconstruction of coronaries. For each view, 15 images were taken during a dye injection in the left coronary artery in one heartbeat. As a pre-processing step, image subtraction is applied to enhance the vessels of interest and to eliminate the presence of irrelevant structures. After that, a matching filter is used to enhance the structures corresponding to a vessel profile with variable orientation. It also combines multiple resolutions by using various matching templates corresponding to small, medium and large vessels. A binary image is obtained by using a threshold to identify which pixels may belong to a vessel, separating background and possible arteries. To detect the centrelines, skeletonisation and smoothing are also performed. A knowledge-based approach [79] is then used for the reconstruction and labelling of the arterial tree. Here it is assumed that changes in the positions of arteries' centrelines are exclusively produced by respiratory and cardiac motion. Coronary reconstruction and motion estimation are combined in a prediction-projection-optimization loop. For each iteration, the method works in a point-by-point mode:

1. Given the first reconstruction of 3D vessel points at time t, the coronary motion is assumed to be smooth along arteries centrelines and rigid for each segment. This is used to predict each point position at time $t + 1$.

2. The predicted 3D point displacement is projected onto the left view and right view images at time $t+1$. Within a pre-defined search area around the 3D point and its projection, a correction process is carried out through aligning the 2D images at time t and time $t + 1$ using cross correlation as a similarity metric, in each view. The corrected 3D point at time $t + 1$ is then reconstructed, and its displacement is measured as the difference with respect to its position at time t.

3. Finally, a global optimization of the reconstructed centreline at time $t + 1$ is performed by minimising a cost function built on a residual error and 3D motion gradient, under the 2D/3D geometrical and epipolar constraints.

For all subsequent images from the sequences, position prediction, projection and optimization are iterated to obtain the reconstruction and displacement vectors for all centrelines [183].

3.2 Coronary Motion Modelling from Biplane Angiography

To study the dynamic movements of the epicardial surface during the cardiac cycle, bifurcations of the coronary arteries on the epicardial surface in biplane angiograms can be used as landmarks, localised in space and followed in time [117]. Kong *et al.* [117] used coronary artery bifurcations as natural landmarks, establishing an explicit correspondence between frames of the sequence. Epicardial motion was analysed by dividing the epicardial surface into three transversal and three longitudinal regions, each having 10-20 bifurcation points. Each pair of consecutive points along an arterial branch formed a unique segment that was studied in both projections. Bifurcation displacements were compared to those obtained using implanted markers placed near the bifurcations, showing a strong correlation. The tracked artery segments are recorded and measured to yield a reproducible curves reflecting ventricular contraction and filling. The results can be used to quantify and compare the onset, duration, extent and rate of segment shortening in multiple areas of the heart. Using coronary bifurcations as landmarks facilitates the assessment of regional myocardial performance.

Prior to the work of Ruan *et al.* [192], most image analysis work on biplane X-ray images of coronaries focused on static reconstruction that relies on epipolar geometry and feature matching techniques. The proposal of coupled reconstruction-motion estimation in [192] initiated the motion tracking of the coronary centrelines over two sequences of projection images. Motion estimation of the coronaries is performed on 3D centrelines. It is based on the same prediction-projection-optimization loop proposed in [183] and described in the previous section.

In order to allow the physicians to observe closely a particular point on the artery tree over the cardiac cycle, Dubuisson-Jolly *et al.* [62] proposed to rigidly register the coronary angiography sequence so that the area around the point of interest appears stable. The proposed algorithm automatically extracts a section of the artery of interest, models it as a polyline, and tracks its motion. The problem is formulated as an energy minimization problem which is solved by finding a shortest path in a graph. The motion compensated sequence is then obtained by translating every pixel so that the point of interest remains stable. Compared with [192], this work only tracks the coronary segments in 2D as opposed to 3D tracking. While being sufficient for the proposed application, the tracked motion only reflects the coronary movement in a particular 2D projection. Also, the arteries deform in a more complex non-rigid manner.

In [99], vessel skeletons are extracted in each X-ray angiogram by calculating the gradient response and choosing the low response region surrounded by high gradient response borders. Then a motion trajectory is computed for each point on the segmented artery tree independently. A set of vectors describing the general motion of each artery branch is created to describe the 2D motion of the coronary arteries in X-ray angiograms. This only reflects the coronary motion in a specific 2D projection plane without considering any 3D geometrical information.

Chen *et al.* proposed a different framework in [46]: Firstly, the 3D static model of coronary arterial tree is reconstructed from 2D X-ray cine angiograms; Secondly, temporal motion tracking of the reconstructed 3D coronary model is performed with the smoothness constraints; Finally, the kinematics and deformations of the reconstructed 3D coronary artery trees are analysed throughout the cardiac cycle. Particularly, the magnitude of displacement, the velocity and acceleration obtained from the 3D left coronary arterial tree is computed and analysed.

Mourgues *et al.* [160] proposed a method to construct a 3D+t model of the coronary artery tree from non-simultaneous sequences, synchronized with an ECG and acquired on a standard single-view angiograph. Their approach includes the following four steps: Firstly, 2D segmentation and labelling consists of semi-automatic extraction and labelling of the coronary artery tree in one image from each projection sequence. The labelling is performed with an interactive tool that relies on a multi-scale model-based pre-processing. Then, the hierarchical structure of the tree is automatically determined. The segmentation and labelling information is propagated to other images from all projections during at least one cardiac beat. Based on the hierarchical description of the coronary tree, the arteries are modelled by B-snakes with an internal energy defined from the multi-scale model-based pre-processing. A two stage optimization procedure is used to reduce the effects of large displacements, crossing and overlapping arteries. Thirdly, a coherent 3D model is constructed by alternately matching the artery pixels from two segmented projections corresponding roughly to the same point in the cardiac cycle. Finally, the 3D skeleton is enriched with cross-sections estimated from the acquisition geometry and the scales extracted in the multi-scale pre-processing.

Based on the work by Mourgues *et al.* [160], Shechter *et al.* [206] presented a 3D method for tracking the coronary arteries through a temporal sequence of biplane X-ray angiography images. They reconstruct a 3D centreline model of the coronary vasculature from a biplane image pair at one time frame and represent it as an ensemble of 3D B-spline curves. Its motion is tracked using a coarse-to-fine hierarchy of motion models: A global 3D rigid transformation, global 3D affine transformation, and finally local 3D tensor product B-spline transformation are used to represent the motion of the coronary artery. An energy minimization problem within a registration framework is formulated in order to deform the coronary artery tree consistently with the angiogram image pairs at later time frames. Using 3D constraints on changes in the lengths of the coronary arteries and on the spatial regularity of their motion, a hierarchical set of coarse-to-fine 3D motion models is used to recover the temporal dynamics of the coronary tree. Their algorithm was clinically validated in five patients by tracking the motion of the left coronary tree over the cardiac cycle. The performance of the tracking algorithm was quantified in 3D using a deforming vascular phantom. RMS errors were computed between centreline models tracked in the X-ray images and gold-standard centreline models of the phantom generated from a gated 3D MR image acquisition.

Furthermore, Shechter *et al.* measured the 3D displacements and velocities of the coronary arteries due to myocardial motion and breathing [207]. First, a static 3D model of the coronary arteries was reconstructed at mid-diastole from one pair of images. The images were processed with filters that enhance the arteries, and the arterial centrelines were semi-automatically drawn in the two images. Point-to-point correspondences between the arteries drawn in the two projections were computed automatically and a 3D model was reconstructed using knowledge of the geometry of the imaging system. Using the static coronary tree model as initial state, the 3D motion of the arteries was recovered using an automatic motion tracking algorithm. This algorithm calculates the best 3D transformation of the reconstructed coronary tree model such that the projection of the arteries remains consistent with the temporally changing image sequence. An energy minimization framework was formulated that uses gradient descent to recover the parameters of the rigid, affine, and local deformations.

The motion field recovered from each dataset represents the arteries while the heart is beating and the patient is breathing. Thus the motion field is a function of cardiac phase and respiratory phase. A parametric model is then designed to decompose the motion field into independent cardiac and respiratory motion components. It is reported that the arteries move consistently towards the left, inferior and anterior during a cardiac contraction. The displacement and velocity of the right coronary artery during a cardiac contraction was larger than those of the left coronary branch [207].

Lorenz *et al.* [139] presented a model of the coronary artery tree. The geometrical component of their model is based on the mean end-diastolic model of the coronary centrelines from bi-planar coronary angiography images of 37 patients in [58]. Based on the point sets of Dodge *et al.*, Lorenz *et al.* [139] constructed a tree model of the coronary centrelines represented as point sets connected by line segments. The diameter of the main coronary arteries is chosen according to Dodge *et al.* in [59]. Applicability of the model has been studied by matching the model to individual cardiac CT images of 33 patients. For all patients the centrelines of the three main coronary arteries (left anterior descending coronary artery, left circumflex coronary artery and right coronary artery) are manually delineated and annotated. The model was adapted to the patient data by minimizing the Euclidean distances between data points and model lines. A downhill simplex optimization procedure was used to search for the optimal transformation parameters. Finally, they verified that their end-diastolic coronary artery model could be adapted to patient data within an accuracy of a few millimetres.

Further work about a comprehensive shape model of the heart is presented in Lorenz *et al.* [137]. In this paper, for the first time, a comprehensive cardiac shape model comprising all four heart chambers, the trunks of the connected vasculature, the coronary arteries and a set of cardiac landmarks is presented. The new model can serve as a general geometrical reference model supporting various tasks associated with cardiac image analysis.

Nwogu *et al.* [167] reconstructed a moving 3D coronary vessel by identifying the vessel-of-interest in two biplane images, transforming them into centrelines, and tracking them in the subsequent images using deformable templates and graph techniques for optimization. The whole process has three major stages:

1. The vessel is identified and abstracted into its centreline;
2. The centreline is approximated by a polyline and tracked using deformable templates;
3. The 3D vessel is reconstructed.

Different from previous work dedicated on segmentation and motion tracking from X-ray biplane angiograms of coronary arteries, Johnson *et al.* [103] used biplane X-ray angiography films to study coronary motion in order to utilise this prior knowledge to alleviate the detrimental effect on the image quality imposed by coronary artery motion during coronary MRA and CTA acquisition. In this study, the 3D motion of the coronary arteries along the entire vessel length is characterised. The temporal location and the periods of relatively low cardiac motion are identified from biplane X-ray angiograms acquired at 30 frames per second with simultaneous electrocardiogram recording for 15 patients with coronary artery disease. The right coronary, LAD and LCX arteries are divided into proximal, mid and distal segments. The displacement and velocity of a point in each segment were calculated throughout the heart cycle. The 3D+t motion of each segment on each vessel was determined. The displacement of the proximal, middle and distal segments of the right coronary artery are plotted over the cardiac cycle as shown in Figure 3.1. All segments have a similar motion pattern, with mid and distal segments exhibiting slightly more motion.

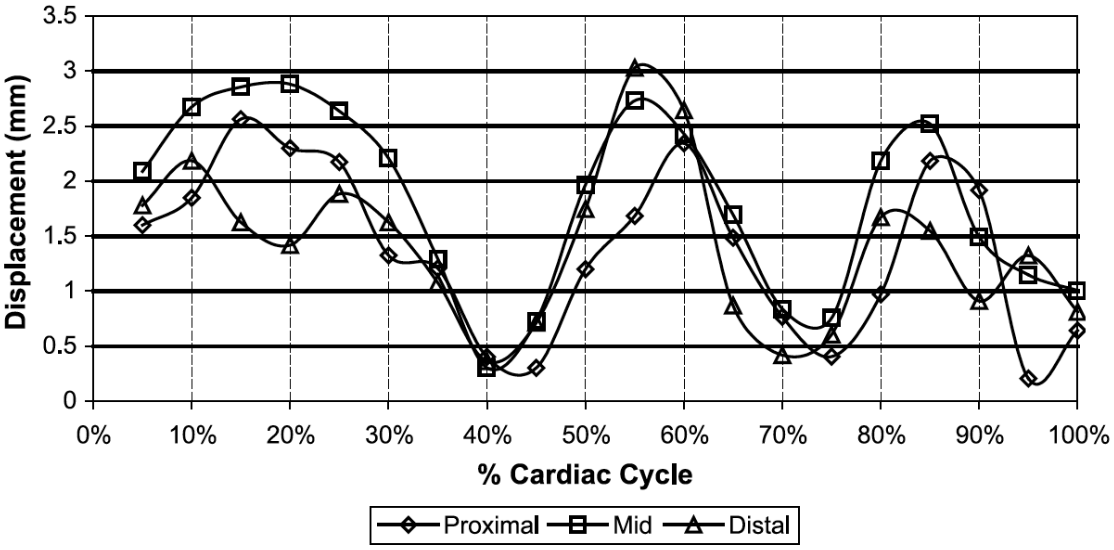

Figure 3.1: Frame-to-frame displacement of the proximal, mid and distal parts of right coronary artery over the cardiac cycle [103].

This study in [103] has also identified those periods of the heart cycle during which maximal displacement was less than 1mm/frame for each artery. It is shown that there are two periods in the cardiac cycle in which all three coronary arteries have relatively little coronary motion (< 1 mm/frame or 30 mm/sec) [103]. The first of these periods can be found at the completion of ventricular systole (34±8% of the cardiac cycle) with duration of 118 ±78 msec. The temporal location of this rest period, however, varied significantly among the three coronary arteries. No acquisition window was able to capture the rest period of all segments of all arteries at the same time. A second period of low motion was found at mid-diastole (72±5% of the cardiac cycle) with duration of 187±119 msec. This period was more consistent throughout the three coronary arteries and allowed for a window of 6% of the cardiac cycle during which, on average, all segments of the LAD, LCX, and RCA are “at rest”. This period of low motion potentially is the best time window for CTA or MRA acquisitions.

3.3 Coronary Motion Modelling from Rotational Angiography

The 3D coronary tree may be obtained from biplane angiography, since this modality provides two synchronised projections of the coronary arteries. Alternatively, it can also be reconstructed by selecting two views from two single-plane angiograms. However, using only two projections is not sufficient to provide a precise point correspondence as illustrated in Figure 3.2. This restriction can be eliminated by rotational X-ray coronary angiography. By selecting the angiograms that correspond to the same cardiac phase in a rotational acquisition, the number of projections used for reconstruction of coronary arteries can be increased as required.

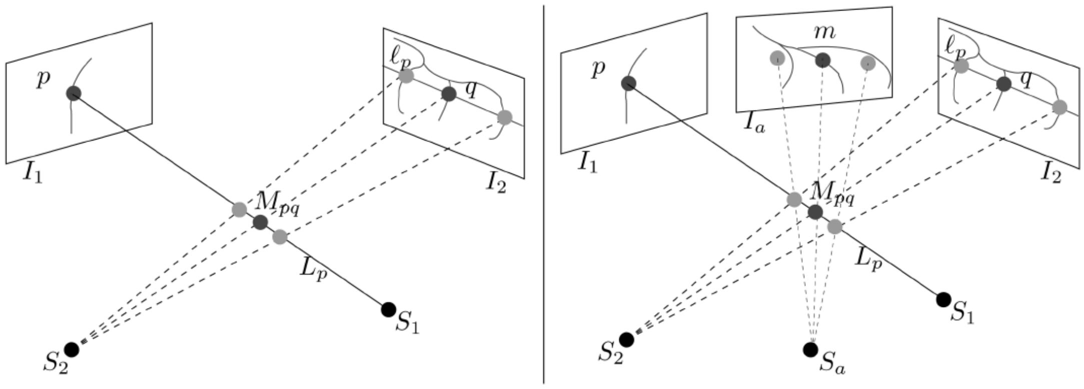

Figure 3.2: Epipolar constraint [26]. The 3D point M_{pq} that projects at p in image I_1 is located on the 3D line L_p that joins p to source position S_1. The same point's projection in image I_2 consequently is located on the projection ℓ_p of line L_p. In this example, with two projection images (left), there are three possible 3D points could be reconstructed as there are three intersections of ℓ_p with vessels in I_2. However, only one of these three points projects on a vessel in the additional image I_a (right). This extra image eliminates the spurious reconstructed 3D points as shown next to M_{pq} in light grey.

Blondel *et al.* [26] presented a method to compute a 4D tomographic representation of coronary arteries from a single rotational monoplane X-ray sequence, allowing for the visualization of the coronary arteries from any point of view and at any cardiac cycle time. The authors use 4D B-spline solids to model coronary motion with reported computation time of 15 to 30 min.

The 4D reconstruction of coronary artery as proposed by Blondel *et al.* [26] consists of three major steps:

1. Static 3D reconstruction of coronary artery centrelines from the reference frames $I_1, I_2, ..., I_n$, $n \geq 3$ at a given cardiac phase. These reference images are selected from one single sequence. They all are acquired at the same cardiac phase but from distinct viewing angles. Thus, it is reasonable to assume that these images are not affected by cardiac motion.

2. Estimation of 4D coronary motion from the resulting set of 3D centrelines. A 4D tensor product of 1D B-splines is chosen for the motion parameterization. This preserves the spatial and temporal smoothness of coronary artery motion.

3. The derived coronary motion can then be integrated into the 3D tomographic reconstruction of coronary arteries at all other phases [27].

Bouattour *et al.* [30] proposed a technique for 4D reconstruction of the coronary arteries from a sequence of monoplane X-ray angiograms. An initial 3D model of the coronary centrelines is reconstructed from two selected views by using epipolar geometry. These two views are selected based on three criteria, namely, orthogonality, its position within the sequence and ECG information. A semi-automatic graphical tool is then used to select corresponding points on the coronaries of interest in order to reconstruct a 3D coronary model. The temporal tracking of the 3D coronary model is then formulated as a 3D-2D registration problem. In this registration framework the 3D model deforms in space to best fit a given set of 2D angiograms. The 4D motion is tracked hierarchically and modelled using rigid, affine and B-spline transformations. The registration is guided by a sum of energy terms which measures the goodness of the 3D-2D mapping and constrains the deformation of the model.

In Tsin *et al.* [222], the authors start from a reconstructed 3D model of coronaries for a relatively static cardiac phase, and proceed to explicitly estimate the coronary tree deformations from one cardiac phase to the next. The deformations of the 3D coronary tree are tracked to yield a 4D reconstruction of the coronary tree. In this work, the deformation of a coronary tree is modelled by two 3D parametric deformation models, i.e., rigid and affine. There are three main components of the proposed method in [222]:

- The external deformation force is derived from gradient vector flow (GVF) computed from the vessel enhancement filter responses.
- A cyclic deformation constraint is introduced to preserve the cyclic feature of the cardiac motion.
- A smooth deformation constraint based on Laplacian equation is used to ensure the smoothness of the modelled cardiac motion.

GVF, cyclicity constraint, and smoothness constraint are combined together to form a weighted energy function for 4D coronary tree reconstruction. This energy function is minimised using least-squares optimisation to estimate the deformations between two phases. Although the regularised rigid and affine deformation estimation converges very fast in the tested data sets, instability and overfitting also occurred in ill-conditioned cases. Finally, note that 3D reconstruction of coronary tree incurred errors of 1.5mm and 2.5mm for manually labelled vessel centrelines and automatically labelled ones in [222]. As baseline error, this reduces the accuracy of the motion model considerably. Another major drawback with this work is that a global rigid or affine motion model is insufficient to capture the total deformation of the coronary due to cardiac motion. This restricts the accuracy and flexibility of the motion modelling.

In [203], the authors present a method for projection-based motion compensation and reconstruction of coronary segments and cardiac implantable devices from rotational X-ray angiograms. The method uses markers on a device or guide-wire to identify and estimate the motion of an object or region of interest in order to register the projection images to generate a motion compensated reconstruction. The projection images are motion compensated based on these semi-automatically detected markers and subsequently used for reconstruction.

3.4 Coronary Motion Modelling from MR Angiography

To the best of our knowledge, coronary motion from MR images was first studied in [93]. It is known that the motion of the coronary arteries during the heart cycle can result in image blurring and inaccurate flow quantification, particularly when longer acquisition windows are employed for breath-hold coronary flow measurements. To quantitatively determine this effect, the temporal variation in coronary position is measured in a plane perpendicular to the proximal portion of the vessel. Hofman *et al.* reported the presence of substantial displacement of the coronary arteries in a plane perpendicular to the proximal segment within the cardiac cycle, with a magnitude of motion approximately twice as large for the right as for the left coronary arteries. Furthermore, the authors estimated the resulting vessel blurring. It was concluded that the duration of the acquisition window for high spatial resolution coronary flow acquisitions should be less than 25 to 120 msec, depending on the specific coronary artery studied.

Saranathan *et al.* [195] proposed to track the coronary motion over the cardiac cycle to improve the efficiency of ECG-gated 2D coronary MRA. The coronary tracking in this work was implemented on a spiral gradient-echo pulse sequence with submillimetre in-plane spatial resolution as well as high image signal to noise ratio. The authors computed the imaging efficiency as the percentage of the slices where more than 30 mm of the vessel is visualized with and without coronary tracking. They also evaluated the effect of using a linear motion model as opposed to true motion model of the coronary. It is observed that the use of subject-specific tracking of the vessel positions improved the efficiency of coronary artery imaging on breath-hold 2D coronary MRA.

In [69], Fischer *et al.* analysed the residual coronary artery motion in the breath-hold MRI and in free-breathing MRI acquired with affine motion compensation. An image containing a coronary artery cross section was acquired at each heartbeat to visualise and measure the respiratory induced motion. The amount of residual coronary artery displacement was directly measured to evaluate the performance of the respiratory motion correction method. It is concluded that free breathing studies with affine motion compensation displayed a similar amount of residual motion as a single breath-hold, with the advantage of allowing for larger gating windows.

Dewan *et al.* [55] developed a multiple-template based tracking approach to track the cardiac structures in order to improve the speed and quality of imaging those structures in MR. The two main contributions of this work are:

1. A bidirectional coordinate-descent algorithm to improve the accuracy and performance of motion tracking;
2. A method to choose an optimal set of templates for tracking.

The authors also validated the efficacy of the proposed approach by tracking the coronaries and cardiac valves reliably and accurately in thousands of high-resolution cine and low-resolution real-time MR images.

Based on their previous work [55], Dewan *et al.* further developed a method to reduce the effect of motion variability of the coronary arteries in MRI [54]. In this work, real-time low-resolution images in specific orthogonal orientations are used to extract the coronary motion by the proposed tracking approach. The derived motion information is then used to guide the high-resolution MR image acquisition on a beat-to-beat basis.

3.5 Coronary Motion Modelling from CT

3.5.1 Electron Beam Computed Tomography (EBCT)

Both Achenbach *et al.* [4] and Kakadiaris *et al.* [109] presented thorough studies on coronary artery motion from EBCT. The understanding of coronary motion potentially would help the designing of suitable motion modelling algorithms for tracking coronaries in temporal domain.

In [4], Achenbach *et al.* investigated the speed and changes of the speed of coronary arterial movement from 25 patients during the cardiac cycle scanned with EBCT. Each scan has 20 consecutive cross-sectional images acquired at the mid right coronary artery. Movement velocity in the transverse imaging plane was calculated and correlated with the simultaneously recorded ECG on the basis of the displacement of LAD, LCX and RCA cross sections from image to image. The authors reported that the velocity of in-plane coronary arterial motion varied considerably during the cardiac cycle. It is also observed that the mean velocity of RCA movement was significantly faster than that of the LAD or LCX. The lowest mean velocity was reported at 48% of the cardiac cycle [4].

Kakadiaris *et al.* [109] designed a physics-based deformable model framework for morphological and motion analysis of the LAD during the cardiac cycle. The major contribution of this work is defining a local coordinate system for the heart and parameterising both the shape and motion of the LAD in a single framework. The shape of the LAD is modelled as a parametric generalized cylinder without assuming any particular tubular shape. The complex motion of LAD during the heart cycle is modelled as a composite of three components: Longitudinal deformation, radial displacement, and angular displacement over the cardiac cycle.

3.5.2 Multislice Computed Tomography (MSCT)

A temporal tracking algorithm for the coronary central axis in a 3D dynamic sequence in MSCT was proposed by Laguitton *et al.* in [122]. The proposed method is based on geometric moments and a local cylindrical approximation. The local characteristics of the vessel (position on the vessel central axis, local diameter, intravascular and background intensities) are estimated on the first volume of the sequence, and then used to track the vessel along the sequence. The correspondence between two volumes is established through region matching with a distance criterion that combines geometric moment-based descriptors with intensity information.

Husmann *et al.* performed a study [98] to prospectively determine the heart rate (HR) dependency of 3D coronary artery motion by incorporating the durations of systole and diastole into analysis. Thirty patients underwent ECG-gated 64-section CTA screening to determine coronary motion velocities at bifurcation points. The significance of velocity differences was determined by using analysis of variance for repeated measures. HR dependency was determined by using linear regression analysis. It is found that HR significantly affected 3D coronary motion through nonproportional shortening of systole and diastole, leading to percentage reconstruction interval shifts of coronary velocity troughs and peaks. Results suggest that image reconstruction algorithms at CT coronary angiography be adapted to the individual patient's HR.

Metz *et al.* [151] presented a method to derive patient specific coronary artery motion models from ECG-gated CTA data. In this work, a 4D (3D+t) deformation model of the coronary arteries is derived by 1) extraction of a 3D coronary model at an appropriate cardiac phase, 2) non-rigid registration of the CTA images at different ECG phases to obtain a deformation model and 3) deforming the extracted 3D coronary model according to the obtained deformation field to yield a 4D motion coronary motion model. Furthermore, Metz *et al.* aligned the coronary motion model with the X-ray data using a 2D+t/3D+t registration approach [151].

Yang *et al.* [249] presented a method for the charcaterization of coronary artery motion using MSCT sequences. Coronary trees are first extracted by a spatial vessel tracking method in each volume of MSCT sequence. A point-based matching algorithm, with feature landmark constraints, is then applied to match the 3D extracted centrelines between two consecutive frames throughout the cardiac cycle. The transformations and correspondence matrices are estimated simultaneously and used for deformable fitting of the vessels over the volume series. The authors derived both point-based or branch-based motion features, and conducted experiments to evaluate the performance of the proposed method with a matching error analysis.

3.6 Coronary Motion Modelling from Other Image Modalities

Coronary artery tissue motion has also been studied from 2D IVUS images of a coronary artery. Danilouchkine *et al.* [52] presented a method for estimating this tissue motion based on the classical LK algorithm for optical flow. The OF vector field quantifies the amount of misalignment between two consecutive frames in a sequence of images. This work made two improvements on the classical LK approach. First, using a simplified representation of the vessel wall as a medium with randomly distributed scatterers, it was shown that the OF equation satisfies the integral brightness conservation law. Second, a scale-space embedding for the OF equation was derived under the assumption of spatial consistency in IVUS acquisitions. The spatial coherence is equivalent to a locally affine motion model. The latter effectively captures and appropriately describes a complex deformation pattern of the coronary vessel wall under the varying physiological conditions (i.e. pulsatile blood pressure). The performance of the classical LK and proposed approach was then compared using simulated IVUS images with an atherosclerotic lesion.

3.7 Summary

In this chapter, an up-to-date review of previous work on coronary artery motion modelling is presented. The different publications are organised according to the image modalities used for the motion modelling. Table 3.2 gives a brief summary of the work on coronary motion modelling in literature.

Most work utilise the 2D angiogram sequences for the coronary motion tracking. One important example from the literature is presented by Shechter *et al.* [206, 207] where the coronary artery motion is tracked in a temporal sequence of biplane X-ray angiography images. In their approach, a 3D coronary model is reconstructed from extracted 2D centrelines in end-diastolic angiography images. The deformation throughout the cardiac cycle is then recovered by a motion tracking algorithm based on non-rigid registration [193]. The limitation of using 2D X-ray angiograms is that 3D reconstruction of the coronary from 2D X-ray images is required in order to study the motion of the coronaries in 3D. In the following chapters, the coronary motion is directly modelled from 4D CTA sequence in our work when no 3D reconstruction is necessary.

Table 3.2: A list of previous work on coronary motion modelling.

Image Modality	Publications
X-ray Angiography	[192], [206], [207], [220], [196], [191], [183], [117], [62], [99], [46], [160], [139], [167], [103], [26], [30], [222], [203]
MR Angiography	[93], [195], [69], [55], [54]
CT	[4], [109], [122], [151], [249], [188]
Others	[52]

Although much work has been done on tracking coronary arteries from 2D+t angiograms, coronary motion modelling from 3D+t MSCT sequences has received little attention until very recently. The advantage of using 3D+t pre-operative MSCT sequences to model the coronary motion and the challenges involved have not been fully investigated. In the following chapters, we propose various approaches of coronary motion tracking from 4D MSCT angiography data.

Chapter 4

Ridge-based Coronary Motion Tracking

The extraction of blood vessels has been studied extensively in the past two decades. Previous research on vessel extraction has concentrated on 2D X-ray angiography, 3D MRA and CTA, focusing on retinal, brain, liver, lung and cardiac images. For the coronary artery, the recent advances in computed tomography of coronary arteries [53] have attracted a number of studies on using CTA for coronary artery disease diagnosis and surgical planning. An up-to-date review of coronary artery segmentation techniques is given in Chapter 2. Although coronary artery segmentation has been well studied, e.g., as part of the Grand Challenge of Coronary Artery Centreline Extraction [153], constructing motion models of coronaries from pre-operative CTA sequences to assist the intervention and surgery is a topic which has received little attention.

The work in this thesis differs significantly from the 3D vessel segmentation approaches. Our aim is not the extraction of the coronaries in single-phase high-quality CTA datasets as in [153], but instead focuses on tracking the coronaries throughout the cardiac cycle in dynamic cardiac CTA sequences. In this chapter and the following chapters, we present our original contributions to building patient-specific coronary motion models from 4D CTA images prior to the TECAB surgery. By temporally and spatially aligning the pre-operative motion model with intraoperative endoscopic views of the patient's beating heart, this work can be used to assist the surgeon to identify and locate the correct coronaries during TECAB procedures [67, 68]. Potentially, it could reduce the 20%-30% conversion rate from TECAB surgery to conventional invasive surgical approach due to the restricted view of the stereo endoscopic images as observed in [158, 60]. However, the alignment of pre-operative coronary motion model and intra-operative endoscopic images is beyond the scope of this thesis.

4.1 Related Work and Overview

Existing vessel extraction methods can broadly be divided into two categories: skeleton and non-skeleton approaches. Skeleton methods explicitly extract the vessel centrelines and represent the results as parametric curves or discrete sets of points. Two main skeleton methods are closely related to the work we present in this chapter:

1. Frangi *et al.* [72] propose a model-based method using a deformable contour technique. A central vessel axis curve coupled with a tensor product B-spline surface is used to model the linear vessel segments. In this approach the vessel centreline is approximated using a B-spline curve. The deformation process is based on moving the control points of the B-spline curve towards points which have a high likelihood of lying along the central vessel axis. A vesselness filter is used as the external force to drive the deformation. The vesselness filter reaches its maximum at the center of the vessel and explicitly takes information of vessel radius into account. Additionally, a tensor product B-spline surface is used to model the vessel wall.

2. Based on the observation that vessel centrelines often corresponds to an intensity ridge in the TOF-MRA images, Aylward *et al.* [14, 12] propose a ridge traversal algorithm to track the vessel centrelines. This method begins from a user-supplied seed point on or near a vessel, then it optimises a pre-defined ridgeness function to obtain the closest local ridge point from where the next guess is made. This process is repeated until the full extent of the vessel ridge is traversed.

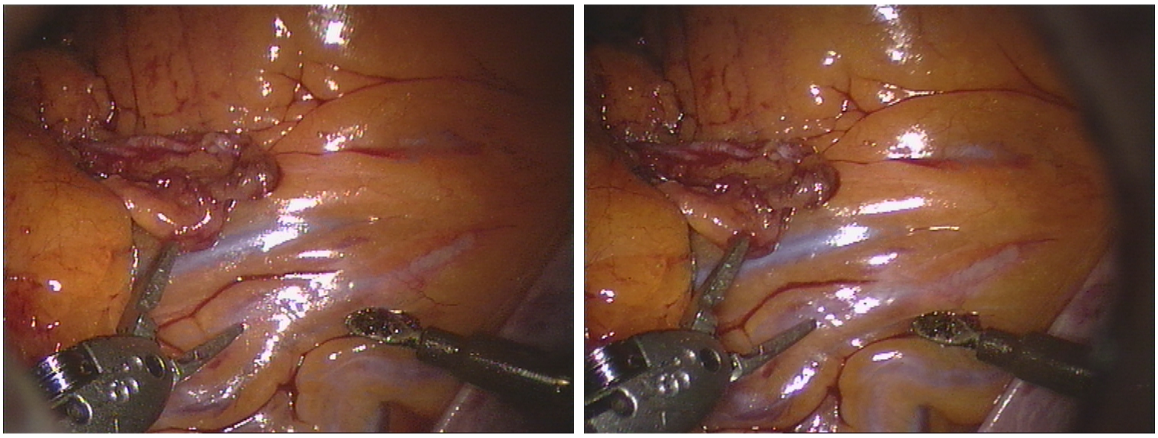

Figure 4.1: Endoscopic stereo views (left and right) of the coronary arteries and the surgical instruments during the TECAB surgery.

A patient-specific 4D motion model of the beating heart with coronary arteries is needed for planning and guiding the TECAB procedure. In this chapter, modelling the coronary motion is achieved by extracting the vessel centrelines from the end-diastolic time frame of the CTA image sequence using the ridge traversal algorithm (Section 4.3), aligning the sequence of cardiac CTA images to the end-diastolic time frame (Section 4.4), and applying the deformation to the extracted coronaries at end-diastole (Section 4.5). The resulting patient-specific coronary motion model potentially can be used to augment the intraoperative images acquired with the stereo-endoscope of the daVinci robot as shown in Figure 4.1. A less comprehensive version of the work in this chapter has previously been presented in [253].

4.2 Multi-scale Vessel Enhancement Filtering for Scale Selection

Various vessel enhancement techniques have been proposed in last decade. Three of the most popular techniques for curvilinear structure filtering have been proposed by Frangi *et al.* [73, 72], Lorenz *et al.* [138] and Sato *et al.* [197]. All of these approaches are based on extracting information from the second order intensity derivatives at multiple scales to identify local structures in the images. Based on that information it is possible to classify the local intensity structure as tubular-like, plane-like or blob-like.

In this thesis, we choose to use a multiscale Hessian-based vessel enhancement filter by Frangi *et al.* [72] because of its superior performance compared with other tubular filters [170]. The filter utilizes the 2nd-order derivatives of the image intensity after smoothing (using a Gaussian kernel) at multiple scales to identify bright tubular-like structures with various diameters. The six second-order derivatives of the Hessian matrix at each voxel are computed by convolving the image with second-order Gaussian derivatives at pre-selected scales.

Assuming a continuous image function $I(\mathbf{x})$, $\mathbf{x} = (x, y, z)$, the Hessian matrix $\mathcal{H}$ for the 3D image at any voxel $\mathbf{x}$ is defined as:

$$\mathcal{H}(\mathbf{x}) = \begin{bmatrix} \dfrac{\partial^2 I(\mathbf{x})}{\partial x \partial x} & \dfrac{\partial^2 I(\mathbf{x})}{\partial x \partial y} & \dfrac{\partial^2 I(\mathbf{x})}{\partial x \partial z} \\[2ex] \dfrac{\partial^2 I(\mathbf{x})}{\partial x \partial y} & \dfrac{\partial^2 I(\mathbf{x})}{\partial y \partial y} & \dfrac{\partial^2 I(\mathbf{x})}{\partial y \partial z} \\[2ex] \dfrac{\partial^2 I(\mathbf{x})}{\partial x \partial z} & \dfrac{\partial^2 I(\mathbf{x})}{\partial y \partial z} & \dfrac{\partial^2 I(\mathbf{x})}{\partial z \partial z} \end{bmatrix} \tag{4.1}$$

At a pre-defined scale σ, Hessian $\mathcal{H}$ can be computed by convolving the image $I(\mathbf{x})$

with second-order Gaussian derivatives shown in Figure 4.2 (a):

$$\mathcal{H}_\sigma(\mathbf{x}) = \begin{bmatrix} \frac{\partial^2 G_\sigma(\mathbf{x})}{\partial x^2} & \frac{\partial^2 G_\sigma(\mathbf{x})}{\partial x \partial y} & \frac{\partial^2 G_\sigma(\mathbf{x})}{\partial x \partial z} \\ \frac{\partial^2 G_\sigma(\mathbf{x})}{\partial x \partial y} & \frac{\partial^2 G_\sigma(\mathbf{x})}{\partial y^2} & \frac{\partial^2 G_\sigma(\mathbf{x})}{\partial y \partial z} \\ \frac{\partial^2 G_\sigma(\mathbf{x})}{\partial x \partial z} & \frac{\partial^2 G_\sigma(\mathbf{x})}{\partial y \partial z} & \frac{\partial^2 G_\sigma(\mathbf{x})}{\partial z^2} \end{bmatrix} \star I(\mathbf{x}) \tag{4.2}$$

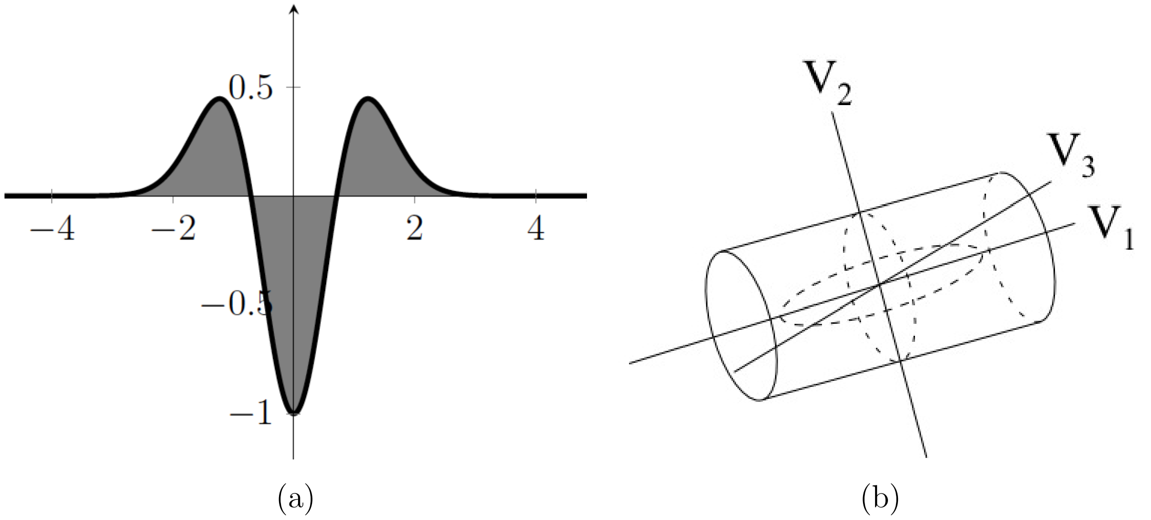

(a) (b)

Figure 4.2: Illustrations of second order Gaussian derivative and ellipsoid. (a): The second order derivative of a Gaussian kernel at scale $\sigma = 1$. (b): The ellipsoid that locally describes the second order structure of the image with illustration of the principal directions of curvature.

A vesselness term $v_\sigma(\mathbf{x})$ is then defined as in Frangi *et al.* [72] and is based on the eigenvalues and eigenvectors of $\mathcal{H}_\sigma(\mathbf{x})$. Let $|\lambda_1| \leq |\lambda_2| \leq |\lambda_3|$ denote the eigenvalues of the Hessian $\mathcal{H}_\sigma(\mathbf{x})$ and $\vec{v}_1$,$\vec{v}_2$,$\vec{v}_3$ are the corresponding eigenvectors. The principal curvature directions are then given by $\vec{v}_2$ and $\vec{v}_3$ as shown in Figure 4.2 (b).

Since coronary arteries have higher intensity values in CTA images than surrounding soft tissues, the vessel centre points are the ones with maximal local intensities after smoothing. Thus the corresponding eigenvalues λ_2 and λ_3 should be negative for voxels on the arteries in CTA image; otherwise, the *vesselness response* should be zero. As in [72, 73], the *vesselness response* $v_\sigma(\mathbf{x})$ at voxel $\mathbf{x}$ with scale σ is formulated as in Equation 2.5.

Because the size of the cross-sectional profile of the coronaries varies substantially from the root to distal end, a single-scale vesselness response is not sufficient to capture the whole range of coronaries. The vesselness response of the filter reaches a maximum at a scale that approximately matches the size of the vessel to detect. Thus, integrating the vesselness response at different scales meets the requirement imposed by varying vessel sizes. In our work, the response is computed at a range of scales, exponentially distributed between σ_{min} and σ_{max}. For scale sampling, we refer to Lindeberg *et al.* [135]. The *maximum vesselness response* $\mathcal{V}(\mathbf{x})$ with the corresponding optimal scale $\sigma_{\mathrm{optimal}}(\mathbf{x})$ is then obtained for each voxel $\mathbf{x}$ of the image:

$$\mathcal{V}(\mathbf{x}) = \max_{\sigma_{\mathrm{min}} \leq \sigma \leq \sigma_{\mathrm{max}}} v_{\sigma}(\mathbf{x}). \tag{4.3}$$

The scale $\sigma_{\mathrm{optimal}}(\mathbf{x})$ approximates the radius of the local vessel segment centred at $\mathbf{x}$. There are two groups of outputs of this vessel enhancement algorithm:

- First, the final *vesselness image* denoted as I_v is constructed using the maximum response $\mathcal{V}(\mathbf{x})$ of each voxel $\mathbf{x}$ as the intensity value;
- Second, the optimal scale $\sigma_{\mathrm{optimal}}(\mathbf{x})$ is selected for each voxel $\mathbf{x}$.

As for ridge traversal, only the optimal scale at each voxel is utilised in the rest of this chapter.

4.3 Ridge Traversal

As for coronary CTA images, a coronary segment can be approximated as a tubular object surrounded by dark background with highest intensity along its centreline. This high intensity centreline can be seen as an intensity ridge. Given an image function $I(\mathbf{x})$, if the intensity value is considered as the height from zero, ridge points are those where the image has a local maximum in the direction of the principal curvature of $I(\mathbf{x})$. Ridge points are distinguished by the local extrema of principle curvatures.

Consistent with the notation used in Section 4.2, the Hessian $\mathcal{H}$ at any voxel $\mathbf{x}$ in a CTA image I is computed as in Equation 4.2, using the optimal scale $\sigma_{\mathrm{optimal}}$ at voxel $\mathbf{x}$ selected by Equation 4.3. The gradient ∇I is computed by convolving the image I with first-order Gaussian derivative with kernel $\sigma_{\mathrm{optimal}}(\mathbf{x})$ for each voxel $\mathbf{x}$:

$$\nabla I(\mathbf{x}) = \begin{bmatrix} \dfrac{\partial G_{\sigma_{\mathrm{optimal}}(\mathbf{x})}(\mathbf{x})}{\partial x} \star I(\mathbf{x}) \\ \dfrac{\partial G_{\sigma_{\mathrm{optimal}}(\mathbf{x})}(\mathbf{x})}{\partial y} \star I(\mathbf{x}) \\ \dfrac{\partial G_{\sigma_{\mathrm{optimal}}(\mathbf{x})}(\mathbf{x})}{\partial z} \star I(\mathbf{x}) \end{bmatrix}^{\mathrm{T}} \tag{4.4}$$

The scale factor $\sigma_{\mathrm{optimal}}$ is crucial for effective ridge traversal. It specifies the width of the Gaussian kernel used for computing the gradient and Hessian of I at each voxel $\mathbf{x}$.

This procedure suppresses the image noise and also creates a central intensity ridge resembling a tubular structure.

The notations for eigenvectors and eigenvalues are also consistent with those in Section 4.2: When the eigenvalues are ordered as $|\lambda_1| \leq |\lambda_2| \leq |\lambda_3|$, the principal curvature directions are then given by $\vec{v}_2$ and $\vec{v}_3$. The zero-crossing points of the image gradient ∇I in the principal curvature directions satisfy the following two conditions:

$$\vec{v}_2 \cdot \nabla I = 0 \tag{4.5}$$

$$\vec{v}_3 \cdot \nabla I = 0 \tag{4.6}$$

Since vessels have higher intensity in CTA images than soft tissues, one can define vessels in terms of intensity ridges. For an n-dimensional image ridge points can be defined as points which are local intensity maxima in $n-1$ dimensions. Thus, for a 3D image the corresponding eigenvalues λ_2 and λ_3 for ridge points should be negative:

$$\lambda_2 < 0 \tag{4.7}$$

$$\lambda_3 < 0 \tag{4.8}$$

Voxels that satisfy Equations 4.5, 4.6, 4.7 and 4.8 are defined as ridge points in the 3D intensity space.

Ridge traversal as a method for extracting vessel centrelines has originally been presented in Aylward *et al.* [14] and further extended in [12]. The method starts from a user-supplied seed point at or near the vessel centre, searches for the local ridge point via optimising a pre-defined evaluation function, generates next guess from the newly found ridge point and repeats this process until the full extent of the vessel ridge is extracted.

We minimise the evaluation function as proposed in [14] to move the user-supplied seed point to the closest centreline. This evaluation function is referred to as a ridgeness function $\mathcal{J}$:

$$\mathcal{J}(\mathbf{x}) = (\vec{v}_2 \cdot \nabla I)^2 + (\vec{v}_3 \cdot \nabla I)^2 \approx 0 \tag{4.9}$$

In this thesis, the Broyden-Fletcher-Goldfarb-Shanno (BFGS) method [182] is used to solve this non-linear optimisation problem.

For an ideal bright tubular structure with little intensity variation along its tangent direction, the eigenvalue with smallest magnitude satisfies:

$$\lambda_1 \approx 0 \tag{4.10}$$

The eigenvector $\vec{v}_1$ corresponding to this smallest eigenvalue λ_1 can be used to approximate the tangent direction of the vessel and to define the local vessel orientation. Thus, the next prediction point $\mathbf{p}_i$ along the vessel ridge can be found by stepping in the direction $\vec{v}_1$ with a small step size t from current ridge point $\mathbf{x}_{i-1}$. If $\mathcal{J}(\mathbf{p}_i)$ is above a pre-defined threshold level which implies $\mathbf{p}_i$ is not on the vessel intensity ridge, the BFGS optimisation is reapplied to move $\mathbf{p}_i$ to the closest ridge point $\mathbf{x}_i$. This process is shown in Figure 4.3. It is repeated ideally until the stopping criteria is met, e.g., the extracted vessel being long enough for the clinical interest or the intensity value of the newly found ridge point being too low.

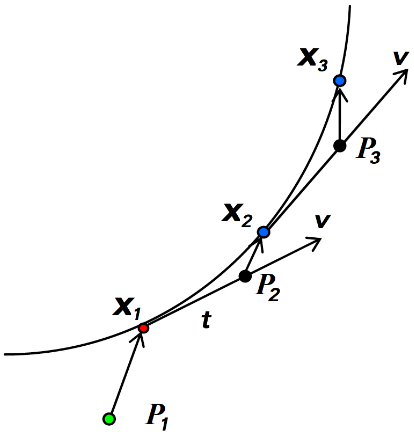

Figure 4.3: Illustration of ridge traversal. Starting from seed point $\mathbf{p}_1$, the first ridge point $\mathbf{x}_1$ is found by the minimisation of $\mathcal{J}(\mathbf{p}_1)$. Next seed point $\mathbf{p}_2$ is estimated by stepping in the direction $\vec{v}_1$ of local tubular structure with a step size t. The cost function $\mathcal{J}(\mathbf{p}_2)$ is minimised again to search for next ridge point $\mathbf{x}_2$. This process is repeated for the extraction of the vessel.

4.4 Cardiac Motion Tracking by Non-rigid Registration

Many methods have been developed for the extraction of cardiac motion from dynamic image sequences, e.g., optical flow [61], active contour models [168], harmonic phase (HARP) [173] and image registration approaches [43]. Compared with other methods which rely on specialized image sequences such as tagged MR or HARP, non-rigid image registration based on voxel similarity measures does not require any explicit feature extraction and can be used on both MR and CTA images. Moreover, given different types of images, the voxel similarity measure can be chosen to calculate a suitable metric for that particular type of image. For cardiac motion tracking, non-rigid registration based on a free-form deformation (FFD) model has shown promising results in previous work presented by Chandrashekara *et al.* [42]. Thus a similar approach is adopted for our study of cardiac motion tracking from 4D CTA.

In this section, we assume the coronary displacement can be recovered together with the ventricle motion from the temporal non-rigid registration of the entire sequence of cardiac CTA images. The motion of the heart is obtained from non-rigid image registration using a free-form deformation model based on cubic B-splines [193]. Assume that a free form deformation is parametrised by a set of vectors Φ. Each vector $\boldsymbol{\phi}_{i,j,k}$ denotes a control point that is arranged on a regular lattice of size $n_x \times n_y \times n_z$ with uniform spacing of δ along each dimension. The index i, j, k denotes the location of its associated control point within the lattice. By using the cubic B-spline basis functions to blend the control point vectors, a continuously varying displacement is defined at each point of the image domain. As in [193], the free form deformation for a voxel $\mathbf{x} = \{x, y, z\}$ is formulated as the 3D tensor product of the 1D cubic B-splines:

$$\mathbf{T}(x, y, z) = \sum_{l=0}^{3} \sum_{m=0}^{3} \sum_{n=0}^{3} B_l(q) B_m(s) B_n(w) \boldsymbol{\phi}_{i+l,j+m,k+n} \tag{4.11}$$

where $i = \left\lfloor \frac{x}{n_x} \right\rfloor - 1$, $j = \left\lfloor \frac{y}{n_y} \right\rfloor - 1$, $k = \left\lfloor \frac{z}{n_z} \right\rfloor - 1$, $q = \frac{x}{n_x} - \left\lfloor \frac{x}{n_x} \right\rfloor$, $s = \frac{y}{n_y} - \left\lfloor \frac{y}{n_y} \right\rfloor$, $w = \frac{z}{n_z} - \left\lfloor \frac{z}{n_z} \right\rfloor$. The functions B_l, B_m, and B_n represent the *l-th*, *m-th* and *n-th* B-spline basis functions respectively:

$$\begin{aligned}
B_0(u) &= \frac{(1-u)^3}{6} \\
B_1(u) &= \frac{3u^3 - 6u^2 + 4}{6} \\
B_2(u) &= \frac{-3u^3 + 3u^2 + 3u + 1}{6} \\
B_3(u) &= \frac{u^3}{6}
\end{aligned}$$

The goal of non-rigid registration is to match one image to the other one. The B-spline based free-form deformation model is used to warp the source image until it best matches the reference image. To quantify this alignment, a similarity metric between two images needs to be formulated. For a detailed review of similarity measures in literature, we refer to [85].

In this chapter, for the experiments we evaluate and optimize four different similarity measures, namely, sum of squared differences (SSD), correlation coefficient (CC), mutual information (MI) and normalized mutual information (NMI).

Given two images, a reference I_R and a source I_S, and a transformation $\mathbf{T}$, the overall similarity of two images is given by the sum of the intensity differences at each corresponding voxel location $\mathbf{x}$ over the image domain Ω. Assuming $I_R(\mathbf{x})$ denotes the image intensity of voxel location $\mathbf{x}$ in the reference image, $I_S(\mathbf{T}(\mathbf{x}))$ is the intensity of the transformed voxel position $\mathbf{T}(\mathbf{x})$ in the source image, sum of squared differences (SSD) of two images is then given by:

$$\mathcal{S}_{\mathrm{SSD}} = \sum_{\mathbf{x}\in\Omega} \left(I_R(\mathbf{x}) - I_S(\mathbf{T}(\mathbf{x}))\right)^2 \ . \tag{4.12}$$

Ideally, when two images are aligned after registration, this metric has the minimal value of zero. However, this metric can be strongly affected by a small set of voxels having significantly different intensities in two images.

The correlation coefficient metric assumes a linear relationship between the intensity values of corresponding voxels in two images and is more robust than SSD. It is defined as:

$$\mathcal{S}_{\mathrm{CC}} = \frac{\sum_{\mathbf{x}\in\Omega}(I_R(\mathbf{x}) - \langle I_R(\mathbf{x})\rangle)\cdot (I_S(\mathbf{T}(\mathbf{x})) - \langle I_S(\mathbf{T}(\mathbf{x}))\rangle)}{\sqrt{\sum_{\mathbf{x}\in\Omega}(I_R(\mathbf{x}) - \langle I_R(\mathbf{x})\rangle)^2\cdot \sum_{\mathbf{x}\in\Omega}(I_S(\mathbf{T}(\mathbf{x})) - \langle I_S(\mathbf{T}(\mathbf{x}))\rangle)^2}} \ . \tag{4.13}$$

Here $\langle\cdot\rangle$ represents the mean intensity of a given image. The metric $\mathcal{S}_{\mathrm{CC}}$ increases as the two images are better aligned. However, it is sensitive to local differences in brightness and contrast of two images.

Mutual information as a similarity metric for image registration was proposed in [49, 228]. Instead of comparing voxel intensities directly, mutual information measures how much information one image contains about another. It is based on the marginal entropy of each image and the joint entropy of the pair. The marginal entropy of an image I is defined as:

$$H(I) = -\sum_{i\in I} p(i) \log p(i) \ , \tag{4.14}$$

where $p(i)$ is the probability of voxels with intensity i occurring in image I. Without incorporating the deformation information, the basic joint entropy formulation of two images I_S and I_R with intensities $i_S \in I_S$ and $i_R \in I_R$ respectively is given by:

$$H(I_R, I_S) = -\sum_{i_R\in I_R}\sum_{i_S\in I_S} p(i_R, i_S) \log p(i_R, i_S) \ , \tag{4.15}$$

where $p(i_R, i_S)$ is the joint probability density function of the images I_R and I_S. As the anatomical structures in two images are better aligned, their joint entropy decreases. The mutual information of two images I_R and I_S is defined as:

$$\mathcal{S}_{\mathrm{MI}} = H(I_R) + H(I_S) - H(I_R, I_S) = \sum_{i_R\in I_R}\sum_{i_S\in I_S} p(i_R, i_S) \log \frac{p(i_R, i_S)}{p(i_R)\cdot p(i_S)} \ . \tag{4.16}$$

If two images I_R and I_S are completely independent, we have $p(i_R, i_S) = p(i_R)\cdot p(i_S)$ which leads to $\mathcal{S}_{\mathrm{MI}}(I_R, I_S) = 0$. As the two images become more dependent, or equivalently, the information one image contains about the other one increases, the mutual information $\mathcal{S}_{\mathrm{MI}}$ also increases. However, both joint entropy and mutual information are dependent on the overlap between two images. In certain cases, a reduction in the overlap of the anatomical structures of interest still leads to a decrease of joint entropy or increase of mutual information, e.g., when the background of reference image and transformed source image are perfectly aligned and not the anatomical structures. To address this problem, a metric invariant to image overlap has been proposed in [214] called normalised mutual information (NMI):

$$\mathcal{S}_{\mathrm{NMI}} = \frac{H(I_R) + H(I_S)}{H(I_R, I_S)} \ . \tag{4.17}$$

For further information on mutual information as similarity measure, we refer to the survey by Pluim *et al.* [180].

Once the deformation model and similarity metric are chosen, the registration task is essentially to optimise the similarity measure by adjusting the transformation parameters. The intrinsic differences among the various similarity metrics help to choose the suitable one for a specific image registration problem. For contrast-enhanced coronary CTA images, the choice of similarity metric also depends on the image characteristics of each 4D CTA sequence. A gradient descent optimization procedure can be used to optimise the selected similarity metric in order to find the optimal deformation. As for the experiments in this chapter, the correlation coefficient measure provides superior results over the other measures. From the results of the non-rigid image registration of two adjacent images, we can determine the corresponding deformation $\mathbf{T}$ for these two images due to the cardiac motion in the 4D CTA datasets.

4.5 Coronary Motion Modelling and Evaluation

After tracking the cardiac motion, the 4D motion model of the coronary arteries is built by extracting the vessel centrelines from the end-diastolic time frame of the 4D CTA image sequence via ridge traversal, aligning the rest of the sequence of cardiac CTA images to the end-diastolic time frame via the aforementioned non-rigid registration, and finally applying the obtained deformation information to the extracted coronaries at end-diastole in order to derive the coronaries' locations in all other time frames.

To obtain the cardiac motion, we performed non-rigid registration on four 4D CTA sequences with 10 time frames each. Two datasets referred to *SM4DCTA* were acquired from patients with coronary artery diseases in St. Mary's Hospital, London.

The other two denoted as *RB4DCTA* were acquired from patients at Royal Brompton Hospital, London. Table 4.1 shows the scanner information and the size of each 4D CTA data.

Table 4.1: 4D CTA data *RB4DCTA* and *SM4DCTA*

Dataset	CT scanner	Phases	Image size (voxels)	Voxel size (mm^3)
RB4DCTA (I, II)	Toshiba Aquilion 64	10	$512 \times 512 \times 231$ $512 \times 512 \times 298$	$0.62 \times 0.62 \times 0.5$ $0.36 \times 0.36 \times 0.5$
SM4DCTA (III, IV)	Philips Brilliance 64	10	$512 \times 512 \times 382$ $512 \times 512 \times 335$	$0.4 \times 0.4 \times 0.4$ $0.4 \times 0.4 \times 0.4$

For each 4D CTA, the image at the end-diastolic frame of the cardiac cycle in each sequence is chosen as the reference image. In our test datasets, the end-diastole corresponds to 60% of the cardiac cycle. For simplicity, we refer to the end-diastolic phase as I_6 in the remainder of this section. Each of the rest of the image sequence I_t $(t = 0, 1, 2, 3, 4, 5, 7, 8, 9)$ is chosen as the source image and temporally registered to the reference image I_6. Here t denotes the temporal position of each image within one 4D sequence.

The natural deformation of the heart throughout the cardiac cycle from one patient dataset is illustrated in first two rows of Figure 4.4. The corresponding transformed images after alignment with reference image are shown in the bottom two rows of Figure 4.4. Here we have used the cross correlation coefficient to measure the similarity between the images. We expect that a certain amount of coronary motion can be recovered from the cardiac deformation information obtained from this non-rigid registration.

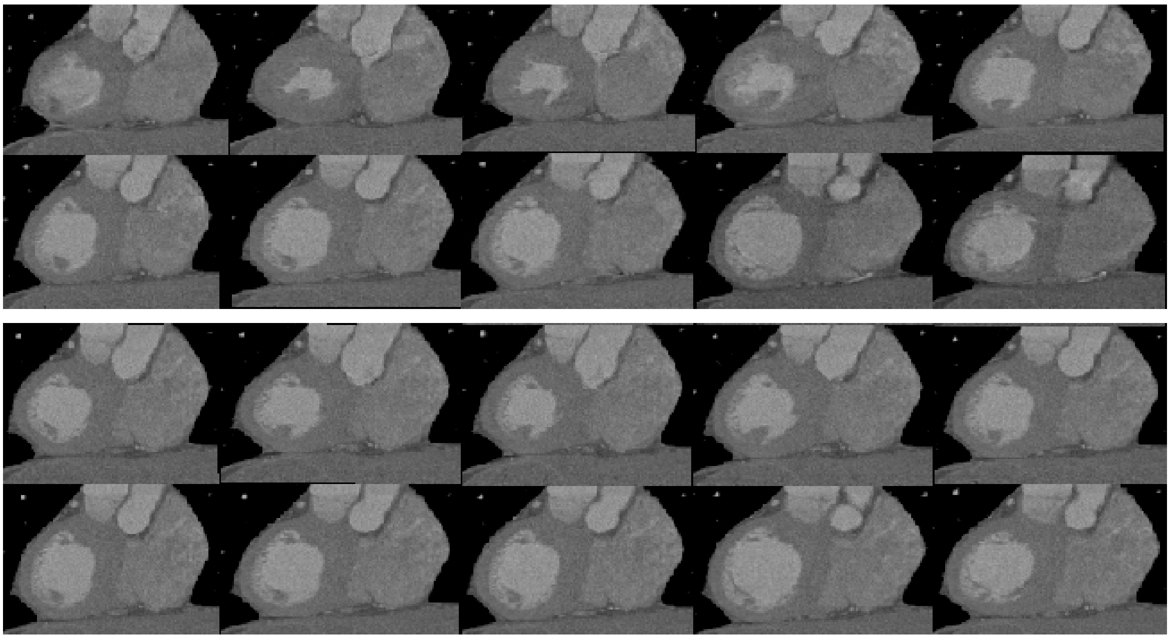

Figure 4.4: Example of 10 time frames of a patient dataset before non-rigid registration shown in top two rows (from left to right, top to bottom sequentially) and after non-rigid registration (as shown in bottom two rows). The 2nd frame in row 2 corresponding to 60% of the cardiac cycle was chosen as the reference image.

To select the scales using multi-scale vessel enhancement filtering, we set the parameters $\alpha = 0.5$, $\beta = 0.5$, $\gamma = 1$ for computing the vesselness response in Equation 2.5, following Frangi *et al.* [73]. The vesselness response is computed at different scales, namely $\sigma = 0.5, 1, 2, 4, 8$mm. The maximal response with its corresponding optimal scale is obtained for each voxel of the image. The optimal scale for each voxel is used to facilitate the ridge traversal of the coronaries. Using this method the coronaries can be extracted in real-time as only local information is used in vessel tracking in 3D space.

A volume rendering of preoperative end-diastolic cardiac CTA image from one patient is shown in Figure 4.5. The coronary arteries and myocardial surfaces are displayed in three different views. The extracted 3D coronary centrelines via ridge traversal from this volume are shown as the lines with large width in Figure 4.6.

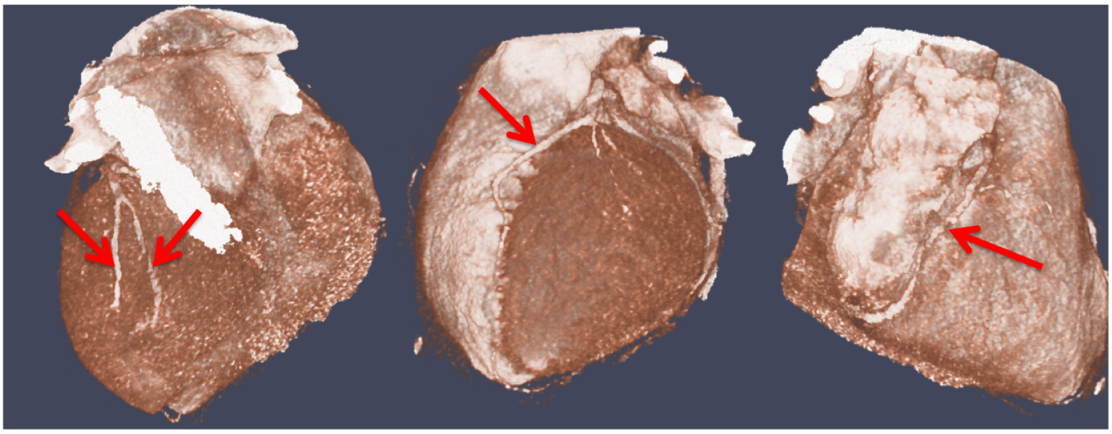

Figure 4.5: Volume rending of CTA image in the end-diastolic time frame from one patient dataset. From left to right, left circumflex artery and branches (LCX), left anterior descending artery and a diagonal branch (LAD) and right coronary artery (RCA) are visible and indicated by the red arrows.

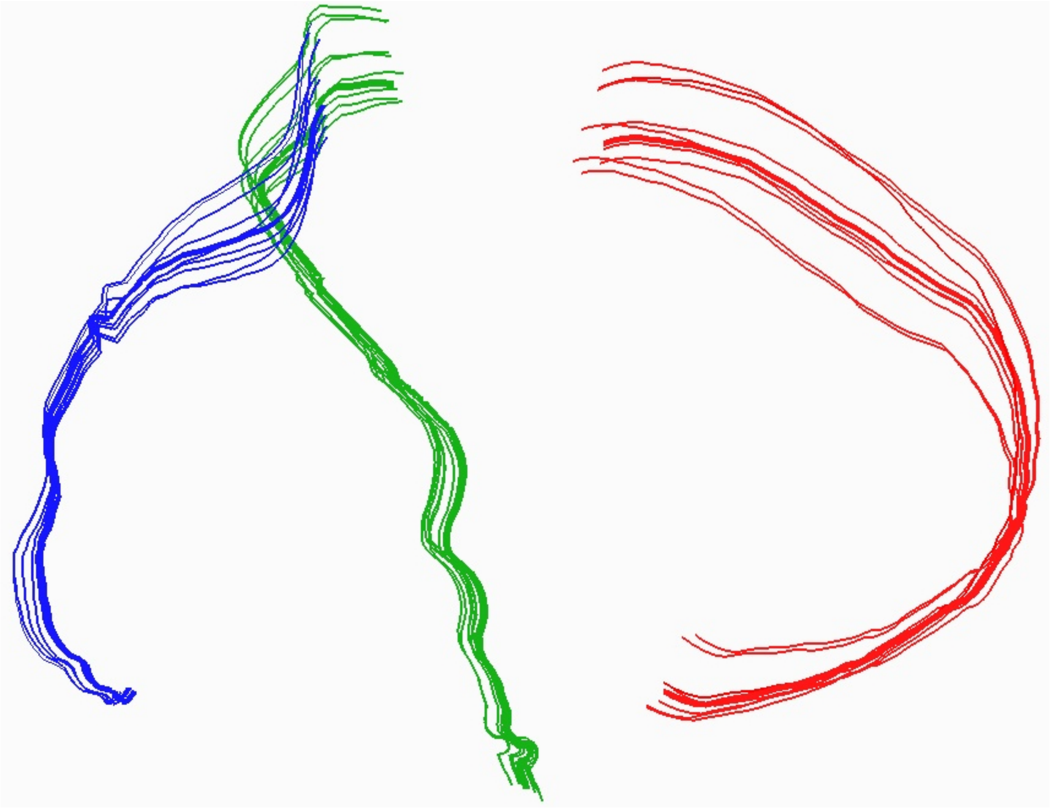

Figure 4.6: Extracted coronary centrelines at ED (shown as the line with large width) and predicted coronary centrelines at the remaining time frames (shown as the line with small width). Red: right coronary artery; Green: left anterior descending coronary artery and branch; Blue: circumflex artery and branch.

The cardiac motion derived above is then used to predict the motion of coronaries in every time frame. For this the coronaries extracted from the end-diastolic time frame via the ridge traversal method are transformed with the obtained deformation information $\mathbf{T}_t$ to each time frame to form the coronary motion model. An example is shown in Figure 4.6.

To evaluate the proposed approach for coronary motion modelling, for each 4D sequence the coronary artery centrelines are also extracted semi-automatically via ridge traversal from the rest of the phases I_t ($t = 0, 1, 2, 3, 4, 5, 7, 8, 9$). For quantitative assessment, the distance between the centreline M predicted by the non-rigid registration method and the semi-automatically extracted centreline U of each time frame is measured to assess the accuracy of the coronary motion prediction. We define this distance as:

$$\mathcal{D}(M, U) = \frac{1}{N_M + N_U} \left(\sum_{i=1}^{N_M} \|\mathbf{m}_i - l(\mathbf{m}_i, U)\|_2 + \sum_{j=1}^{N_U} \|\mathbf{u}_j - l(\mathbf{u}_j, M))\|_2 \right) \tag{4.18}$$

where N_M and N_U are the number of points representing vessel M and vessel U correspondingly. For each point $\mathbf{m}_i \in M$, $l(\mathbf{m}_i, U)$ calculates the closest point of $\mathbf{m}_i$ on the automatically extracted vessel U. Similarly, for each point $\mathbf{u}_j \in U$, $l(\mathbf{u}_j, M)$ defines the closest point of $\mathbf{u}_j$ on the vessel M. We designed this distance measure to be symmetric and to have the flexibility to discard or include the points from one set which are missing in the other set. In this thesis, all the points from both sets are used for evaluating the distance error. This ensures that the misalignment tangential to the centreline direction is included in the distance measure.

In Figure 4.7 and Figure 4.8, we compare the predicted location of the centrelines obtained by applying the non-rigid deformation with the actual position of the centrelines. Figure 4.7 and Figure 4.8 both show that the registration method can only recover part of the coronary motion. The reasons for this are two-fold: First, the image quality of dynamic cardiac CTA is limited. This is especially true for CTA image reconstructions during those parts of the cardiac phase in which the heart moves rapidly. The second problem is the fact that the image registration is driven by features at large scales such as the epicardium and endocardium. Transformation and registration models focusing on small structures like coronaries need to be developed in order to overcome these problems and improve the prediction of the coronary motion.

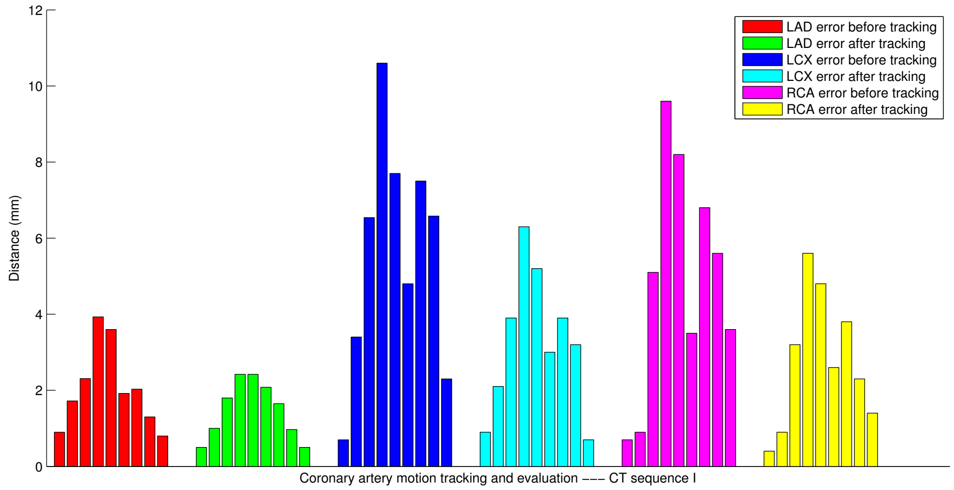

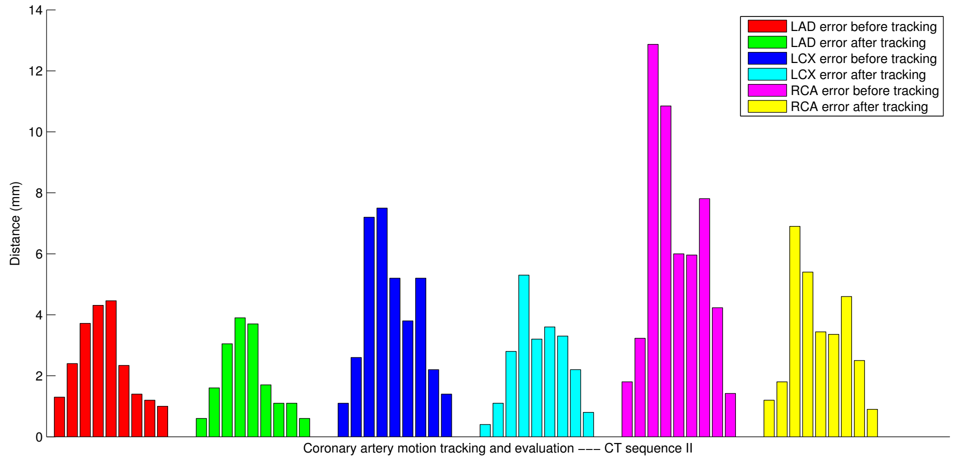

Figure 4.7: Ridge-based coronary motion tracking and evaluation in CTA sequence I and II. The LAD error before tracking is the natural displacement of LAD measured as the distance between the extracted centreline at end-diastole and all the other extractions in the remaining time frames. The LAD error after tracking is the residual motion after motion tracking, calculated as the distance between the extracted LAD and the predicted LAD centreline at each phase. Same measurements are presented for RCA and LCX.

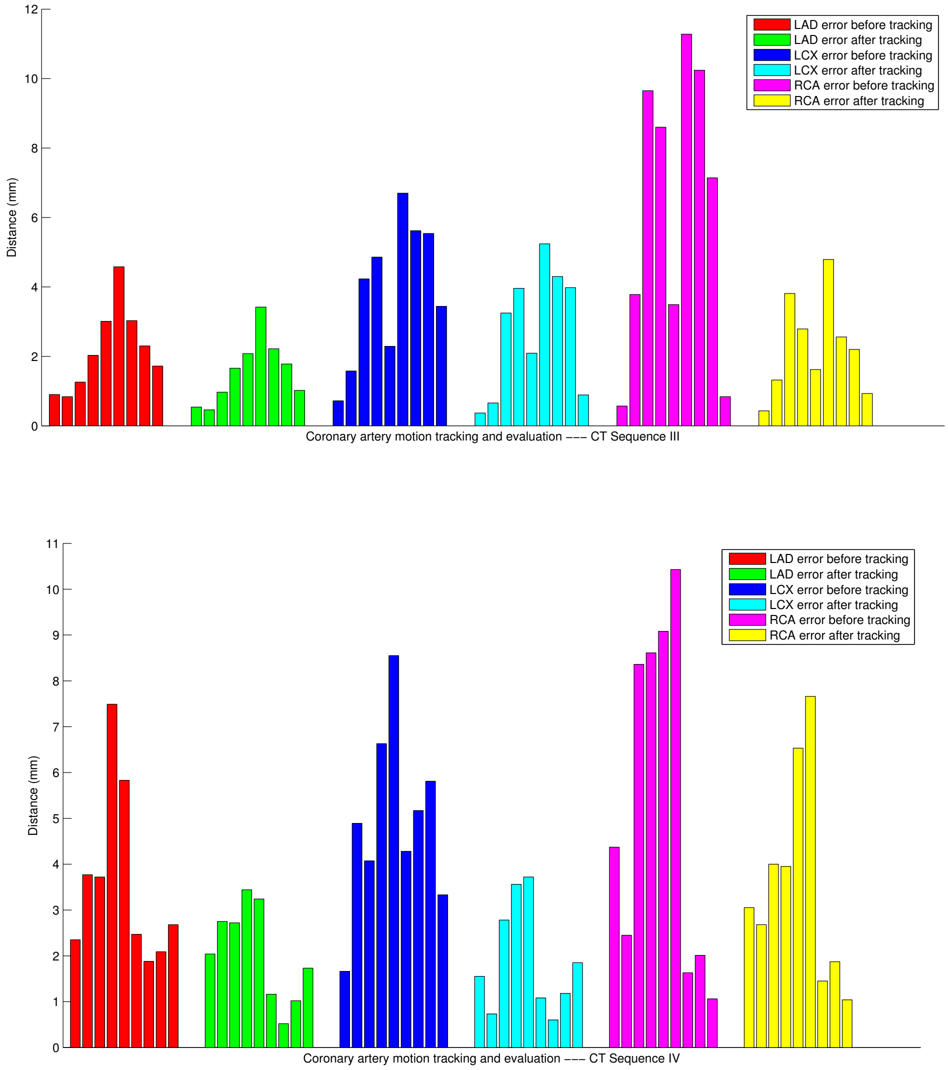

Figure 4.8: Ridge-based coronary motion tracking and evaluation in CTA sequence III and IV. The LAD error before tracking is the natural displacement of LAD measured as the distance between the extracted centreline at end-diastole and all the other extractions in the remaining time frames. The LAD error after tracking is the residual motion after motion tracking, calculated as the distance between the extracted LAD and the predicted LAD centreline at each phase. Same measurements are presented for RCA and LCX.

4.6 Summary

In this chapter, we have presented an approach for patient-specific coronary tree construction and motion modelling from CTA images to assist the totally endoscopic coronary artery bypass surgery. The proposed method utilises non-rigid registration based on free-form deformations to derive cardiac motion, extracts the coronary centrelines as intensity ridges from end-diastolic CTA image and finally propagates the extracted centrelines to other time frames using the derived deformation in order to form the coronary motion model. This approach has been tested on the clinical CTA datasets acquired from four subjects. The experiments show that only part of the coronary motion can be tracked using the proposed method due to limitations imposed by the image quality and the lack of emphasis on coronary structures during the registration process.

Another drawback of this approach is the demand of user-interaction during the centreline extraction procedure. The ridge traversal performs well on idealised bright tubular structure in a dark background. However, for the clinical 4D CTA data acquired for our research, poor image quality frequently occurs due to three reasons:

1. Artefacts caused by the rapid motion of the heart during the acquisition, e.g., displaced reduplications of structures in different time frames (known as ghosting [8]);
2. Stair-step artefacts resulted from misregistration of CT data acquired during multiple cardiac cycles [234]. The cardiac cycles vary in length and therefore the acquisition of different frames occurs in slightly different phases of the ventricular contraction/relaxation. Consequently, the reconstructed image shows inclined surfaces or discontinued objects in longitudinal sections referred to as stair-step artefacts [231].
3. Low signal-to-noise ratio in certain phases caused by the application of ECG pulsing windows to reduce the radiation dose for the patient [239].

The presence of artefacts and region of low signal-to-noise ratio in the 4D CTA images cause the early termination during the ridge traversal. Also, the extraction method could not correct itself, i.e., once the computed vessel ridge point deviates from the actual one, the algorithm is not able to recover. This leads to further deviation of the subsequently detected ridge points that could fall out of the vessel region. Moreover, the ridge traversal algorithm starts from the user-placed seed point and extracts any vessel branch satisfying the search criteria. Particularly, when branching happens, the extracted vessel may not be the one of clinical interest. To correct the aforementioned three types of errors, user intervention is required to restart the ridge traversal procedure by placing a new seed point on or close to the vessel ridge.

Chapter 5

Graph-based Coronary Motion Tracking

Following the work in previous chapter on vessel centreline extraction via a ridge traversal algorithm, this chapter presents our work on coronary centreline extraction from 4D CTA using an A* graph search algorithm. At each phase of the 4D CTA sequence, the coronary centrelines are extracted as the minimal cost paths via the A* graph search algorithm with prior information obtained from image registration of the adjacent frames from the 4D CTA sequence. By extracting RCA, LAD and LCX centrelines in all time frames through this method, a patient-specific coronary motion model can be constructed from the extracted centrelines. The contributions of this chapter are two-fold:

- We develop a more robust centreline extraction method than the ridge traversal algorithm in order to segment the coronary centrelines from the pre-operative CTA datasets provided, particularly for CTA scans with severe stair-step artefacts or noise as shown in Figure 5.1;

- Instead of tracking the coronary motion by non-rigid registration, we rely on the extracted centrelines at all phases in each 4D CTA sequence to form the coronary motion model. By doing so, we expect to achieve better accuracy of the constructed coronary model as opposed to the one presented in Chapter 4.

Since the coronary motion model is built from the 4D CTA sequence prior to the operation for assisting surgical planning or providing intra-operative guidance, the accuracy of the model is more important than its being constructed automatically or in real-time.

5.1 Multi-scale Vessel Enhancement

A coarse segmentation of the coronaries arteries in CTA images is performed using a multi-scale Hessian-based vessel enhancement filter by Frangi *et al.* [72], as presented in Section 4.2. For any 3D image I from a 4D CTA sequence, the *vesselness image* I_v is computed through the method in Section 4.2, together with the corresponding optimal scale $\sigma_{\text{optimal}}(\mathbf{x})$ for each voxel $\mathbf{x}$ in image I.

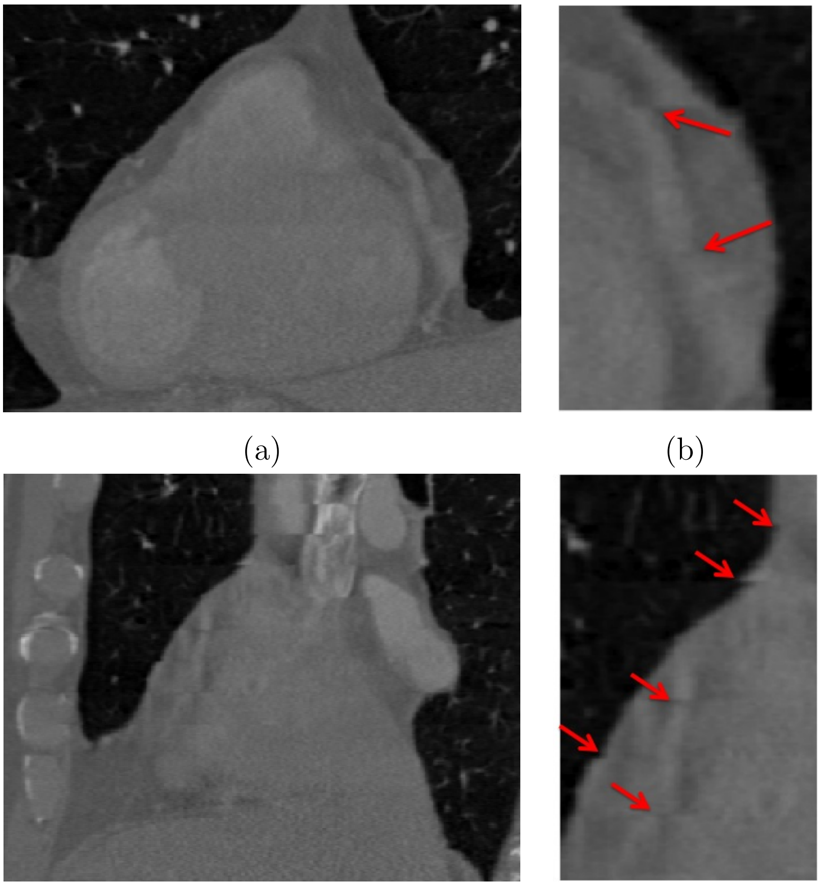

(a) (b)

(c) (d)

Figure 5.1: CTA images with stair-step artefacts. (a) and (c): Two slices of a CTA dataset showing the coronary artery in regions with stair-step artefacts highlighted in (b) and (d) respectively. The red arrows point to the location where stair-step artefacts occur.

5.2 A* Graph Search Algorithm for Extracting Minimal Cost Path

Various methods have been presented in literature restating the vessel segmentation problem as an optimisation problem, e.g., [245, 244, 171, 246]. The task of extracting vessel centrelines can be converted to finding the minimal cost paths given a predefined cost function. In Section 2.3.1.7, we provide a detailed review of the basic algorithms for segmenting vessel centrelines through extracting minimal cost paths.

In our work, the A* graph search algorithm [87] is implemented to find the minimum cost path from a start node S to an end node E. For each vessel branch, a pair of start node S and end node E on the vessel are supplied by the user in each time frame. The uni-directional graph search algorithm evaluates the smallest cost from node S to current node $\mathbf{x}$ denoted as $g(\mathbf{x})$ and the heuristic cost from current node to node E denoted as $h(\mathbf{x})$ to determine which voxel will be searched next. This procedure is repeated until the end node E is reached. The search algorithm finds the optimal path only if the heuristic underestimates the true cost. The Euclidean distance from $\mathbf{x}$ to E is used to calculate the heuristic cost in our application. In our applications, this heuristic measurement is guaranteed to be lower than the true optimal path cost.

Compared with the ridge traversal algorithm in Chapter 4, using the A* graph search algorithm for finding the coronary centrelines has two advantages:

1. The A* graph search algorithm is particularly useful when multiple branches originate from the start node or any node along the vessel, since specifying the end node guarantees the extraction of the vascular branch of interest.

2. When artefacts (e.g., stair-step) or stenoses occur in the coronary region, the A* graph search algorithm is capable of bridging those gaps and finding the optimal path if a suitable heuristic term is applied.

In contrast, the ridge traversal algorithm does not guarantee the extraction of vessel of interest in these two cases.

5.3 Prior Information for Coronary Motion Tracking

In some frames of the dynamic CTA sequence, the coronaries are difficult to extract. This is especially true in those phases during the cardiac cycle in which the heart is rapidly contracting or expanding. To allow the reliable extraction of the coronary arteries in these frames we have extended the basic A* graph search for extracting minimal-cost path approach as presented in previous section to a framework that incorporates prior information about the location and shape of the coronary arteries into the extraction process.

The basic idea of using prior information for tracking is that the location and shape of the coronary arteries is likely to be similar in adjacent frames. Thus, we are using the extracted coronary centrelines from time frame I_t to assist the extraction in next frame I_{t+1}. We define the prior probability of a voxel in time frame I_{t+1} to be part of the coronaries as a Gaussian probability P distribution centred at the voxel locations of the coronaries in time frame I_t. The size of the Gaussian kernel σ is chosen depending on the amount of motion between two adjacent time frames.

In order to improve the estimate of the prior probability described above we additionally estimate the cardiac motion between time frames and then transform the prior probability using the resulting transformation $\mathbf{T}$. In our case the cardiac motion between two adjacent frames is obtained from non-rigid image registration using a free-form deformation model based on cubic B-spline [193]. The details of this non-rigid image registration approach have been presented in Section 4.4.

A series of registration steps is performed to register each time frame I_t to its subsequent time frame I_{t+1}. The non-rigid registration algorithm optimizes correlation coefficient (CC) as similarity measures between time frames as formulated in Equation 4.13. A gradient ascent optimization is used to maximise the similarity measure $\mathcal{S}_{\mathrm{CC}}$ in order to find the optimal transformation. Using the resulting transformation the prior probability information is propagated from each time frame to its subsequence time frame.

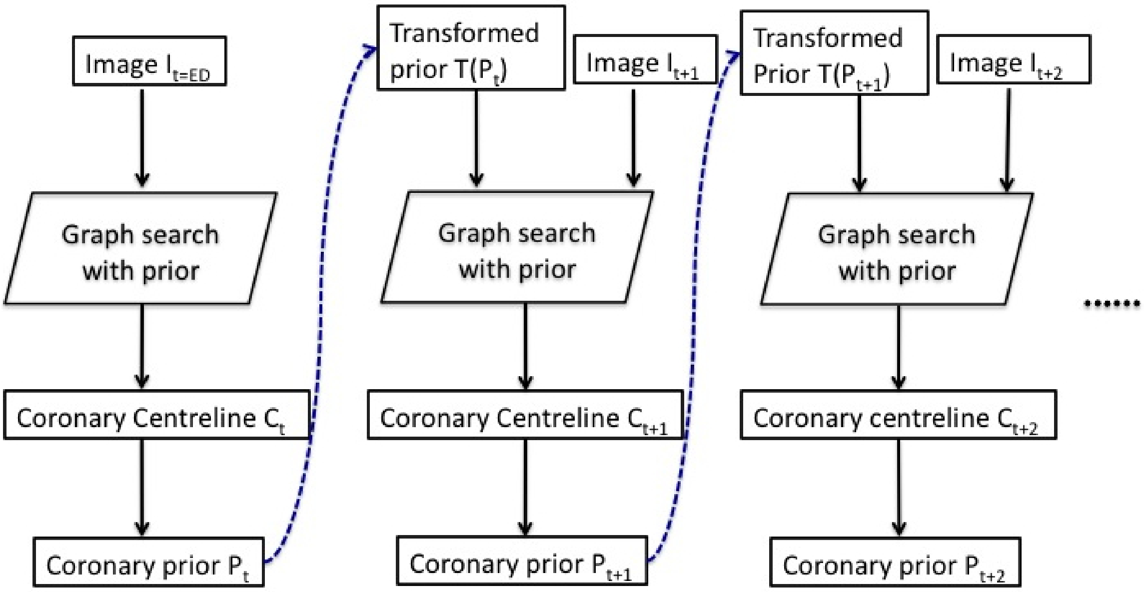

Figure 5.2: Illustration of graph search algorithm with prior information.

Figure 5.2 illustrates how the coronary prior probability is incorporated to assist the graph search. This procedure starts at end-diastolic phase where the coronaries have good visibility and can be extracted without prior information. It is then repeated until the extraction of the coronaries from all time frames.

5.4 Coronary Motion Tracking Using the A* Graph Search Algorithm with Prior Information

The multi-scale vessel enhancement in Section 5.1 only measures local contrast without taking the average intensity of surrounding region into account. For example, bronchi in CTA images appear to be surrounded by dark background regions with very high contrast, thus bronchi are often enhanced in the vesselness image too. To identify and highlight the intensity regions containing coronaries, a smooth windowing function based on the Gaussian error function erf is constructed as in [152]:

$$W(\mathbf{x}) = \frac{1}{2}\left(\operatorname{erf}\left(b\left(I(\mathbf{x}) - a_1\right)\right) + 1\right) \cdot \left(1 - \frac{1}{2}\left(\operatorname{erf}\left(b\left(I(\mathbf{x}) - a_2\right)\right) + 1\right)\right) \tag{5.1}$$

Here a_1 and a_2 can either be in Hounsfield units or voxel intensity values. Due to the lack of DICOM information for our 4D CTA sequences, there is no information available for calculating the corresponding Hounsfield units from the voxel intensity value. Thus, in this chapter, a_1 is estimated as the lowest intensity value for a voxel along the coronaries, a_2 is the highest one. The parameter b controls the steepness of the smoothing window. Figure 5.3 (a) shows an example profile of this intensity transformation function. Transforming the image intensity through this Equation 5.1 essentially creates a *weighting image* that highlights the coronary region and the regions within same intensity range while suppressing others.

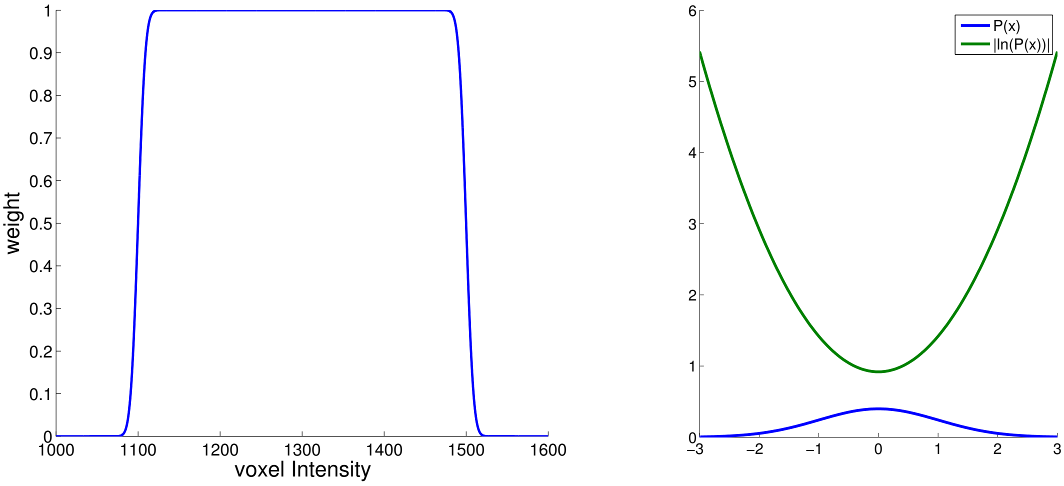

(a)

(b)

Figure 5.3: (a): An example of intensity transformation function given by Equation 5.1 with $a_1 = 1100$, $a_2 = 1500$ and $b = 0.1$. (b): The Gaussian probability profile with $\sigma = 1$ and its corresponding multiplier $(|\ln(P(\mathbf{x}))|)^{\eta}$ for the cost image when $\eta = 1$.

Using the intensity transformation function as formulated in Equation 5.1 and combining it with the vesselness filter from Section 5.1, we define the cost CI, for each voxel $\mathbf{x}$ as:

$$CI(\mathbf{x}) = \frac{1}{\mathcal{V}(\mathbf{x})(W(\mathbf{x}))^{\kappa} + \epsilon} \tag{5.2}$$

where $\mathcal{V}(\mathbf{x})$ is the *maximal vesselness response* of voxel $\mathbf{x}$ at the optimal scale σ_{optimal} as calculated via Equation 4.3 in Section 4.2. Parameter κ controls the influence of W. ϵ is a small positive constant added in to avoid the singularities as the vesselness value approaches zero. Figure 5.4 (e) shows an example of a cost image derived from a vesselness image (c) and a weighting image (d) in Figure 5.4.

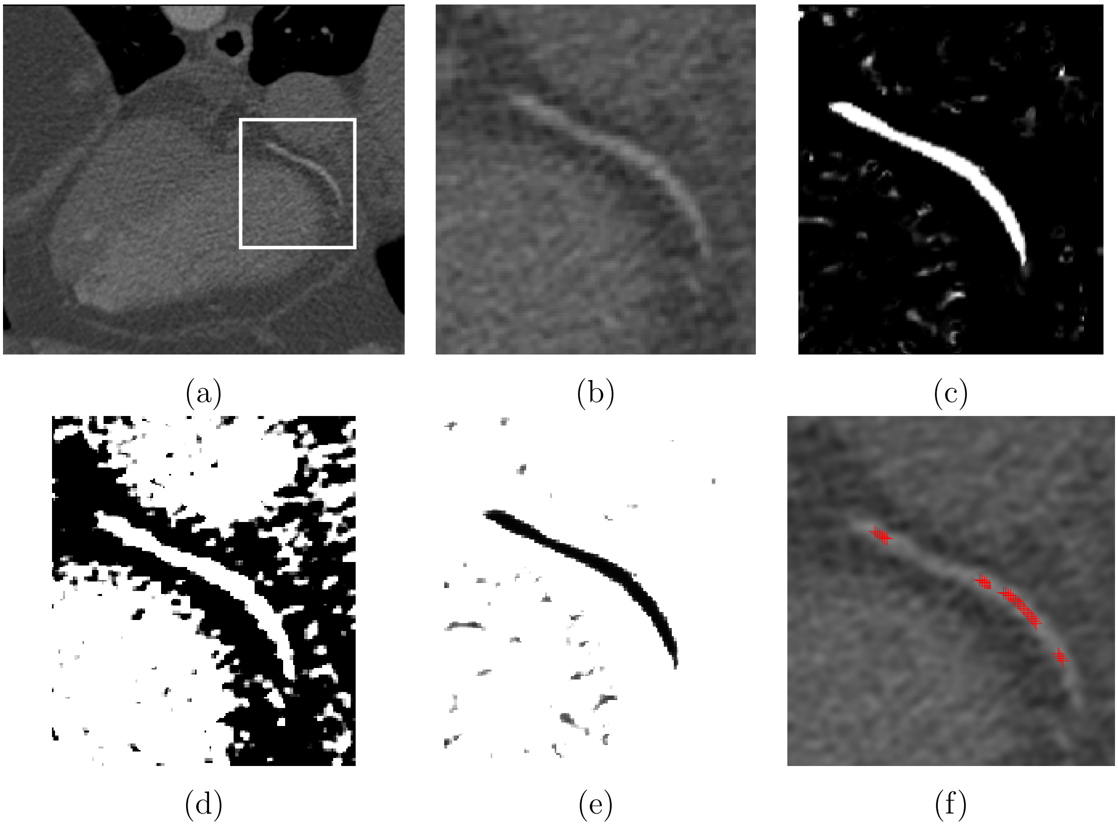
(a) (b) (c)

(d) (e) (f)

Figure 5.4: (a): A slice of a CTA image containing the distal part of the right coronary artery; (b): Region of interest from the highlighted area in (a); (c): Vesselness image of (b); (d): Weighting image of (b) computed by Equation 5.1; (e): Cost image of (b) computed by Equation 5.2; (f): Extracted centreline marked by red crosses. Note only part of the extracted centreline is visible in this 2D slice.

Given a pair of start node S and end node E for each vessel, in order to automatically extract the coronaries from the CTA sequences with poor image quality, we additionally add the prior information into the A* graph search algorithm. We evaluate the score $g(\mathbf{x})$ as:

$$g(\mathbf{x}) = g(\mathbf{x}') + CI(\mathbf{x}) * (|\ln(P(\mathbf{x}))|)^{\eta}. \tag{5.3}$$

where the parameter η defines the importance of prior information for the centreline extraction in current frame. To initialize the cost function, $g(\mathbf{x}')$ for the start node S is set to be zero. $P(\mathbf{x})$ is the prior probability for voxel $\mathbf{x}$ at the current time frame obtained from section 5.3. Figure 5.3 (b) shows an example profile of $P(\mathbf{x})$ and $|\ln(P(\mathbf{x}))|$ with $\sigma = 1$. As illustrated, the lower the probability $P(\mathbf{x})$, the higher the cost of including voxel $\mathbf{x}$ in the minimal cost path.

After adding a heuristic term $h(\mathbf{x})$, the whole cost function for assessing each candidate node $\mathbf{x}$ is defined as:

$$f(\mathbf{x}) = g(\mathbf{x}) + \delta h(\mathbf{x}) \tag{5.4}$$

For the centreline extraction from 4D CTA, δ is computed as the ratio of the minimum cost of the vessel to the Euclidean distance of the start and end nodes in the previous time frame. By using this heuristic term, the search space is greatly reduced and the minimum cost path can be found in real-time. When node E is reached and it also has lower value of f than any other candidates in the search queue, the minimum cost path is reconstructed by tracing backwards to node S. However, if node E is to be reached through a node with a higher value of f than other candidates in the search queue, the A* algorithm will then backtrack to find the optimal solution, rather than continue to make adjustments to approach a local minimum. This backtracking guarantees that the A* graph search algorithm finds the minimum cost path, unlike the ridge traversal algorithm that is unable to recover from the erroneous steps.

The graph-search based minimum cost path algorithm results in a discrete path consisting of an ordered set of discrete locations (voxels). After extraction of the path we estimate a B-spline representation of the centerline of the coronaries which smoothly interpolates these voxel locations. By repeating this process for all other time frames, the centrelines of RCA, LAD, and LCX are extracted from all phases of the 4D CTA sequence.

Here the coronary motion model is estimated via the minimal-cost path extractions from all time frames of the cardiac CTA sequence assisted by the prior information that is derived from the non-rigid image registration. The coronary centrelines are extracted as minimal-cost paths via A* graph search algorithm at end-diastolic phase. Patient-specific phase-specific prior information of the coronary location and shape is formed as in Section 5.3. Non-rigid registration based on B-spline free form deformation is used to capture the motion between two adjacent time frames from the CTA sequence. This derived deformation is used to transform the prior model from one time frame in order to predict the new position of coronary arteries for next time frame as in Section 5.3. By doing so, this registration-assisted minimal cost path algorithm results in extracted centrelines for all discrete time frames of the 4D CTA. Potentially a continuous motion model of coronary can be formed by interpolating these centrelines in the temporal domain.

5.5 Results and Evaluation

5.5.1 Coronary Artery Extraction

For evaluation, clinical 4D CTA data *SM4DCTA* and *RB4DCTA* were used in our experiments. The details of the four test sequences are provided in Table 4.1. The first test dataset (CT sequence I) has minor artefacts due to the reconstruction errors when rapid cardiac motion occurs. The parameters for this dataset are selected as: $a_1 = 1100$ and $a_2 = 1500$ for the intensity transformation function (Equation 5.1). We have also tested the algorithm on another data set (CT sequence II) which is characterized by more severe artefacts, in particular along the right coronary artery and the left circumflex artery. The parameters a_1 and a_2 are chosen as 1000 and 1450 respectively. For CT sequence III, $a_1 = 1150$ and $a_2 = 1550$. As for CT sequence IV, $a_1 = 1050$ and $a_2 = 1400$ are chosen. Parameter b is fixed as 0.1 for all data.

In all experiments, the parameters for graph search are fixed as $\kappa = 1, \eta = 1$. We set the paramters $\alpha = 0.5$, $\beta = 0.5$ whereas γ is chosen as the largest norm of the eigenvalues across the whole image for the vesselness computation in Equation 2.5. Here the choice of γ serves to rescale the vesselness response to an intensity range that can easily be visualised. The vesselness response is computed at five different scales, namely $\sigma = 0.5, 1, 2, 4, 8$mm. For detailed information on scale selection, we refer to [135, 134] by Lindeberg *et al.* The maximum response $\mathcal{V}$ of the vesselness filter at the corresponding optimal scale is computed for each voxel of the image via Equation 4.3. The calculated vesselness image is used to facilitate the coronary extraction and tracking.

For all data sets, prior coronary models were constructed for each frame to test the probabilistic approach. A heuristic is also used to reduce the searching time. At each time frame of the 4D CTA sequence, the centrelines of RCA, LAD and LCX are semi-automatically extracted using the graph search algorithm with a single pair of start and end nodes for each vessel branch as presented in Section 5.4.

Figure 5.5 and 5.6 show two examples of extracted coronary centrelines using A* graph search approach to extract the minimal cost paths from both a region with good contrast and no artefacts and a region with low contrast and stair-step artefacts. It can be observed that A* graph search method works robustly even when the image quality deteriorates.

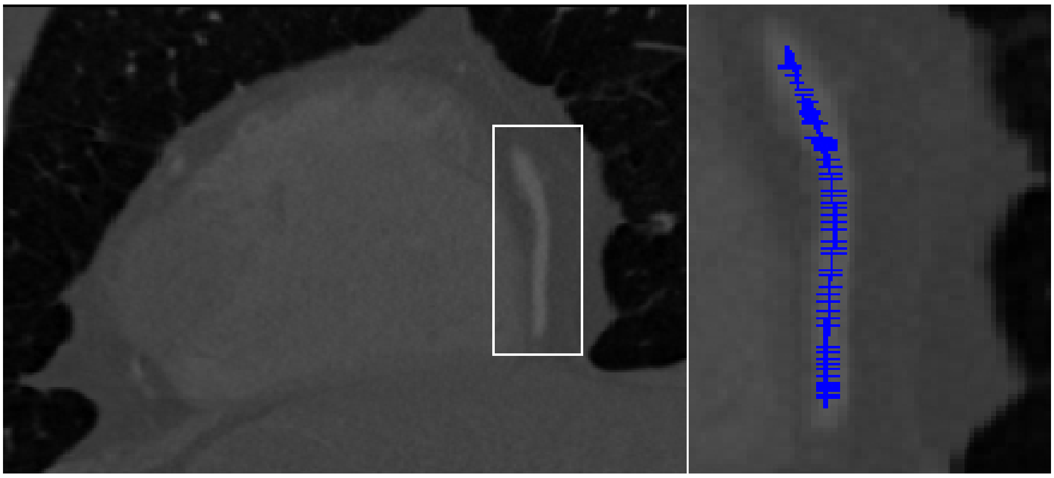

Figure 5.5: Good quality CTA image and extracted coronary artery centreline. Left: CTA slice with the rectangle marking the region of interest. Right: extracted coronary centreline marked with blue crosses from the CTA image on the left.

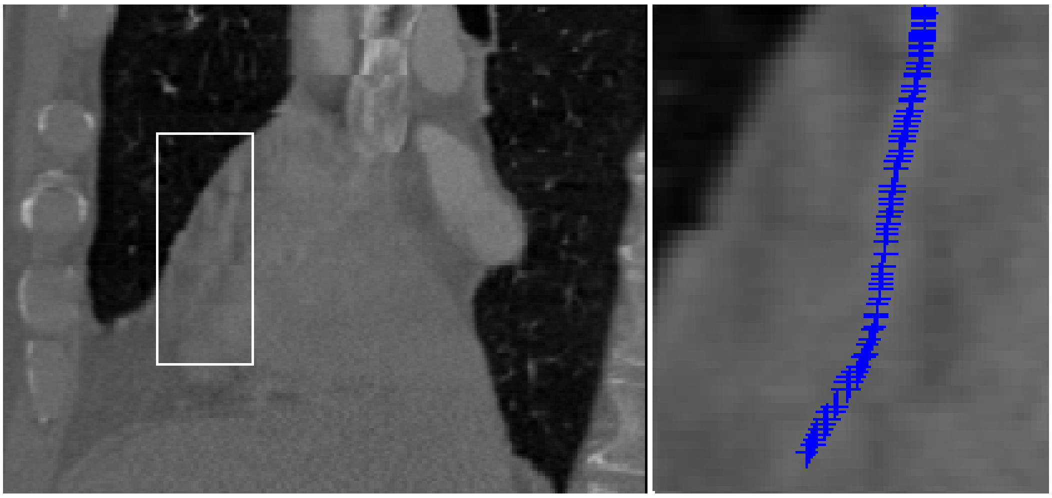

Figure 5.6: CTA image with stair-step artefacts and its extracted coronary artery centreline. Left: CTA slice with the rectangle marking the region of interest. Right: extracted coronary centreline from the region highlighted by the white box in the CTA image.

5.5.2 Evaluation of the Coronary Motion Model

By semi-automatically tracking the coronaries in each time frame in CTA sequences, the coronary motion can be estimated. As an example, the semi-automatically extracted coronary centrelines from one dynamic CTA sequence consisting of ten phases are shown in Figure 5.7.

Figure 5.7: Extracted coronary artery Centrelines from 4D CTA. The red lines denote the right coronary artery, the green lines for the left anterior descending and its branches, and the blue lines for the left circumflex artery and its branches.

We performed experiments on four CTA sequences using the proposed approach and evaluated the accuracy of the constructed motion model by assessing the error between the manual annotations and the tracked coronary centrelines. The distance measure defined in Equation 4.18 is used for this quantitative assessment, with U corresponding to the manual annotation and M to the semi-automatically tracked centreline at corresponding time frame. Figure 5.8 and Figure 5.9 show the motion tracking results by using this measurement.

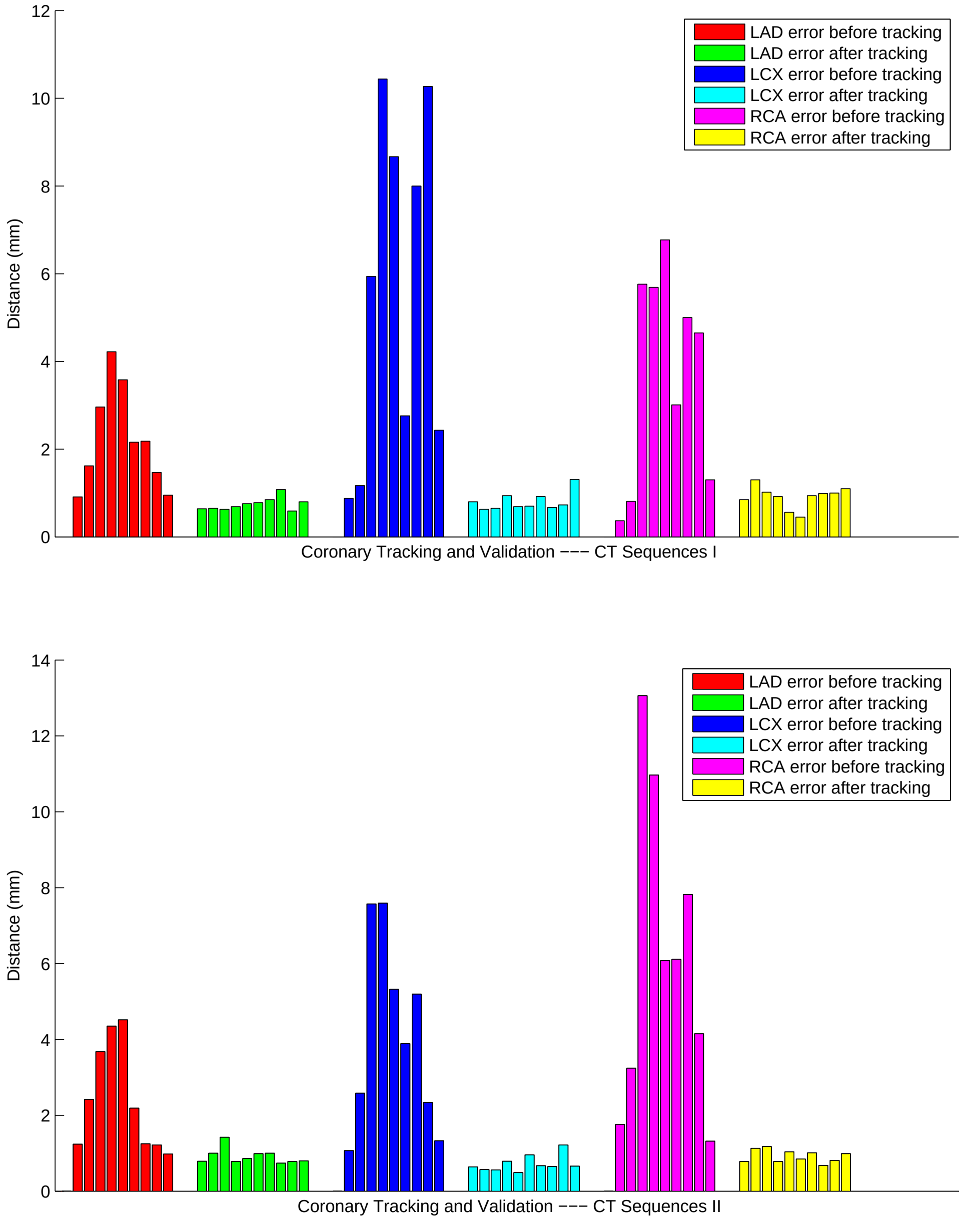

Figure 5.8: Graph-based coronary motion tracking and evaluation in CTA sequence I and II. The coronary displacement before tracking is measured as the distance between the semi-automatically extracted centerline at end-diastole of the cardiac cycle and all the other semi-automatic extractions in the remaining time frames. The error after tracking is calculated as the distance between the manual and semi-automatic extraction for each coronary artery in each of the ten frames.

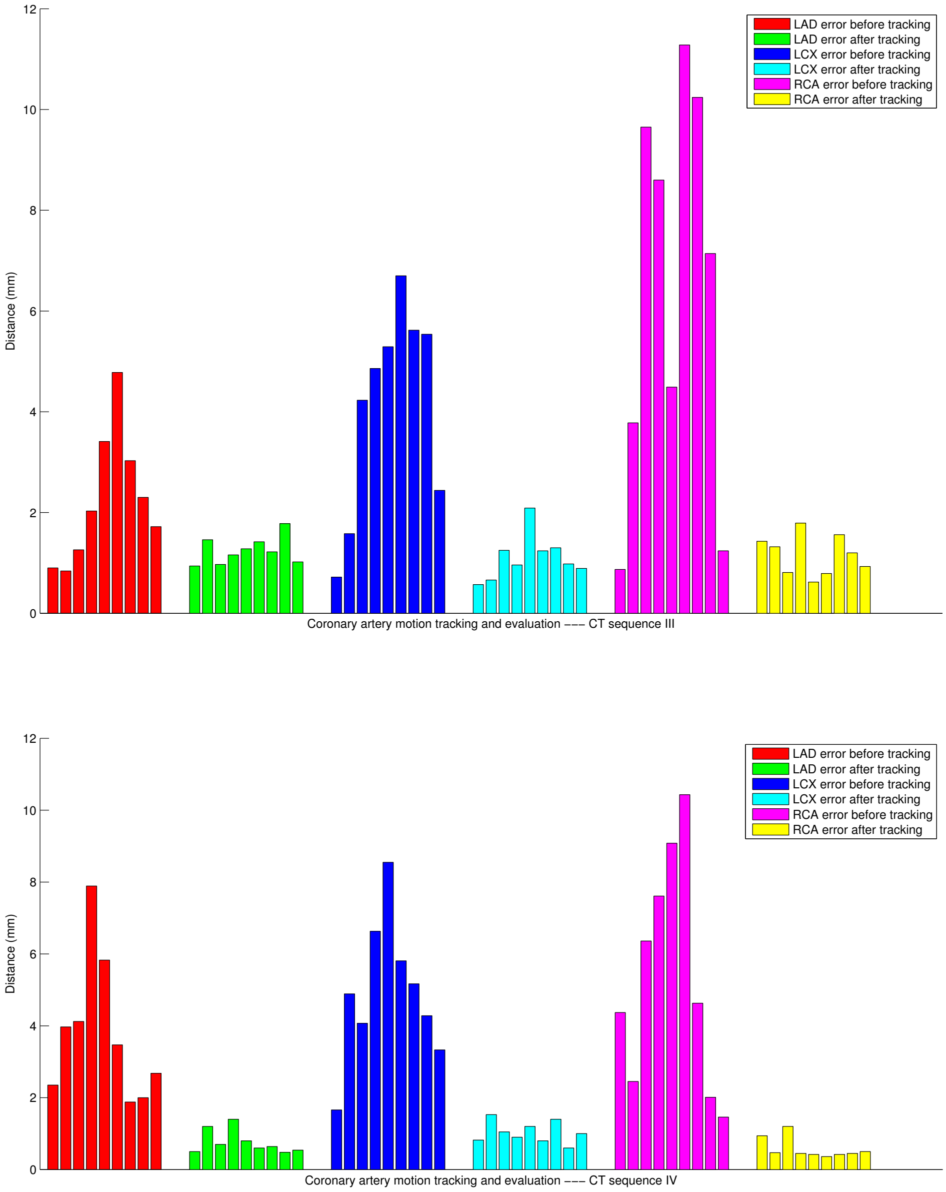

Figure 5.9: Graph-based coronary motion tracking and evaluation in CTA sequence III and IV. The coronary displacement before tracking is measured as the distance between the semi-automatically extracted centerline at end-diastole of the cardiac cycle and all the other semi-automatic extractions in the remaining time frames. The error after tracking is calculated as the distance between the manual and semi-automatic extraction for each coronary artery in each of the ten frames.

5.6 Summary

In this chapter, we have presented another approach for patient-specific coronary artery tracking and motion model construction from dynamic cardiac CTA images to assist totally endoscopic coronary artery bypass surgery. To summarise the proposed method, beginning from the end-disatolic phase, the following steps are repeated until coronaries are extracted in all time frames:

1. The coronary vessel centrelines are extracted as minimal cost paths via A* graph search algorithm at time frame t;
2. The prior probability of a voxel in time frame $t+1$ to be part of the coronaries is estimated as a Gaussian probability P_t distribution centred at the voxel locations of the coronaries in time frame t.
3. Non-rigid registration is performed to align image I_t and image I_{t+1} resulting in deformation field $\mathbf{T}_t$.
4. The coronary prior P_t created in step 2 for image I_{t+1} is deformed to $P_t^{'}$ according to $\mathbf{T}_t$ to increase its accuracy for prediction. The deformed prior $P_t^{'}$ is then used to assist the centreline extraction in I_{t+1} using A* graph search.

Finally, once the centrelines for RCA, LAD and LCX are obtained for all time frames in the 4D sequence, a coronary motion model can be formed.

In order to assess the quality of semi-automatic extraction results, the distance between the manual segmentations and semi-automatic extractions of the coronaries in each time frame is evaluated quantitatively. The proposed method has been tested on the clinical CTA datasets acquired from four subjects.

However, the A* graph search for vessel centreline extraction has one disadvantage: The choice of heuristic term is a delicate matter. When the value of $\delta h(\mathbf{x})$ is too high as opposed to the score $g(\mathbf{x})$, short cuts can occur in the resulting minimal cost paths. In this case, the extracted centreline deviates from the real centreline by taking a direct route from one voxel to another nonadjacent voxel as part of the vessel path, as illustrated in Figure 5.10. This especially hinders the centreline delineation of vessel segments with high curvature. However, if the heuristic term is chosen to be smaller than necessary, the search space gets larger. Hence, more nodes will be evaluated and the computational cost increases.

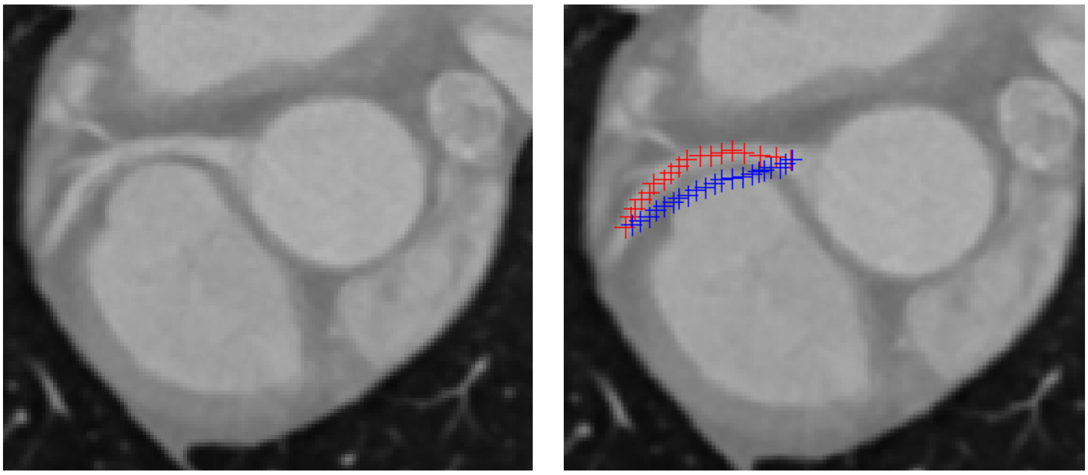

(a) (b)

Figure 5.10: An example of correct vessel centreline and a wrong centreline caused by short-cuts. (a): A CTA image region showing the left main artery and a short segment of its LAD branch; (b): The red crosses mark the true vessel centreline extracted using our proposed method, whereas the blue ones show the short cut in an extreme situation for illustration purpose.

Chapter 6

Template-based Coronary Motion Tracking

In contrast to the work in Chapter 4 and Chapter 5, this chapter presents template-based approaches for coronary artery motion modelling. The coronary motion modelling methods presented in the previous chapters rely on coronary segmentation strategies that utilise the intensity information of individual voxels without taking regional information into account. The accuracy of the segmented centreline points can be affected by the heterogeneous distribution of the contrast agent, the calcification within part of the vessel wall or the short-cut effect illustrated in Figure 5.10. In this chapter, two template based approaches are proposed to overcome these limitations, to improve the robustness of coronary motion modelling algorithms and also reduce the amount of user-interaction required. The proposed methods are:

- Coronary motion tracking using template matching and minimal cost path extraction via the A* graph search algorithm. For each vessel at the end-diastolic phase, a pair of start and end nodes are identified by the user and transformed to all the other phases. Template matching is used to refine the positions of the transformed start and end nodes at each phase. The coronary centrelines at those phases are then extracted as minimal cost paths from the start node to the end node.

- Coronary motion tracking by combining non-rigid registration and template matching into one framework to reduce user-interaction and improve the accuracy of the tracking. Coronary centrelines are first extracted as minimal cost paths in the end-diastolic phase and transformed to the rest of the time frames to provide a coarse prediction. At each time frame, the transformed centreline is subsampled and template matching is performed at every voxel in the subsampled centreline to refine the centre of the vessel. The refined centre points are then smoothly interpolated using B-splines to generate the final vessel centreline for each frame.

These two approaches are presented and evaluated in Section 6.5 and 6.6 respectively. Both methods are assessed against the non-rigid registration approach (similar to that in Section 4.4) in terms of tracking accuracy. Prior to that, this chapter is organised as follows:

1. Image pre-processing techniques used by both methods are presented in Section 6.1. The procedure of utilising these pre-processing techniques is listed in the end of Section 6.1.3.
2. As opposed to Section 5.4, we simplify the A* graph search to be performed without prior information in Section 6.2 because of the improvement of CTA image quality of the clinical data available for this part of the thesis.
3. A tubular-template model is adopted for the coronary extraction and tracking in Section 6.3. Additionally, as in Section 6.3.3, the coronary lumen can be segmented by combining the minimal cost path and template model matching together.

6.1 Image Pre-processing

6.1.1 Histogram Equalisation and Its Variations

Contrast enhancement essentially aims to design a lookup table or mapping function to allow the 1-to-1 intensity transform from an input image to an output image, with the aim of increasing the contrast in the output image. This mapping function can be either linear or non-linear. A well-known non-linear technique is histogram equalisation (HE) which is based on the assumption that a good grey-level assignment scheme should depend on the frequency distribution (histogram) of the image grey levels. As the number of voxels in a certain class of grey levels increases, a wider range of the available output grey levels should be assigned to this group of voxels. Consequently, the histogram of the resulting image is approximately flat which indicates an optimal distribution of the grey values. However, HE in its basic form can give a result that is less informative about the structures of interest than its original image, because of the following two reasons:

1. Large peaks in the original histogram can be caused by irrelevant structures (e.g. background noise). In this case, HE mainly amplifies the image noise.

2. The basic HE technique does not adapt to the local contrast requirements. Subtle contrast differences can be entirely missed when the number of voxels falling in a particular greylevel range is small, e.g., a small coronary vessel in large dark background region.

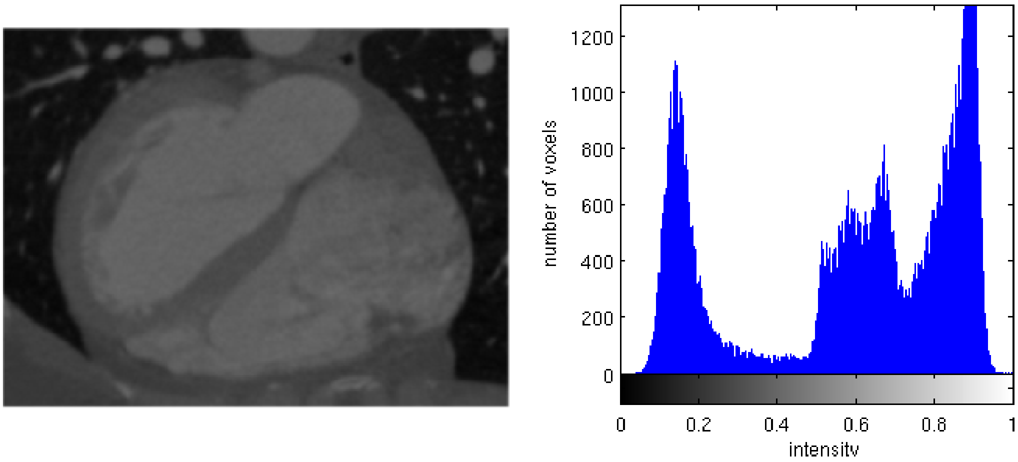

Figure 6.1: CTA image (left) and its histogram (right) before HE.

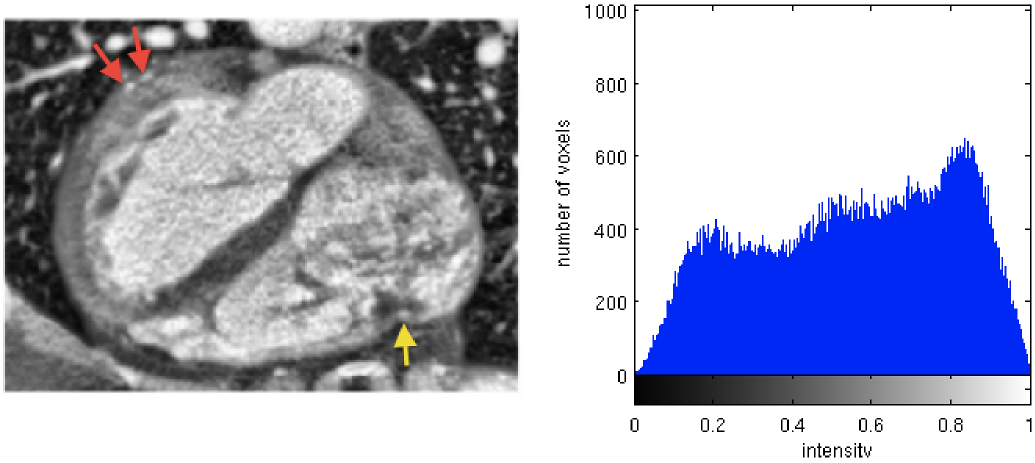

Figure 6.2: CTA image after CLAHE using $8 \times 8 \times 8$ contextual regions (left) and its histogram (right).

To overcome these limitations of HE, contrast limited adaptive histogram equalisation (CLAHE) has been proposed [260]. CLAHE operates on small regions in the image (referred to as tiles) rather than the entire image. Each tile's contrast is first enhanced. The neighbouring tiles are then combined using interpolation to eliminate artificially induced boundaries. The contrast, especially in homogeneous areas, is limited by a contrast factor to avoid amplifying any noise that might be present in the image. A slice from a 3D CTA image is shown before and after CLAHE with its corresponding histogram in Figure 6.1 and 6.2 respectively. As illustrated, vessel structures exhibit better visibility in Figure 6.2, e.g., at the cross-section of the right coronary artery marked by the yellow arrow and the cross-section of the left circumflex arteries pointed to by the red arrow.

6.1.2 Automatic Thresholding

Otsu *et al.* [174] proposed to automatically perform histogram shape-based image thresholding. The proposed method calculates the best threshold that separates an image into foreground and background components by minimising the intraclass variance or equivalently maximising the interclass variance.

Let an image I have N voxels with grey levels from 1 to L. The number of voxels with grey level l is denoted as f_l. The probability of grey level l in image I is $p_l = \dfrac{f_l}{N}$. In the case of separating the voxels of an image into two classes, the voxels are divided into class C_1 with grey levels $[1, ..., t]$ and class C_2 with grey levels $[t+1, ..., L]$. The grey level probability distributions for classes C_1 and C_2 are:

$$C_1 : \frac{p_1}{\omega_1(t)}, ..., \frac{p_t}{\omega_1(t)} \tag{6.1}$$

$$C_2 : \frac{p_{t+1}}{\omega_2(t)}, ..., \frac{p_L}{\omega_2(t)} \tag{6.2}$$

where $\omega_1(t) = \sum_{l=1}^{t} p_l$ and $\omega_2(t) = \sum_{l=t+1}^{L} p_l$. From this definition, we can derive for any threshold level t, $\omega_1 + \omega_2 = 1$. The mean intensity for classes C_1 and C_2 are given as:

$$\mu_1 = \sum_{l=1}^{t} \frac{l p_l}{\omega_1(t)} \tag{6.3}$$

$$\mu_2 = \sum_{l=t+1}^{L} \frac{l p_l}{\omega_2(t)} \tag{6.4}$$

The mean intensity μ_I for the whole image I can be calculated as:

$$\mu_I = \omega_1 \mu_1 + \omega_2 \mu_2 \tag{6.5}$$

The between-class variance σ_B^2 of the thresholded image I is formulated by Otsu *et al.* [174] as:

$$\sigma_B^2 = \omega_1(\mu_1 - \mu_I)^2 + \omega_2(\mu_2 - \mu_I)^2. \tag{6.6}$$

The optimal threshold value t^* is chosen so that the between-class variance σ_B^2 is maximised.

In our work, this two-class method is extended to multiple class thresholding for 4D CTA sequences. For multiple class thresholding of image I, we assume there are $K-1$ threshold values, $t_1, t_2, ..., t_{K-1}$. Using these thresholds, the image I can then be divided into K classes, C_1 for grey levels $[1, ..., t_1]$, C_2 for grey levels $[t_1+1, ..., t_2]$, ..., and C_K for $[t_{K-1}+1, ..., L]$. The between-class variance for the K classes is defined as:

$$\sigma_B^2 = \sum_{k=1}^{K} \omega_k (\mu_k - \mu_I)^2 \tag{6.7}$$

where ω_k is the sum of the probabilities of grey levels belonging to the k-th class, μ_k is the mean grey level of k-th class and μ_I is the mean intensity for the whole image I. The optimal thresholds $[t_1^*, t_2^*, ..., t_{K-1}^*]$ are then found by maximising the between-class variance σ_B^2 in Equation 6.7.

Similar to the original method [174], the extended method relies on a histogram of the image intensity. This makes the method applicable to an image with any dimensionality. Given the number of classes, the method exhaustively search for threshold values that maximise the inter-class variance.

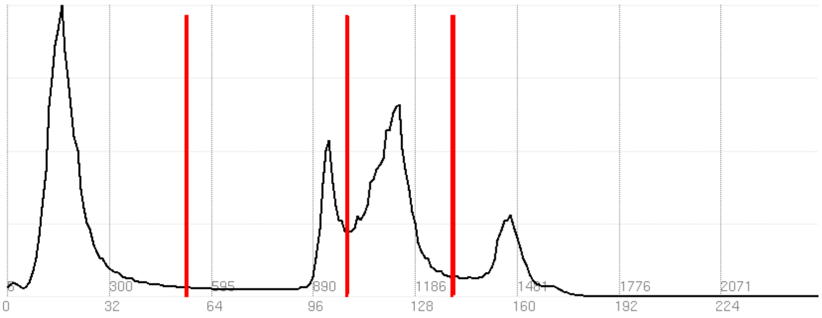

Figure 6.3: Histogram of a 4D CTA image sequence. The red bars show the optimal three thresholds.

Figure 6.3 shows the histogram of one 4D CTA sequence containing 20 phases, with the automatically obtained threshold values highlighted as red vertical bar to separate the classes. For two phases and three slices from each phase, the CTA image and the segmentations via thresholding are shown in Figure 6.4. The CTA image in this example is segmented into four classes.

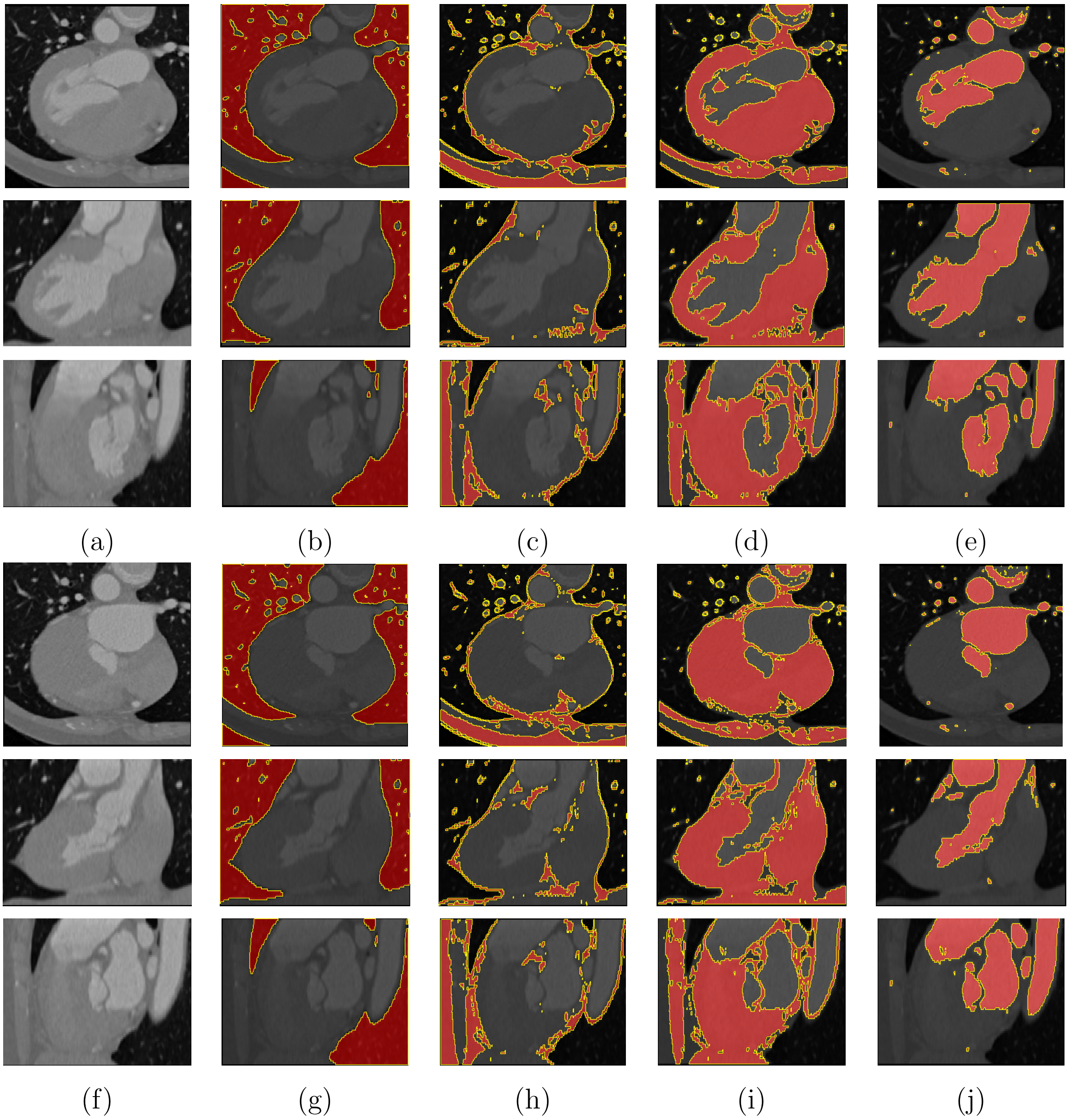

Figure 6.4: An example of segmentation via 4D thresholding. (a): a region of CTA image at one time frame from a 4D sequence shown in three views after contrast adjustment; (f): the same region of a CTA image at another time frame in three views after contrast adjustment; (b) and (g): Background; (c) and (h): Fatty deposit; (d) and (i): Tissue; (e) and (j): Blood and others. Each class is shown in red within the yellow isolines.

6.1.3 Vessel Enhancement by Anisotropic Diffusion

Prior to the coronary artery segmentation, vessel enhancing diffusion [146] is adopted to improve the visibility of the coronaries in CTA images. A detailed review on anisotropic diffusion filtering is given in Section 2.2.3. Figure 6.5 shows the effect of vessel enhancement diffusion on two regions of a CTA image. The images after diffusion display better smoothness along the vessels and exhibit less noise in the background region. In our experiments on clinical CTA, the parameters for the diffusion process have to be determined on a case-by-case basis, due to the large variation of image quality of the 4D CTA data sets.

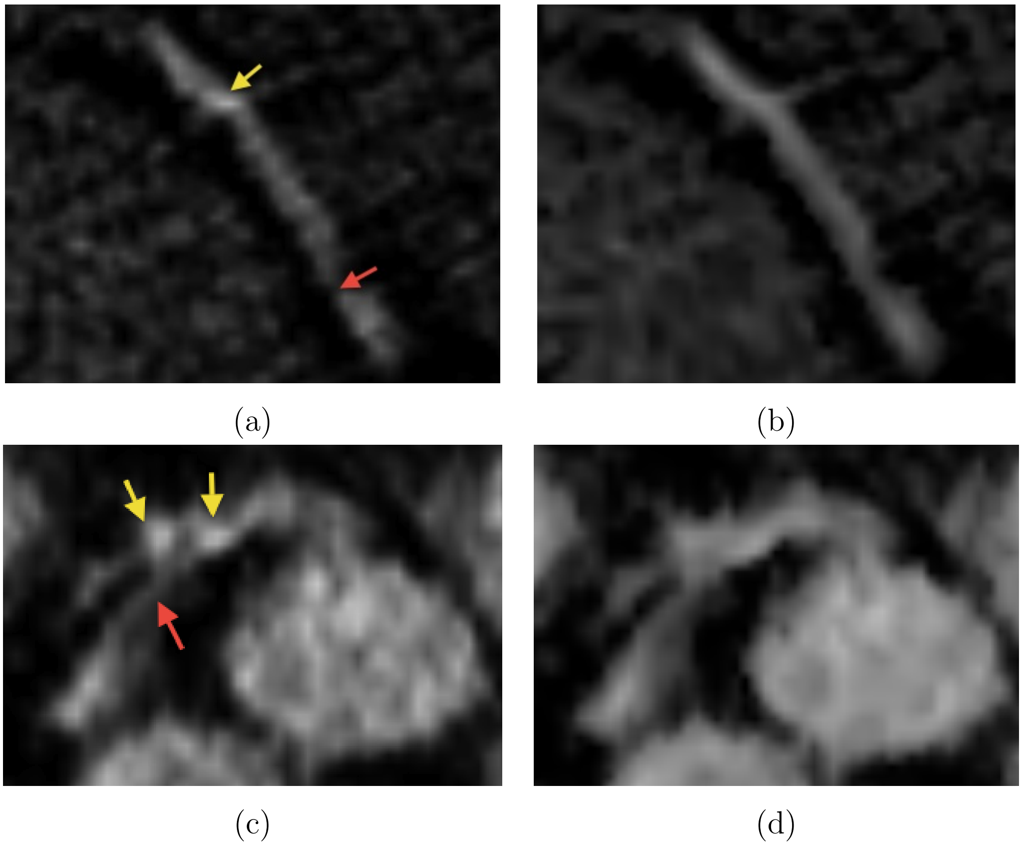

Figure 6.5: Examples of vessel enhancement diffusion. (a): A segment of the RCA in a CTA image after contrast adjustment; (b): The resulting image of (a) after vessel enhancement diffusion; (c): The left main coronary artery and LAD segments in CTA image after contrast adjustment; (d): The resulting image of (c) after diffusion. The yellow arrows point to calcifications. The red arrows point to narrowing in the arteries.

Before the coronary arteries are extracted, their visibility in the cardiac CTA image sequences is enhanced by performing contrast limited adaptive histogram equalization (Section 6.1.1). This improves the contrast and enhances the coronary arteries. Note that this step is carried out for the entire 4D image sequence so that intensities in all time frames are treated similarly and consistently.

Due to the ECG pulsing windows applied in the acquisition and reduced radiation dose [239], the signal-to-noise ratio is varying in multiple-phase 4D CTA data sets. To improve the image quality, 4D anisotropic diffusion (Section 6.1.3) is used to reduce this noise and preserve the boundaries of the cardiac chambers and vessel structures. After histogram equalization, we perform anisotropic diffusion [146] for the entire 4D image sequence so that neighbouring time frames influence the diffusion at the current time frame.

Furthermore, to reduce the effect of the presence of inhomogeneous background (e.g. air and tissue mixed region) or other irrelevant neighboring structures (e.g. bone or metal implant), four thresholds $[t_{\text{background}}, t_{\text{fat}}, t_{\text{tissue}}, t_{\text{blood}}]$ are selected automatically by the multi-level thresholding as in Section 6.1.2 for each 4D data set. The intensities of the background voxels ($< t_{\text{tissue}}$) are increased to t_{tissue} so that they match the average myocardial intensity level. Voxels with intensities above the upper threshold level ($> t_{\text{blood}}$) that represents bone structures are assigned average myocardium intensity value t_{tissue}. One pair of thresholds t_{tissue} and t_{blood} is used for each 4D sequence.

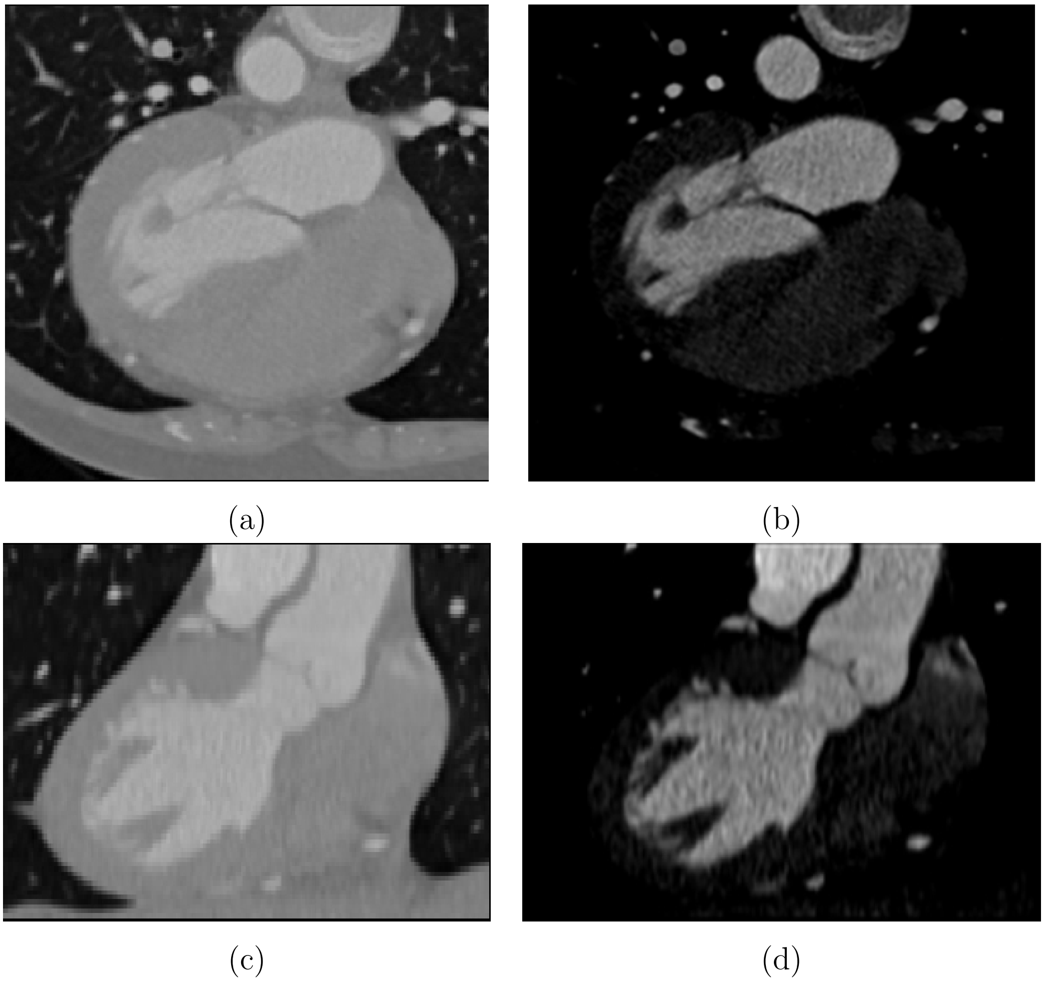
(a) (b) (c) (d)

Figure 6.6: Example of an CTA image before and after pre-processing. (a) and (c): The original CTA image after contrast adjustment. (b) and (d): The post-processed CTA images showing better visibility of the coronaries.

In summary, for each 4D CTA image sequence, the aforementioned three pre-processing procedures are performed to improve the visibility of the coronaries and also eliminate interference from other irrelevant structures for the template matching algorithm. Figure 6.6 shows an example of an original CTA image and its post-processed image from two views.

6.2 Coronary Centreline Extraction via A* Graph Search without Prior Information

The A* graph search approach with prior information in Chapter 5 was specially designed in the early stage of this thesis for extracting coronary centrelines on CTA images with severe artefacts. In the course of this PhD project, a new 4D CTA acquisition protocol [239] has improved the image quality substantially. In particular, two types of artefacts have been reduced: the low signal-to-noise ratio and the stair-step artefacts. Thus, the newly acquired data allows the use of A* graph search approach without using prior information.

In order to extract the minimal cost paths of the coronaries in CTA images using A* graph search, similar to Chapter 5 we first perform a coarse segmentation of the coronary arteries using a multi-scale Hessian-based vessel enhancement filter [72]. For a 3D image $I(\mathbf{x})$, the vesselness response $v_\sigma(\mathbf{x})$ is computed based on the eigenvalues and eigenvectors of the Hessian $\mathcal{H}_\sigma(\mathbf{x})$ at a given voxel $\mathbf{x}$ at scale σ. The vesselness response is computed at a range of scales. The maximum response $\mathcal{V}(\mathbf{x})$ of the vesselness filter with the corresponding optimal scale is obtained for each voxel of the image as in Section 4.2. Once the vesselness $\mathcal{V}(\mathbf{x})$ at each voxel is computed, it can be used to define a minimal cost path between the start and end nodes.

The minimal cost path between the start S and end node E is obtained using the A* graph search algorithm [87] in the CTA image. The locations of the pair of nodes S and E are specified interactively. A uni-directional graph search algorithm evaluates the smallest cost $g(\mathbf{x})$ from node S to current node $\mathbf{x}$ and the heuristic cost $h(\mathbf{x})$ from current node to node E to determine which voxel is to be selected as next path node. The search algorithm finds the optimal path only if the heuristic underestimates the true cost. The Euclidean distance from $\mathbf{x}$ to E is used to calculate the heuristic cost in this chapter. We assess each candidate node by calculating the whole cost $f(\mathbf{x})$ as:

$$f(\mathbf{x}) = g(\mathbf{x}') + \frac{1}{\mathcal{V}(\mathbf{x}) + \epsilon} + \delta h(\mathbf{x}). \tag{6.8}$$

where $\mathbf{x}'$ is the node preceding current node $\mathbf{x}$. To initialize the cost function, $g(\mathbf{x}')$ is set to be zero for the start node S. A small positive constant ϵ is added in order to avoid singularities. The parameter δ is estimated as the ratio of the minimum cost of the vessel to the Euclidean distance of the start and end nodes.

The heuristic term based on the Euclidean distance limits the search space and ensures that the minimum cost path can be found in real-time. When node E is reached, the minimum cost path is reconstructed by tracing backwards to node S which results in an ordered set of discrete voxels. A B-spline representation of the vessel centreline is created by smoothly interpolating these voxel locations.

6.3 Tubular Model for Template Matching

6.3.1 Tubular Model

A tubular model [76] is adopted to map a spatial coordinate $\mathbf{x}$ in $\mathbb{R}^n$ to the intensity range $[0, 1]$ through a template function $\mathcal{T}(\mathbf{x}; r, \mathbf{x}_0, \mathbf{v})$. The template function defines an ideal vessel segment centred at point $\mathbf{x}_0$ running in the direction $\mathbf{v}$ with radius r. The template is assumed to have a circular cross-section. A vessel profile is needed to model the image intensity variation in the cross-sectional plane perpendicular to the vessel direction. A Gaussian vessel profile has been used previously in the literature [119]. The Gaussian profile fits well when the images have been smoothed, but when detecting small vessels, large scale smoothing should be avoided in order to preserve the high frequency vessel structures. In this case, a steeper vessel profile is preferred as in [76]:

$$p(d^2; r) = \frac{r^\gamma}{(d^2)^{\gamma/2} + r^\gamma} \,, \tag{6.9}$$

where d is the minimum distance from $\mathbf{x}$ in the template to the central axis running in the direction of $\mathbf{v}$ through the centre point $\mathbf{x}_0$ as illustrated in Figure 6.7 (a) and shown as a 2D example in Figure 6.8 (a). Parameter γ controls the size of the template. In our experiments, we chose $\gamma = 8$. Parameter r is the radius of the tubular model as in template function $\mathcal{T}(\mathbf{x}; r, \mathbf{x}_0, \mathbf{v})$. Figure 6.7 (b) illustrates the vessel profile as the solid line as opposed to the Gaussian profile in dotted line.

The vessel template function is then defined as the composition of the profile function $p(d^2; r)$ and the distance function $d^2(\mathbf{x}; \mathbf{x}_0, \mathbf{v})$. After combining the two functions together, the template function is formulated as:

$$\mathcal{T}(\mathbf{x}; r, \mathbf{x}_0, \mathbf{v}) = \frac{r^\gamma}{\left(\|\mathbf{x} - \mathbf{x}_0\|^2 - [(\mathbf{v}^{\mathrm{T}})(\mathbf{x} - \mathbf{x}_0)]^2\right)^{\gamma/2} + r^\gamma} \tag{6.10}$$

An example of a 2D vessel template is shown in Figure 6.8 (b).

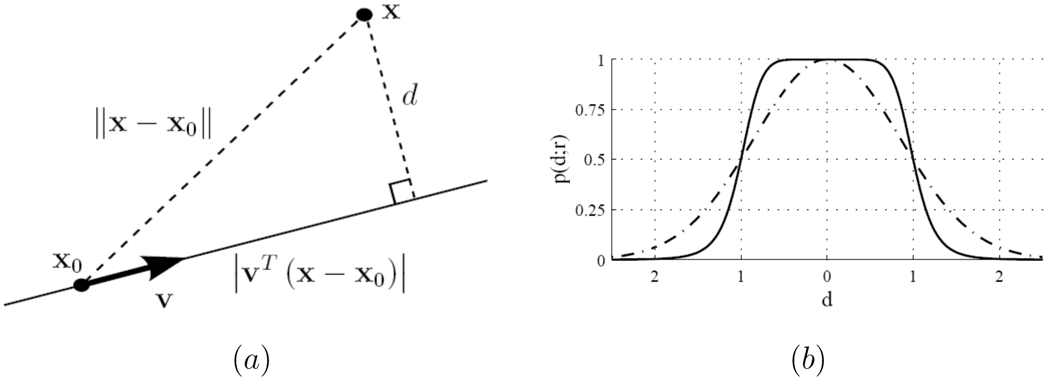

Figure 6.7: Distance function and vessel profile [76]. (a): Distance d from a point $\mathbf{x}$ to a straight line parameterized by the centre point $\mathbf{x}_0$ and direction $\mathbf{v}$; (b): Vessel profile $p(d^2; r)$ with $r = 1$ is shown as solid line, whereas an equivalent Gaussian profile is depicted by dash-dotted line.

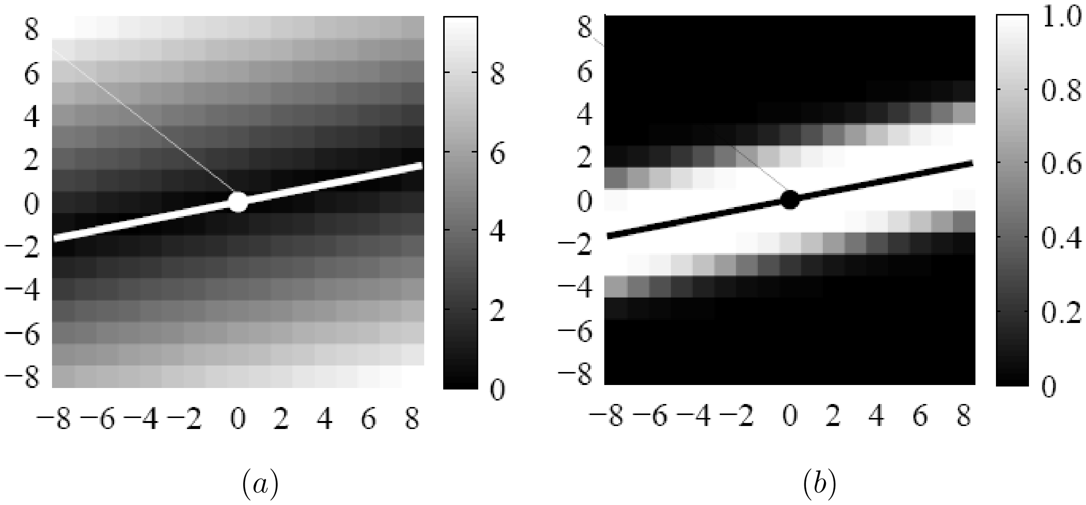

Figure 6.8: Example of a 2D vessel template [76]. (a): Distance to a straight line parameterized by a centre point $\mathbf{x}_0$ and direction $\mathbf{v}$. (b): The 2D template obtained by applying the vessel profile function parameterized by radius r to the distance function as defined in Equation 6.10, with size 17 × 17, intensity range [0, 1]. The black dot represents the centre, the bold line delineates the central axis of the vessel tube.

6.3.2 Template Fitting

Using this template model, the local image neighbourhood containing a vessel is modelled [76] as:

$$I(\mathbf{x}) = k\mathcal{T}(\mathbf{x}; r, \mathbf{x}_0, \mathbf{v}) + m + \epsilon(\mathbf{x}) \tag{6.11}$$

where $I(\mathbf{x})$ represents the intensity at voxel $\mathbf{x}$. Parameters k and m denote the vessel contrast and image background intensity respectively; $\epsilon(\mathbf{x})$ represents noise. The aim of the template fitting procedure essentially is to find the optimal values for the intensity parameters (k and m) and template parameters ($\mathbf{x}_0, \mathbf{v}$ and r) in order to achieve the maximal similarity between the local image region and the template model.

Given the image data $\mathbf{I}$, template values T for all the voxels $\mathbf{x}_i, i = 1, ..., n$ covered in the template region and a diagonal weighting matrix $\mathbf{W}$, the following weighted least squares problem is then formulated to solve for the parameters $r, \mathbf{x}_0, \mathbf{v}, k, m$:

$$\min_{r,\mathbf{x}_0,\mathbf{v},k,m} \|\mathbf{W}(r, \mathbf{x}_0, \mathbf{v})[k\mathsf{T}(r, \mathbf{x}_0, \mathbf{v}) + m - \mathbf{I}]\|^2 \tag{6.12}$$

where T is a $n \times 1$ matrix by stacking the intensity value of each voxel in the template $\mathcal{T}(\mathbf{x}_i; r, \mathbf{x}_0, \mathbf{v}), i = 1, ..., n$ together, and $\mathbf{I}$ is a $n \times 1$ matrix with corresponding intensity values from the image I at voxel locations $\mathbf{x}_i, i = 1, ..., n$.

This least-squares problem is linear for the intensity parameters (k, m) and nonlinear for the template parameters $(\mathbf{x}_0, \mathbf{v}, r)$. The problem can be solved iteratively: the linear parameters are estimated while keeping the nonlinear ones constant and vice versa. The nonlinear parameters are found by using the Levenberg-Marquardt optimisation [182], given an initial guess for the parameter values. Once the template is fitted to the local image region, its parameter r approximates the radius of the local vessel segment. Figure 6.9 and Figure 6.10 show two examples of fitting the template with the local image region of right coronary artery in pre-processed and post-processed CTA images.

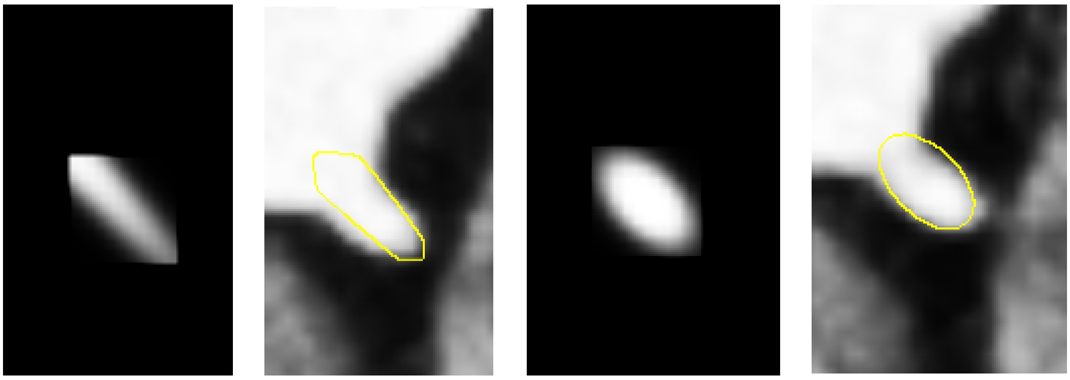

(a) (b) (c) (d)

Figure 6.9: Illustration of template estimation and fitting for a post-processed CTA image. (a) Initial estimation of the template and (b) its misalignment with the vessel segment. The template (a) is shown as the yellow contour in (b). (c) The fitted template after optimization and (d) its matching with the vessel segment.

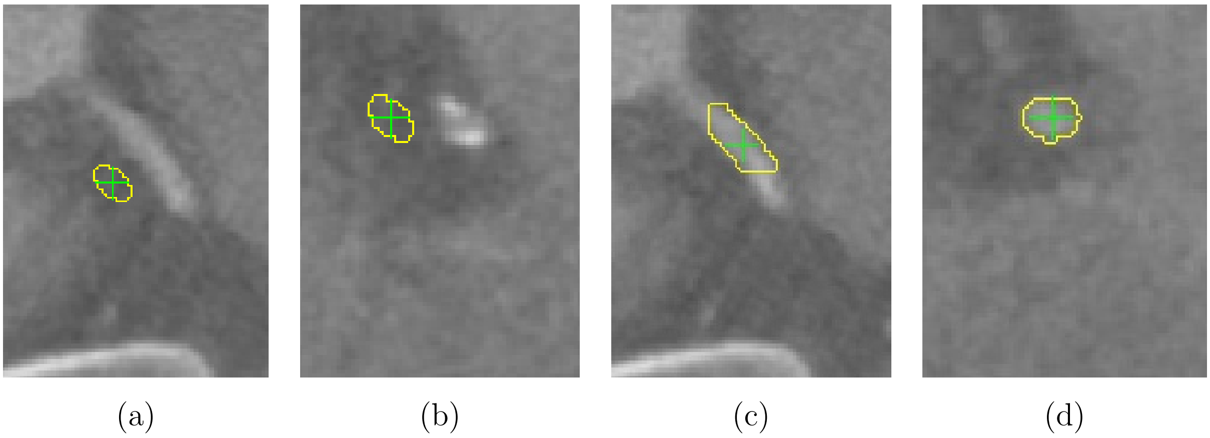

(a) (b) (c) (d)

Figure 6.10: Illustration of template estimation and fitting for an original CTA image. (a) and (b): Initial estimation of the template marked by the yellow contour with the green cross as the center and its misalignment with the vessel segment shown in two different views. (c) and (d): The fitted template shown as the yellow contour and centred at the green cross.

6.3.3 Coronary Lumen Segmentation Using Minimal Cost Path and Tubular Model

Given the coronary artery centreline $\mathcal{C}$ extracted as a minimal cost path via the A* graph search approach, the coronary lumen can be segmented by subsampling the centreline $\mathcal{C}$ to a set of discrete points $\mathbf{p}_{i,i=1,\ldots,N}$ on the vessel and performing template fitting at each point $\mathbf{p}_i$. At each location $\mathbf{p}_i$, the template fitting produces an updated vessel centre point $\mathbf{p}'_i$, a direction $\mathbf{v}_i$ and radius r_i. A vascular tube representing the coronary lumen is then generated by connecting the tubular segments through interpolating the radius r and centre points $\mathbf{p}'_i$. Figure 6.11 shows an example of this procedure.

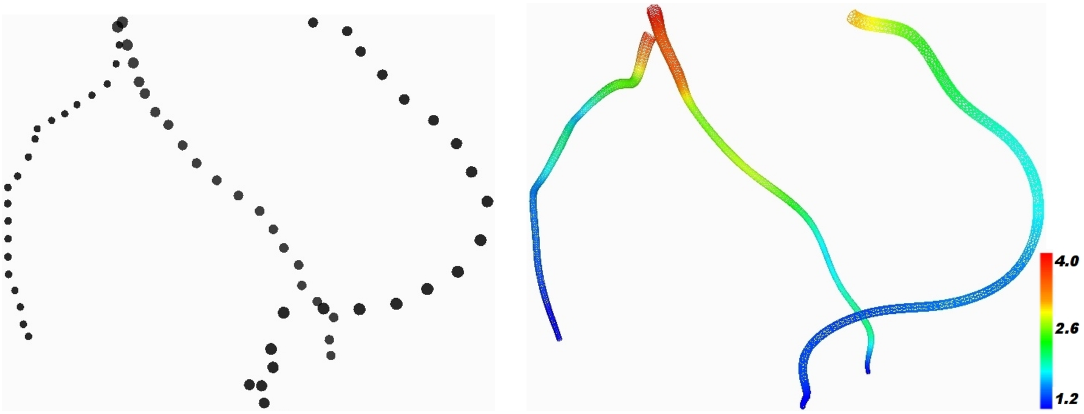

(a) (b)

Figure 6.11: Illustration of coronary lumen segmentation via template fitting. (a): Subsampled coronary centrelines. (b): Segmented coronary lumen. The radius information in mm is colour coded.

6.4 Coronary Motion Estimation Using Hierarchic Non-rigid Image Registration

In this section, we present a method for tracking the coronaries through estimating the cardiac motion, closely related to the method in Section 4.4. This method forms the basis for the two template-based approaches for coronary motion tracking in this chapter. The coronary motion model generated here is also quantitatively evaluated against the two template-based coronary motion tracking approaches we present later in Section 6.5 and Section 6.6.

The method here for tracking the coronaries temporally throughout the cardiac CTA sequence is based on a series of hierarchical non-rigid image registrations: The coronary motion is obtained by estimating cardiac motion via non-rigid image registration using a free-form deformation model based on cubic B-splines [193]. A series of registration steps is performed to register each time frame to the reference image at end-diastolic phase. For each frame we use the previous registration results as initial estimation as shown in the middle row of Figure 6.12. Different from the registration framework in Chapter 4 and 5, here each registration proceeds in a multi-resolution fashion, starting with a control point spacing of 40mm, progressing to 20mm, 10mm, and ending with a spacing of 5mm.

Prior to the acquisition of 4D coronary CTA images, a contrast agent is routinely injected into the patient's body for imaging the vessel. As the contrast agent flows within the vessels and gets diluted, the distribution of the contrast material becomes heterogeneous spatially and temporally. This causes variation in the intensity values of the vessels from one time frame to the other. In this case, an identity or linear relationship, as for metric $\mathcal{S}_{\mathrm{SSD}}$ (Equation 4.12) and $\mathcal{S}_{\mathrm{CC}}$ (Equation 4.13) respectively, cannot be assumed between intensities of two adjacent CTA images. However, the similarity between two CTA images can be be more accurately measured by entropy-based methods that take the information of the whole image into account. Here the non-rigid registration algorithm uses normalised mutual information [214] as the similarity measure between time frames. A gradient descent optimization is used to find the optimal transformation. The derived deformations from coarse level are used to initialize the finer level of registration.

The extracted coronary artery centrelines in the end-diastolic phase are mapped to the other cardiac phases by applying the finest deformation obtained from the registration step as illustrated in the bottom row of Figure 6.12. The derived centerlines are then compared with the segmented centerlines from minimal cost path approach at each time frame to measure the accuracy of the multi-resolution non-rigid registration based motion modelling.

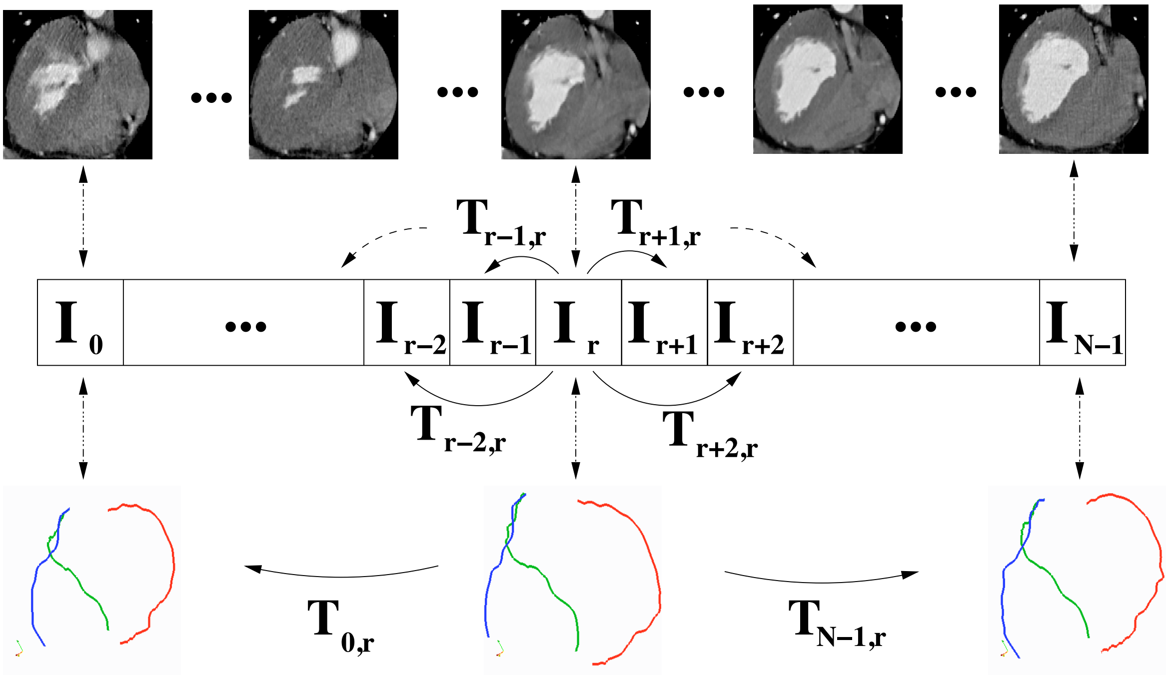

Figure 6.12: Illustration of coronary motion tracking using a non-rigid registration approach. The bottom row shows the extracted coronary centerlines from end-diastolic phase I_{r} (in the middle) and the transformed centerlines for I_0 and I_{N-1} in the left and right. Right coronary artery is shown in red, left anterior descending artery in green, left circumflex artery in blue.

6.5 Coronary Motion Tracking Using Graph Search and Template Matching

In this section, we propose an approach that is based on a template fitting and tracking algorithm which automatically identifies the start and end points of each vessel in every time frame. Once the start and end points have been identified, the vessel is extracted as the minimal cost path between both points. This newly proposed method simplifies the 4D motion modelling of coronaries significantly. After performing tests on clinical 4D CTA data, the results of this proposed approach are quantitatively compared to those from two other methods:

1. Manual motion tracking of the coronaries by extracting the coronary centrelines in all time frames using the graph search algorithm without prior information as in Section 6.2. The start and end nodes are manually identified for the coronary centreline extraction in all CTA images.

2. A hierarchic non-rigid registration based approach as presented in Section 6.4.

6.5.1 Methodology

We first use the 4D contrast limited adaptive histogram equalization to improve the image contrast for each CTA sequence (Section 6.1.1), followed by 4D vessel enhancement anisotropic diffusion to reduce the noise and enhance the vessel structures (Section 6.1.3). Lastly, for the template matching algorithm, the minimum and maximum thresholds are selected automatically by 4D multi-level thresholding (Section 6.1.2).

Using the Euclidean distance as the heuristic term, A* graph search is performed at each phase in each dataset to extract the coronaries, based on user-supplied start and end points for each vessel as in Section 6.2. The extracted centrelines form the manual motion model of the coronaries. We then estimate the coronary motion automatically using the hierarchical non-rigid registration of the CTA sequence (Section 6.4). By transforming the end-diastolic coronary centrelines to the rest of the time frames according to the resulting deformation information, a coronary motion model is generated based on the non-rigid registration of CTA images. Last, but most importantly, we propose a new coronary motion tracking approach combining graph search and template matching. Given a pair of start and end nodes in end-diastolic, both nodes are transformed to all other time frames according to the deformation information obtained in Section 6.4 to predict the locations of start and end nodes at those time frames. Template estimation and fitting is used to refine the predicted start and end points of the coronaries. Combined with the graph search, this enables the automatic identification of seed points in each vessel and also enables the utilisation of the accurate extraction of vessel paths based on a minimal cost graph search approach. We then compare this template-based approach with the non-rigid registration one (Section 6.4) by performing a non-parametric Kruskal-Wallis test [121].

The new approach for tracking the coronaries temporally throughout the cardiac CTA sequence is based on template localization and fitting. A tubular segment model as presented in Section 6.3 is utilised here for this purpose.

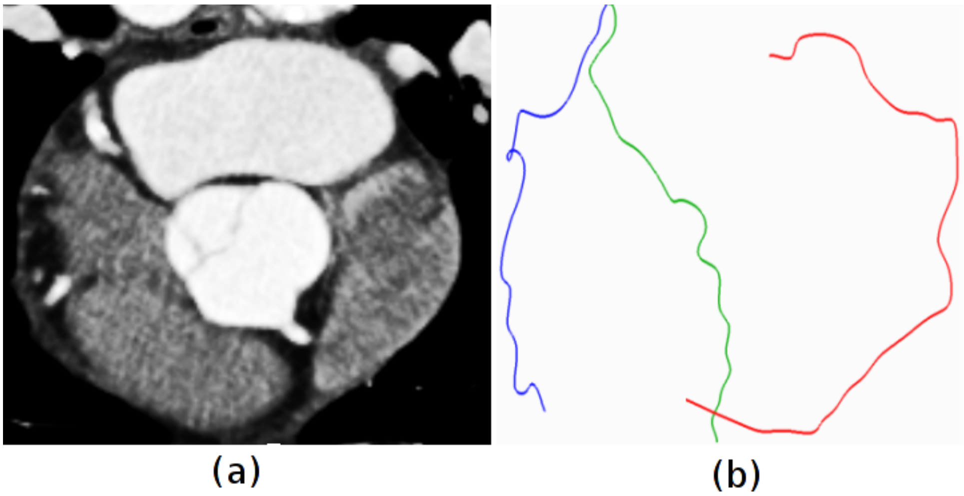

Figure 6.13: Post-processed CTA image and its extracted coronary centrelines. (a): Post-processed end-diastolic image; (b): Its extracted coronary centerlines. The right coronary artery is shown in red, the left anterior descending artery in green, and the left circumflex artery in blue.

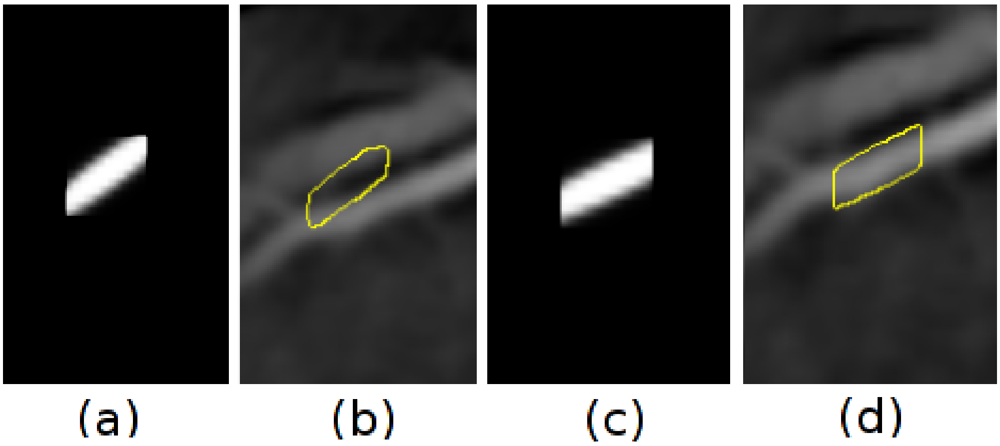

Figure 6.14: Illustration of template estimation and fitting. (a) Initial estimation of the template and (b) its mismatch with the vessel segment. The template (a) is shown as yellow contour; (c) fitted template after optimization and (d) its match with the vessel segment.

Given the coronary centrelines extracted in the end-diastolic time frame as shown in Figure 6.13, the start and end points are selected from each vessel centerline as the estimated locations of the centers of the vessel templates. For each of the start and end points, the optimal vessel template together with its refined centre location, the corresponding local contrast and local mean intensity parameters are obtained by solving the weighted least squared problem using Levenberg-Marquardt algorithm [77] in the end-diastolic time frame. We then transform the center location $\mathbf{x}_0$ of each template to its new estimated position $\mathbf{x}_0'$ in the adjacent time frame by using the deformation information obtained in Section 6.4. The direction and radius estimates for each template at the previous time frame are used to initialize the corresponding template at current time frame. The template parameters are optimized again using Levenberg-Marquardt optimization. After this the minimal cost path for this time frame is determined between the updated template locations. This procedure is repeated in a pair-wise fashion until the centerlines in all time frames are obtained. We then quantitatively measure the accuracy of these centerlines against the manual tracking results and their difference from the motion model created from Section 6.4.

To illustrate the procedure, a post-processed image is shown in Figure 6.13, together with the extracted coronary arteries at the end-diastolic phase for this data set. Start point $\mathrm{S_r}$ and end point $\mathrm{E_r}$ are selected from the right coronary artery in the end-diastolic reference image I_{r}. Templates are then constructed at these two points to fit with the vessel segments in image I_{r} which results in an updated pair of template centres. The new pair of template centres created from points $\mathrm{S_r}$ and $\mathrm{E_r}$ are then transformed to next time frame $I_{\mathrm{r+1}}$ in order to construct the initial templates. Then they are fitted to the local region of the image $I_{\mathrm{r+1}}$. For illustration, Figure 6.14 shows the distal of the right coronary artery in image $I_{\mathrm{r+1}}$. It also shows the initial template position and the template position after matching with the local image region.

6.5.2 Results and Evaluation

To assess the performance of the two motion modelling strategies we have performed experiments on five 4D cardiac CTA sequences denoted as $EMC4DCTA_1$. The 4D CTA images were acquired using Somatom Sensation 64 and Definition CT scanners in Erasmus MC, University Medical Center Rotterdam, The Netherlands. The protocol for acquiring the 4D data sets $EMC4DCTA_1$ is published in [239]. For each sequence, 20 phases are reconstructed for the cardiac cycle according to the recorded ECG signals. The five CTA image sequences have various image dimensions ranging from 256 × 256 × 89 voxels to 256 × 256 × 188 voxels. Three datasets have voxel dimensions of 0.7 × 0.7 × 0.8 mm^3. The other two datasets have voxel dimensions of 0.64 × 0.64 × 1.5 mm^3. All datasets have various degrees of mild artifacts that affect the segmentation and registration procedure. In particular the fast motion of the heart in some time frames can lead to blurring or ghosting artifacts, e.g., a ghosting artery occurs along the actual right coronary artery in Figure 6.14 (b).

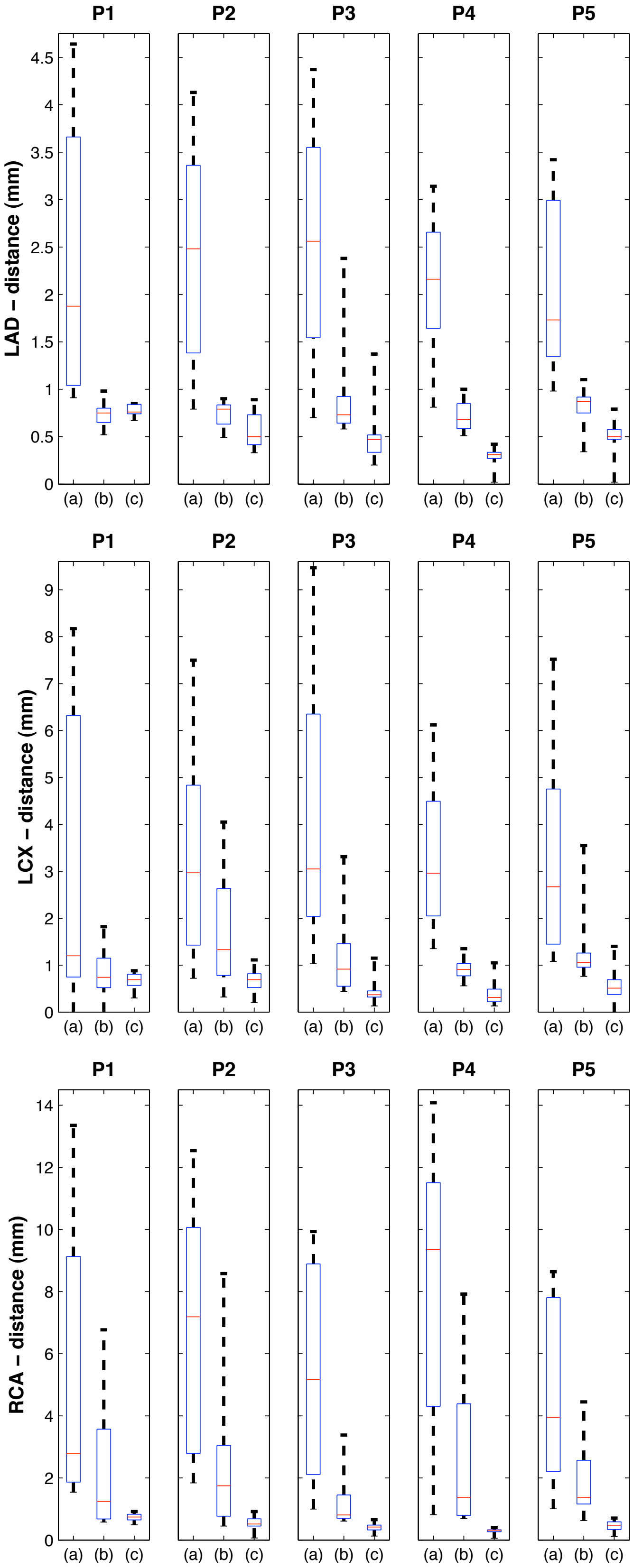

Figure 6.15: The total coronary displacement (LAD, LCX, RCA) is shown in column (a). The residual coronary displacement after non-rigid registration is shown in column (b) and after template-based tracking is shown in column (c). The results show that the template-based tracking is able to model the coronary motion best.

In order to have a gold standard to evaluate the two different motion modelling approaches, the left anterior descending artery (LAD), left circumflex artery (LCX) and right coronary artery (RCA) are extracted as minimal cost paths using the A* graph search algorithm without prior information from five CTA sequences, P1, P2, P3, P4, and P5. In all five patients, the start and end points of the vessels have been identified manually and the results of the minimal cost path extraction has been judged as correct by two obervers. The results of this are compared with the motion estimates of the LAD, LCX and RCA as provided by the non-rigid registration approach from Section 6.4 and template matching based approach as in Section 6.5.1. To measure the agreement between the gold standard and the motion tracking approaches, the distance measure formulated in Equation 4.18 is used to quantify the coronary motion tracking errors. The results are shown in Figure 6.15. The initial displacement of each coronary artery is computed as the distance between the centerline at end-diastole phase and the centerline at each other phase and is shown in the first column (a). The second column (b) shows the tracking error using the non-rigid registration based approach. It is measured as the distance between centrelines estimated via non-rigid registration and the gold standard for each phase. The third column (c) shows the tracking error using the template matching approach. Again, it is measured as the distance between centerlines estimated via template fitting and the gold standard for each phase.

To measure whether the errors are significantly reduced using the template fitting method compared to the non-rigid registration method, a non-parametric Kruskal-Wallis test is performed to compare the errors obtained for each vessel and for each subject using these two methods. The results of this analysis is shown in Table 6.1 . We consider that the errors are significantly smaller using template-based approach when p-value of the test is below 0.05. From Figure 6.15 and Table 6.1, we can conclude that the proposed graph search and template fitting approach outperformed the non-rigid registration-based approach in terms of accuracy, while the latter only compensate for part of the deformation.

Table 6.1: P-values of Kruskal Wallis test on the errors

	P1	P2	P3	P4	P5
LAD	0.44	0.0093	1.7e-06	1.2e-07	0.0018
LCX	0.43	0.0015	1.2e-04	1.4e-06	1.7e-05
RCA	0.049	2.6e-05	2.1e-07	6.2e-07	1.8e-07

6.6 Coronary Motion Tracking Using Non-rigid Registration and Template Matching

Prior to the coronary extraction and motion tracking, pre-processing is performed for each 4D CTA sequence using the same methods as in Section 6.5.1. Through combining the non-rigid registration and template matching techniques together, the proposed coronary motion tracking approach here consists of three steps:

- Firstly, the coronary arteries are extracted in the end-diastolic time frame using a minimal cost path approach. To achieve this, the start and end points of the coronaries are identified interactively and the minimal cost path between the start and end points is computed using A* graph search algorithm.
- Secondly, the cardiac motion is estimated throughout the cardiac cycle by using a non-rigid image registration technique based on a free-form B-spline transformation model and maximization of normalized mutual information (Section 6.4).
- Finally, coronary arteries are tracked automatically through all other phases of the cardiac cycle. This is estimated by deforming the extracted coronaries at end-diastole to all other time frames according the motion field acquired in second step. The estimated coronary centerlines are then refined by template matching algorithm to improve the accuracy.

As in Section 6.5, here we also compare the proposed approach with two alternative approaches: The first approach is based on the minimal cost path extraction of the coronaries with start and end points manually identified in each time frame while the second approach is based on propagating the extracted coronaries from the end-diastolic time frame to other time frames using image-based non-rigid registration only.

6.6.1 Coronary Motion Tracking Using Non-rigid Registration and Template Fitting

Combined with the deformation information obtained via the non-rigid registration as shown in Figure 6.12, the method here refines the tracking of the coronaries throughout the cardiac CTA sequence based on template localization and fitting. A tubular segment model [77, 76] is adopted for this purpose (Section 6.3.3).

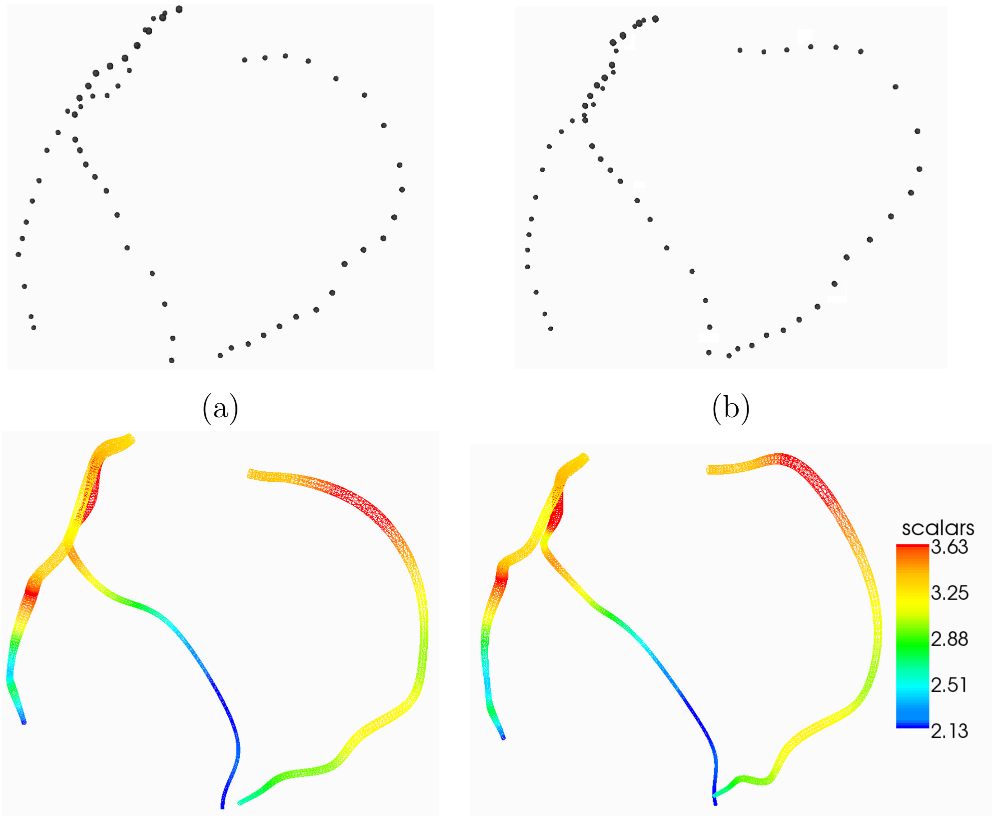

(a) (b)

(c) (d)

Figure 6.16: Combination of non-rigid deformation and template matching. (b) shows the resampled coronary branches extracted at end-disatole. (d) shows the vessel lumen by chaining the fitted templates together at end-diastole. (a) shows estimation for the coronary at end-systole. (c) is coronary artery lumen obtained by fitting the templates with corresponding local region in end-systolic CTA image. The varying radii (mm) are represented by different colors as in the legend.

First, an equidistant sample of vessel points from each extracted coronary centerline via A* graph search without using prior information in Section 6.2 at end-diastolic phase is chosen for refining the coronary segmentation as shown in Figure 6.16 (b). Each point from these samples is used as the initial center for the template fitting procedure. For each point, the optimal vessel template together with the corresponding local contrast and local mean intensity parameters are obtained by solving the weighted least squared problem using Levenberg-Marquardt algorithm [76] in the end-diastolic time frame. This yields a more detailed coronary segmentation with center location, radius, local contrast and mean intensity parameters for each template. By chaining these templates together, we obtain the coronary lumen at end-diastole as shown in Figure 6.16 (d).

Given the coronary centrelines extracted in the end-diastolic time frame as shown in the middle bottom of Figure 6.12, we can estimate the coronary centerline positions for other time frames by using the B-spline based free-form deformation information obtained using the same approach as in Section 6.4 to transform the end-diastolic extractions. An equidistant sample of vessel points are chosen from each vessel centerline at each non-end diastolic phase as the estimated locations of the centers of the vessel templates. The template fitting algorithm is performed on all these vessel points to provide an accurate match of the template with the local region. To achieve this, the template parameters are optimized again using Levenberg-Marquardt optimization. After this, the new discrete center points and their corresponding radii for each vessel are interpolated using B-spline. The coronary lumen is represented with a tubular mesh. This procedure is repeated in pair-wise fashion until the coronary lumen in all time frames is obtained. We then quantitatively measure the accuracy of these coronary lumen centerlines by assuming the minimal cost centerlines obtained via A* graph search as "ground truth". We also compare their difference from the estimated centerlines using only non-rigid registration method as in Section 6.4.

To illustrate the procedure, segmented coronary lumen from two phases are shown in Figure 6.16, together with the resampled minimal cost paths which are used as initialization for template matching. For illustration, in Figure 6.17, a right coronary artery segment is randomly chosen from one image. It shows template matching improves the accuracy of the estimated centerlines.

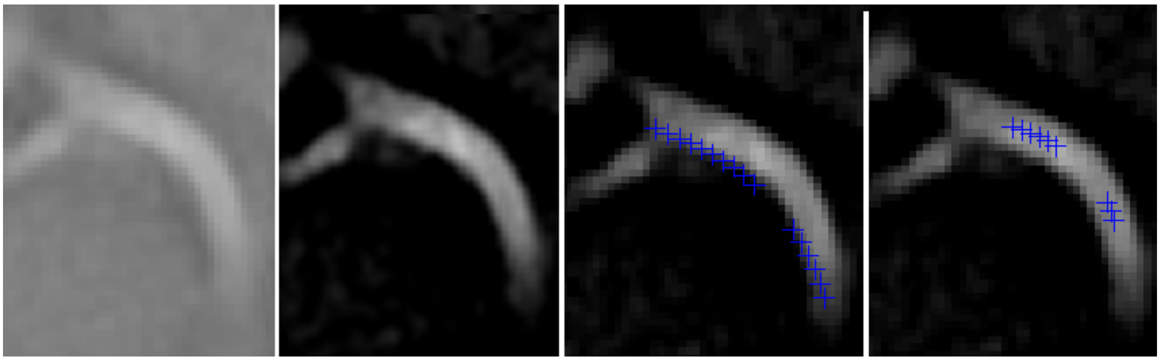

Figure 6.17: Illustration of template position estimation and fitting. (a): A small region of CTA image containing right coronary artery. (b): After pre-processing. (c): The estimated right coronary artery position using non-rigid registration. Blue cross shows the estimated vessel centerlines. (d): The vessel centerlines after template fitting. The discontinuity of the centreline appears because only one slice is shown in the 2D representation.

6.6.2 Results and Evaluation

To assess the performance of the proposed motion tracking strategy we have performed experiments on eight cardiac CTA sequences. We denote these eight datasets as *EMC4DCTA*$_2$. Same as for dataset *EMC4DCTA*$_1$, they are also acquired using the same protocol from the Somatom Sensation 64 and Definition CT scanners in Erasmus

MC, University Medical Center Rotterdam, The Netherlands. Each CTA sequence has twenty phases with various image dimensions ranging from 256 × 256 × 89 to 512 × 512 × 335 voxels. The voxel dimensions varies from 0.4 × 0.4 × 0.5 mm^3 to 0.7 × 0.7 × 1.5 mm^3. All datasets have varying image quality throughout the cardiac cycle, mild stair-step due to reconstruction error, and ghosting artefacts occurring due to the rapid cardiac motion which affect the segmentation and registration procedure.

In order to have a gold standard to evaluate the two different motion modelling approaches, the LAD, LCX and RCA are extracted using the graph search algorithm (Section 6.2) from eight CTA sequences (P1, P2, P3, P4, P5, P6, P7 and P8). In all eight patients, the start and end points of the vessels have been identified manually and the results of the minimal cost path extraction have been judged as correctly falling inside the vessel lumen. However, the accuracy of these extractions are restricted by the shortcut effect as shown in [129]. The results are compared with motion estimates of the LAD, LCX and RCA as obtained using the non-rigid registration and template matching based approaches. Quantitative analysis is performed using measure defined in Equation 4.18.

The evaluation results are shown in Figure 6.18. The total displacement of each coronary artery shown in the first column (a) is computed as the distance between the minimal cost centerline at end-diastole phase and the minimal cost centerline at each other phase. The second column (b) shows the tracking error from purely non-rigid registration based approach. It is measured as the distance between centrelines estimated via non-rigid registration and the gold standard for each phase. The third column (c) shows the tracking error using the registration and template matching combined approach. It is measured as the distance between centrelines estimated via the proposed method and the gold standard for each phase.

We compare the accuracy of the non-rigid registration based tracking method with the proposed approach in Table 6.2. The average motion is calculated as the average of the total displacements of each coronary artery for each patient. The row "Mean error 1" shows the average residual motion for the non-rigid registration based tracking method. The row "Mean error 2" shows the average residual motion for the non-rigid registration and template-matching based approach.

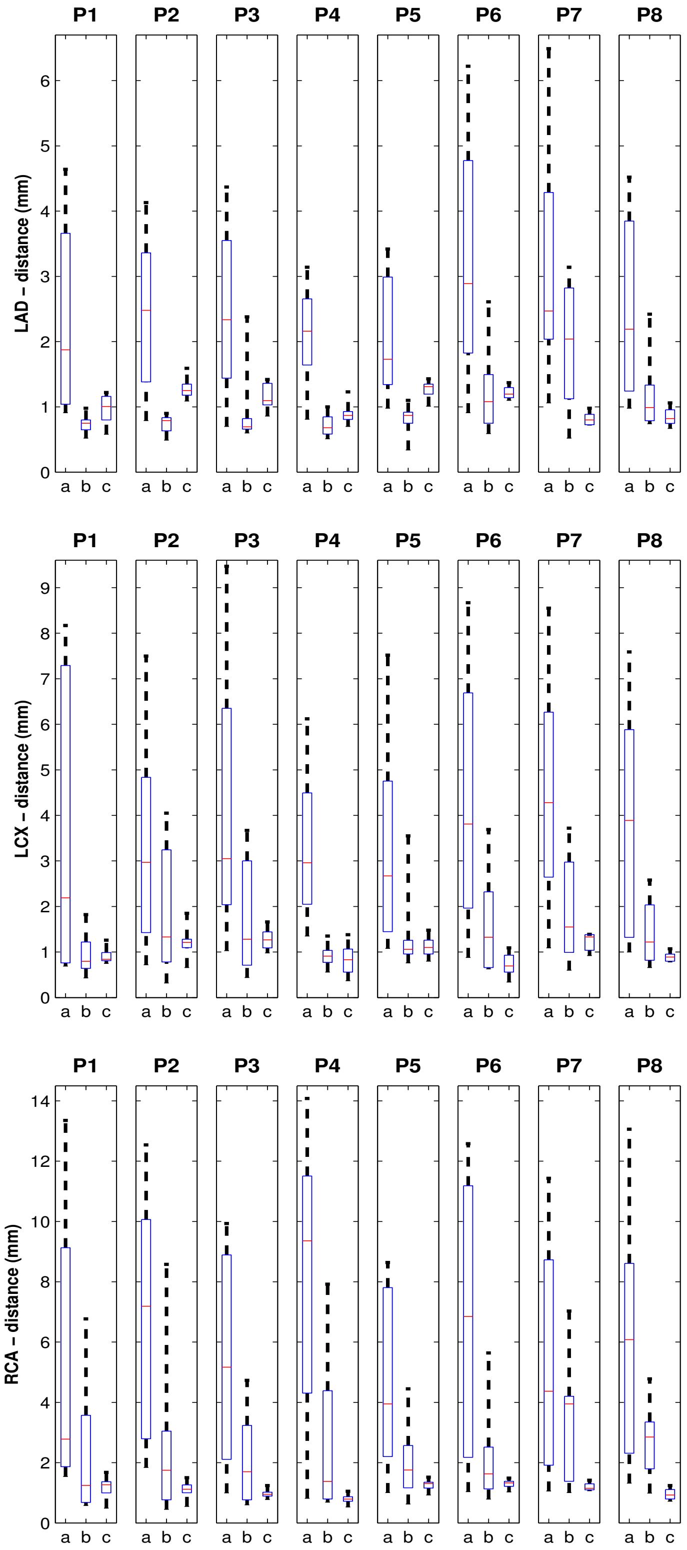

Figure 6.18: Comparison of coronary motion tracking results. The total coronary displacement (LAD, LCX, RCA) is shown in column (a). The residual coronary displacement after non-rigid registration is shown in column (b) and after the combined registration and template-based tracking is shown in column (c). The results show that the proposed tracking method is able to model the coronary motion with acceptable errors (under 2 voxels) and in most cases it performed better.

Table 6.2: Average coronary motion and mean errors of motion tracking

LAD

	P1	P2	P3	P4	P5	P6	P7	P8
Average Motion (mm)	2.39	2.40	2.53	2.12	2.06	3.26	3.29	2.43
Mean error 1 (mm)	0.74	0.73	0.90	0.72	0.79	1.23	2.01	1.15
Mean error 2 (mm)	0.97	1.27	1.14	0.90	1.27	1.21	0.81	0.84

LCX

	P1	P2	P3	P4	P5	P6	P7	P8
Average Motion (mm)	3.41	3.23	4.42	3.28	3.10	4.31	4.47	3.92
Mean error 1 (mm)	0.92	1.81	1.77	0.90	1.31	1.61	1.89	1.45
Mean error 2 (mm)	0.90	1.19	1.28	0.84	1.12	0.72	1.21	0.89

RCA

	P1	P2	P3	P4	P5	P6	P7	P8
Average Motion (mm)	5.53	6.83	5.33	8.14	4.89	6.62	5.44	5.96
Mean error 1 (mm)	2.35	2.62	2.19	2.83	1.90	2.27	3.23	2.68
Mean error 2 (mm)	1.19	1.10	0.95	0.79	1.26	1.29	1.19	0.94

We also consider that the motion tracking is successful when the distance between modeled coronary and the minimal cost path is under 1.4mm which is twice of the voxel size for most test data sets. By considering this error threshold for right coronary artery motion modelling, 92% of vessel tracking are performed successfully by using our proposed method, compared to 46% when using the purely non-rigid registration approach. By choosing 2.8mm as threshold, the right coronary tracking is successful in our method while the non-rigid registration approach produces 72% success rate. From Figure 6.18 and Table 6.2, we can conclude that combining the non-rigid registration with the template matching together improve the motion tracking accuracy in most cases, particularly in the frames when the rapid cardiac motion occurs. The variance of tracking error is greatly reduced by using the proposed method.

In this section, a method combining the template matching and non-rigid registration algorithm is presented for patient-specific coronary artery motion modelling from cardiac CTA sequences. It has been tested on eight clinical CTA datasets and proved to be more robust than purely non-rigid registration approach. The limitation of this study is the lack of manual annotated coronary centerlines and lumen for the CTA images. By assuming the semi-automatically extracted minimal cost paths as "ground truth", the accuracy of the proposed tracking method is potentially under-estimated particularly for LAD and LCX. For more accurate evaluation, manual annotations are needed. However, it is very time-consuming and laborious to obtain manual annotations of the coronaries. More importantly, in this thesis, we focus more on the motion tracking of the coronaries from 4D pre-operative CTA scans. The vesselness based graph search algorithm provides us reliable and fast coronary artery extractions that can be used as "ground truth".

6.7 Summary

Two tubular-model based approaches are presented in this chapter for modelling the coronary motion from 4D CTA. Each method is quantitatively evaluated using clinical data. From the quantitative assessments we have performed, both approaches proposed here are shown to be more robust and accurate than the approach relying on non-rigid registration solely. Compared with the graph search based coronary motion construction method in Chapter 5, far fewer manual annotations of the start and end nodes for the graph search are required here. Using the newly proposed template-based approaches, the coronary motion tracking achieves a satisfactory (Section 6.6) or similar level of accuracy (Section 6.5) compared to manual tracking.

Chapter 7

Atlas-based Coronary Motion Tracking

In this chapter, we present an atlas based coronary motion modelling algorithm. We propose a method for constructing a probabilistic atlas of the coronary arteries in Section 7.1. The constructed probabilistic atlas of the coronaries is then used in Section 7.2 for a new coronary lumen segmentation method. In Section 7.3, a novel coronary motion modelling method is proposed based on the probabilistic atlas and multi-level multi-channel diffeomorphic registration. Finally, the proposed method is evaluated in 4D CTA sequences from eight subjects in Section 7.4.

A detailed review on coronary motion modelling has been presented in Chapter 3. The most related approach is the one by Metz *et al.* [151] which proposes an approach for tracking the coronary motion from cardiac CTA. In their approach, the coronaries are manually or semi-automatically identified at one time frame and then tracked throughout the cardiac cycle using non-rigid registration of the multi-phase cardiac CTA images. The restriction of this approach is that highly localized motion of the coronaries cannot be fully recovered by the motion tracking of the entire heart, particularly for right coronary artery as shown in Figure 2 and Figure 3 in [151]. The same conclusion can be drawn from the results of our experiments as shown in Figure 6.15 and Figure 6.18.

Different from the approaches in previous chapters and [151], the coronary motion tracking in this chapter is achieved by forming a probabilistic atlas of the coronaries and using a multi-channel extension of the Large Deformation Diffeomorphic Metric Mapping (LDDMM) registration method [20, 40]. This newly proposed multi-level multi-channel diffeomorphic registration here can more accurately capture the rapid motion of right coronary artery compared to other non-rigid registration techniques.

The formalism of LDDMM makes large diffeomorphic (smooth and invertible) transformations possible when registering two shapes. Contrary to alternative methods

ods [11, 227], the LDDMM formalism is designed to compute shape deformations that are geodesics. An optimal flow of deformations is estimated between the source and target images according to a regularization metric and a similarity measure. Minimising the resulting objective function yields the optimal path between the source and target images. In this context and for coronary motion tracking from CTA sequences, the registration of the grey level images does not capture accurately the highly localized coronary motion which is surrounded by large anatomical structures. The LDDMM method in [20] has previously been extended to treat vector-valued, tensor-valued images [36] and multi-channel images [227].

The methodological contribution of this chapter is to use multi-channel registration, where each channel contains a different level of description of the registered shapes: (1) original images, (2) vesselness images after the enhancement using tensor voting and (3) highly smoothed original images. To differentiate from the multi-channel method in [227], we denote our approach as Multi Level- or ML-LDDMM. Using vesselness response of the coronary artery region as channel 2 contributes to matching the vessels over long distance while limiting the influence from the surrounding cardiac structures.

7.1 Coronary Artery Atlas Construction

Chillet *et al.* [47] presented a method for forming brain and liver vascular atlases using a vessel-to-image affine registration method. The proposed atlas construction process includes four main steps:

- The vessel centrelines are extracted from the images using the segmentation method in [12];
- One subject's vascular model is chosen as a template and its vascular distance map (DM) is computed;
- All other extracted vascular models are registered with the DM template using a vascular model-to-image affine registration method;
- The DM images are computed for all aligned vascular models and used to calculate the mean and variance images of the DM images in order to form the vascular atlas.

We propose an alternative approach to build a probabilistic atlas of the coronary arteries using image-to-image affine registration. A group of 26 CTA images we used for this purpose are denoted as *EMC3DCTA* that are collected at Erasmus MC, University Medical Center Rotterdam, The Netherlands. The images were acquired from 26 subjects with Siemens Somatom Sensation 64 and Definition scanners, and reconstructed at end-diastolic phase using retrospective ECG gating. The sizes of the reconstructed CTA images vary from $512 \times 512 \times 268$ voxels to $512 \times 512 \times 346$ voxels, and the voxel dimensions vary from $0.27 \times 0.27 \times 0.40$ mm^3 to $0.37 \times 0.37 \times 0.40$ mm^3. The coronary artery centrelines are manually annotated in all 26 CTA images. After affine alignment, the centrelines are shown in Figure 7.1.

Figure 7.1: Coronary artery centrelines from 26 subjects after affine alignment. Red: Right coronary artery; Green: Left anterior descending coronary artery; Blue: Left circumflex artery.

A 3D probabilistic atlas of the coronaries $\mathcal{A}$ containing LAD, LCX and RCA is constructed from these manually marked centrelines. The CTA scan of patient i is denoted as I_i and its corresponding centreline as $\mathcal{C}_i$ with $1 \leq i \leq n, n = 26$. The atlas construction consists of four steps:

1. One subject's CTA scan I_n is chosen as reference image $\mathcal{R}$ randomly. The rest of the CTA scans $(I_1, ..., I_{n-1})$ are chosen as source image and affinely aligned with $\mathcal{R}$.

2. The manually segmented centrelines $\mathcal{C}_1, ..., \mathcal{C}_{n-1}$ are transformed according to the resulting affine transformation $\mathbf{T}_1, ..., \mathbf{T}_{n-1}$ in order to match with the centreline $\mathcal{C}_n$ from the reference subject.

3. All the transformed centrelines $\mathcal{C}_{\mathbf{T}_1}, ..., \mathcal{C}_{\mathbf{T}_{n-1}}$ and the corresponding reference centreline $\mathcal{C}_n$ are then modelled as a tubular structure with a pre-defined radius

and subsequently blurred with a Gaussian kernel. By doing so, a probabilistic image is created for each transformed centreline $\mathcal{C}_{\mathbf{T}_i}$ where the vessel is modelled using a Gaussian probability density function which is centred at the vessel centreline and whose standard deviation is proportional to the radius of the vessel.

4. For each coronary artery, its probabilistic atlas is created by averaging the corresponding probabilistic images from the 26 subjects.

The process is repeated for all three coronary arteries in order to create a probabilistic atlas for each artery. By combining the three atlases together, a probabilistic atlas of the coronary artery tree $\mathcal{A}$ is formed as shown in Figure 7.2.

By affine alignment of the reference image $\mathcal{R}$ used for creating the probabilistic atlas and the end-diastolic phase (ED) of a new patient CTA sequence, this atlas $\mathcal{A}$ is affinely registered to the patient dataset to create a patient-specific probabilistic atlas of the coronaries $\mathcal{M}_{ED}$. For each patient CTA sequence, the 3D atlas $\mathcal{M}_{ED}$ can then be warped to create a 4D atlas by temporal non-rigid registration [193] of the CTA sequence. Each patient-specific, phase-specific coronary atlas is then used to select the coronary artery region from its corresponding vessel response image and incorporated in the vascular segmentation and registration procedure.

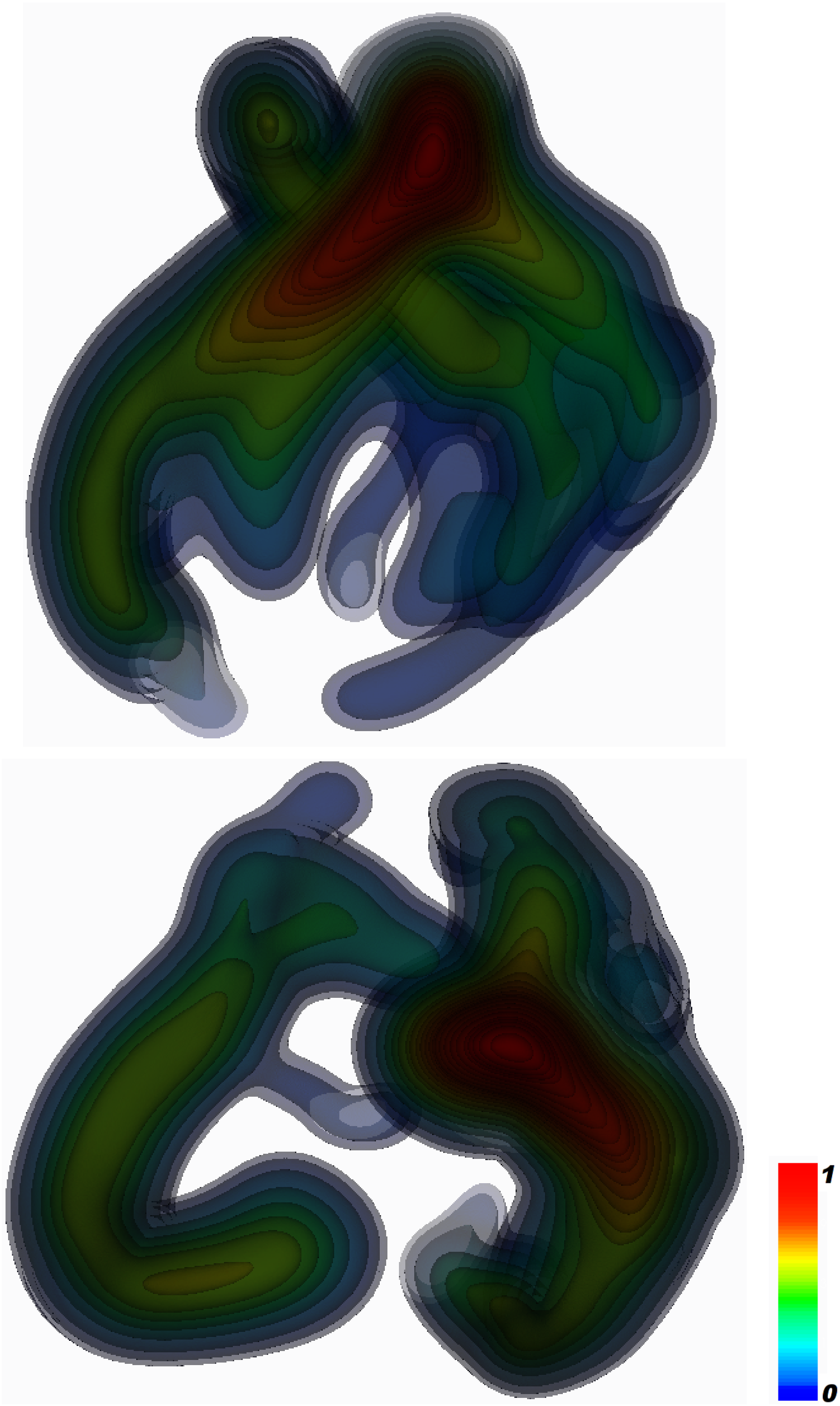

Figure 7.2: Surface rendering with multiple iso-probability contours of the probabilistic atlas of the coronaries from two views. Red indicates a high probability of a coronary at a voxel whereas blue indicates a low probability.

7.2 Atlas-based Coronary Lumen Segmentation

The coronary lumen can be segmented using the constructed coronary atlas in Section 7.1. The segmentation using this approach consists of the following steps:

1. Affine registration of the atlas reference image $\mathcal{R}$ as in Section 7.1 and the end-diastolic CTA image to be segmented I. The derived transformation is denoted as $\mathbf{T}_{\text{affine}}$;

2. Compute the multi-scale vesselness image I_v as in Section 4.2 from image I after vessel enhancement diffusion (Section 6.1.3);

3. Transform the coronary atlas $\mathcal{A}$ for one coronary branch from Section 7.1 according to the derived deformation $\mathbf{T}_{\text{affine}}$ in step 1 to create the patient-specific coronary atlas $\mathcal{M}$ for the corresponding branch in image I;

4. Use the atlas $\mathcal{M}$ from step 3 to select the coronary region from I_v. The vessel lumen of this branch is chosen as the largest connected component from the selected region of the vesselness image I_v.

5. Repeat step 3 & 4 for other coronary branches. Finally, the coronary lumen tree is obtained for image I by combining the segmented branches.

This method extracts the coronary lumen fully automatically. However, it requires high image quality and only works for CTA image with good contrast and few artefacts. Figure 7.3 (d) shows the segmented coronary lumen from one CTA scan at ED phase.

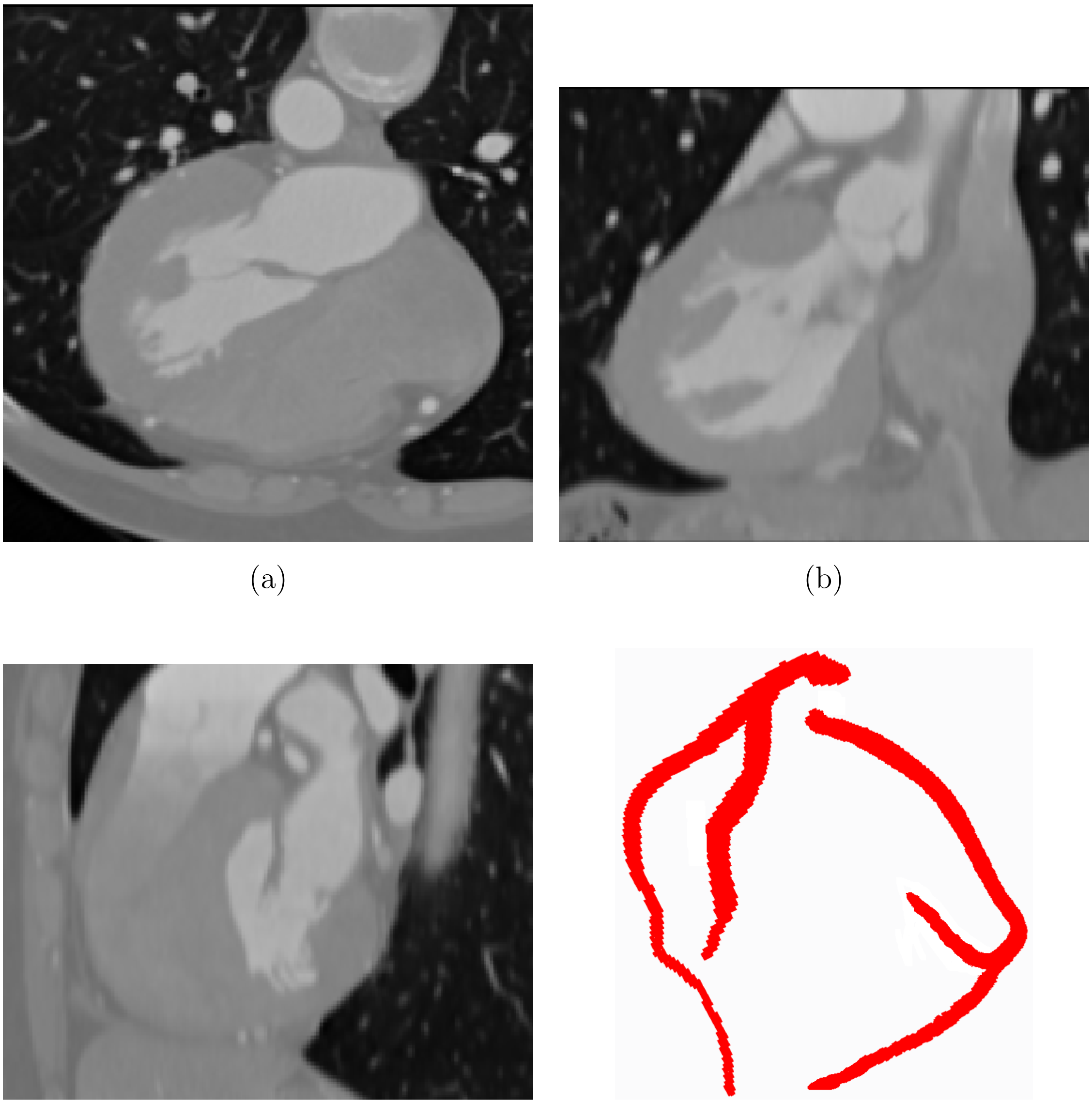

(a) (b)

(c) (d)

Figure 7.3: Automatically segmented coronary lumen from the end-diastolic phase of one CTA sequence. (a), (b) and (c): The CTA image is shown in three views. (d): The segmented coronary lumen.

7.3 Coronary Motion Estimation Using a Probabilistic Atlas and Diffeomorphic Registration

In this section, a method for coronary artery motion estimation from 4D CTA is presented using a probabilistic atlas of the coronaries and diffeomorphic registration. The proposed approach consists of three steps:

1. Prior to motion tracking, a probabilistic atlas of the coronaries is constructed from manual segmentations of the CTA scans of a number of subjects (See Sec-

tion 7.1).

2. The vesselness response image is calculated and enhanced for end-diastolic and end-systolic CTA images in each 4D sequence.

3. A special purpose registration framework is designed for tracking the highly localized coronary motion. It combines the probabilistic atlas of the coronaries, the intensity information from the CTA image and the corresponding vesselness image to fully automate the coronary motion tracking procedure and improve its accuracy.

We perform pairwise 3D registration of cardiac time frames by using a multi-channel implementation of the Large Deformation Diffeomorphic Metric Mapping (LDDMM) framework [20], where each channel contains complementary information about the coronary arteries. For validation, we compare the automatically tracked coronaries from end-systole to end-diastole with manual annotations at end-diastolic phase for each subject. The advantages of the proposed approach are two-fold:

- It requires less manual pre-processing, since no manual segmentation or user-interaction is required for patient-specific coronary motion modelling. Also, same as the approaches we proposed in previous chapters, no 3D reconstruction from X-ray images is required in order to perform 3D coronary motion tracking as in [206, 207].

- By combining the greylevel CTA image, its vesselness image and the probabilistic atlas of the coronaries in a unified registration framework, this approach provides a robust estimation of the coronary motion in 4D CTA.

7.3.1 Framework of LDDMM Algorithm with Multiple Channels

The probabilistic atlas of the coronaries $\mathcal{A}$ constructed in Section 7.1 is used here to assist the registration. By affine registration of the reference image $\mathcal{R}$ used for creating the probabilistic atlas and the end-diastolic phase of a new CTA sequence, a patient-specific probabilistic atlas of the coronaries $\mathcal{M}_{ED}$ is created. The 3D atlas $\mathcal{M}_{ED}$ is then deformed to create an atlas $\mathcal{M}_{ES}$ corresponding to end-systolic phase by non-rigid registration [193] of the CTA sequence. The patient-specific coronary masks $\mathcal{M}_{ED}$ and $\mathcal{M}_{ES}$ are then used to select the coronary artery regions from their corresponding vesselness images and incorporated in the multi-level LDDMM registration.

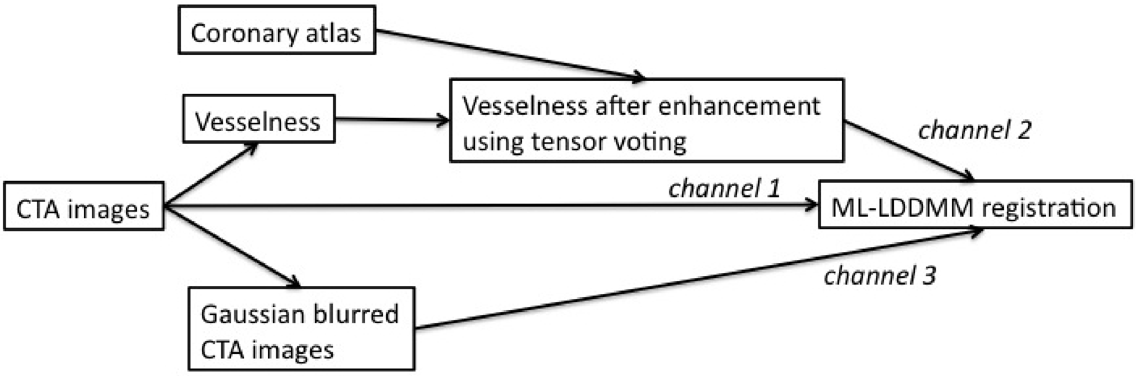

Figure 7.4: Overview of the proposed coronary motion estimation method.

By using a patient-specific coronary atlas $\mathcal{M}_{ES}$ as a mask to select the region of interest from its vesselness image, tensor voting and extracting the largest connected components, the coronary lumen is segmented from the post-processed vesselness response image at end-systolic phase for each 4D CTA sequence. The segmented coronary lumen is then transformed to the end-diastolic time frame according to the deformation estimated from the ML-LDDMM registration. The estimated coronary lumen at end-diastolic is then compared to manual tracking of the coronaries at end-diastolic phase. Figure 7.4 shows an overview and illustrates the connections between the components in the proposed algorithm.

7.3.2 Tensor Voting

Segmenting the vessels directly from the Hessian-based vesselness images does not provide satisfactory results when the CTA image quality is low because of various reasons mentioned in Section 4.6. To alleviate the negative effects caused by the low quality of CTA images, we propose to use a post-processing step based on tensor voting [84, 102, 187] to enhance the extraction of the coronary vessels. Tensor voting was initially developed to reconstruct shapes from point clouds but was also shown to efficiently recover volumes, surfaces and curves from noisy images. In our context, the tensor voting is adapted to fill discontinuities in the vesselness image as shown in Figure 7.5.

Consider a 3D vesselness image $I_v \in \Omega$. We associate a tensor-valued image $\mathbf{TV} \in \Omega$ with I_v. Each voxel of the $\mathbf{TV}$ is a 3×3 tensor (or matrix) that allows local communication between the noisy data of I_v. Using the framework of [187], each non-zero voxel $\mathbf{x}_i$ of I_v is considered as an island token i, where $i \in \{1, ..., N\}$. This token generates a tensor field $\mathbf{TV}_i$ around $\mathbf{x}_i$. For $\mathbf{x} \in \Omega$, $\mathbf{TV}_i(\mathbf{x})$ is computed as the tensor product of a vector $\mathbf{Q}_i(\mathbf{x})$ with itself:

$$\mathbf{TV}_i(\mathbf{x}) = \mathbf{Q}_i(\mathbf{x}) \otimes \mathbf{Q}_i(\mathbf{x}) = \mathbf{Q}_i(\mathbf{x})(\mathbf{Q}_i(\mathbf{x}))^T. \quad (7.1)$$

The vector $\mathbf{Q}_i(\mathbf{x})$ is defined as:

$$\mathbf{Q}_i(\mathbf{x}) = \frac{\mathbf{x} - \mathbf{x}_i}{d(\mathbf{x}_i, \mathbf{x})} \, e^{-\frac{d(\mathbf{x}_i, \mathbf{x})^2}{\delta^2}}, \tag{7.2}$$

where $d(\mathbf{x}_i, \mathbf{x})$ is the Euclidian distance between $\mathbf{x}_i$ and $\mathbf{x}$, and δ is a scale at which the structures of interest are recovered. This formulation ensures that the magnitude of $\mathbf{Q}_i(\mathbf{x})$ decreases while the distance between voxels $\mathbf{x}$ and $\mathbf{x}_i$ increases. Note that in practice, we only compute $\mathbf{TV}_i(\mathbf{x})$ in a bounding box in which its values are not negligible. The size of the bounding box is chosen to be $9\delta \times 9\delta \times 9\delta$. For the voxels outside of this region, the energy of the tensor field is negligible. In our computations, we set δ to 7mm which is slighly higher than the radii of the vessels. The communication between the island tokens is then performed in $\mathbf{TV}$ by calculating:

$$\mathbf{TV}(\mathbf{x}) = \sum_{i=1}^{N} \mathbf{TV}_i(\mathbf{x}), \quad \forall \mathbf{x} \in \Omega. \tag{7.3}$$

By using the saliency map to a curve [187, 84]: $L(\mathbf{x}) = \lambda_1(\mathbf{x}) - \lambda_2(\mathbf{x})$, where $\lambda_1(\mathbf{x})$ and $\lambda_2(\mathbf{x})$ are the two highest eigenvalues of $\mathbf{TV}(\mathbf{x})$, we finally measure how the point $\mathbf{x}$ fits into a curve according to its neighbourhood. This map enhances the coronary vessels even where the contrast between the vessels and the surrounding tissues is low. Note that this simple interpretation of the tensor voting generates a small ghosting effect around the vessel centerlines. The saliency map $L(\mathbf{x})$, also referred to as *tensor enhanced vesselness image*, is smoothed with a Gaussian filter of standard deviation $\delta/2$.

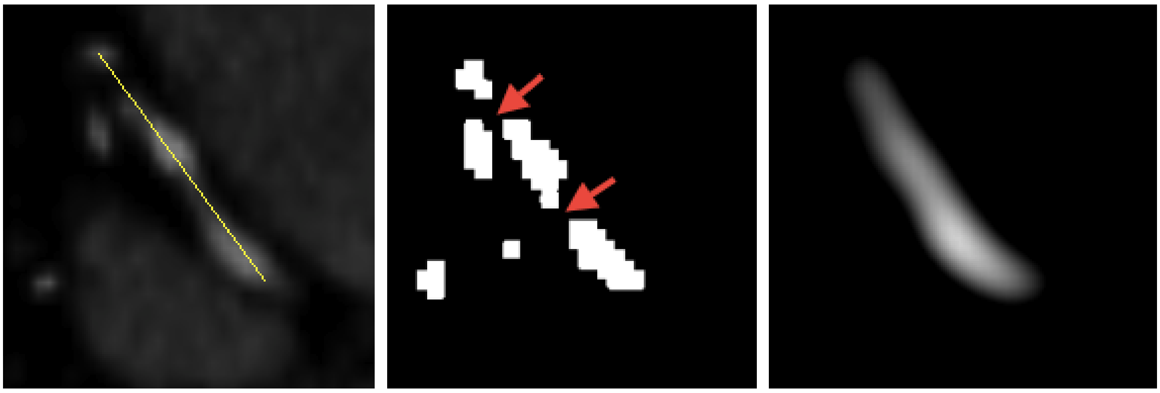

Figure 7.5: An example of tensor voting. Left: A small region of CTA image with right coronary artery marked via the yellow line; Middle: Vesselness image with gaps pointed by the arrows; Right: Vesselness image after tensor voting.

7.3.3 Multi-level LDDMM registration

Image registration is performed using three channels ($C_{1,S}$, $C_{2,S}$, $C_{3,S}$) and ($C_{1,T}$, $C_{2,T}$, $C_{3,T}$) computed from the source image I_S and the target image I_T using the approach summarized in Figure 7.4. These channels represents different levels of information of the registered images:

- The first channel C_1 contains the original images I_S and I_T.
- The second channel C_2 contains the tensor enhanced vesselness images L_S and L_T, calculated in Section 7.3.2.
- Finally, the third channel C_3 represents the original images smoothed by a Gaussian filter.

In the registration framework, the channel C_3 forces the source image to match the target image without taking details into account, so the global motion of major anatomical structures in the CTA images is tracked. Channel C_2 has a similar role, but only focuses on the coronary region. Finally, the channel C_1 is complementary to C_2 and C_3 since it takes image details into account.

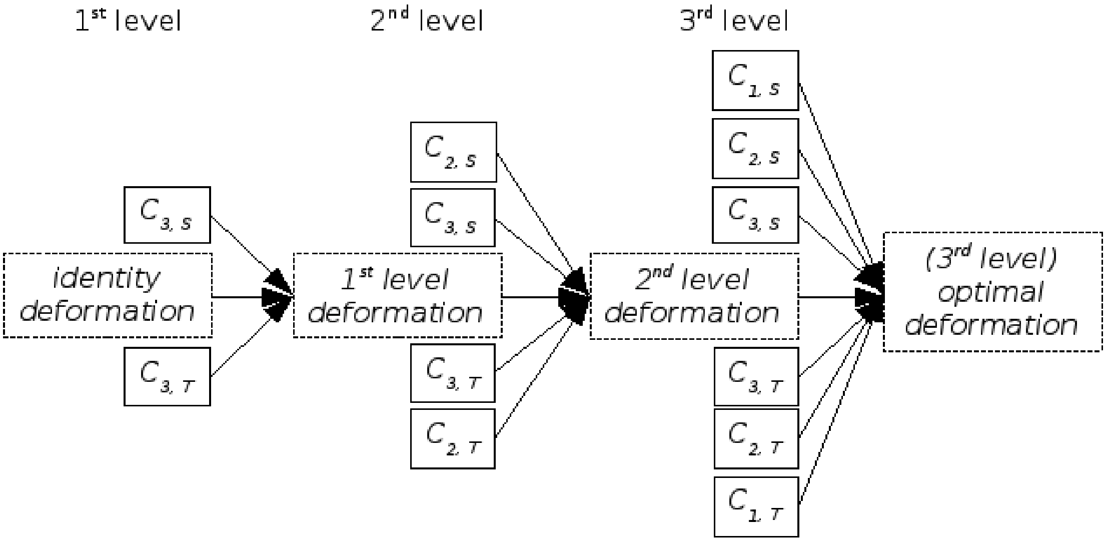

Figure 7.6: Multi-level strategy of the LDDMM registration.

A multi-level strategy, as in Figure 7.6, is adopted to register the images efficiently. In the first level, an initial estimation of optimal deformation is obtained using the smoothed images C_3, then this estimation is refined using registration based on the second channel C_2. Finally, by introducing channel C_1, all information is taken into account for the finest estimation of deformation. This strategy is particularly robust and fast. For the first two levels, it can be performed on the images downsampled by a factor of 2 in each dimension without losing accuracy. Figure 7.7 and 7.8 show examples of the result of the first level and the third level of the registration.

The registrations are performed using the LDDMM framework [20, 40]. In this framework, the images are deformed through diffeomorphic transformations ϕ_t, $t \in [0,1]$, which are defined by a time dependent velocity field v as follows:

$$\partial_t \phi_t = v_t(\phi_t), \tag{7.4}$$

where ϕ_0 is the identity deformation and $t \in [0,1]$. The velocity field v_t deforms the image coordinates at time t and ϕ_t is the induced deformation. For notational convenience, we introduce:

$$\phi_{t,s} \doteq \phi_s \circ \phi_t^{-1}. \tag{7.5}$$

Contrary to [20], where the similarity measure is computed directly from I_S and I_T, the images are indirectly compared here using the information contained in the channels. The energy we minimize, as a function of v, is then:

$$E(v) = \int_0^1 \frac{1}{2} ||v_t||_V^2 \mathrm{d}t + \sum_{i=1}^{3} \left(\alpha_i ||\mathrm{C}_{i,S} \circ \phi_1^{-1} - \mathrm{C}_{i,T}||_{L^2}^2 \right), \tag{7.6}$$

where the first part of the equation computes the energy of the deformation field to be used as a regularisation term, and the second part is the sum of the similarity measures for the three channels. The parameters $\alpha_i \in [0,1]$ control the weight of the channel i. These weights are tuned so that each channel has a similar influence. In the energy of the deformations, the time dependent velocity field v is assumed to lie in $L^2([0,1], V)$, where V is a Hilbert space of vector fields. Underlying this space, there exists a smooth matrix valued kernel K that controls the spatial correlation of the deformations. The minimization of the energy is described hereafter.

We denote $D_t^{i,S} = \mathrm{C}_{i,S} \circ \phi_{t,0}$ and $D_t^{i,T} = \mathrm{C}_{i,T} \circ \phi_{1,t}$. The Jacobian of $\phi_{t,1}$ at time t is also noted $|D\phi_{t,1}|$. The minimization of the variational problem in Equation 7.6 is performed by using a steepest gradient descent approach. This involves the iterative use of the gradient of the functional E at time t:

$$\nabla_v E_t = v_t - K \star \left(|D\phi_{t,1}| \sum_{i=1}^{3} \left(\alpha_i \nabla D_t^{i,S} (D_t^{i,S} - D_t^{i,T}) \right) \right), \tag{7.7}$$

where $\star$ is the convolution operator. In our computations, we used an isotropic Gaussian kernel K of standard deviation 10mm. Such kernel offers a good balance between enough spatial correlation to ensure that the vessel radius is preserved and enough spatial flexibility to properly match curved vessels.

7.4 Experiments and Evaluation

The proposed motion estimation algorithm is tested in 4D CTA sequences from eight subjects. These eight, 20-phased CTA sequences are denoted as $EMC4DCTA_3$ data that is acquired similarly as the $EMC4DCTA_2$ data (Section 6.6.2). Prior to the registration, 4D vessel enhancement anisotropic diffusion and multi-level thresholding are performed in the same way as presented in the end of Section 6.1.3. A coarse segmentation of the coronary arteries in the CTA image is performed using a multiscale Hessian-based vessel enhancement filter [72]. In our expriments, we set the parameters $\alpha = 0.5$, $\beta = 0.5$, and choose γ as the largest norm of the eigenvalues across the whole image. The vesselness response is computed at six different scales within the range $[0.8, 5.6]$. The maximum response of the vesselness filter at the corresponding optimal scale is computed for each voxel of the image. The calculated vesselness image I_v is used to facilitate the coronary extraction and tracking. The parameters for balancing the influence of different channels in the registration process are: $\alpha_1 = 5 \times 10^{-3}$, $\alpha_2 = 7.5 \times 10^{-4}$ and $\alpha_3 = 1$. Note that the intensity range of the vesselness image after tensor voting is much higher than those from the other two channels. Thus a small α_2 is chosen. All the aforementioned parameters are fixed for all eight 4D CTA data.

The registration results using the proposed registration framework are shown in Figure 7.7, 7.8, 7.9 and 7.10. For each subject, we segmented the coronary lumen automatically and used a thinning algorithm to extract the coronary tree centerlines from both end-systolic (ES) and end-diastolic (ED) phases. The centerlines in ES phase are then deformed according to the optimal deformation from ML-LDDMM registration to estimate the coronary positions in ED phase.

In order to quantitatively measure the accuracy of the motion tracking algorithm, we also manually marked the centerlines for the ED and ES phases in these eight CTA sequences. We compare the transformed centerlines with the manually marked ones in ED phase as in the third row of Table 7.1. The distance between the manual segmentation and the automatic tracked coronaries in each time frame is evaluated by Equation 4.18.

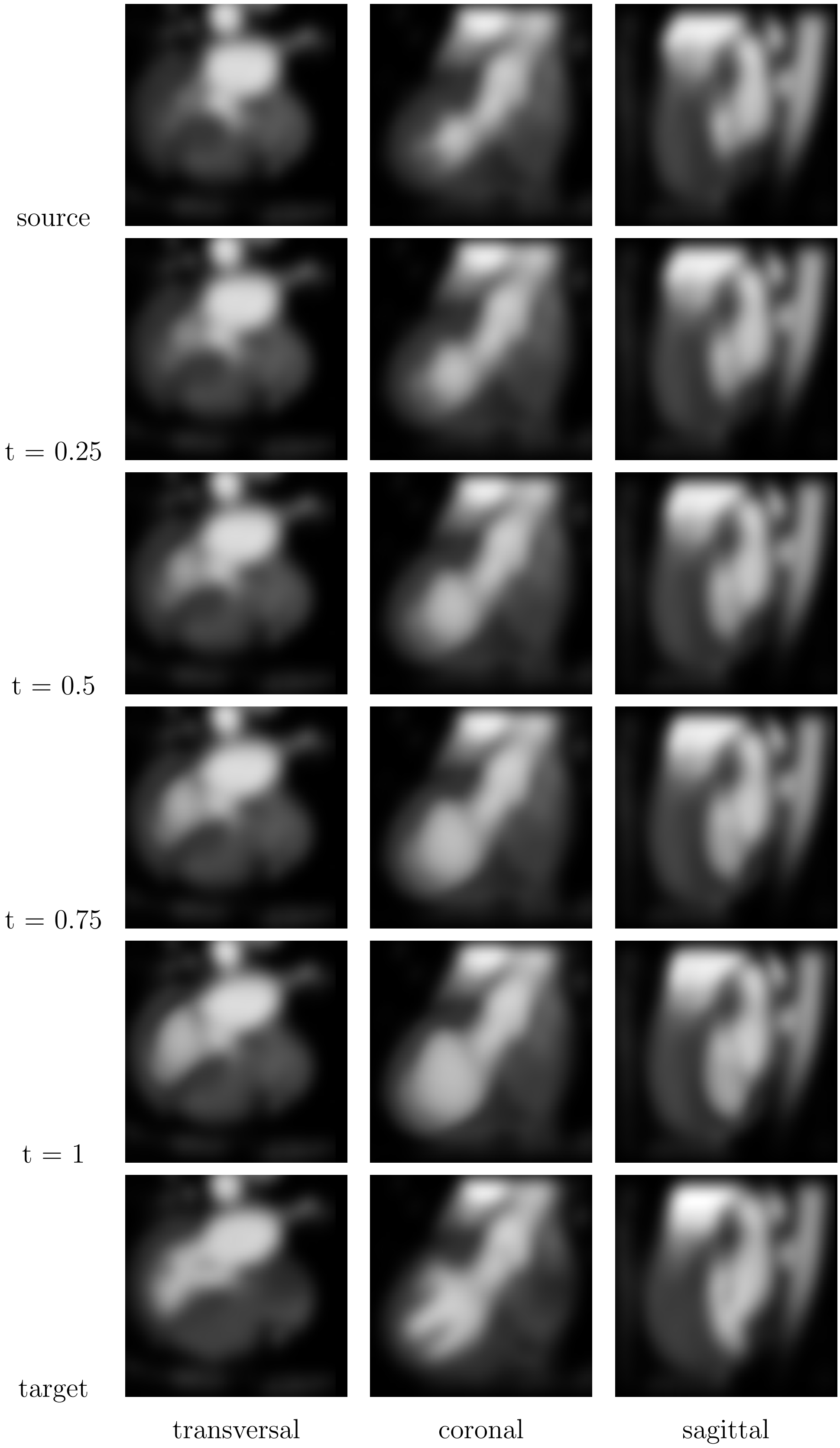

Figure 7.7: ML-LDDMM registration results of level I from three different views as shown in columns. From top to bottom, source image $C_{3,S}$, intermediate transformed results ($t = 0.25, 0.5, 0.75$), final result ($t = 1$) and target image $C_{3,T}$.

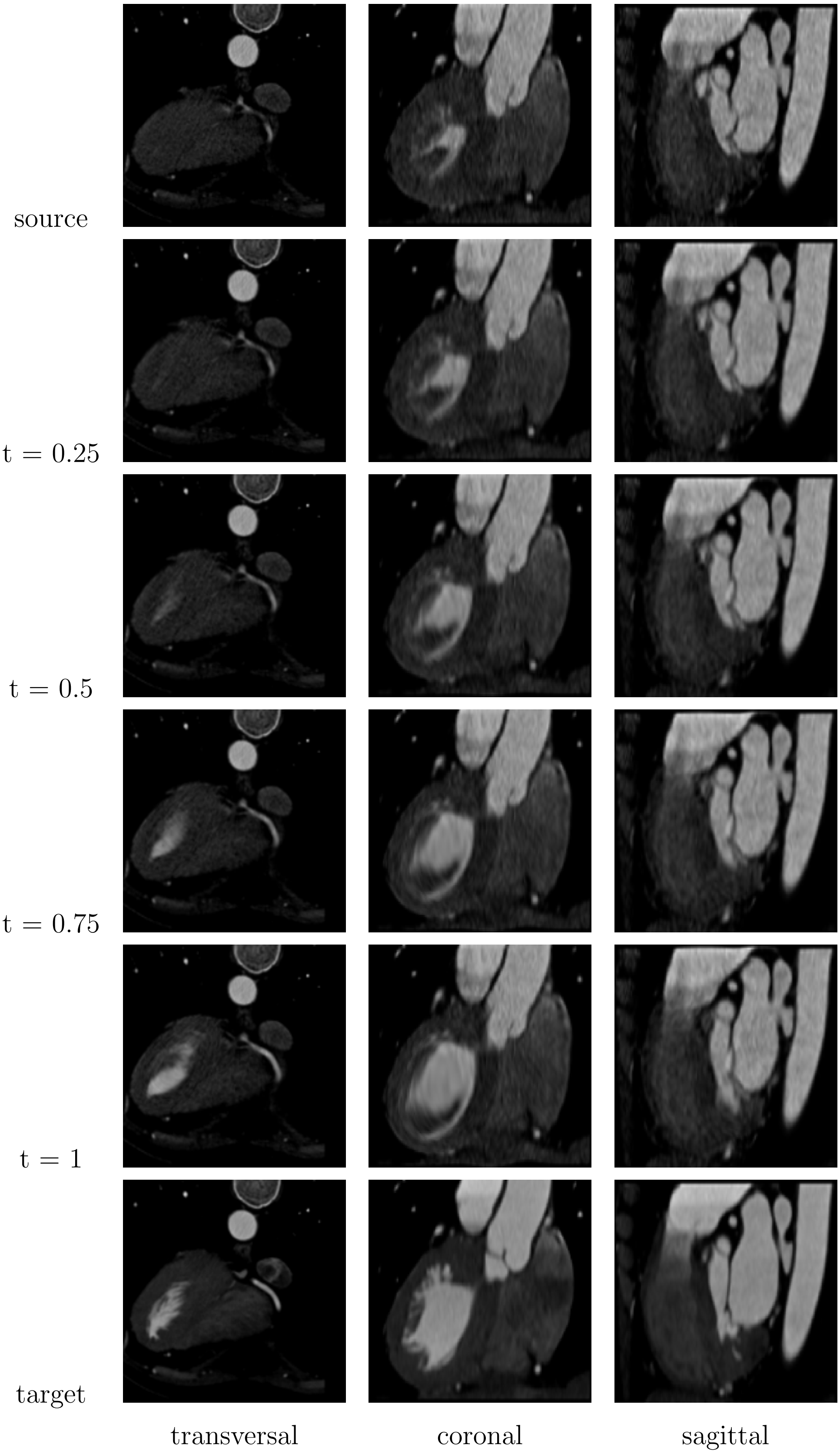

Figure 7.8: ML-LDDMM registration results of level III from three different views as shown by column. From top to bottom, source image I_S, intermediate transformed results ($t = 0.25, 0.5, 0.75$), final result ($t = 1$) and target image I_T.

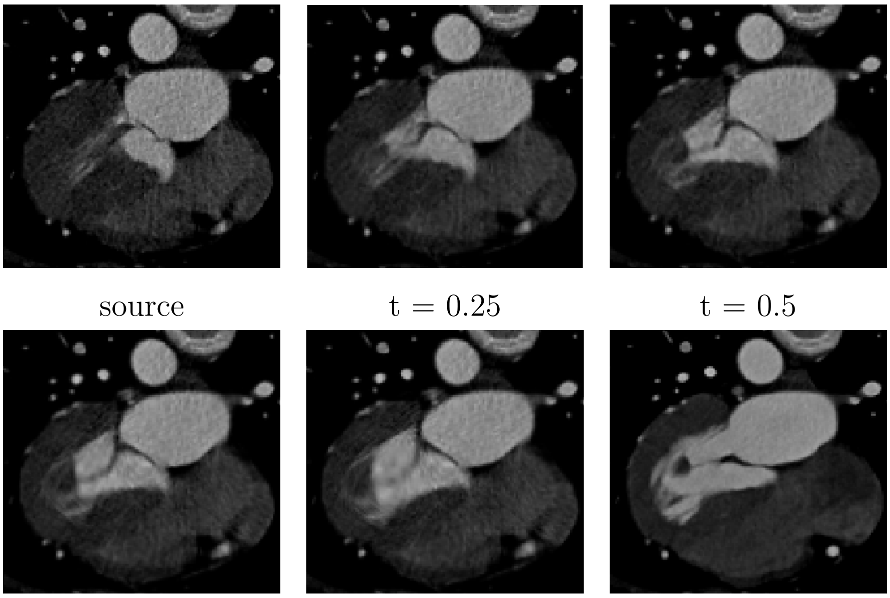
source t = 0.25 t = 0.5

t = 0.75 t = 1 target

Figure 7.9: ML-LDDMM registration results. From left to right, source image I_S, intermediate transformed results ($t = 0.25, 0.5, 0.75$), final result ($t = 1$) and target image I_T.

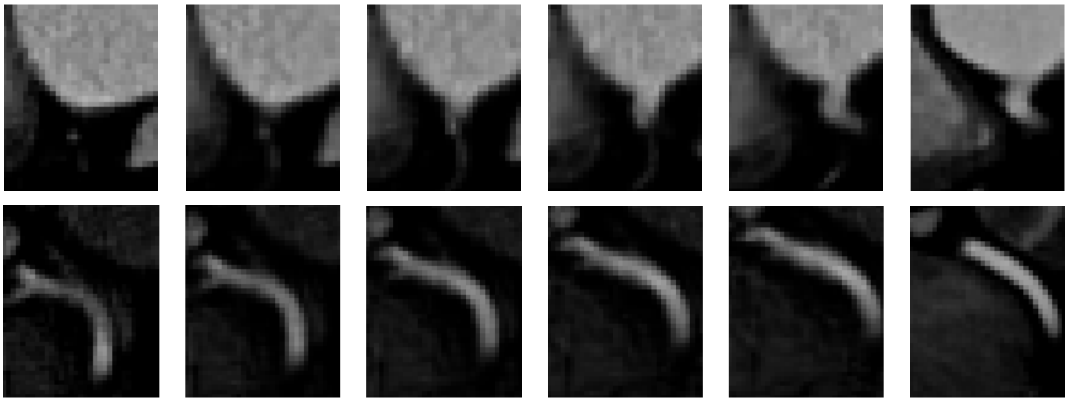
source t = 0.25 t = 0.5 t = 0.75 t = 1 target

Figure 7.10: Registration results. The top row shows starting position of RCA. From left to right, the source image, the intermediate transformed source images ($t = 0.25, 0.5, 0.75$), the final result ($t = 1$) and the target image. Similarly, the bottom row shows the mid-section region of RCA deforming from source to match with target. Note that in each row all images were taken in the same region of interest.

As a comparison, we also present the natural displacement of the coronary tree from ES to ED as in the second row in Table 7.1. The fourth row shows the percentage of coronary displacement that has been compensated by our motion estimation method. The results show that ML-LDDMM registration based motion estimation has performed robustly and accurately. By automatically segmenting the coronary artery and tracking the coronaries from ES to ED in CTA sequences, the patient-specific coronary model and motion estimation are performed robustly in all eight testing subjects.

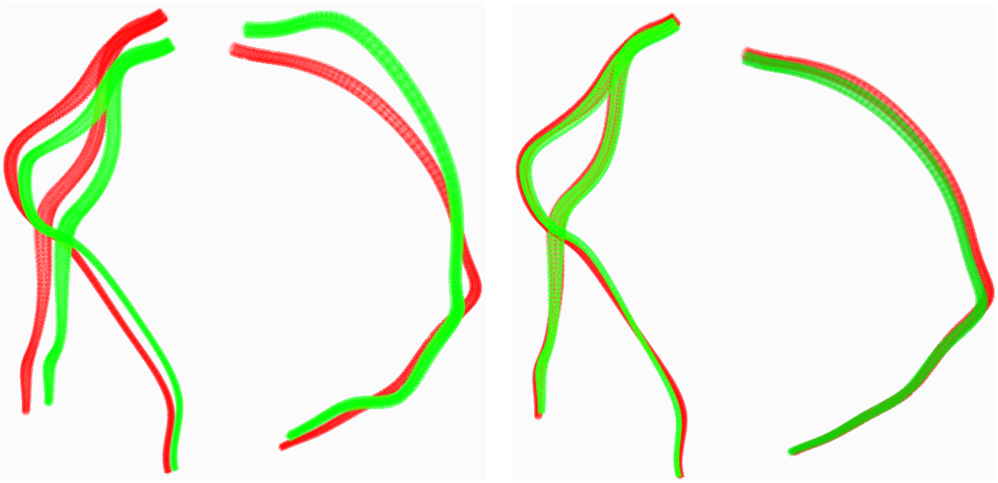

Figure 7.11: Coronary artery lumen (P6). Left: segmented coronary artery lumen at ES (green) and ED (red) phases. Right: estimated coronary lumen at ED phase (green) compared with segmented lumen at ED (red).

Table 7.1: Coronary displacement and error of motion estimation

	P1	P2	P3	P4	P5	P6	P7	P8
Displacement (mm)	8.18	7.63	8.36	7.79	8.62	10.05	8.09	7.88
Estimation error (mm)	1.79	1.26	1.43	1.25	0.69	1.19	1.35	1.04
Compensation (%)	78.12	83.49	82.89	83.95	92.00	88.16	83.31	86.80

7.5 Summary

In this chapter, we have presented a registration framework for patient-specific coronary artery segmentation and motion estimation from dynamic cardiac CTA sequences that significantly improves the robustness of motion tracking and eliminates the manual interaction. This method has been tested on the clinical CTA datasets acquired from eight subjects.

Prior to the coronary motion modelling for assisting the TECAB procedures, accurate segmentation of the coronary centrelines is important in the identification of correct vessel structures of interest. It is also essential to obtain the coronary lumen for the diagnosis of coronary artery disease. However, diagnosis is not our priority in this thesis. Thus the accuracy of the lumen segmentation is only visually inspected rather than quantitatively measured.

A coronary artery atlas constructed from 26 patients' 3D CTA scans is presented in this chapter. However, the coronary anatomy varies substantially among population. For example, we selected another eight patients' scans in which the coronary anatomy varies significantly. Figure 7.12 shows the coronary centrelines from another eight patient scans after affine alignment. As noted in [78], based on which artery supplies the posterior descending artery (PDA), coronary anatomy can be classified into three types, namely, left-dominant, right-dominant and co-dominant. As the name implies, the PDA is supplied by the LCX artery in left-dominance; by the RCA in right-dominance and by both RCA and LCX in co-dominance. This imposes a challenge for coronary atlas construction. Due to the number of CTA scans available for this work, we do not differentiate the coronary centrelines based on their dominance. Thus the constructed coronary atlas only represents a limited group of the population. However, the constructed probabilistic atlas is shown to be sufficient for the purpose of coronary motion tracking as in the experiments in this chapter.

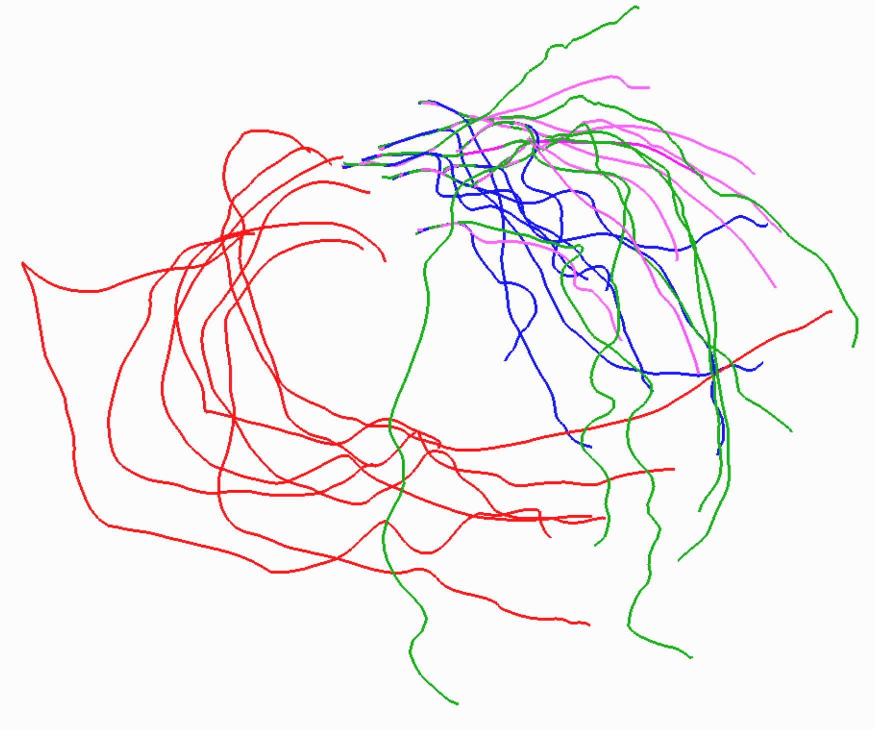

Figure 7.12: Coronary centrelines extracted from another eight patients' CTA images at end-diastole.

Chapter 8

Conclusion and Outlook

Coronary artery motion modelling is a difficult and challenging task. The principal contribution of this thesis is the development and comparison of multiple methods for patient-specific coronary artery motion modelling from the pre-operative 4D CTA images as presented in Chapter 4 to Chapter 7. To build a coronary motion model, it is a necessity to obtain a coronary segmentation. Therefore, another contribution of this work is to develop suitable centreline extraction methods for the pre-operative 4D CTA datasets provided, particularly for CTA scans with severe stair-step artefacts, ghosting or other artefacts introduced during the CTA image acquisition and reconstruction. We have presented two groups of methods for coronary centerline extraction:

- Vessel centrelines are extracted as intensity ridges from CTA images via a ridge-traversal algorithm (Section 4.3);
- Centreline extraction using A* graph search and prior information (Section 5.4); This approach is simplified in Section 6.2 where centrelines are extracted as minimal cost paths via the A* graph search method only.

Although coronary lumen segmentation is not essential in our work, it potentially can be used for stenosis quantification and aneurysm diagnosis. We present two approaches for coronary lumen segmentation:

1. Coronary lumen segmentation using pre-extracted centrelines and tubular model fitting (Section 6.3.3);
2. Coronary lumen segmentation using a probabilistic atlas of the coronaries, vessel enhancement and mathematical morphology (Section 7.2).

For the coronary motion modelling, four groups of methods are presented and evaluated:

1. Ridge traversal combined with non-rigid registration (Chapter 4);

2. A* graph search with prior information obtained from non-rigid registration (Chapter 5);

3. Template-based tracking approaches using template matching, A* graph search, and non-rigid registration (Chapter 6);

4. Motion tracking using multi-level and multi-channel LDDMM registration (Chapter 7).

The work in Chapter 4 serves as the foundation for the rest of contributions of the thesis. The methods in Chapter 5, 6 and 7 have demonstrated a good level of accuracy and robustness according to our evaluations using the clinical 4D CTA data. Note that, our goal in this thesis is to track the coronary artery motion throughout the cardiac cycle in dynamic CTA sequence, rather than the extraction of coronary centrelines in single-phase high-quality 3D CTA image as in [153]. Thus, compared with the "gold-standard", the tracking results in Chapter 5, 6 and 7 meet the clinical accuracy requirements since the average residual displacements are lower than the vessel radii.

8.1 Discussion

Two main assumptions underlie the work in this thesis:

- We assume all the patients have periodic heart motion. Under this assumption, the coronary motion derived from the ECG-gated 4D CTA sequence of a patient acquired during one cardiac cycle can be used to generalise and describe the coronary motion of the patient.

- We assume that the coronary motion pattern of the patient is the same before and during the TECAB surgery. This assumption justifies the pre-operative coronary motion models. However, this requirement could be relaxed in clinical applications by allowing the matching of the pre-operative motion model to the intra-operative data to account for differences in the motion pattern.

A limitation of the proposed image registration based motion tracking methods is that, if there are other irrelevant vessels or *ghost vessels*[1] appearing close to the actual vessel of interest, the motion tracking algorithms may get confused and possibly "lock" onto the wrong vessel instead. There are a number of other factors related to the image acquisition that have an influence on the accuracy and robustness of coronary motion reconstruction:

---

[1] Ghost vessels are displaced reduplications of vessels from other time frames which are shown at current time frame.

1. Heterogeneous distribution of the contrast agent;
2. Arrhythmic heart signals, residual breathing motion or other movement of the patient during the image acquisition;
3. Interference of metal implants that are close to the anatomical structures to be modelled.

Another limitation of our work lies in the lack of manual annotations ("gold-standard") of the coronary centrelines in 4D CTA sequences for validating the coronary motion models. We manually annotated a limited number of data sets for evaluating the proposed motion tracking method. However, for the evaluation in other data sets, we used the extracted minimal-cost paths via the A* graph search subject to visual inspection as the "gold-standard". Although visual inspection guarantees these "gold-standard" to be within the coronary lumen, they still may deviate from the actual centrelines. This may underestimate the accuracy of coronary motion models constructed by the proposed methods. Potentially, through constructing patient-specific coronary motion models from other modalities (e.g. biplane X-ray angiogram sequences [206]), we can evaluate and validate the motion model obtained from 4D CTA data by checking its consistency with models from other modalities.

The work in this thesis consists of motion modelling of the three main coronary artery branches, namely, LAD, LCX and RCA. More comprehensive patient-specific coronary motion models including other coronary branches could be constructed, providing further improvement of the 4D CTA imaging quality for small vessels in future. The probabilistic atlas of coronary arteries formed in Chapter 7 is sufficient for selecting the vesselness region in our motion tracking framework. However, for future study, more detailed atlases that reflect the variation of coronary anatomies (e.g., left-dominance, right-dominance and central-dominance) can be formed from the CTA scans of a large population. A quantitative comparison of the proposed algorithms in Chapter 5, 6 and 7 can also be performed in future.

In the following section, we present some initial results pointing towards two other possible directions for future research: automatic left ventricle segmentation in CTA images and the simultaneous motion tracking of coronary arteries and LV. This is followed by an outlook for future work on utilising pre-operative coronary and LV motion models through registering the models with the intra-operative endoscopic videos. Ultimately, this 2D-3D registration could provide guidance for the TECAB surgery and prevent its conversion to conventional bypass surgery.

8.2 Future Work

To facilitate the TECAB procedure and prevent its conversion to conventional invasive surgery, we aim to construct a joint patient-specific 4D left ventricle (LV) and coronary artery motion model from preoperative cardiac CTA sequences. The main challenge of this part of the work is first to obtain automatic segmentation of both structures and follow the deformation of both of them accurately. Here, we propose to use an atlas-based segmentation method and registration-based motion tracking framework to achieve this goal. Finally, through temporally and spatially aligning the coronary and left ventricle motion model with the intraoperative endoscopic views of the patient's beating heart, this work has the potential to assist the surgeon to identify and locate the correct coronaries during the robotically-controlled TECAB procedures.

8.2.1 Atlas-based Segmentation of the LV from CTA

Prior to motion modelling to assist the TECAB surgery, it is essential to segment the left ventricle (LV) and coronary arteries accurately. The segmentation and motion tracking of the coronary arteries have been addressed in previous chapters. In this section, we focus on the segmentation of left ventricle.

The segmentation of the left ventricle (myocardium) from CTA images is achieved using an atlas propagation scheme [257]. The atlas used here is constructed from MR images for the whole heart segmentation in [258]. A number of MR images acquired using the same MRI sequence from various subjects are used to construct this atlas. All MR images are registered to a selected reference image. An atlas intensity image is then computed as the mean intensity image from this group of registered MR images, shown in Figure 8.1 (a). An labelled atlas image, as shown in Figure 8.1 (b), is also created by manually labelling each anatomical structure of the reference image, including the blood pool of each chamber, great vessels and left ventricle myocardium.

Given the 3D cardiac atlas, the main challenges of the segmentation for any new patient scan are the initialisation of the substructures and imposition of shape constraints. This segmentation scheme is based on a registration framework consisting of three steps [258]:

1. A global affine registration for localization;
2. A locally affine registration method (LARM) for substructure initialization;
3. A nonrigid free-form deformation (FFD) registration for refining the segmentation results from previous stage.

This registration scheme has been shown to be robust against the large variability of the heart shape [257], and it is particularly useful for our application as our CTA data mainly come from pathological cases.

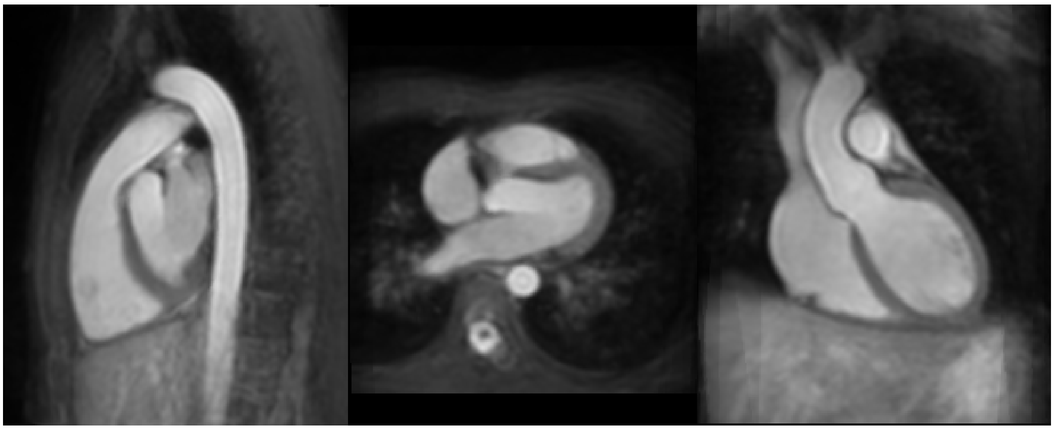

(a): A 3D MR atlas intensity image of the heart using a reference space of the mean shape of 10 volunteer scans shown in three views;

(b): Labelled image of the atlas (a).

Figure 8.1: MR atlas intensity image and labelled image of the heart [258]. The images are shown in sagittal, transverse and coronal views from left to right.

By using the normalized mutual information (NMI) as the similarity measure in the non-rigid registration step, the MR atlas can also be used to segment the major components from cardiac CTA images as argued in Zhuang *et al.* [257]. The gradient ascent method and the multiresolution scheme as in [219] are used to optimise the similarity metric.

Figure 8.2 shows the automatically segmented cardiac structures, including left ventricle using the proposed method from three patients' CTA scans. By visual inspection, these results are promising. However, quantitative assessment should be performed for clinical evaluation in future.

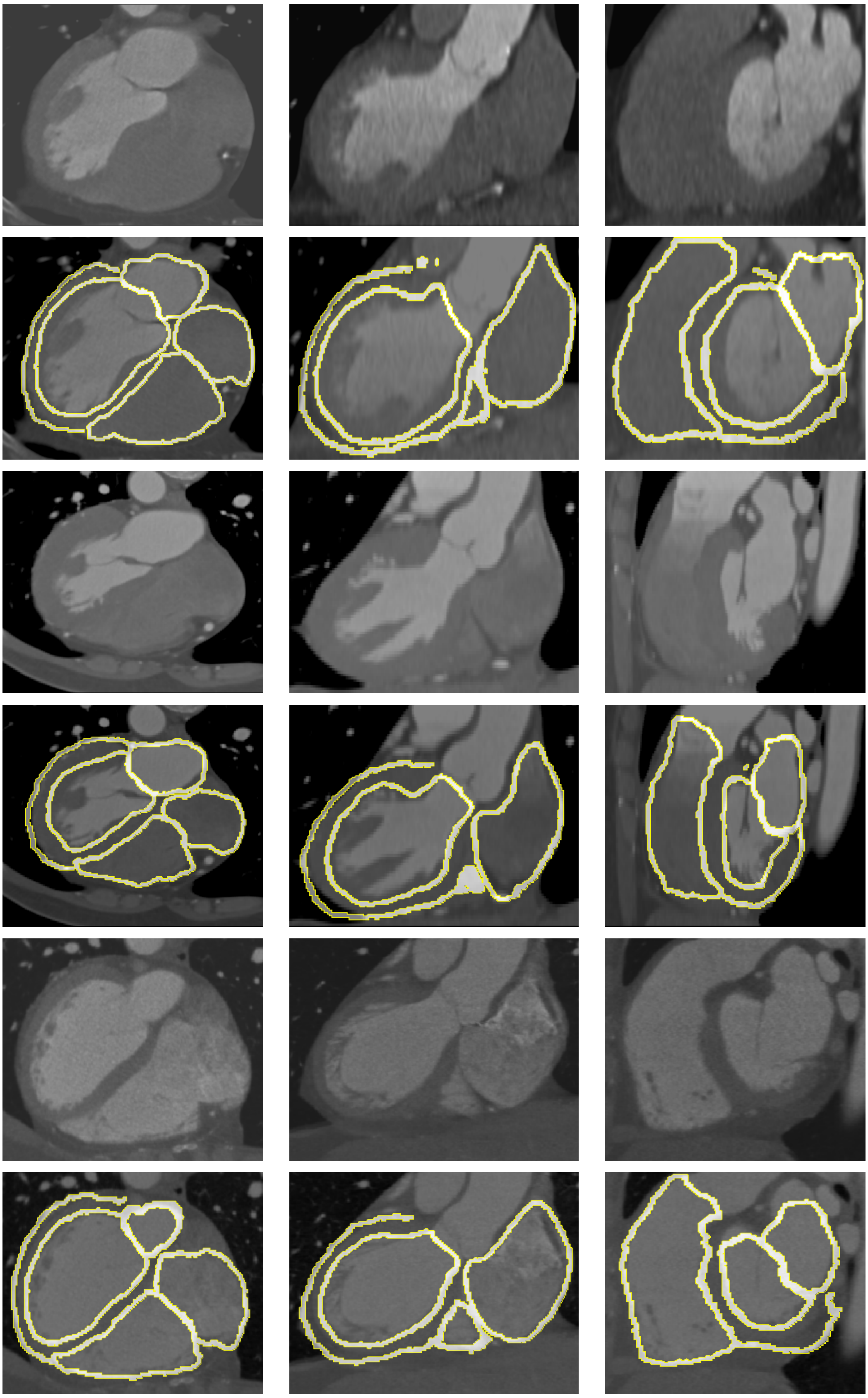

Figure 8.2: Examples of CTA image segmentation. (1st, 3rd and 5th rows): CTA example images in three views; (2nd, 4th and 6th rows): the CTA images overlaid with segmentation surfaces shown in light-grey with yellow contour.

8.2.2 Simultaneous Motion Tracking of LV and Coronary Artery

Here we propose an approach for the simultaneous motion tracking of left ventricle and coronary arteries from 4D CTA sequences. We first use the multi-scale vesselness filter proposed by Frangi *et al.* [72] to perform a coarse segmentation of the coronary arteries in the cardiac CTA images. The coronary centrelines are then extracted as the minimal cost path from the enhanced images in all time frames. The centrelines at the end-diastolic (ED) phase are used as prior input for the motion tracking. All other centrelines are used to evaluate the accuracy of the motion tracking. To segment the left ventricle at the ED phase automatically, we perform three levels of registration using a cardiac atlas obtained from MR images as in Section 8.2.1. The cardiac motion is derived from cardiac CTA sequences by using local-phase based non-rigid registration. The CTA image at each time frame is registered to the ED frame by minimizing the proposed cost function and following a *serial propagation* scheme. Once the images have been aligned, a dynamic motion model of the left ventricle can be obtained by applying the computed free-form deformations to the segmented left ventricle at ED phase. A similar propagation method also applies to the coronary arteries. To validate the accuracy of the motion models, we propose to compare the actual position of the coronaries and left ventricle in each time frame with the predicted ones as estimated from the proposed tracking method.

A 4D motion model of the beating heart with coronary arteries is needed for guiding the TECAB procedure. To achieve this, we first segment the left ventricle and extract the vessel centerlines from the ED time frame of the CTA image sequence. Secondly, we align the sequence of cardiac CTA images to the ED time frame by using our proposed registration method. Finally, we apply the derived deformation to the segmented ventricle and extracted coronaries. The resulting patient-specific motion model can then be used to augment the intraoperative view from endoscope cameras by 2D-3D alignment.

For cardiac segmentation, previous research by Peters *et al.* [179] and Zhuang *et al.* [257] are closely related to our proposed method in this section. As for cardiac motion tracking, non-rigid registration based on a B-spline free-form deformation (FFD) model has shown promising results [43, 42].

The segmentation of the left ventricle (myocardium) is achieved using an atlas propagation scheme as presented in Section 8.2.1. For the coronary segmentation, the CTA images are first processed with multiscale Hessian-based vessel enhancement filter [72]. The centrelines of coronary arteries are then extracted as minimal cost paths connecting the start and end nodes as in Section 6.2.

Normalised mutual information has been widely used as a similarity metric for nonrigid image registration. To align two images using NMI, the structures of interest should be initialized close enough to guarantee a majority overlap. However, this is practically difficult for the registration of the coronary artery because of its thin and elongated shape, as shown in Figure 8.3 (c). Furthermore, the thin structure of vessels has little impact on the NMI similarity measure when the similarity is computed for registering the whole heart. As a result, the NMI similarity measure may not capture the motion of vessels sufficiently. To tackle this problem, we propose to use local phase [82] to capture the deformation and register the thin structure of coronary arteries. The local phase ϕ is derived using the monogenic signal [82]:

$$\phi(\mathrm{x}) = \mathrm{atan2}\left(\sqrt{\sum_{i=1}^{3}(g(\mathrm{x}) * h_i(\mathrm{x}) * I(\mathrm{x}))^2},\ g(\mathrm{x}) * I(\mathrm{x})\right), \tag{8.1}$$

where g is a zero mean bandpass filter such as the log-Gabor filter [82], convolved with I to constitute the even component of the signal; $\{h_i\}$ are the odd anti-symmetric filters in the spatial domain, $i = 1, 2, 3$, whose expression in frequency domain H_i is:

$$\mathrm{H}_i(u_1, u_2, u_3) = \frac{u_i}{\sqrt{u_1^2 + u_2^2 + u_3^2}}. \tag{8.2}$$

The local orientation of the signal can be estimated as:

$$O_d(\mathbf{x}) = \frac{g(\mathbf{x}) * h_d(\mathbf{x}) * I(\mathbf{x})}{\sqrt{\sum_{d=1}^{3}(g(\mathbf{x}) * h_d(\mathbf{x}) * I(\mathbf{x}))^2}} \tag{8.3}$$

Local phase provides a quantitative and continuous description of local features, such as the thin structure of vessels in CTA images. Figure 8.3 shows two CTA images (a, c) and their corresponding phase images (b, d).

For the registration of other substructure of interests such as ventricles, we require the intensity information for computing the similarity measure. Therefore, we combine both the intensity and local phase for the computation of the cost function, as follows:

$$\mathcal{F}(I_t, I_s, \mathbf{T}) = w_1\mathcal{S}(I_t, I_s, \mathbf{T}) + w_2\mathcal{S}(\phi_t, \phi_s, \mathbf{T}) - w_3\mathcal{P}(\mathbf{T}), \tag{8.4}$$

where I_t and I_s denote the target and source image respectively, $\mathbf{T}$ is the free-form deformation; $\mathcal{S}$ is similarity metric such as NMI or normalized cross correlation (NCC) for the image intensity and local phase, $\mathcal{P}(\mathbf{T})$ is the bending energy of $\mathbf{T}$ for smoothness regularisation; w_1, w_2 and w_3 are weights for the three terms respectively.

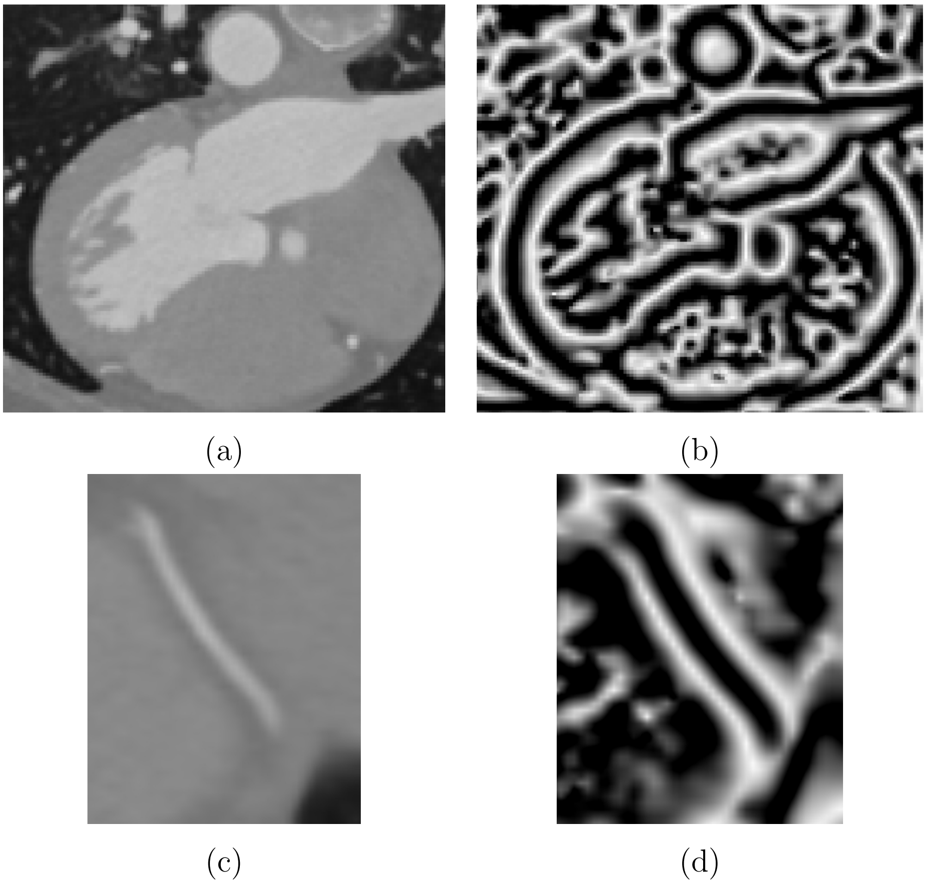
(a) (b)

(c) (d)

Figure 8.3: A CTA image (a) and its local phase image (b); A CTA image region containing right coronary artery segment (c) and its local phase (d).

To register different frames of a CTA dataset to a selected reference frame, we use the *serial propagation* registration to model the large deformation field required for the registration between two frames that are far apart from each other, such as between the ED and ES frames. In the *serial propagation*, we first register the two neighboring frames to the reference frame. The resulting transformation is used to initialize the registration of next pair. The process continues until all images are aligned with the reference, as shown in Figure 6.12.

The cardiac motion extracted by the phase-based method is used to predict the motion of left ventricle and coronaries here. The coronaries and left ventricles extracted from ED phase are deformed according to the obtained deformation information to all other phases to form the coronary and left ventricle motion models. Figure 8.4 shows an example of registration results, both the left ventricle and coronary artery (pointed by red arrow) are aligned after using proposed registration scheme.

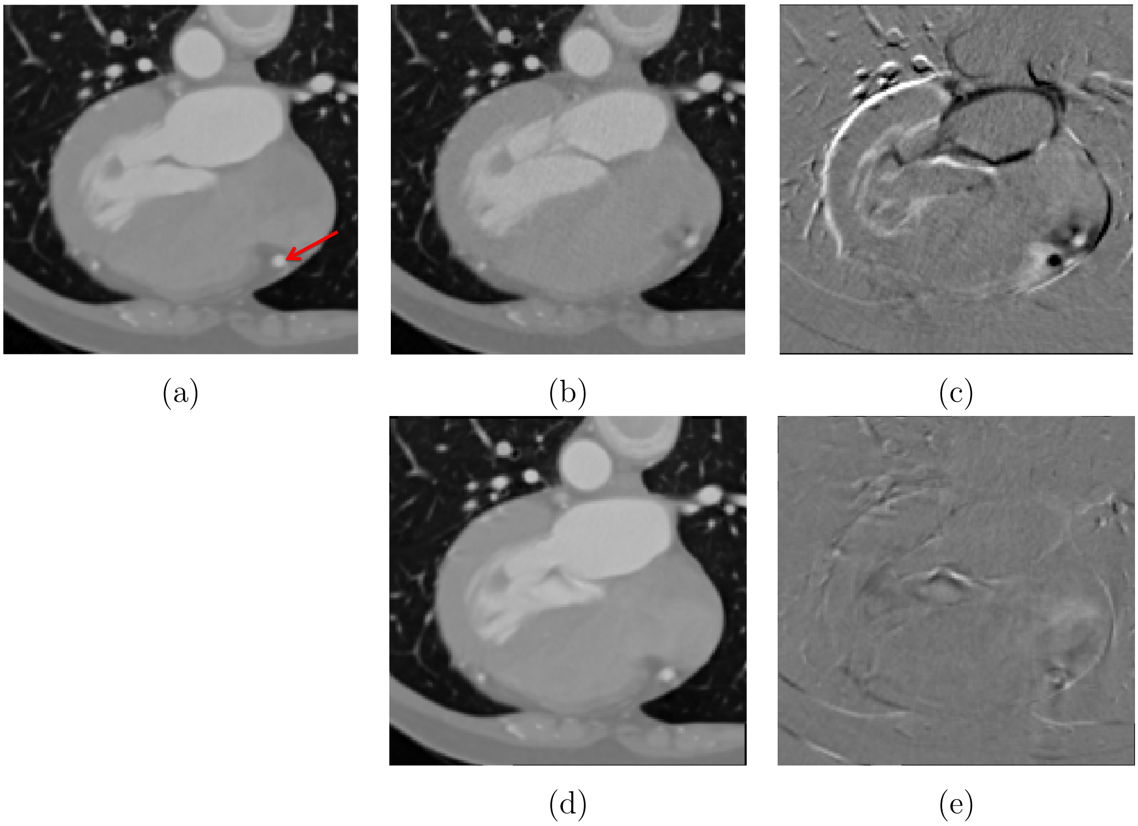

Figure 8.4: Registration results using local phase based method. (a): Reference image; (b): Source image; (c): Subtraction of (a) and (b) before registration. (d): Deformed image of (b) after registration; (e): Subtraction of (a) and (d). Note the red arrow points to a coronary artery cross-section in reference image (a).

For future quantitative evaluation, we propose to assess the motion tracking accuracy for the left ventricle and coronary arteries separately. For the left ventricle, we compute the distance between the manually annotated surface and the surface computed from our proposed motion tracking as in Zhuang *et al.* [257]. To assess the quality of coronary motion model, coronary centerlines are extracted semi-automatically from all time frames of the CTA sequence. We propose to compare the predicted location of the centrelines obtained by applying the non-rigid deformation with the extractions of the centrelines.

In this subsection 8.2.2, we have proposed an approach for the simultaneous motion tracking of patient-specific left ventricle and coronary tree from CTA sequences to assist the totally endoscopic coronary artery bypass surgery. The proposed method has been tested on the clinical CT datasets acquired from four subjects and good results have been visually observed. Further tests and quantitative analysis are required to confirm these preliminary results.

8.2.3 2D-3D Registration of Intra-operative Images and Pre-operative Models

One further extension of our work would be to align the constructed pre-operative coronary and left ventricle motion model with the series of 2D endoscopic images captured during the operation to provide a fused visualisation.

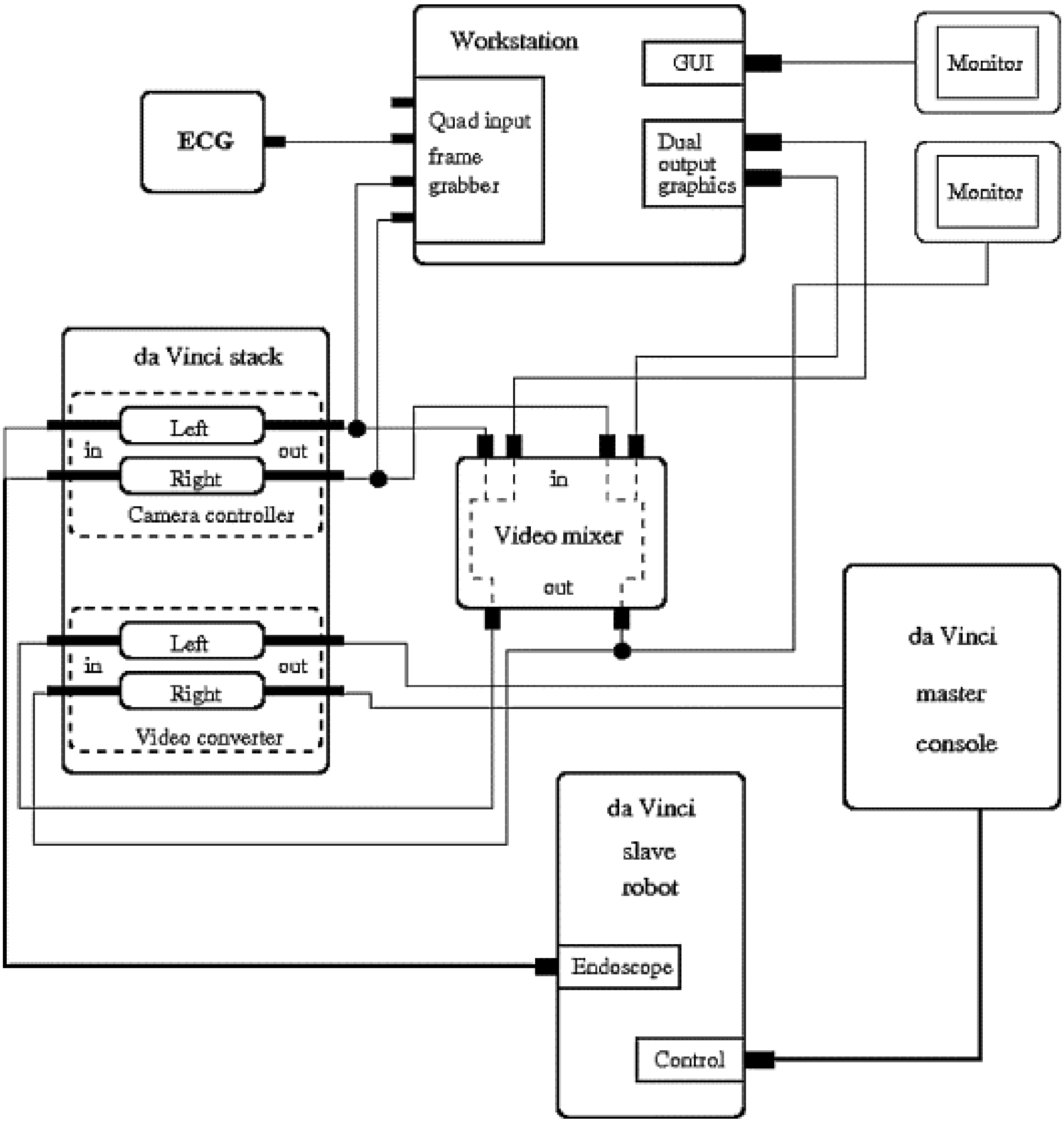

Figure 8.5: The layout of the system in theatre [68]. ECG and the stereo video are grabbed by the machine to gain parameters we need for the image overlay, e.g. the heart and breathing frequencies. The resulting images from the dual graphics output are overlaid to the real video images using video mixers. There is no delay of the real video images in the view of the surgeon as they are just copied to our PC (there is a direct connection from the camera controller via the video mixer to the converter and the master console).

Some work has been done in 2D-3D image registration based on clinical images [83, 41, 194] or on phantom images [223]. Markelj *et al.* [148] provide an up-to-date review on 2D-3D registration. However, to the best of our knowledge, registering patient-specific LV and coronary motion model with the intra-operative endoscopic videos has not been widely investigated in the literature.

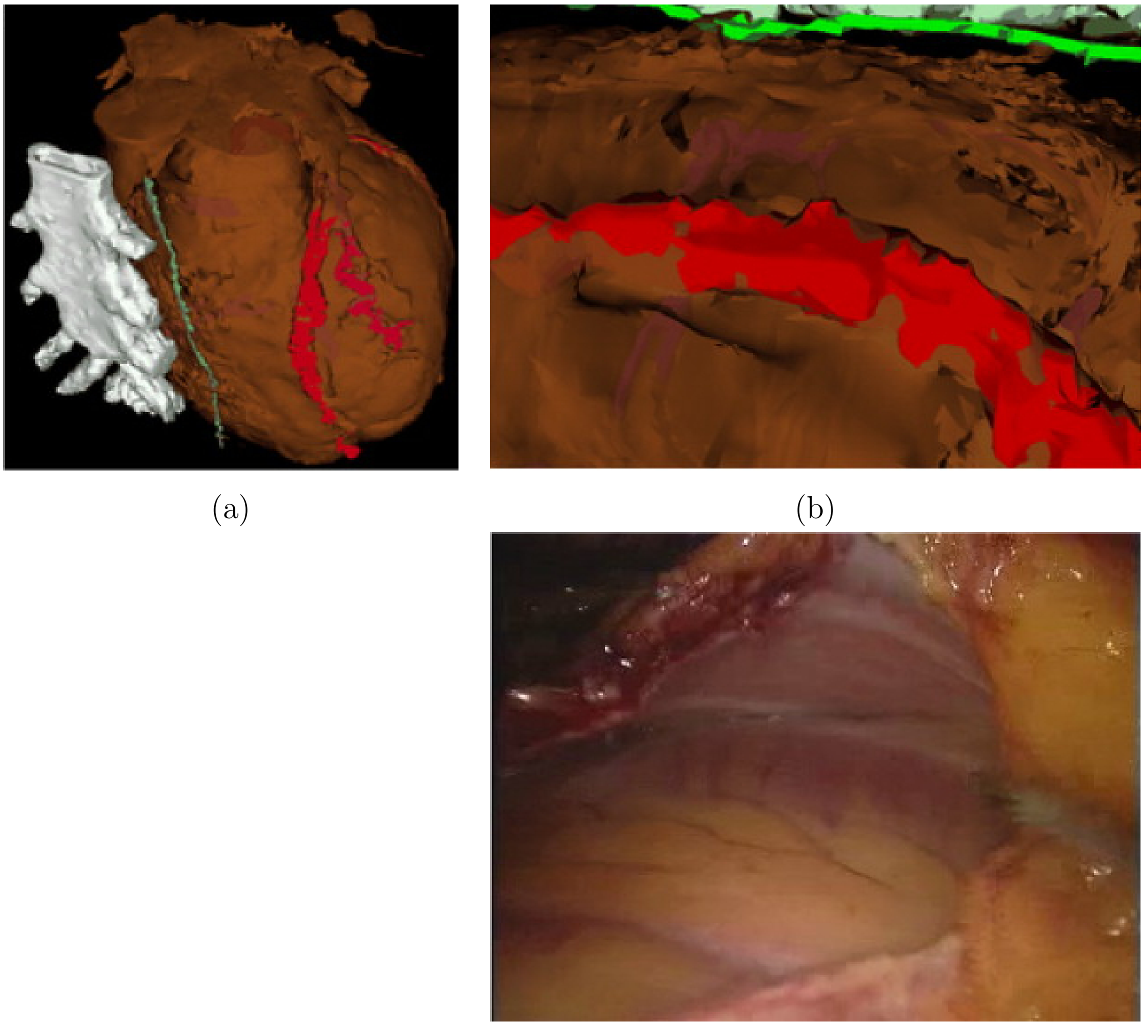
(a)

(b)

(c)

Figure 8.6: A rendering of preoperative model and its alignment with an endoscopic view [68]. (a): A rendering of the preoperative model showing the myocardial surface, left internal mammary artery, left anterior descending artery and a diagonal branch. (b): an aligned rendering and (c) its corresponding endoscope view.

In [68], Figl *et al.* presented our initial work on this challenging topic and the preliminary results. Figure 8.5 shows the layout of the image-guided TECAB surgical system in the theatre, while Figure 8.6 shows a rendering of the pre-operative LV and coronary model and its alignment with an endoscopic image after 2D-3D registration. This 2D-3D matching potentially could help to assist the planning and conducting of TECAB surgery and therefore reduce the conversion rate from TECAB to more invasive conventional procedures.

Publications

1. D. P. Zhang, X. H. Zhuang, P. Edwards, S. Ourselin and D. Rueckert. Motion tracking of left ventricle and coronaries in 4D CTA. (In Proceedings) *SPIE Medical Imaging*, 2011, USA.

2. D. P. Zhang, L. Risser, F.-X. Vialard, P. Edwards, C. Metz, L. Neefjes, N. Mollet, W. Niessen and D. Rueckert. Coronary Motion Estimation from CTA Using Probability Atlas and Diffeomorphic Registration. (In Proceedings) *5th International Workshop on Medical Imaging and Augmented Reality (MIAR 2010)*, Beijing (China), September 2010 (*oral presentation*).

3. D. P. Zhang, L. Risser, O. Friman, C. Metz, L. Neefjes, N. Mollet, W. Niessen and D. Rueckert. Nonrigid Registration and Template Matching for Coronary Motion Modeling from 4D CTA. (In Proceedings) *4th International Workshop on Biomedical Image Registration (WBIR 2010)*, Lübeck (Germany), July 2010 (*oral presentation*).

4. D. P. Zhang, L. Risser, C. Metz, L. Neefjes, N. Mollet, W. Niessen and D. Rueckert. Coronary Artery Motion Modeling from 3D Cardiac CT Sequences Using Template Matching and Graph Search. (In Proceedings) *IEEE International Symposium on Biomedical Imaging: From Nano to Macro (ISBI 2010)*, Rotterdam (Netherlands), April 2010 (*oral presentation*).

5. D. P. Zhang, O. Pedro, K. Mori, P. J. Edwards and D. Rueckert. Coronary Artery Tracking from Dynamic Cardiac CT Sequences. (In Proceedings) *13th Annual Conference on Medical Image Understanding and Analysis*, London, July 2009 (*oral presentation*).

6. D. P. Zhang, E. Edwards, L. Mei and D. Rueckert. 4D motion modeling of the coronary arteries from CT images for robotic assisted minimally invasive surgery. (In Proceedings) *SPIE Medical Imaging*, Volume 7259, February 2009 (*oral presentation*).

7. M. Figl, D. Rueckert, D. J. Hawkes, R. Casula, M. Hu, O. Pedro, D. P. Zhang, G. P. Penny, F. Bello and P. J. Edwards. Image Guidance for Robotic Minimally

Invasive Coronary Artery Bypass. *Computerized Medical Imaging and Graphics*, 2009.

8. M. Figl, D. Rueckert, D. J. Hawkes, R. Casula, M. Hu, O. Pedro, D. P. Zhang, G. P. Penny, F. Bello and P. J. Edwards. Coronary Motion Modeling for Augmented Reality Guidance of Endoscopic Coronary Artery Bypass. *International Symposium on Biomedical Simulation - ISBMS 2008*, pp.197-202, 2008.
9. M. Figl, D. Rueckert, D. J. Hawkes, R. Casula, M. Hu, O. Pedro, D. P. Zhang, G. P. Penny, F. Bello and P. J. Edwards. Image Guidance for Robotic Minimally Invasive Coronary Artery Bypass. *International Workshop on Medical Imaging and Augmented Reality 2008*. pp. 202-209, 2008.
10. M. Figl, D. Rueckert, D. J. Hawkes, R. Casula, M. Hu, O. Pedro, D. P. Zhang, G. P. Penny, F. Bello and P. J. Edwards. Augmented Reality Image Guidance for Minimally Invasive Coronary Artery Bypass. (In Proceedings) *SPIE Medical Imaging: Visualization, Image-guided procedures and Modeling.* Vol. 6918, 2008

This thesis is available in electronic format at `http://www.doc.ic.ac.uk/~dz05/thesis`.

Bibliography

[1] *Proceedings of the 2008 IEEE International Symposium on Biomedical Imaging: From Nano to Macro, Paris, France, May 14-17*, 2008.

[2] *Proceedings of 12th International Conference on Medical Image Computing and Computer-Assisted Intervention (MICCAI), London, UK, September 20-24, Part I*, volume 5761 of *Lecture Notes in Computer Science*. Springer, 2009.

[3] *Proceedings of the 2009 IEEE International Symposium on Biomedical Imaging: From Nano to Macro, Boston, MA, USA, June 28 - July 1*. IEEE, 2009.

[4] S. Achenbach, D. Ropers, J. Holle, G. Muschiol, W.G. Daniel, and W. Moshage. In-plane coronary arterial motion velocity: Measurement with electron-beam CT. *Radiology*, 216(2):457–463, 2000.

[5] G. Agam, S.G.III Armato, and C.H. Wu. Vessel tree reconstruction in thoracic CT scans with application to nodule detection. *IEEE Transactions on Medical Imaging*, 24(4):486 –499, 2005.

[6] G. Agam and C.H. Wu. Probabilistic modeling-based vessel enhancement in thoracic CT scans. In *Proceedings of the 2005 IEEE Computer Society Conference on Computer Vision and Pattern Recognition (CVPR'05)*, volume 2, pages 684–689, 2005.

[7] S. Allender, V. Peto, P. Scarborough, A. Kaur, and M. Rayner. *Coronary heart disease statistics 2008*. British Heart Foundation, London, 2008.

[8] I. Andersson and D.L. Resnick. *The Encyclopaedia of Medical Imaging: Musculoskeletal and Soft Tissue Imaging*, volume 3. Taylor & Francis, 1999.

[9] L. Antiga, B. Ene-Iordache, and A. Remuzzi. Computational geometry for patient-specific reconstruction and meshing of blood vessels from angiography. *IEEE Transactions on Medical Imaging*, 22(5):674–684, 2003.

[10] L. Antiga and D.A. Steinman. Robust and objective decomposition and mapping of bifurcating vessels. *IEEE Transactions on Medical Imaging*, 23(6):704–713, 2004.

[11] B.B. Avants, C.L. Epstein, M. Grossman, and J.C. Gee. Symmetric diffeomorphic image registration with cross-correlation: Evaluating automated labeling of elderly and neurodegenerative brain. *Medical Image Analysis*, 12(1):26–41, 2008.

[12] S.R. Aylward and E. Bullitt. Initialization, noise, singularities, and scale in height ridge traversal for tubular object centerline extraction. *IEEE Transactions on Medical Imaging*, 21(2):61–75, 2002.

[13] S.R. Aylward, J. Jomier, S. Weeks, and E. Bullitt. Registration and analysis of vascular images. *International Journal of Computer Vision*, 55(2-3):123–138, 2003.

[14] S.R. Aylward, S. Pizer, D. Eberly, and E. Bullitt. Intensity ridge and widths for tubular object segmentation and description. In *Workshop on Mathematical Methods in Biomedical Image Analysis (MMBIA)*, 1996.

[15] S.R. Aylward, S. Weeks, and E. Bullitt. Analysis of the parameter space of a metric for registering 3D vascular images. In W. J. Niessen and M. A. Viergever, editors, *MICCAI*, volume 2208 of *Lecture Notes in Computer Science*, pages 932–939. Springer, 2001.

[16] J. Balzer, H. Kuhl, T. Rassaf, R. Hoffmann, P. Schauerte, M. Kelm, and A. Franke. Real-time transesophageal three-dimensional echocardiography for guidance of percutaneous cardiac interventions: first experience. *Clinical Research in Cardiology*, 97:565–574, 2008.

[17] C. Barillot, D.R. Haynor, and P. Hellier, editors. *Medical Image Computing and Computer-Assisted Intervention – MICCAI 2004, Part I*, volume 3216 of *Lecture Notes in Computer Science*. Springer, 2004.

[18] C. Bauer and H. Bischof. Extracting curve skeletons from gray value images for virtual endoscopy. In T. Dohi, I. Sakuma, and H. Liao, editors, *MIAR*, volume 5128 of *Lecture Notes in Computer Science*, pages 393–402. Springer, 2008.

[19] C. Bauer and H. Bischof. A novel approach for detection of tubular objects and its application to medical image analysis. In G. Rigoll, editor, *DAGM-Symposium*, volume 5096 of *Lecture Notes in Computer Science*, pages 163–172. Springer, 2008.

[20] F.M. Beg, M.I. Miller, A. Trouvé, and L. Younes. Computing large deformation metric mappings via geodesic flows of diffeomorphisms. *International Journal of Computer Vision*, 61(2):139–157, February 2005.

[21] T. Behrens, K. Rohr, and H.S. Stiehl. Robust segmentation of tubular structures in 3-D medical images by parametric object detection and tracking. *IEEE Transactions on Systems, Man, and Cybernetics, Part B: Cybernetics*, 33(4):554–561, 2003.

[22] F. Benmansour and L.D. Cohen. Fast object segmentation by growing minimal paths from a single point on 2D or 3D images. *Journal of Mathematical Imaging and Vision*, 33(2):209–221, 2009.

[23] F. Benmansour and L.D. Cohen. A new interactive method for coronary arteries segmentation based on tubular anisotropy. In *ISBI* [3], pages 41–44.

[24] F. Benmansour and L.D. Cohen. Tubular anisotropy segmentation. In Xue-Cheng Tai, Knut Morken, Marius Lysaker, and Knut-Andreas Lie, editors, *SSVM*, volume 5567 of *Lecture Notes in Computer Science*, pages 14–25. Springer, 2009.

[25] F. Benmansour, L.D. Cohen, M.W.K. Law, and A.C.S. Chung. Tubular anisotropy for 2D vessel segmentation. In *IEEE Conference on Computer Vision and Pattern Recognition*, pages 2286–2293, 2009.

[26] C. Blondel, G. Malandain, R. Vaillant, and N. Ayache. Reconstruction of coronary arteries from a single rotational x-ray projection sequence. *IEEE Transactions on Medical Imaging*, 25(5):653–663, May 2006.

[27] C. Blondel, R. Vaillant, G. Malandain, and N. Ayache. 3D tomographic reconstruction of coronary arteries using a precomputed 4D motion field. *Physics in Medicine and Biology*, 49(11):2197–2208, 2004.

[28] D.S. Bloomberg and L. Vincent. Pattern matching using the blur hit-miss transform. *Journal of Electronic Imaging*, 9(2):140–150, 2000.

[29] D.A. Bluemke, S. Achenbach, M. Budoff, T.C. Gerber, B. Gersh, L.D. Hillis, W.G. Hundley, W.J. Manning, B.F. Printz, M. Stuber, and P.K. Woodard. Noninvasive coronary artery imaging, magnetic resonance angiography and multidetector computed tomography angiography. *Circulation*, 118(5):586–606, July 2008.

[30] S. Bouattour, R. Arndt, and D. Paulus. 4D reconstruction of coronary arteries from monoplane angiograms. In *Computer Analysis of Images and Patterns*, volume 3691, pages 724–731, 2005.

[31] B. Bouraoui, C. Ronse, J. Baruthio, N. Passat, and P. Germain. Blur grey-level hit-or-miss transform for fully automatic 3D segmentation of coronary arteries. In *9th International Symposium on Mathematical Morphology*, pages 37–40, 2009.

[32] B. Bouraoui, C. Ronse, J. Baruthio, N. Passat, and P. Germain. 3D segmentation of coronary arteries based on advanced mathematical morphology techniques. *Computerized Medical Imaging and Graphics*, 34:377–387, 2010.

[33] K. Bühler, P. Felkel, and A. La Cruz. Geometric methods for vessel visualization and quantification- a survey. In G. Brunnett, B. Hamann, and H. Müller, editors, *Geometric Modelling for Scientific Visualization*, pages 399–420. Springer-Verlag, 2003.

[34] E. Bullitt and S. Aylward. Volume rendering of segmented tubular objects. In Wiro Niessen and Max Viergever, editors, *Medical Image Computing and Computer-Assisted Intervention MICCAI 2001*, volume 2208 of *Lecture Notes in Computer Science*, pages 161–168. 2001.

[35] E. Bullitt and S.R. Aylward. Volume rendering of segmented image objects. *IEEE Transactions on Medical Imaging*, 21(8):998–1002, 2002.

[36] Y. Cao, M. Miller I., S. Mori, R. L. Winslow, and L. Younes. Diffeomorphic matching of diffusion tensor images. In *Proceedings of the 2006 Conference on Computer Vision and Pattern Recognition Workshop*, page 67, 2006.

[37] J.F. Carrillo, M. Orkisz, and M.H. Hoyos. Extraction of 3D vascular tree skeletons based on the analysis of connected components evolution. In André Gagalowicz and Wilfried Philips, editors, *CAIP*, volume 3691 of *Lecture Notes in Computer Science*, pages 604–611. Springer, 2005.

[38] C. Caero and P. Radeva. Vesselness enhancement diffusion. *Pattern Recognition Letters*, 24(16):3141–3151, 2003.

[39] WHO Media Center, editor. *The 10 leading causes of death by broad income group (2004).* World Health Organization, October 2008.

[40] C. Ceritoglu, K. Oishi, X. Li, M.C. Chou, L. Younes, M. Albert, C. Lyketsos, P.C. van Zijl, M.I. Miller, and S. Mori. Multi-contrast large deformation diffeomorphic metric mapping for diffusion tensor imaging. *Neuroimage*, 47(2):618–627, 2009.

[41] H.M. Chan, A.C.S. Chung, S.C.H. Yu, and W.M.I.I.I. Wells. 2D-3D vascular registration between digital subtraction angiographic (dsa) and magnetic resonance angiographic (mra) images. In *IEEE International Symposium on Biomedical Imaging: Nano to Macro*, pages 708 – 711 Vol. 1, 2004.

[42] R. Chandrashekara, R. Mohiaddin, R. S. Razavi, and D. Rueckert. Nonrigid image registration with subdivision lattices application to cardiac MR image analysis. In *MICCAI*, volume 4791, pages 335–342. Springer, 2007.

[43] R. Chandrashekara, R. Mohiaddin, and D. Rueckert. Analysis of 3D myocardial motion in tagged MR images using nonrigid image registration. *IEEE Transactions on Medical Imaging*, 23(10):1245–1250, 2004.

[44] Y.L. Chang and X.B. Li. Adaptive image region-growing. *IEEE Transactions on Image Processing*, 3(6):868–872, 1994.

[45] S. Chaudhuri, S. Chatterjee, N. Katz, M. Nelson, and M. Goldbaum. Detection of blood vessels in retinal images using two-dimensional matched filters. *IEEE Transactions on Medical Imaging*, 8(3):263–269, sep. 1989.

[46] S.Y.J. Chen and J.D. Carroll. Kinematic and deformation analysis of 4-d coronary arterial trees reconstructed from cine angiograms. *IEEE Transactions on Medical Imaging*, 22(6):710–721, June 2003.

[47] D. Chillet, J. Jomier, D. Cool, and S.R. Aylward. Vascular atlas formation using a vessel-to-image affine registration method. In Randy E. Ellis and Terry M. Peters, editors, *MICCAI (1)*, volume 2878 of *Lecture Notes in Computer Science*, pages 335–342. Springer, 2003.

[48] J.-L. Coatrieux, K. Rioual, C. Goksu, E. Unanua, and P. Haigron. Ray casting with “on-the-fly” region growing: 3-D navigation into cardiac MSCT volumes. *IEEE Transactions on Information Technology in Biomedicine*, 10(2):417–420, 2006.

[49] A. Collignon, F. Maes, D. Delaere, D. Vandermeulen, P. Suetens, and G. Marchal. Automated multimodality image registration using information theory. In Y. Bizais, C. Barillot, and R. Di Paola, editors, *Proceedings of Information Processing in Medical Imaging*, pages 263–274, 1995.

[50] D. Comaniciu and P. Meer. Mean shift: A robust approach toward feature space analysis. *IEEE Transactions on Pattern Analysis and Machine Intelligence*, 24(5):1–18, 2002.

[51] O. Commowick and S.K. Warfield. Estimation of inferential uncertainty in assessing expert segmentation performance from STAPLE. *IEEE Transactions on Medical Imaging*, 29(3):771–780, 2010.

[52] M.G. Danilouchkine, F. Mastik, and A.F.W. van der Steen. A study of coronary artery rotational motion with dense scale-space optical flow in intravascular ultrasound. *Physics in Medicine and Biology*, 54(6):1397, 2009.

[53] P.J. de Feyter and G. Krestin, editors. *Computed Tomography of the Coronary Arteries*. Informa Healthcare, 2 edition, July 2008.

[54] M. Dewan, G.D. Hager, and C.H. Lorenz. Image-based coronary tracking and beat-to-beat motion compensation: Feasibility for improving coronary MR angiography. *Magnetic Resonance in Medicine*, 60(3):604–615, 2008.

[55] M. Dewan, C.H. Lorenz, and G.D. Hager. Deformable motion tracking of cardiac structures (demotracs) for improved MR imaging. In *IEEE Conference on Computer Vision and Pattern Recognition (CVPR '07)*, pages 1 –8, 17-22 2007.

[56] A. Diegeler, T. Walther, S. Metz, V. Falk, R. Krakor, R. Autschbach, and F.W. Mohr. Comparison of MIDCAP versus conventional CABG surgery regarding pain and quality of life. *Heart Surgery Forum*, 2(4):290–295, 1999.

[57] E. Dittrich, R. Neji, T. Schmoll, S. Schriefl, C. Ahlers, R.A. Leitgeb, and G. Langs. Detection of capillary vessels in Optical Coherence Tomography based on a probabilistic kernel. In *Medical Image Understanding and Analysis*, 2009.

[58] J.T. Dodge, B.G. Brown, E.L. Bolson, and H. T. Dodge. Intrathoracic spatial location of specified coronary segments on the normal human heart. applications in quatitative arteriography, assessment of regional risk and contraction, and anatomic display. *Circulation*, 78:1167–1180, 1988.

[59] J.T. Dodge, B.G. Brown, E.L. Bolson, and H.T. Dodge. Lumen diameter of normal human coronary arteries. influence of age, sex, anatomic variation, and left ventricular hypertrophy or dilation. *Circulation*, 86:232–246, 1992.

[60] S. Dogan, T. Aybek, E. Andressen, C. Byhahn, S. Mierdl, K. Westphal, G. Matheis, A. Moritz, and G. Wimmer-Greinecker. Totally endoscopic coronary artery bypass grafting on cardiopulmonary bypass with robotically enhanced telemanipulation: Report of forty-five cases. *Journals of Thoracic Cardiovascular Surgery*, 123:1125–1131, 2002.

[61] L. Dougherty, J.C. Asmuth, A.S. Blom, L. Axel, and R. Kumar. Validation of an optical flow method for tag displacement estimation. *IEEE Transactions on Medical Imaging*, 18(4):359–363, 1999.

[62] M.-P. Dubuisson-Jolly, Cheng-Chung Liang, and A. Gupta. Optimal polyline tracking for artery motion compensation in coronary angiography. In *Sixth International Conference on Computer Vision*, pages 414–419, 1998.

[63] T. Todd Elvins. A survey of algorithms for volume visualization. *SIGGRAPH Comput. Graph.*, 26(3):194–201, 1992.

[64] E.K. Fishman et al. *CT is us.* The Advanced Medical Imaging Laboratory, Department of Radiology, Johns Hopkins Medical Institutions, Baltimore, MD, 2006.

[65] P. Fallavollita and F. Cheriet. Robust coronary artery tracking from fluoroscopic image sequences. In *Image Analysis and Recognition*, volume 4633, pages 889–898, 2007.

[66] P. Felkel, R. Wegenkittl, and A. Kanitsar. Vessel tracking in peripheral CTA datasets – an overview. In *SCCG '01: Proceedings of the 17th Spring conference on Computer graphics*, page 232. IEEE Computer Society, 2001.

[67] M. Figl, D. Rueckert, D. Hawkes, R. Casula, M. Hu, O. Pedro, D.P. Zhang, G. Penney, F. Bello, and P. Edwards. Augmented reality image guidance for minimally invasive coronary artery bypass. In *Proc. SPIE Medical Imaging: Visualization, Image-Guided Procedures, and Modeling*, volume 6918, pages 69180P–69180P–7, 2008.

[68] M. Figl, D. Rueckert, D. Hawkes, R. Casula, M. Hu, O. Pedro, D.P. Zhang, G. Penney, F. Bello, and P. Edwards. Image guidance for robotic minimally invasive coronary artery bypass. *Computerized Medical Imaging and Graphics*, 34(1):61–68, 2010.

[69] R.W. Fischer, R.M. Botnar, K. Nehrke, P. Boesiger, W.J. Manning, and D.C. Peters. Analysis of residual coronary artery motion for breath hold and navigator approaches using real-time coronary MRI. *Magnetic Resonance in Medicine*, 55(3):612–618, 2006.

[70] C. Florin, N. Paragios, and J. Williams. Particle filters, a quasi-Monte Carlo solution for segmentation of coronaries. In J.S. Duncan and G. Gerig, editors, *Medical Image Computing and Computer-Assisted Intervention MICCAI 2005*,

volume 3749 of *Lecture Notes in Computer Science*, pages 246–253. Springer Berlin / Heidelberg, 2005.

[71] A.F. Frangi. *Three-dimensional model-based analysis of vascular and cardiac images.* PhD thesis, University Medical Center Utrecht, The Netherlands, 2001.

[72] A.F. Frangi, W. Niessen, R. Hoogeveen, T. van Walsum, and M. Viergever. Model-based quantitation of 3D magnetic resonance angiographic images. *IEEE Transactions on Medical Imaging*, 18(10):946–956, 1999.

[73] A.F. Frangi, W.J. Niessen, K.L. Vincken, and M.A. Viergever. Multiscale vessel enhancement filtering. In *Medical Image Computation and Computer-Assisted Intervention - MICCAI 98*, volume 1496 of *Lecture Notes in Computer Science*, pages 130–137. Springer, 1998.

[74] Y. Fridman. *Extracting branching object geometry via cores.* PhD thesis, University of North Carolina at Chapel Hill, Chapel Hill, NC, USA, 2004.

[75] Y. Fridman, S.M. Pizer, S.R. Aylward, and E. Bullitt. Segmenting 3D branching tubular structures using cores. In Randy E. Ellis and Terry M. Peters, editors, *MICCAI (2)*, volume 2879 of *Lecture Notes in Computer Science*, pages 570–577. Springer, 2003.

[76] O. Friman, M. Hindennach, C. Khnel, and H.O. Peitgen. Multiple hypothesis template tracking of small 3D vessel structures. *Medical Image Analysis*, 14(2):160–171, 2010.

[77] O. Friman, M. Hindennach, and H. O. Peitgen. Template-based multiple hypotheses tracking of small vessels. In *5th IEEE International Symposium on Biomedical Imaging: From Nano to Macro* [1], pages 1047–1050.

[78] V. Fuster, R.A. O'Rourke, R. Walsh, and P. Poole-Wilson. *Hurst's the Heart.* McGraw-Hill Medical, 12 edition, Dec. 2007.

[79] M. Garreau, J.L. Coatrieux, R. Collorec, and C. Chardenon. A knowledge-based approach for 3-d reconstruction and labeling of vascular networks from biplane angiographic projections. *IEEE Transactions on Medical Imaging*, 10(2):122–131, 1991.

[80] M. Garreau, A. Simon, D. Boulmier, J.-L. Coatrieux, and H. L. Breton. Assessment of left ventricular function in cardiac MSCT imaging by a 4D hierarchical surface-volume matching process. *International Journal of Biomedical Imaging*, pages 1–10, 2006.

[81] J.-M. Gorce, D. Friboulet, and I.E. Magnin. Estimation of three-dimensional cardiac velocity fields: assessment of a differential method and application to three-dimensional CT data. *Medical Image Analysis*, 1(3):245–261, 1997.

[82] V. Grau, H. Becher, and J. A. Noble. Registration of multiview real-time 3-D echocardiographic sequences. *IEEE Transactions on Medical Imaging*, 26(9):1154–1165, September 2007.

[83] M. Groher, D. Zikic, and N. Navab. Deformable 2D-3D registration of vascular structures in a one view scenario. *IEEE Transactions on Medical Imaging*, 28(6):847–860, 2009.

[84] G. Guy and G. Medioni. Inference of surfaces, 3D curves, and junctions from sparse, noisy, 3D data. *IEEE Transactions on Pattern Analysis and Machine Intelligence*, 19(1):1265–1277, 1997.

[85] J.V. Hajnal, D.L.G. Hill, and D.J. Hawkes., editors. *Medical Image Registration*. CRC Press, 2001.

[86] K. Haris, S.N. Efstratiadis, N. Maglaveras, C. Pappas, J. Gourassas, and G. Louridas. Model-based morphological segmentation and labeling of coronary angiograms. *IEEE Transactions on Medical Imaging*, 18(10):1003–1015, 1999.

[87] P.E. Hart, N.J. Nilsson, and B. Raphael. A formal basis for the heuristic determination of minimum cost paths. *IEEE Transactions on Systems Science and Cybernetics*, 4(2):100–107, 1968.

[88] W. Harvey. *Anatomical Studies on the Motion of the Heart and Blood*. Springfield, Illinois Charles C. Thomas, 5 edition, 1970. Translator: C.D. Leake.

[89] D.G. Heath, P.A. Soyer, B.S. Kuszyk, D.F. Bliss, P.S. Calhoun, D.A. Bluemke, M.A. Choti, and E.K. Fishman. Three-dimensional spiral CT duing arterial portography: comparison of three rendering techniques. *Radiographics*, 15(4):1001–1011, 1995.

[90] R.A. Heckemann, J.V. Hajnal, P. Aljabar, D. Rueckert, and A. Hammers. Automatic anatomical brain MRI segmentation combining label propagation and decision fusion. *NeuroImage*, 33(1):115–126, 2006.

[91] C. Herbradson. *Learning the Cardiovascular System*. Kellogg Community College, USA, 1999.

[92] R.J. Herfkens, C.B. Higgins, H. Hricak, M.J. Lipton, L.E. Crooks, P. Lanzer, E. Botvinick, B. Brundage, P.E. Sheldon, and L. Kaufman. Nuclear magnetic resonance imaging of the cardiovascular system: normal and pathologic findings. *Radiology*, 147(3):749–759, 1983.

[93] M.B.M. Hofman, S.A. Wickline, and C.H. Lorenz. Quantification of in-plane motion of the coronary arteries during the cardiac cycle: Implications for acquisition window duration for MR flow quantification. *Journal of Magnetic Resonance Imaging*, 8(3):568–576, 1998.

[94] M. Hosono, Y. Sasaki, M. Sakaguchi, and S. Suehiro. Intraoperative fluorescence imaging during surgery for coronary artery fistula. *Interactive Cardiovascular and Thoracic Surgery*, 10(3):476–477, 2010.

[95] R. Howe. Fixing the beating heart: Ultrasound guidance for robotic intracardiac surgery. In *Functional Imaging and Modeling of the Heart*, volume 5528 of *Lecture Notes in Computer Science*, pages 97–103. Springer, 2009.

[96] M.H. Hoyos, A. Anwander, M. Orkisz, J.P. Roux, P. Douek, and I.E. Magnin. A deformable vessel model with single point initialization for segmentation, quantification and visualization of blood vessels in 3D MRA. In Scott L. Delp, Anthony M. DiGioia, and Branislav Jaramaz, editors, *MICCAI*, volume 1935 of *Lecture Notes in Computer Science*, pages 735–745. Springer, 2000.

[97] D. Huang, E.A. Swanson, C.P. Lin, J.S. Schuman, W.G. Stinson, W. Chang, M.R. Hee, T. Flotte, K. Gregory, C.A. Puliafito, and et al. Optical coherence tomography. *Science*, 254(5035):1178–1181, 1991.

[98] L. Husmann, S. Leschka, L. Desbiolles, T. Schepis, O. Gaemperli, B. Seifert, P. Cattin, T. Frauenfelder, T. G. Flohr, B. Marincek, P.A. Kaufmann, and H. Alkadhi. Coronary artery motion and cardiac phases: Dependency on heart rateimplications for CT image reconstruction. *Radiology*, 245(2):567–576, 2007.

[99] C. Ingrassia, P. Windyga, and M. Shah. Segmentation and tracking of coronary arteries. In *Proceedings of the First Joint BMES/EMBS Conference*, volume 1, page 203, 1999.

[100] Heart & Vascular Institute. *Heart Valve Surgery.* http://www.clevelandclinic.org, 2006.

[101] Inc Intuitive Surgical. *da Vinci surgical system.* http://www.intuitivesurgical.com, 2005.

[102] J. Jia and C.K. Tang. Image repairing: Robust image synthesis by adaptative Nd tensor voting. In *Proceedings of the 2003 IEEE Computer Society Conference on Computer Vision and Pattern Recognition (CVPR'03)*, 2003.

[103] K.R. Johnson, S.J. Patel, A. Whigham, A. Hakim, R.I. Pettigrew, and J.N. Oshinski. Three-dimensional, time-resolved motion of the coronary arteries. *Journal of Cardiovascular Magnetic Resonance*, 6(3):663–673, 2004.

[104] P.T. Johnson, D.G. Heath, B.S. Kuszyk, and E.K. Fishman. CT angiography with volume rendering: advantages and applications in splanchnic vascular imaging. *Radiology*, 200(2):564–568, 1996.

[105] J. Jomier and S.R. Aylward. Rigid and deformable vasculature-to-image registration: A hierarchical approach. In Barillot et al. [17], pages 829–836.

[106] J. Jomier, V. LeDigarcher, and S.R. Aylward. Automatic vascular tree formation using the mahalanobis distance. In James S. Duncan and Guido Gerig, editors, *MICCAI*, volume 3750 of *Lecture Notes in Computer Science*, pages 806–812. Springer, 2005.

[107] J. Jomier, V. LeDigarcher, and S.R. Aylward. Comparison of vessel segmentations using STAPLE. In James S. Duncan and Guido Gerig, editors, *MICCAI*, volume 3749 of *Lecture Notes in Computer Science*, pages 523–530. Springer, 2005.

[108] A.C. Kak and M. Slaney. *Principles of Computerized Tomographic Imaging.* IEEE Press, 1988.

[109] I. Kakadiaris, A. Santamaria-Pang, and A. Pednekar. Functional morphology analysis of the left anterior descending coronary artery in EBCT images. *IEEE Transactions on Biomedical Engineering*, 57(8):1886–1896, 2010.

[110] A. Kanitsar, D. Fleischmann, R. Wegenkittl, P. Felkel, and E. Groller. CPR - curved planar reformation. In *IEEE in Visualization*, pages 37–44, 2002.

[111] A. Kanitsar, D. Fleischmann, R. Wegenkittl, D. Sandner, P. Felkel, and E. Groller. Computed tomography angiography: a case study of peripheral vessel investigation. In *IEEE in Visualization*, pages 477–481, 2001.

[112] A. Kanitsar, R. Wegenkittl, D. Fleischmann, and M.E. Groller. Advanced curved planar reformation: Flattening of vascular structures. In *Proceedings of the 14th IEEE Visualization 2003*, pages 43–50, 2003.

[113] A.P. King, R. Boubertakh, K.S. Rhode, Y.L. Ma, P. Chinchapatnam, G. Gao, T. Tangcharoen, M. Ginks, M. Cooklin, J.S. Gill, D.J. Hawkes, R.S. Razavi, and T. Schaeffter. A subject-specific technique for respiratory motion correction in image-guided cardiac catheterisation procedures. *Medical Image Analysis*, 13(3):419–431, 2009.

[114] A.P. King, C. Jansen, K.S. Rhode, D. Caulfield, R.S. Razavi, and G.P. Penney. Respiratory motion correction for image-guided cardiac interventions using 3-D echocardiography. *Medical Image Analysis*, 14(1):21–29, 2010.

[115] C. Kirbas and F. Quek. A review of vessel extraction techniques and algorithms. *ACM Computing Surveys*, 36(2):81–121, 2004.

[116] J. Kittler, M. Hatef, R.P.W. Duin, and J. Matas. On combining classifiers. *IEEE Transactions on Pattern Analysis and Machine Intelligence*, 20(3):226–239, 1998.

[117] Y. Kong, J.J. Morris Jr., and H.D. McIntosh. Assessment of regional myocardial performance from biplane coronary cineangiograms. *The American Journal of Cardiology*, 27(5):529–537, 1971.

[118] K. Krissian. Flux-based anisotropic diffusion applied to enhancement of 3-D angiograms. *IEEE Transactions on Medical Imaging*, 21(11):1440–1442, 2002.

[119] K. Krissian, G. Malandain, N. Ayache, R. Vaillant, and Y. Trousset. Model based detection of tubular structures in 3D images. *Computer Vision and Image Understanding*, 80(2):130–171, 2000.

[120] K. Krissian, X. Wu, and V. Luboz. Smooth vasculature reconstruction with circular and elliptic cross sections. In *Medicine Meets Virtual Reality Conference (MMVR06)*, volume 119, pages 273–278. IOS Press, 2005.

[121] W.H. Kruskal and W.A. Wallis. Use of ranks in one-criterion variance analysis. *Journal of the American Statistical Association*, 47(260):583–621, 1952.

[122] S. Laguitton, C. Boldak, A. Bousse, G. Yang, and C. Toumoulin. Temporal tracking of coronaries in MSCTA by means of 3D geometrical moments. In *28th Annual International Conference of the IEEE Engineering in Medicine and Biology Society (EMBS)*, pages 924–927, 2006.

[123] T. Lange, H. Lamecker, M. Hünerbein, S. Eulenstein, S. Beller, and P.-M. Schlag. Validation metrics for non-rigid registration of medical images containing vessel trees. In Thomas Tolxdorff, Jürgen Braun, Thomas Martin Deserno, Heinz

Handels, Alexander Horsch, and Hans-Peter Meinzer, editors, *Bildverarbeitung für die Medizin*, Informatik Aktuell, pages 82–86. Springer, 2008.

[124] D. Lesage. *Models, features and extraction schemes for vascular segmentation: application to the delineation of coronary arteries from 3D Computed Tomography data.* PhD thesis, Telecom ParisTech, France, 2009.

[125] D. Lesage, E.D. Angelini, I. Bloch, and G. Funka-Lea. Medial-based bayesian tracking for vascular segmentation: Application to coronary arteries in 3D CT angiography. In *ISBI* [1], pages 268–271.

[126] D. Lesage, E.D. Angelini, I. Bloch, and G. Funka-Lea. Bayesian maximal paths for coronary artery segmentation from 3D CT angiograms. In *MICCAI (1)* [2], pages 222–229.

[127] D. Lesage, E.D. Angelini, I. Bloch, and G. Funka-Lea. Design and study of flux-based features for 3D vascular tracking. In *ISBI* [3], pages 286–289.

[128] D. Lesage, E.D. Angelini, G. Funka-Lea, and I. Bloch. A review of 3D vessel lumen segmentation techniques: Models, features and extraction schemes. *Medical Image Analysis*, 13:819–845, 2009.

[129] H. Li and A. Yezzi. Vessels as 4D curves: Global minimal 4D paths to extract 3D tubular surfaces. In *Computer Vision and Pattern Recognition Workshop (CVPRW '06)*, pages 82–89, 2006.

[130] H. Li and A. Yezzi. Vessels as 4D curves: Global minimal 4D paths to extract 3D tubular surfaces and centerlines. *IEEE Transactions on Medical Imaging*, 26(9):1213–1223, 2007.

[131] H. Li, A.J. Yezzi, and L.D. Cohen. 3D multi-branch tubular surface and centerline extraction with 4D iterative key points. In Guang-Zhong Yang, David J. Hawkes, Daniel Rueckert, J. Alison Noble, and Chris J. Taylor 0002, editors, *MICCAI (1)*, volume 5762 of *Lecture Notes in Computer Science*, pages 1042–1050. Springer, 2009.

[132] Q. Li and K. Doi. Selective enhancement filters for nodules, vessels, and airway walls in two- and three-dimensional CT scans. *Medical Physics*, 30(8):2040–2051, 2003.

[133] Qingfen Lin. *Enhancement, Extraction, and Visualization of 3D Volume Dataset.* PhD thesis, Department of Electrical Engineering, Linköping University, Sweden, 2003.

[134] T. Lindeberg. Edge detection and ridge detection with automatic scale selection. *Int. J. Comput. Vision*, 30:117–156, Nov. 1998.

[135] T. Lindeberg. Feature detection with automatic scale selection. *International Journal of Computer Vision*, 30:79–116, 1998.

[136] W.E. Lorensen and H.E. Cline. Marching cubes: A high resolution 3D surface reconstruction algorithm. *SIGGRAPH Comput. Graph.*, 21(3):163–169, July 1987.

[137] C. Lorenz and J. Von Berg. A comprehensive shape model of the heart. *Medical Image Analysis*, 10(4):657–670, 2006.

[138] C. Lorenz, I.-C. Carlsen, T.M. Buzug, C. Fassnacht, and J. Weese. Multi-scale line segmentation with automatic estimation of width, contrast and tangential direction in 2D and 3D medical images. In *CVRMed-MRCAS '97: Proceedings of the First Joint Conference on Computer Vision, Virtual Reality and Robotics in Medicine and Medial Robotics and Computer-Assisted Surgery*, pages 233–242, 1997.

[139] C. Lorenz, J. von Berg, T. Bülow, S. Renisch, and S. Wergandt. Modeling the coronary artery tree. In *IEEE International Conference on Shape Modeling and Applications (SMI)*, pages 354–357, 2004.

[140] L.M. Lorigo, O. Faugeras, W.E.L. Grimson, R. Keriven, R. Kikinis, A. Nabavi, and C.-F. Westin. Codimension-two geodesic active contours for the segmentation of tubular structures. In *IEEE Conference on Computer Vision and Pattern Recognition*, volume 1, pages 444–451, 2000.

[141] L.M. Lorigo, O.D. Faugeras, W.E.L. Grimson, R. Keriven, R. Kikinis, A. Nabavi, and C.-F. Westin. CURVES: Curve evolution for vessel segmentation. *Medical Image Analysis*, 5(3):195–206, 2001.

[142] M.A. Luengo Oroz, M.J. Ledesma Carbayo, J.J. Gomez Diego, M.A. Garcia Fernandez, M. Desco, and A. Santos. Extraction of the coronary artery tree in cardiac computer tomographic images using morphological operators. In *Functional Imaging and Modeling of the Heart*, volume 4466, pages 424–432, 2007.

[143] National Heart Lung and Blood Institute. Coronary artery disease. *Diseases and Conditions Index*, 2009.

[144] Z. Luo, Y.Y. Wang, and W.Q. Wang. Estimating coronary artery lumen area with optimization-based contour detection. *IEEE Transactions on Medical Imaging*, 22(4):564–566, April 2003.

[145] M. Magnusson, R. Lenz, and P.E. Danielsson. Evaluation of methods for shaded surface display of CT volumes. *Computerized Medical Imaging and Graphics*, 15(4):247–256, 1991.

[146] R. Manniesing, M. A. Viergever, and W.J. Niessen. Vessel enhancing diffusion: A scale space representation of vessel structures. *Medical Image Analysis*, 10(6):815–825, 2006.

[147] R. Manniesing, M. A. Viergever, and W.J. Niessen. Vessel axis tracking using topology constrained surface evolution. *IEEE Transactions on Medical Imaging*, 26(3):309–16, 2007.

[148] P. Markelj, D. Tomazevic, B. Likar, and F. Pernus. A review of 3D/2D registration methods for image-guided interventions. *Medical Image Analysis*, In Press, Corrected Proof:–, 2010.

[149] Y. Masutani, T. Schiemann, and K. H. Höhne. Vascular shape segmentation and structure extraction using a shape-based region-growing model. In *MICCAI '98: Proceedings of the First International Conference on Medical Image Computing and Computer-Assisted Intervention*, pages 1242–1249, London, UK, 1998. Springer-Verlag.

[150] R.L. Maurice, J. Ohayon, Y. Fretigny, M. Bertrand, G. Soulez, and G. Cloutier. Noninvasive vascular elastography: Theoretical framework. *IEEE Transactions on Medical Imaging*, 23(2):164–180, February 2004.

[151] C. Metz, M. Schaap, S. Klein, L. Neefjes, E. Capuano, C. Schultz, R. J. van Geuns, P. W. Serruys, T. van Walsum, and W. J. Niessen. Patient specific 4D coronary models from ECG-gated CTA data for intra-operative dynamic alignment of CTA with X-ray images. In *MICCAI (1)* [2], pages 369–376.

[152] C. Metz, M. Schaap, T. van Walsum, and W. Niessen. Two point minimum cost path approach for CTA coronary centerline extraction. *Midas Journal - 2008 MICCAI Workshop - Grand Challenge Coronary Artery Tracking*, 2008.

[153] C. Metz, M. Schaap, T. van Walsum, A.G. van der Giessen, A.C. Weustink, N.R.A. Mollet, G. P. Krestin, and W.J. Niessen. Editorial: 3D segmentation in the clinic: A grand challenge II - coronary artery tracking. In *MICCAI 2008 workshop proceedings*, 2008.

[154] C. Metz, M. Schaap, A.C. Weustink, N.R.A. Mollet, T. van Walsum, and W.J. Niessen. Coronary centerline extraction from CT coronary angiography images using a minimum cost path approach. *Medical Physics*, 36(12):5568–5579, 2009.

[155] J. Mille and L.D. Cohen. Deformable tree models for 2D and 3D branching structures extraction. *Computer Vision and Pattern Recognition Workshop*, pages 149–156, 2009.

[156] J. Mille and L.D. Cohen. 3d CTA image segmentation with a generalized cylinder-based tree models. In *IEEE International Symposium on Biomedical Imaging: From Nano to Macro*, pages 1045–1048, 2010.

[157] P. Modi, E. Rodriguez, and W.R. Chitwood. Robot-assisted cardiac surgery. *Interact Cardio Vasc Thorac Surg*, 9:500–505, 2009.

[158] F.W. Mohr, V. Falk, A. Diegeler, T. Walther, J.F. Gummert, J. Bucerius, S. Jacobs, and R. Autschbach. Computer-enhanced ”robotic” cardiac surgery: Experience in 148 patients. *Journal of Thoracic and Cardiovascular Surgery*, 121(5):842 – 853, 2001.

[159] V. Mor-Avi, L. Sugeng, and R.M. Lang. Real-time 3-dimensional echocardiography: an integral component of the routine echocardiographic examination in adult patients? *Circulation*, 119:314–329, 2009.

[160] F. Mourgues, F. Devernay, G. Malandain, and È. Coste-Manière. 3D+t modeling of coronary artery tree from standard non simultaneous angiograms. In *Medical Image Computing and Computer-Assisted Intervention*, volume 2208 of *Lecture Notes in Computer Science*, pages 1320–1322, 2001.

[161] D. Mueller and A. Maeder. Robust semi-automated path extraction for visualising stenosis of the coronary arteries. *Computerized Medical Imaging and Graphics*, 32:463–475, 2008.

[162] B. Naegel, N. Passat, and C. Ronse. Grey-level hit-or-miss transforms–part I: Unified theory. *Pattern Recognition*, 40(2):635–647, 2007.

[163] B. Naegel, N. Passat, and C. Ronse. Grey-level hit-or-miss transforms–part II: Application to angiographic image processing. *Pattern Recognition*, 40(2):648–658, 2007.

[164] D. Nain, A. J. Yezzi, and G. Turk. Vessel segmentation using a shape driven flow. In Barillot et al. [17], pages 51–59.

[165] S. Nakamura, A. Colombo, A. Gaglione, Y. Almagor, S.L. Goldberg, L. Maiello, L. Finci, and J.M. Tobis. Intracoronary ultrasound observations during stent implantation. *Circulation*, 89:2026–2034, 1994.

[166] S. Napel, G.D. Rubin, and R.B. Jeffrey. STS-MIP: a new reconstruction rechnique for CT of the chest. *Journal of Computer Assisted Tomography*, 17(5), 1993.

[167] I. Nwogu and L.M. Lorigo. Fast temporal tracking and 3D reconstruction of a single coronary vessels. In *IEEE International Conference on Image Processing (ICIP)*, pages 537–540, 2007.

[168] W.C. O'Dell, C.C. Moore, W.C. Hunter, E.A. Zerhouni, and E.R. McVeigh. Three-dimensional myocardial deformations: Calculation with displacement field fitting to tagged MRI images. *Radiology*, 195(3):829–835, 1995.

[169] T. O'Donnell, T.E. Boult, X.S. Fang, and A. Gupta. The extruded generalized cylinder: a deformable model for object recovery. In *IEEE Computer Society Conference on Computer Vision and Pattern Recognition*, pages 174–181, 1994.

[170] S.D. Olabarriaga, M. Breeuwer, and W. Niessen. Evaluation of Hessian-based filters to enhance the axis of coronary arteries in CT images. In H.U. Lemke, M.W. Vannier, K. Inamura, A.G. Farman, K. Doi, and J.H.C. Reiber, editors, *Computer Assisted Radiology and Surgery*, volume 1256 of *International Congress Series*, pages 1191–1196, 2003.

[171] S.D. Olabarriaga, M. Breeuwer, and W. Niessen. Minimum cost path algorithm for coronary artery central axis tracking in CT images. In R.E. Ellis and T.M. Peters, editors, *Medical Image Computing and Computer-Assisted Intervention*, volume 2879 of *Lecture Notes in Computer Science*, pages 687–694, 2003.

[172] P. Orlowski and M. Orkisz. Efficient computation of Hessian-based enhancement filters for tubular structures in 3D images. *IRBM*, 30(3):128 – 132, 2009.

[173] N. F. Osman, E. R. McVeigh, and J. L. Prince. Imaging heart motion using harmonic phase MRI. *IEEE Transactions on Medical Imaging*, 19(3):186–202, 2000.

[174] N. Otsu. A threshold selection method from gray-level histograms. *IEEE Transactions on Systems, Man and Cybernetics*, 9(1):62–66, 1979.

[175] N. Passat, C. Ronse, J. Baruthio, J.P. Armspach, and C. Maillot. Magnetic resonance angiography: From anatomical knowledge modeling to vessel segmentation. *Medical Image Analysis*, 10(2):259–274, 2006.

[176] M. Pechaud, R. Keriven, and G. Peyre. Extraction of tubular structures over an orientation domain. *IEEE Computer Society Conference on Computer Vision and Pattern Recognition*, pages 336–342, 2009.

[177] K. Perisinakis, N. Theocharopoulos, J. Damilakis, E. Manios, P. Vardas, and N. Gourtsoyiannis. Fluoroscopically guided implantation of modern cardiac resynchronization devices. *Journal Of The American College Of Cardiology*, 46(12):2335–2339, 2005.

[178] B. Perrenot, R. Vaillant, R. Prost, G. Finet, P. Douek, and F. Peyrin. Motion correction for coronary stent reconstruction from rotational X-ray projection sequences. *IEEE Transactions on Medical Imaging*, 26(10):1412–1423, October 2007.

[179] J. Peters, O. Ecabert, C. Meyer, R. Kneser, and J. Weese. Optimizing boundary detection via simulated search with applications to multi-modal heart segmentation. *Medical Image Analysis*, 14:70–84, 2009.

[180] J.P.W. Pluim, J.B.A. Maintz, and M.A. Viergever. Mutual-information-based registration of medical images: a survey. *IEEE Transactions on Medical Imaging*, 22(8):986–1004, August 2003.

[181] R. Poli and G. Valli. An algorithm for real-time vessel enhancement and detection. *Computer Methods and Programs in Biomedicine*, 52(1):1–22, 1997.

[182] W.H. Press, S.A. Teukolsky, W.T. Vetterling, and B.P. Flannery. *Numerical Recipes in C++: The Art of Scientific Computing.* Cambridge University Press, Cambridge, UK, 2nd edition, 2002.

[183] J. Puentes, C. Roux, M. Garreau, and J.L. Coatrieux. Dynamic feature extraction of coronary artery motion using DSA image sequences. *IEEE Transactions on Medical Imaging*, 17(6):857–871, 1998.

[184] A.F.R. Rahman and M.C. Fairhurst. Multiple classifier decision combination strategies for character recognition: A review. *International Journal on Document Analysis and Recognition*, 5:166–194, 2003.

[185] E. Regar, A.M.G.J. van Leeuwen, and P.W. Serruys, editors. *Optical Coherence Tomography in Cardiovascular Research.* Informa Healthcare, 1 edition, March 2007.

[186] J.T. Reston, S.J. Tregear, and C.M. Turkelson. Meta-analysis of short-term and mid-term outcomes following off-pump coronary artery bypass grafting. *The Annals of Thoracic Surgery*, 76(5):1510–1515, Nov 2003.

[187] L. Risser, F. Plouraboue, and X. Descombes. Gap filling of 3-D microvascular networks by tensor voting. *IEEE Transactions on Medical Imaging*, 27(5):674–687, 2008.

[188] C. Rohkohl, G. Lauritsch, L. Biller, M. Prmmer, J. Boese, and J. Hornegger. Interventional 4-d motion estimation and reconstruction of cardiac vasculature without motion periodicity assumption. *Medical Image Analysis*, In Press, Accepted Manuscript:–, 2010.

[189] T. Rohlfing and C.R. Maurer. Shape-based averaging. *IEEE Transactions on Image Processing*, 16(1):153–161, 2007.

[190] K. Rohr, H.S. Stiehl, R. Sprengel, T.M. Buzug, J. Weese, and M.H. Kuhn. Landmark-based elastic registration using approximating thin-plate splines. *IEEE Transactions on Medical Imaging*, 20:526–534, 2001.

[191] J.H. Rong, J.L. Coatrieux, and R. Collorec. Motion estimation in digital subtraction angiography. In *Proceedings of the Annual International Conference of the IEEE Engineering in Medicine and Biology Society*, volume 1, pages 567–568, 9-12 1989.

[192] S. Ruan, A. Bruno, and J.L. Coatrieux. 3-Dimensional motion and reconstruction of coronary-arteries from biplane cineangiography. *Image and Vision Computing*, 12(10):683–689, 1994.

[193] D. Rueckert, L. I. Sonoda, C. Hayes, D. L. Hill, M. O. Leach, and D. J. Hawkes. Nonrigid registration using free-form deformations: application to breast MR images. *IEEE Transactions on Medical Imaging*, 18(8):712–721, 1999.

[194] D. Ruijters, B.M. ter Harr Romeny, and P. Suetens. Vesselness-based 2D-3D registration of the coronary arteries. *International journal of computer assisted radiology and surgery*, 4(4):391–397, 2009.

[195] M. Saranathan, V. B. Ho, M. N. Hood, T. K. F. Foo, and C. J. Hardy. Adaptive vessel tracking: Automated computation of vessel trajectories for improved efficiency in 2D coronary MR angiography. *Journal of Magnetic Resonance Imaging*, 14(4):368–373, 2001.

[196] L. Sarry, M. Zanca, J.Y. Boire, A. Veyre, and J. Cassagnes. Comparison of spatio-temporal tracking methods for coronaries in DSA. In *Proceedings of the 16th Annual International Conference of the IEEE Engineering in Medicine and Biology Society*, volume 1, pages 680–681, 1994.

[197] Y. Sato, N. Shiraga, H. Atsumi, S. Yoshida, T. Koller, G. Gerig, and R. Kikinis. Three-dimensional multi-scale line filter for segmentation and visualization of curvilinear structures in medical images. *Medical Image Analysis*, 2(2):143–168, 1998.

[198] Y. Sato, N. Shiraga, S. Nakajima, S. Tamura, and R. Kikinis. Local maximum intensity projection (LMIP): a new rendering method for vascular visualization. *Journal of Computer Assisted Tomography*, 22(6):912–917, 1998.

[199] M. Schaap, R. Manniesing, I. Smal, T. van Walsum, A. van der Lugt, and W.J. Niessen. Bayesian tracking of tubular structures and its application to carotid arteries in CTA. In A. Maeder N. Ayache, S. Ourselin, editor, *Medical Image Computing and Computer-Assisted Intervention - MICCAI 2007*, page 562570, 2007.

[200] M. Schaap, C. Metz, T. van Walsum, A.G. van der Giessen, A. Weustink, N. Mollet, C. Bauer, H. Bogunovifa, C. Castro, X. Deng, E. Dikici, T. ODonnell, M. Frenay, O. Friman, M. Hernandez Hoyos, P.H. Kitslaar, K. Krissian, C. Kuhnel, M.A. Luengo-Oroz, M. Orkisz, O. Smedby, M. Styner, A. Szymczak, H. Tek, C.L. Wang, S.K. Warfield, S. Zambal, Y. Zhang, G.P Krestin, and W. Niessen. Standardized evaluation methodology and reference database for evaluating coronary artery centerline extraction algorithms. *Medical Image Analysis*, 13(5):701–714, 2009.

[201] M. Schaap, L. Neefjes, C. Metz, A.G. van der Giessen, A.C. Weustink, N. Mollet, J. J. Wentzel, T. van Walsum, and W. Niessen. Coronary lumen segmentation using graph cuts and robust kernel regression. In Kyle J. Myers Jerry L. Prince, Dzung L. Pham, editor, *Information Processing in Medical Imaging 2009*, pages 528–539, 2009.

[202] M. Schaap, I. Smal, C. Metz, T. van Walsum, and W. Niessen. Bayesian tracking of elongated structures in 3D images. In *IPMI'07: Proceedings of the 20th international conference on Information processing in medical imaging*, pages 74–85, Berlin, Heidelberg, 2007. Springer-Verlag.

[203] G. Schoonenberg, R. Florent, P. Lelong, O. Wink, D. Ruijters, J. Carroll, and B. ter Haar Romeny. Projection-based motion compensation and reconstruction of coronary segments and cardiac implantable devices using rotational X-ray angiography. *Medical Image Analysis*, 13(5):785–792, 2009.

[204] J.D. Schuijf, J.J. Bax, L.J. Shaw, A. de Roos, H.J. Lamb, E.E. van der Wall, and W. Wijns. Meta-analysis of comparative diagnostic performance of magnetic resonance imaging and multislice computed tomography for noninvasive coronary angiography. *American Heart Journal*, 151(2):404–411, 2006.

[205] A. Sen, L. Lan, K. Doi, and K. R. Hoffmann. Quantitative evaluation of vessel tracking techniques on coronary angiograms. *Medical Physics*, 26(5):698–706, 1999.

[206] G. Shechter, F. Devernay, E. Coste Maniere, A. Quyyumi, and E.R. McVeigh. Three-dimensional motion tracking of coronary arteries in biplane cineangiograms. *IEEE Transactions in Medical Imaging*, 22(4):493–503, April 2003.

[207] G. Shechter, J. R. Resar, and E. R. McVeigh. Displacement and velocity of the coronary arteries: cardiac and respiratory motion. *IEEE Transactions on Medical Imaging*, 25(3):369–375, 2006.

[208] G. Shechter, B. Shechter, J.R. Resar, and R. Beyar. Prospective motion correction of X-ray images for coronary interventions. *IEEE Transactions on Medical Imaging*, 24(4):441–450, April 2005.

[209] H. Shim, D. Kwon, I.D. Yun, and S.U. Lee. Robust segmentation of cerebral arterial segments by a sequential Monte Carlo method: Particle filtering. *Computer Methods and Programs in Biomedicine*, 84(2-3):135–145, 2006.

[210] G. Slabaugh, B. Whited, J. Rossignac, T. Fang, and G. Unal. 3D ball skinning using PDEs for generation of smooth tubular surfaces. *Computer-Aided Design*, 42(1):18–26, 2010.

[211] P. Soille. *Morphological Image Analysis: Principles and Applications*. Springer-Verlag New York, Inc., 2nd edition, 2003.

[212] S.M. Song and R.M. Leahy. Computation of 3D velocity fields from 3D cine CT images of a human heart. *IEEE Transactions on Medical Imaging*, 10(3):295–306, 1991.

[213] C. Stehning, P. Boernert, and K. Nehrke. Advances in coronary MRA from vessel wall to whole heart imaging. *Magnetic Resonance in Medical Sciences*, 6(3):157–170, 2007.

[214] C. Studholme, D. L. G. Hill, and D. J. Hawkes. An overlap invariant entropy measure of 3D medical image alignment. *Pattern Recognition*, 32(1):71–86, 1999.

[215] J.S. Suri, K. Liu, L. Reden, and S. Laxminarayan. A review on MR vascular image processing algorithms: acquisition and prefiltering: part I. *IEEE Transactions on Information Technology in Biomedicine*, 6(4):324–337, 2002.

[216] J.S. Suri, K. Liu, L. Reden, and S. Laxminarayan. A review on MR vascular image processing: skeleton versus nonskeleton approaches: part II. *IEEE Transactions on Information Technology in Biomedicine*, 6(4):338–350, 2002.

[217] O. Tankyevych, H. Talbot, P. Dokladal, and N. Passat. Direction-adaptive grey-level morphology - application to 3D vascular brain imaging. In *16th IEEE International Conference on Image Processing (ICIP)*, pages 2261–2264, 2009.

[218] G.J. Tearney, S. Waxman, M. Shishkov, B.J. Vakoc, M.J. Suter, M.I. Freilich, A.E. Desjardins, W.Y. Oh, L.A. Bartlett, M. Rosenberg, and B.E. Bouma. Three-dimensional coronary artery microscopy by intracoronary optical frequency domain imaging. *J Am Coll Cardiol Img*, 1:752–761, 2008.

[219] P. Thévenaz and M. Unser. Optimization of mutual information for multiresolution image registrations. *IEEE Transactions on Image Processing*, 9(12):2083–2099, 2000.

[220] B.C.S. Tom, S.N. Efstratiadis, and A.K. Katsaggelos. Motion estimation of skeletonized angiographic images using elastic registrations. *IEEE Transactions on Medical Imaging*, 13(3):450–460, 1994.

[221] P.T.H. Truc, A.U. Khan, Y.K. Lee, S. Lee, and T.S. Kim. Vessel enhancement filter using directional filter bank. *Computer Vision and Image Understanding*, 113:101–112, 2009.

[222] Y. Tsin, K.J. Kirchberg, G. Lauritsch, and C. Xu. A deformation tracking approach to 4D coronary artery tree reconstruction. In *MICCAI '09: Proceedings of the 12th International Conference on Medical Image Computing and Computer-Assisted Intervention*, pages 68–75, Berlin, Heidelberg, 2009. Springer-Verlag.

[223] G.A. Turgeon, G. Lehmann, G. Guiraudon, M. Drangova, D. Holdsworth, and T. Peters. 2D-3D registration of coronary angiograms for cardiac procedure planning and guidance. *Medical Physics*, 32(12):3737–3749, 2005.

[224] J.A. Tyrrell, E. di Tomaso, D. Fuja, R. Tong, K. Kozak, R.K. Jain, and B. Roysam. Robust 3-D modeling of vasculature imagery using superellipsoids. *IEEE Transactions on Medical Imaging*, 26(2):223–237, 2007.

[225] J.E. van Velzen, J.D. Schuijf1, F.R. de Graaf1, G. Nucifora1, G. Pundziute1, J.W. Jukema1, M.J. Schalij1, L.J. Kroft, A. de Roos, J.H.C. Reiber, E.E. van der Wall, and J.J. Bax. Plaque type and composition as evaluated non-invasively by MSCT angiography and invasively by VH IVUS in relation to the degree of stenosis. *Heart*, 95(24):1990–1996, 2009.

[226] T. van Walsum, M. Schaap, C. Metz, A.G. Giessen, and W.J. Niessen. Averaging centerlines: Mean shift on paths. In Dimitris N. Metaxas, Leon Axel, Gabor

Fichtinger, and Gábor Székely, editors, *MICCAI (1)*, volume 5241 of *Lecture Notes in Computer Science*, pages 900–907. Springer, 2008.

[227] T. Vercauteren, X. Pennec, A. Perchant, and N. Ayache. Diffeomorphic demons: efficient non-parametric image registration. *NeuroImage*, 45(1):S61–S72, 2009.

[228] P.A. Viola and W.M. Wells. Alignment by maximisation of mutual information. In *Proceedings of the 5th International Conference on Computer Vision*, pages 15–23, 1995.

[229] D. Vivas, L. Prez de Isla, and J. Zamorano. Using echocardiography to guide interventional procedures. *Current Cardiovascular Imaging Reports*, 1:9–15, 2008.

[230] B.F. Wall and D. Hart. Revised radiation doses for typical X-ray examinations. *The British Journal of Radiology*, 70:437–439, 1997.

[231] G. Wang and M.W. Vannier. Stair-step artifacts in three-dimensional helical CT: an experimental study. *Radiology*, 191:79–83, 1994.

[232] S. Warfield, K. Zou, and W. Wells III. Simultaneous truth and performance level estimation (STAPLE): An algorithm for the validation of image segmentations. *IEEE Transactions on Medical Imaging*, 23(7):903–21, 2004.

[233] S. Warfield, K. Zou, and W. Wells. Validation of image segmentation by estimating rater bias and variance. *Med Image Comput Comput Assist Interv - MICCAI 2006*, 4191:839–847, 2006.

[234] W.R. Webb and C.B. Higgins. *Thoracic Imaging: Pulmonary and Cardiovascular Radiology.* Lippincott Williams & Wilkins, 1st edition, 2004.

[235] J. Weickert. A review of nonlinear diffusion filtering. In *Scale-Space Theory in Computer Vision*, volume 1252 of *Lecture Notes in Computer Science*, pages 1–28, 1997.

[236] J. Weickert. *Anisotropic Diffusion In Image Processing.* Teubner-Verlag, Stuttgart, Germany, 1998.

[237] S. Wesarg, M.F. Khan, and E.A. Firle. Localizing calcications in cardiac CT data sets using a new vessel segmentation approach. *Journal of Digital Imaging*, 19:249–257, 2006.

[238] C.F. Westin, L. Wigstrom, T. Loock, L. Sjoqvist, R. Kilkinis, and H. Knutsson. Three-dimensional adaptive filtering in magnetic resonance angiography. *Jounal of Magnetic Resonance Imaging*, 14(1):63–71, 2001.

[239] A.C. Weustink, N.R. Mollet, F. Pugliese, W.B. Meijboom, K. Nieman, M.H. Heijenbrok-Kal, T.G. Flohr, L.A. Neefjes, F. Cademartiri, P.J. de Feyter, and G.P. Krestin. Optimal electrocardiographic pulsing windows and heart rate: effect on image quality and radiation exposure at dual-source coronary CT angiography. *Radiology*, 248(3):792–798, 2008.

[240] B. Whited, J. Rossignac, G. Slabaugh, T. Fang, and G. Unal. Pearling: Stroke segmentation with crusted pearl strings. *Pattern Recognition and Image Analysis*, 19:277–283, 2009.

[241] B. Whited, J. Rossignacl, G. Slabaugh, T. Fang, and G. Unal. Pearling: 3D interactive extraction of tubular structures from volumetric images. In *Interaction in Medical Image Analysis and Visualization, held in conjunction with MICCAI*, 2007.

[242] M.H.F. Wilkinson and M.A. Westenberg. Shape preserving filament enhancement filtering. In *Medical Image Computing and Computer-Assisted Intervention MICCAI 2001*, volume 2208, 2001.

[243] D.L. Wilson and J.A. Noble. An adaptive segmentation algorithm for time-of-flight MRA data. *IEEE Transactions on Medical Imaging*, 18(10):938–945, 1999.

[244] O. Wink, W. J. Niessen, and M. A. Viergever. Minimum cost path determination using a simple heuristic function. *International Conference on Pattern Recognition*, 3:998–1001, 2000.

[245] O. Wink, W.J. Niessen, A.F. Frangi, B. Verdonck, and M.A. Viergever. 3D MRA coronary axis determination using a minimum cost path approach. *Magnetic Resonance in Medicine*, 47(6):1169–1175, 2002.

[246] W.C.K. Wong and A.C.S. Chung. Probabilistic vessel axis tracing and its application to vessel segmentation with stream surfaces and minimum cost paths. *Medical Image Analysis*, 11:567–587, 2007.

[247] S. Worz and K. Rohr. Segmentation and quantification of human vessels using a 3-D cylindrical intensity model. *IEEE Transactions on Image Processing*, 16(8):1994–2004, 2007.

[248] Hui Xue. *Computerized Analysis of Magnetic Resonance Images to Study Cerebral Anatomy in Developing Neonates.* PhD thesis, Imperial College London, London, UK, March 2008.

[249] G. Yang, J. Zhou, D. Boulmier, M.P. Garcia, L. Luo, and C. Toumoulin. Characterization of 3D coronary tree motion from MSCT angiography. *IEEE Transactions on Information Technology in Biomedicine*, 14(1):101–106, 2010.

[250] Y. Yang, A. Tannenbaum, D. Giddens, and A. Stillman. Automatic segmentation of coronary arteries using bayesian driven implicit surfaces. In *4th IEEE International Symposium on Biomedical Imaging: From Nano to Macro*, pages 189–192, 2007.

[251] P.J. Yim, J.J. Cebral, R. Mullick, H.B. Marcos, and P.L. Choyke. Vessel surface reconstruction with a tubular deformable model. *IEEE Transactions on Medical Imaging*, 20(12):1411–1421, 2001.

[252] Y. Yuan and A.C.S. Chung. Multi-scale model-based vessel enhancement using local line integrals. In *30th Annual International Conference of the IEEE Engineering in Medicine and Biology Society (EMBS)*, pages 2225 –2228, 2008.

[253] D.P. Zhang, E. Edwards, L. Mei, and D. Rueckert. 4D motion modeling of the coronary arteries from CT images for robotic assisted minimally invasive surgery. In *Proceedings of the SPIE Medical Imaging: Physics of Medical Imaging*, volume 7259, 2009.

[254] X.M. Zhang, S.M. Collins, and M. Sonka. Tree pruning strategy in automated detection of coronary trees in cineangiograms. In *Proceedings of the 1995 International Conference on Image Processing*, volume 3, pages 656–659, 1995.

[255] Y. Zhang, K. Chen, and S. Wong. 3D interactive centerline extraction. *The Midas Journal - 2008 MICCAI Workshop - Grand Challenge Coronary Artery Tracking*, 2008.

[256] X.J. Zhu, Z. Xue, X. Gao, Y.S. Zhu, and S.T.C. Wong. VOLES: Vascularity-oriented level set algorithm for pulmonary vessel segmentation in image guided intervention therapy. In *IEEE International Symposium on Biomedical Imaging*, 2009.

[257] X. Zhuang, K. Rhode, R. Razavi, D. J. Hawkes, and S. Ourselin. A registration-based propagation framework for automatic whole heart segmentation of cardiac MRI. *IEEE Transactions on Medical Imaging*, 29(9):1612–1625, 2010.

[258] X.H. Zhuang. *Automatic Whole Heart Segmentation Based on Image Registration*. PhD thesis, University College London, London, UK, 2010.

[259] A.P. Zijdenbos, B.M. Dawant, R.A. Margolin, and A.C. Palmer. Morphometric analysis of white matter lesions in MR images: method and validation. *IEEE Transactions on Medical Imaging*, 13(4):716–724, 1994.

[260] K. Zuiderveld. Contrast limited adaptive histogram equalization. In *Graphics gems IV*, pages 474–485. Academic Press Professional, Inc., San Diego, CA, USA, 1994.